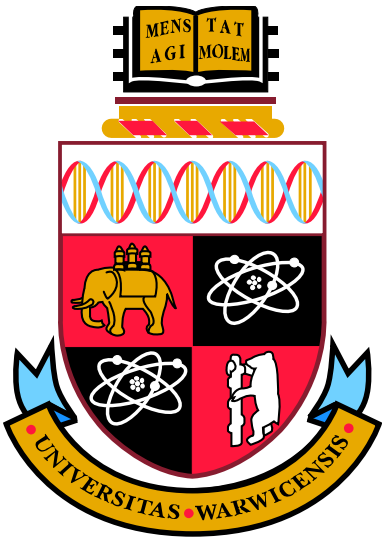

Identification of point defects in treated single crystal diamond

by

Stephanie Liggins

Thesis

Submitted to the University of Warwick

for the degree of

Doctor of Philosophy

Department of Physics

September 2010

THE UNIVERSITY OF WARWICK

Contents

List of Tables

List of Figures

Acknowledgments

I owe my deepest gratitude to Dr. Mark Newton, for his patience, support and guidance, throughout my PhD. My thanks must also go to Dr. Chris Welbourn and Prof. Michael Baker for their perspicacious comments and discussions, to Prof. Malcolm Cooper for the excellent facilities of the department and to all those who have been involved in my education and who have inspired me.

I would like to thank all the people who have contributed with their expertise and work to the realisation of this thesis: the team at DTC - Dr. Philip Martineau, Dr. David Fisher, Dr. Riz Khan; Dr. Daniel Twitchen of Element Six and Dr. Jon Goss from the University of Newcastle. DTC are also thanked for their generous financial support. My thanks also to Chris Kelly and Dr. Jim Butler for their dedicated determination in preparing the excellent stress samples used in this research.

I would like to express my sincere gratitude to all the members of the Warwick Diamond Group, past and present: Robin for sharing his love of uniaxial stress, Andy for all his technological wizardry, Brad and Bianca for their playful banter, Solveig and Ulrika for their fantastic cooking, BenG for his youthful energy and strange cravings, Sue for sharing the many hours of press frustration, Adrian and Bob of the electronics workshop, Keith and all the members of the mechanical workshop. Thank you all!

Finally, special thanks must go to my friends and family for their unconditional support and encouragement, to Ben for all his love and always believing in me and to my Mum and Dad; I hope that I have made you proud and it is to you that I dedicate this thesis.

Declarations

I declare that the work presented in this thesis is my own except where stated otherwise, and was carried out entirely at the University of Warwick, during the period of October 2006 to September 2010, under the supervision of Dr. M. E. Newton. The research reported here has not been submitted, either wholly or in part, in this or any other academic institution, for admission to a higher degree.

Some parts of the work reported and other work not reported in this thesis have been published elsewhere, as listed below:

Published papers

[1] S. Liggins, M. E. Newton, J. P. Goss, P. R. Briddon, and D. Fisher, Physical Review B **81**, 085214 (2010).

[2] S. Felton, B. L. Cann, A. M. Edmonds, S. Liggins, R. J. Cruddace, M. E. Newton, D. Fisher, and J. M. Baker, Journal of Physics: Condensed Matter **21**, 364212 (2009).

Papers in preparation for publication

[1] S. Liggins, M. E. Newton, J. P. Goss, and P. R. Briddon, Physical Review B "***Uniaxial stress investigation of substitutional nitrogen in diamond***" (2011).

[2] S. Liggins, M. E. Newton, and M. Blaauw, Diamond and Reated Materials "***Investigation of neutron irradiation effects on diamond***" (2011).

[3] A. M. Edmonds, S. Liggins, B. Cann, M. E. Newton, J. P. Goss, and P. R.

Briddon, Physical Review B "***Hydrogen related defects in diamond***" (2011).

Conference presentations

[1] S. Liggins and M. E. Newton, *Uniaxial stress splitting of nitrogen related mid and near infrared absorption bands* (2010), poster presentation at the 61st Diamond Conference (Coventry, UK).

[2] S. Liggins, R. J. Cruddace, B. L. Cann, M. E. Newton, R. U. A. Khan, P. M. Martineau, D. J. Twitchen, J. P. Goss, and P. R. Briddon, *Optical and magnetic studies of hydrogen related defects in diamond* (2010), poster presentation at the 61st Diamond Conference (Coventry, UK).

[3] S. Liggins, B. Green, C. Welbourn, and M. E. Newton, *Studies of neutron irradiation damage in natural and synthetic diamond* (2010), poster presentation at the 61st Diamond Conference (Coventry, UK).

[4] U. F. S. D'Haenens Johansson, A. M. Edmonds, S. Liggins, M. E. Newton, P. M. Martineau, R. U. A. Khan, and D. J. Twitchen, *Understanding the spin physics of the silicon split-vacancy defect in the neutral charge state* (2010), poster presentation at the 61st Diamond Conference (Coventry, UK).

[5] S. Liggins, R. J. Cruddace, B. L. Cann, M. E. Newton, R. U. A. Khan, P. M. Martineau, D. J. Twitchen, J. P. Goss, and P. R. Briddon, *EPR, IR and uniaxial stress studies of hydrogen related defects in diamond* (2010), poster presentation at the SBDD XV Hasselt Diamond Workshop (Hasselt, Belgium).

[6] S. Liggins, M. E. Newton, and J. E. Butler, *Identification of the di-nitrogen* $\langle 001 \rangle$*-split interstitial (H1a) in diamond* (2009), poster presentation at the 25th International Conference on Defects in Semiconductors (St. Petersburg, Russia).

[7] S. Liggins, S. Felton, B. L. Cann, A. M. Cruddace, R. J. an Edmonds, M. E. Newton, D. Fisher, J. M. Baker, and J. E. Butler, *Identification of interstitial nitrogen defects in diamond* (2009), oral presentation at the 60th Diamond Conference (Coventry, UK).

[8] S. Liggins, M. E. Newton, and J. E. Butler, *Uniaxial stress investigations of local vibrational modes (LVMs) in diamond* (2009), poster presentation at the 60th Diamond Conference (Coventry, UK).

[9] S. Liggins, B. L. Cann, and M. E. Newton, *Assignment of the 3123 cm^{-1} absorption line to the NVH^0 centre* (2009), poster presentation at the 60th Diamond Conference (Coventry, UK).

[10] S. Felton, S. Liggins, B. L. Cann, M. E. Newton, P. M. Martineau, and D. Fisher, *Interstitial nitrogen in diamond - Optical and EPR studies* (2008), oral presentation at the 19th European Conference on Diamond (Stiges, Spain).

[11] S. Liggins, M. E. Newton, and J. E. Butler, *Uniaxial stress splitting studies on the H1a centre in ^{15}N enriched synthetic diamond* (2008), poster presentation at the Gordon Research Conference - Defects in Semiconductors (New Hampshire, USA).

[12] S. Liggins, M. Newton, and J. E. Butler, *Uniaxial stress with infrared spectroscopy of local vibrational modes in type Ib diamond* (2008), poster presentation at the 59th Diamond Conference (Oxford, UK).

[13] S. Liggins, S. E. Burrows, and M. E. Newton, *Infrared absorption studies on brown single crystal CVD diamond annealed at high temperatures and pressures* (2007), poster presentation at the 58th Diamond Conference (Coventry, UK).

S. Liggins

September, 2010

Abbreviations

Here are a list of abbreviations commonly used in this thesis.

Γ	The representation of a symmetry group
θ/ϕ	Angle
μ	Absorption coefficient
ν	Microwave frequency
ν_m	Magnetic field modulation frequency
σ	Applied stress
$\sigma_{h/v/d}$	Horizontal/vertical/dihedral reflection operation
τ	Lifetime
ω	Oscillation frequency
$\langle hkl \rangle$	A general hkl direction
$[hkl]$	A specific hkl direction
$\{hkl\}$	A general hkl plane
(hkl)	A specific hkl plane
A	Hyperfine interaction term
A	Hydrostatic piezospectroscopic parameter
AFC	Automatic frequency control
A-centre	Two neighbouring nitrogen atoms on adjacent lattice sites
AIMPRO	Ab Initio Modelling Program
at.%	Atomic percentage - for this thesis, the ratio of defect atoms to that

	of carbon
B	Shear piezospectroscopic parameter
B	Applied magnetic field
B_m	Magnetic field modulation amplitude
B_0	Position (in magnetic field) of a resonance line
B_1	Magnetic field component of microwave radiation
C	Shear piezospectroscopic parameter
C_n	n-fold rotation operation
C_{1h}	Monoclinic symmetry
C_{3v}	Trigonal symmetry
C-centre	Isolated single nitrogen atom on a lattice site
CVD	Chemical vapour deposition
CW EPR	Continuous wave electron paramagnetic resonance
D	Zero-field interaction term
e	The identity operation
E	Energy
EM	Electromagnetic
EPR	Electron paramagnetic resonance
FTIR	Fourier transform infra-red
g_e	g value for the free-electron
g_N	Nuclear g value
GOT	Great Orthogonality Theorem
h	The order of a symmetry group
H1a	Di-nitrogen interstitial defect
$\mathscr{H}$	Spin Hamiltonian term(s)
HF-CVD	Hot-filament chemical vapour deposition
HPHT	High-pressure high-temperature
G	A symmetry group of elements obeying the Group Theory criteria
i	Inversion operation
I	Nuclear spin
IR	Infrared

ITC	Intelligent temperature controller
k	Force constant
k_B	Boltzmann constant
LOT	Little Orthogonality Theorem
LVM	Local vibrational mode
m_e	Mass of electron
MIR	Mid infra-red
MP-CVD	Microwave-plasma chemical vapour deposition
N_A	Concentration of acceptors
N_D	Concentration of donors
$\mathrm{N_S}$	Substitutional nitrogen defect
$\mathrm{N_S^0}$	Neutral single substitutional nitrogen defect
$\mathrm{N_S^+}$	Positively charged single substitutional nitrogen defect
NIR	Near infra-red
NV	Nitrogen-vacancy defect
NVH	Nitrogen-vacancy-hydrogen defect
p	Probability of energy level occupation
P	Pressure
P	Quadrupole interaction term
$P_{\mu\mathrm{w}}$	Microwave power
P1	EPR analogue of the C-centre
PIN Diode	P-type Intrinsic N-type diode
PL	Photoluminescence
ppm	Parts per million carbon atoms
ppb	Parts per billion carbon atoms
Q	Quality factor
R	Symmetry operation
R1	Di-interstitial defect
R2	Self-interstitial defect
S	Electronic spin
S_n	n-fold improper rotation operation

SALC	Symmetry-adapted linear combination
SC-CVD	Single crystal diamond grown by chemical vapour deposition
T	Temperature
T_d	Tetragonal symmetry
UV	Ultra-violet
UV-Vis	Ultra-violet visible
VH	Vacancy-hydrogen defect
WAR9	⟨001⟩-nitrogen split interstitial
WAR10	⟨001⟩-nitrogen split interstitial ⟨001⟩-carbon split interstitial pair
ZPL	Zero phonon line

Abstract

The research reported in this thesis is focused on the identification of the structure of point defects in diamond using a variety of spectroscopic techniques. The defects studied are introduced by doping during synthesis, irradiation damage and annealing. Diamond produced by high-pressure high-temperature (HPHT) synthesis and chemical vapour deposition (CVD) are studied.

The nature of the 1344 cm^{-1} local vibrational mode attributed to the neutral single substitutional nitrogen defect (N_S^0), has been studied using fourier transform infrared (FTIR) absorption spectroscopy and uniaxial stress. This work showed that this is a doubly degenerate vibrational mode at a defect with trigonal symmetry. When the stress was applied along the $\langle 111 \rangle$ and $\langle 110 \rangle$ directions, the N_S^0 defect was observed to preferentially reorientate to $\langle 111 \rangle$ directions with lowest energy. It is shown that this is consistent with previously reported electron paramagnetic resonance studies of reorientation.

Studies of the IR absorption spectrum from the N_S^0 defect have confirmed, through shifts observed upon ^{14}N:^{15}N isotopic substitution that the peaks at 950/940 cm^{-1} and 1046/1040 cm^{-1} are vibrations involving nitrogen in the positive charge state. However, uniaxial stress splitting studies on the 1332 cm^{-1} mode arising from the N_S^0 defect were inconclusive.

The vibrational properties of N_{2I} are fully described and with additional data from isotopic substitution, the uniaxial stress splitting data enables unambiguous assignment of the H1a defect to N_{2I}.

The defect responsible for the 3107 cm^{-1} LVM has not yet been identified. New evidence is presented showing that in CVD diamond, on annealing at 2200℃ (with an applied stabilising pressure), the intensity of the 3107 cm^{-1} LVM is proportional to the concentration of substitutional nitrogen squared. Possible structures for this defect are discussed.

It was found that the defect induced one-phonon absorption observed after neutron irradiation in type IIa CVD diamond could be removed by annealing at temperatures below 1600℃. The kinetics of the removal of the defect induced absorption cannot be explained in terms of the bulk migration of vacancies or interstitials.

"A diamond is a chunk of coal that is made good under pressure."

- Henry Kissinger

Chapter 1

Introduction

Definition 1 Diamond *is a mineral composed of pure carbon.*

– *Encyclopedia Britannica*

Diamond has always been of great interest. Predominantly due to its decorative qualities when cut and polished, it can catch the eye of any passer-by and is synonymous with wealth, extravagance and status; but its uses pass far beyond that. Practically, it is known for its outstanding mechanical, optical and electrical properties, making its potential almost endless and inviting extensive scientific investigation.

The term diamond derives from the Greek word "$\acute{\alpha}\delta\acute{\alpha}\mu\alpha\zeta$ - adamas" meaning *untame* or *invincible* and its use in religious icons or as engraving tools dates to early human history [1]. The fantastic properties of diamond can be understood by investigating its electronic and atomic properties, probing the heart of the precious gem.

Diamond is an allotrope of carbon, an atom of six protons and six electrons surrounded by four nearest neighbour carbon atoms in a tetrahedral configuration [2]. This creates a highly symmetric structure and the tight binding of two electrons to the nucleus, leaves the remaining four valence electrons to freely orbit and make the atom chemically active. Bonding carbons each contribute one valance electron to form the bond. This 3-dimensional network of covalent bonds is the basis of the great stability and strength of the structure (Figure 1-1).

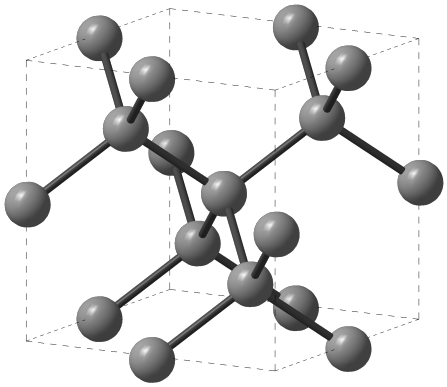

Figure 1-1: The unit cell of diamond. Diamond adopts a face centred cubic Bravais lattice in the Fd3m space group, with a two atom carbon basis at (0,0,0) and $(\frac{1}{4}, \frac{1}{4}, \frac{1}{4})$.

1.1 Synthesis of diamond

Until the mid 20th century, the supply of diamond was wholly from natural production and collected through extensive mining, principally in South Africa. Limited natural supply and growing demand from industry necessitated the development of methods to artificially synthesise diamond with reproducible and engineered properties.

1.1.1 Natural diamond

For the natural synthesis of diamond, an environment of approximately 4 GPa in pressure and a temperature between 1000–1300℃ is required that is stable over giga-years [3]. Two locations in the earth provide these conditions. The first is in the lithosphere, approximately 200 km below the crust. The diamonds found in this region are generally octahedral or twinned octahedral, the actual shape being dependent upon the exact environmental conditions. It is by deep volcanic eruptions that the diamond material is rapidly brought to the surface in magma, which may then erode or be mined to retrieve the diamonds. The second location is at meteorite impact sites.

Areas of diamond mining include south-western Africa, eastern South America, Canada, Russia and Australia. The real surge towards diamond mining began with the rushes in 1866. It soon became an exploitative trade and the diamond heyday

was an era of blood, sweat and tears, where the lucky few emerged to achieve fame, wealth and notoriety. Today, the trade is much more regulated, although still dominated by a few large companies.

1.1.2 Synthetic diamond

The growing need for the use of diamond in industrial applications, has meant that the demand now exceeds the supply of suitable natural material. Methods of synthetic production have developed over the past sixty years, such that the material can now be easily produced at various grades and with specific properties.

Since the late 1800s, it has been claimed that man can artificially replicate diamond in a laboratory [4]. Today it is accepted that these early experiments misidentified transparent, singularly refracting particles as diamond and the first true success was instead by H. T. Hall and General Electric in 1954 [5].

1.1.2.1 HPHT synthesis

High-pressure high-temperature (HPHT) synthesis is a method of replicating the environment of the earth's lithosphere. The "Belt Press", designed by Hall and General Electric, created a local environmental pressure up to 9.6 GPa and temperatures of up to 1800℃ [5]. By subjecting graphitic carbon to high pressures and temperatures in the diamond stable region of the carbon phase diagram (Figure 1-2), the source carbon could be supplied with sufficient energy to disrupt the original bonding. Bundy showed that at pressures greater than 6 GPa, the liquid carbon that resulted was of a higher density than the source carbon and the synthesis of diamond should be possible [6].

In essence, the belt press is formed of two carbide anvils, converging upon a central capsule and generating the extreme pressures and temperatures required for diamond synthesis. Outer bands (belts) compress the cell to allow it to withstand the enormous stresses within. Developments have been made in synthesis by this method. Solvent/catalysts are specifically selected to maximise the growth rate and feed gasses controlled to regulate the impurities incorporated during growth. However, growth is still slow and sample size limited. A history of the development of HPHT production can be found in "The Diamond Makers" by Hazen [7] and

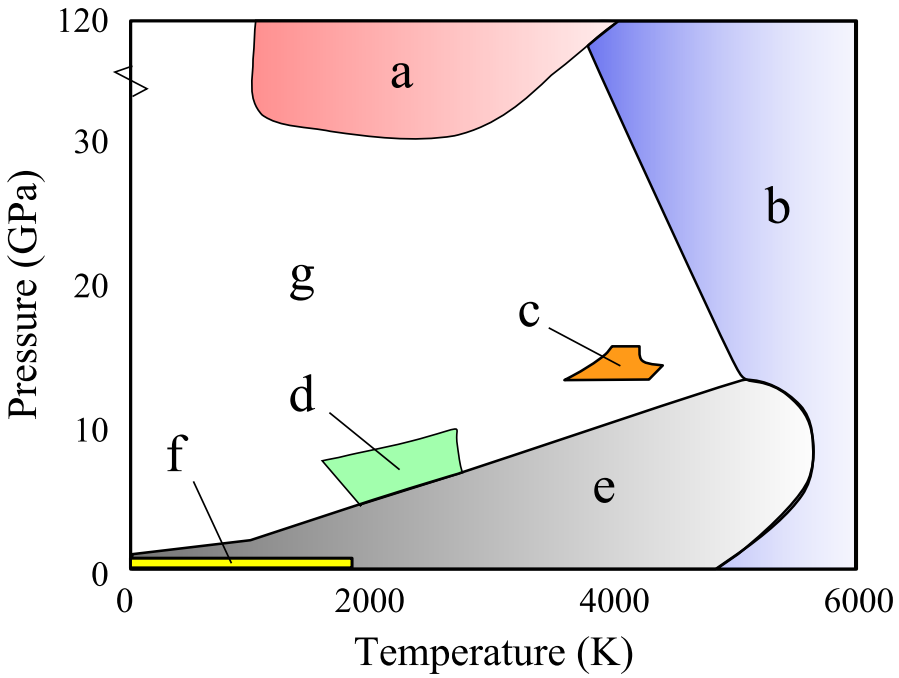

Figure 1-2: Carbon phase diagram highlighting the diamond growth regions. **a** - The region of shockwave synthesis; **b** - liquid carbon region; **c** - zone of non-catalytic HPHT synthesis; **d** - zone catalytic HPHT synthesis; **e** - graphite stable region; **f** - metastable CVD diamond region; **g** - diamond stable region.

for a more scientific review of the process of HPHT growth, the reader is referred to "Growth of Synthetic Diamond" by Burns and Davies [8].

1.1.2.2 CVD synthesis

Chemical vapour deposition (CVD) was first developed by Eversole in the 1950s. The method did not attempt to replicate the natural growth conditions, instead growing diamond from hydrocarbon and hydrogen source materials in the gas phase at low pressures (1-27 kPa). A series of gasses are streamed into a chamber and energised by a hot filament, arc discharge or microwave power to produce a plasma. By a complex chemistry process, growth occurs by deposition onto a suitable substrate, such that carbon forms the 3D bonded structure of diamond.

The results are more reliable, controllable and quickly achieved compared to the HPHT process. The growth rate can be anything from 1-1000 μm/h depending on the quality of diamond required [9].

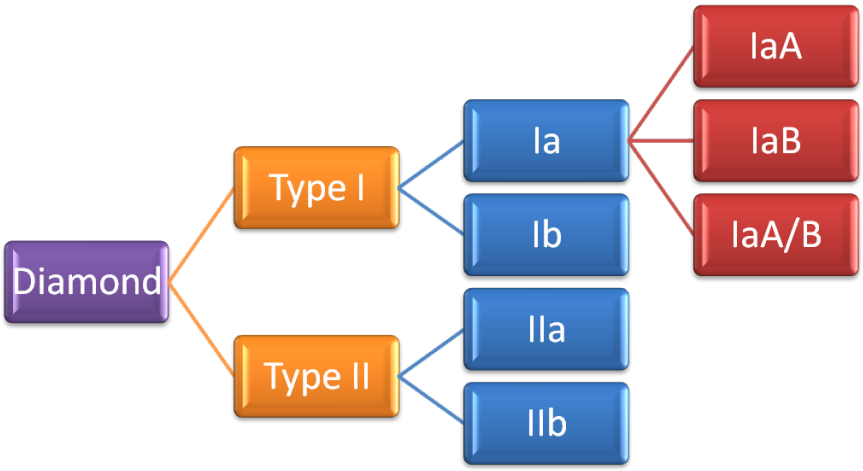

Figure 1-3: The classification of diamond

1.2 Point defects in diamond

Definition 2 *A* **defect** *is an imperfection in the regular geometrical arrangement of the atoms in a crystalline solid.*

– *Encyclopedia Britannica*

Defects and impurities can dramatically alter the bulk material's properties (optical, electrical, thermal and mechanical) and this impacts on the application of the material. The introduction of impurities, vacancies or interstitials, leads to the distortion of the diamond lattice, destroying the local symmetry. Nitrogen is renowned for being the most dominant impurity present in diamond and its influence is heavily researched. Additionally, hydrogen, silicon and boron are all currently being extensively studied, to investigate how they become incorporated, how they migrate and whether the properties resulting from their inclusion can be exploited. Defects are broadly characterised as: point defects, bounded on the atomic scale in three dimensions (e.g. the single substitutional nitrogen defect), line defects, bounded on the atomic scale in two dimensions (e.g. a dislocation) or surface defects, bounded on the atomic scale in one-dimension (e.g. large vacancy discs).

The incorporation of the most common impurities leads to the classification of diamond (Figure 1-3). Type I identifies the diamond to have a concentration of

nitrogen in the lattice detectable by IR spectroscopy (> a few ppm). This may be in a variety of forms which denotes the subclass; Ia indicates the nitrogen to be in clusters, either in the aggregated A-centre form, IaA (two nearest neighbour nitrogen atoms), the B form, IaB (four nearest neighbour nitrogen atoms surrounding a vacancy) or a combination of the two (IaA/B). The type Ib classification, indicates that nitrogen is in the dispersed, single substitutional form.

Alternatively, if the nitrogen concentration level is below detectable limits by infrared spectroscopy (< a few ppm), the sample will be classified as type II. These are very rare in nature. Type IIa samples do not display any impurity related absorption in the UV, visible or infrared parts of the spectrum. Optically, they are the most transparent of all diamonds. Diamond containing boron in an isolated substitutional position in the lattice, is classified as type IIb. Boron is a relatively shallow acceptor and its incorporation increases the electrical conductivity of the material.

Defects do not always have a negative implication for a sample. Some may be detrimental for the operation of a diamond device but in other instances, defects are essential for its performance. An obvious example, is the doping of diamond to achieve p- and n- type characteristics. Identifying shallow donor and acceptor levels is essential to ensure that conduction is realistic at reasonable temperatures. Boron is the p-type dopant in diamond but a good n-type donor that can be readily incorporated has yet to be identified.

Some defects are desirable in their own right, for example the nitrogen-vacancy (NV) centre. The attraction of NV^- is its capability to act as a single photon source and/or a quantum bit in quantum information processing, where its long spin coherence time is exploited [10]. For a greater review on the developments of quantum information processing, the reader is directed to papers by Kennedy, Kok, Walderman and Stoneham [11–14].

1.3 Properties and applications of diamond

The combination of extreme properties is what makes diamond so attractive for a wide range of applications.

Table 1-1: A comparison of the properties of diamond with other semiconductors. Table adapted from Hadlington [18].

Property	**Si**	**SiC**	**GaN**	**Diamond**
Bandgap (eV)	1.1	3.2	3.44	5.5
Breakdown field ($MV\,cm^{-1}$)	0.3	3	5	20
Electronic mobility ($cm^2\,V^{-1}\,s^{-1}$)	1450	900	440	4500
Hole mobility ($cm^2\,V^{-1}\,s^{-1}$)	480	120	200	3800
Thermal conductivity ($W\,m^{-1}\,K^{-1}$)	150	500	130	2400

1. Broad optical transmission spectrum (terahertz to UV)
2. Highest thermal conductivity at room temperature ($2500\,W\,m^{-1}\,K^{-1}$) [15]
3. Low thermal expansion ($1.05\times10^{-6}\,K^{-1}$)
4. High tensile strength
5. Highest Young's modulus (1223 GPa) [16]
6. Highest Knoop hardness ((100) face: 88–147 GPa, (110), (111) face: 98 GPa)
7. Good electrical insulator with a high breakdown field (intrinsic diamond) / Good electrical conductor (doped diamond)
8. High carrier mobility
9. Low dielectric constant (5.7 at 300 K)
10. Wide electronic band gap (5.5 eV) [17]
11. Good bio-compatibility

A summary of electronic properties in diamond in comparison to other semiconductors is outlined in Table 1-1. Many of these unique properties result from the diamond structure. To form four sp^3 hybrid orbitals, it is necessary to promote a 2s electron to the 2p shell ($1s^2 2s^2 2p^2 \rightarrow 1s^2 2s^1 2p^3$). Whilst energetically expensive, the resulting covalent bonding and the sharing of electrons forming complete electron shells, offsets the cost. The sp^3 bonding gives diamond its tetrahedral symmetry.

The strength of these bonds and the three-dimensional stability of the tetrahedral configuration, gives diamond its extreme mechanical hardness, chemical stability and radiation hardness. The covalently bonded structure also permits the transfer of atomic vibrations throughout the lattice with ease and hence gives

rise to the high thermal conductivity.

The combination of hardness and high thermal conductivity gives diamond excellent properties for use in tools for grinding, sawing and drilling (except of steel, where the alloyed materials, including iron, can react with the diamond drill bit and contribute to its degradation). For many of these applications, small, low quality diamonds are required and hence HPHT synthetic material is used.

CVD synthesis gives additional flexibility over the size and shape of the grown material. CVD grown diamond is used in applications where the control over defect inclusion and diamond properties are more important. Developing applications include:

- RF, microwave and laser optics
- Raman lasers
- Protective coatings
- Thermal management
- Power electronics
- Electrochemistry (metallic boron doped diamond)
- Acoustic devices (e.g. diamond tweeters)
- Radiation detectors

1.4 Motivation for research

The HPHT treatment of diamond is known to have the result of improving colour and therefore increasing the value of a gem [19]. Therefore, from the perspective of the gem industry, it is important to be able to differentiate between natural, synthetic and treated (those which have been irradiated and/or annealed) diamonds. As techniques to optimise growth and the properties of diamond rapidly advance, improved and more sophisticated methods of discrimination are essential [20, 21]. Studies of the defects in diamond, their incorporation and their behaviour can help with this. As growth techniques vary, the incorporation of defects will also vary and tell-tale signs of specific processing or growth methods may be identifiable. In addition, the development for semiconductor technologies (e.g. doping in synthesis, defect implantation, annealing etc.), require a sound understanding of

defect formation, structures and interactions. Controlling the properties through defect engineering is often the challenge that must be met for high technological exploitation.

1.5 Thesis outline

This thesis focuses on the investigation of a number of defects found in synthetic material as a result of treatment processes. A number of studies have been executed to investigate these defects, considering their symmetry, structure and behaviour by techniques such as annealing, irradiation, uniaxial stress and optical spectroscopy. The application of these techniques and the theory behind them will be introduced to aid the understanding of the later experimental chapters, where new results will be presented and discussed.

Chapter 2 reviews the literature of the field of diamond growth and defect incorporation. Much work exists on the identification of common defects seen by a multitude of observational techniques and yet the catalogue of defects which are understood in terms of their growth conditions, symmetry and composition, is still limited. This review will consider the specific work published on electron and neutron irradiation of diamond and the two most commonly identified impurities in diamond, nitrogen and hydrogen. It aims to provide an introduction to the work presented in later chapters, bringing the reader up-to-date with the field, areas of interests and related challenges.

Chapter 3 will introduce the theory behind the key research techniques exploited in this thesis. Optical absorption spectroscopy plays a fundamental role and its use in identifying defects, considering composition and understanding symmetry is discussed. The analytical basis of group theory is outlined for use in analysing data from uniaxial stress experiments and identification of crystal symmetry. Following from this, chapter 4 considers the practical application of these theories and their integration into analytical techniques such as annealing, optical spectroscopy and uniaxial stress experiments.

Chapter 5 is the first of the experimental results chapters presented. This extends the work already published considering the single substitutional nitrogen

defects in the neutral and positive charge states in diamond. Uniaxial stress experiments are used to study LVMs observed in infrared absorption spectra originating from substitutional nitrogen defects. Furthermore, evidence for the reorientation of the N_S^0 defect under uniaxial stress is discussed and evidence for the changing site occupation probability, presented.

Chapter 6 reports conclusive identification of the di-nitrogen interstitial defect. The use of optical spectroscopy in conjunction with uniaxial stress has assigned the structure of this defect, achieving a result that is in excellent accord with theory.

Chapter 7 considers some common hydrogen related defects present in CVD diamond, specifically those defects responsible for absorption in the 2750–3400 cm^{-1} C–H stretch region of the infrared spectrum. A conclusive reassignment of the 3123 cm^{-1} defect is made, together with a determination of the conversion factor for the quantification of its concentration. The previously proposed structure responsible for the 3107 cm^{-1} LVM is disproved and reassigned to the 3324 cm^{-1} LVM. Many questions still surround the structure of the defect responsible for the 3107 cm^{-1} LVM. New data on its production in CVD diamond are presented.

Chapter 8 presents new data on the effects of neutron irradiation on type Ib and IIa diamond. Annealing and uniaxial stress studies identify the symmetry of some of the more prominent defects and an insight into the repair of irradiation damage is presented. However, this chapter highlights that more work is required considering the effect of neutron damage in diamond.

Chapter 9 aims to summarise the key results of this research and its contribution to the field of diamond research. It outlines the areas where substantial further work is still required, giving some suggestions for future experimentation.

This thesis aims to be a comprehensive report of the previous three and a half years of experimental work, focussing on gaps in important areas of diamond defect research and contributing to the body of knowledge required for understanding the processing and treatment of diamond.

References

[1] Pliny the Elder, *Natural History - A Selection*, Penguin Classics (Penguin Classics, 1991).

[2] H. O. Pierson, *Handbook of Carbon, Graphite, Diamond and Fullerenes* (Noyes Publications, 1993).

[3] J. W. Harris, *The Properties of Natural and Synthetic Diamond* (Academic Press, 1992), chap. 9 - Diamond Geology, pp. 345–393.

[4] J. E. Hannay, Proceedings of the Royal Society of London **30**, 188 (1880).

[5] H. T. Hall, Tech. Rep., General Electric Company, USA (1955).

[6] F. P. Bundy, Journal of Chemical Physics **38**, 618 (1963).

[7] R. M. Hazen, *The Diamond Makers* (Cambridge University Press, 1999).

[8] R. Burns and G. Davies, *The Properties of Natural and Synthetic Diamond* (Academic Press, 1992), chap. 10 - Growth of Synthetic Diamond, pp. 395–422.

[9] Q. Liang, C.-s. Yan, Y. Meng, J. Lai, S. Krasnicki, H.-k. Mao, and R. J. Hemley, Diamond and Related Materials **18**, 698 (2009).

[10] T. A. Kennedy, J. S. Colton, J. E. Butler, R. C. Linares, and P. J. Doering, Applied Physics Letters **83**, 4190 (2003).

[11] T. A. Kennedy, F. T. Charnock, J. S. Colton, J. E. Butler, R. C. Linares, and P. J. Doering, Physica Status Solidi (b) **233**, 416 (2002).

[12] P. Kok and B. W. Lovett, Nature **444**, 49 (2006).

[13] F. Waldermann, P. Olivero, J. Nunn, K. Surmacz, Z. Wang, D. Jaksch, R. Taylor, I. Walmsley, M. Draganski, P. Reichart, et al., Diamond and Related Materials **16**, 1887 (2007).

[14] A. M. Stoneham, A. H. Harker, and G. W. Morley, Journal of Physics: Condensed Matter **21**, 364222 (2009).

[15] J. W. Vandersande, in *Properties and Growth of Diamond*, edited by G. Davies (INSPEC, London, 1994), chap. 1.7, pp. 33–35.

[16] S.-F. Wang, Y.-F. Hsu, J.-C. Pu, J. C. Sung, and L. G. Hwa, Materials Chemistry and Physics **85**, 432 (2004).

[17] C. D. Clark, P. J. Dean, and P. V. Harris, Proceedings of the Royal Society of London Series A **277**, 312 (1964).

[18] S. Hadlington, IEE Review **51**, 31 (2005).

[19] D. Fisher and R. A. Spits, Gems and Gemology **36**, 42 (2000).

[20] W. Wang, T. Moses, R. C. Linares, J. E. Shigley, M. Hall, and J. E. Butler, Gems and Gemology **39**, 268 (2003).

[21] C. E. Welbourn, Gems and Gemology **42**, 34 (2006).

Chapter 2

Literature Review

2.1 Introduction

To review the entire field of diamond physics would be an immense task and hence this chapter aims to review the key works and results relevant to this thesis. Topic specific reviews can be found in each chapter.

This literature review will provide a brief overview of the current methods of growth for synthetic diamond, since an understanding is beneficial when considering how defects can be incorporated and manipulated. Furthermore, key point defects will be reviewed, together with key methods for their detection.

2.2 The growth of diamond

The process of diamond growth does not differ greatly from the synthesis of other crystals. The complication is that diamond is not the thermodynamically stable form of carbon at room temperature and atmospheric pressure. Two principal methods exist for the growth of synthetic diamond: creating a high-pressure high-temperature (HPHT) environment for a carbon rich material and by chemical vapour deposition (CVD) of carbon.

2.2.1 HPHT growth

The discovery that diamond was solely composed of carbon was reported in 1797 by Smithson Tennant [1] and ever since, there have been efforts to turn other

forms of carbon into diamond, a commodity rated as one of the most precious on earth. Many attempted to replicate the Earth's natural conditions in a laboratory environment and synthesise diamond (Hannay [2], Moisson [3], Parsons [4–6]) but with no success. Greater research was needed on the exact relation of pressure, temperature and diamond growth [7–10]. Experiments by Bridgman operated well within the diamond stable region (Figure 1-2) but still diamond was not successfully synthesised [11]. Simple extreme compression of graphite at higher and higher pressures led to no structural change of the initial material and the conclusions labelled graphite as "*...nature's best spring*". The problem was not therefore simply performing the experiment in the diamond stable region but also the large kinetic barrier between sp^2 and sp^3 hybridised diamond.

There was no reliable report of man-made diamond until the mid-1950s. Discussion exists as to whether the first successful synthesis was made by the Americans or the Swedish. The first "reports" were published by General Electric, who had explored the option of using a metal solvent to overcome the hybridisation problem, as first suggested by Leipunskii in 1939. Bundy developed new equipment capable of holding pressures and temperatures in the diamond stable region for prolonged periods, with Bovenkerk *et al.* investigating carbon in different forms and the effect of the addition of other gasses and impurities [12, 13]. Ultimately, it led to the first successful synthesis of diamond from graphite, which was rapidly followed by the announcement of production by De Beers and the Adamant Research Laboratory. The technique used today remains largely unchanged, utilising metals such as nickel, cobalt and iron as common solvents/catalysts.

The HPHT synthesis process can be divided into two, both involving source materials in solution. The *temperature gradient* method uses a temperature difference between the source materials and the growing diamond, causing a difference in solubility and subsequently supersaturation which drives the growth of the crystal. In the *allotropic change* method, the difference in solubility arises from the allotropic difference between the source and diamond. Ultimately, the exact method depends upon the type of diamond that is required and the job for which it is intended but generally, pressures between 5 and 6 GPa and temperatures of 1300-1500 K are required. The procedure and apparatus of HPHT synthesis is

well reviewed and shall not be discussed further. Instead, the reader is directed towards reviews by Muncke and Wedlake [10, 14].

2.2.1.1 Dopant control in HPHT growth

Nitrogen is the most prevalent incorporated defect in HPHT growth. The growth capsule contains air, acting as a primary source of nitrogen and other abundant gasses. By this technique, the incorporated concentration of nitrogen may be of the order of several hundred parts per million of carbon atoms (ppm) [15]. Typically, nitrogen is incorporated as a single, isolated, substitutional defect [16], although under the high temperature conditions of this process, aggregation can occur during growth, resulting in the formation of A-centres (two nearest neighbour nitrogen atoms) [17].

Commonly, a *nitrogen getter* is added to the solvent/catalyst mixture. Metals such as aluminium, titanium or zirconium are added which have a strong affinity to nitrogen [18–20]. Whilst the concentration of incorporated nitrogen may be reduced, some part of the getter material may become incorporated into the final diamond. An alternative method and one used in the production of samples for this thesis, is that of high-temperature degassing. Prior to growth, the growth capsule is degassed, removing all atmospheric gasses from the growth environment at lower than growth temperatures [21]. This volume can then be purged with a desired alternative, such as $^{15}N_2$ gas or methane, before being taken to the desired conditions for diamond synthesis to occur. Intentional doping can also occur by this method, by the direct addition of gasses, such as diborane (B_2H_6), phosphine (PH_3) or silane (SiH_4) to the growth capsule.

It is understood that the uptake of nitrogen varies between the growth sectors [22–24]. It was found that the {111} sectors demonstrated the greatest uptake of nitrogen followed by {100}, {113} and {110}. The incorporation was also found to have some temperature dependence, with the efficiency of incorporation increasing in the {111} and {100} sectors as temperature increased, this being most significant in the {100} sectors [25]. The solvent/catalyst used can also have a significant effect on the incorporation of nitrogen [26, 27].

2.2.2 CVD growth

In 1962, Eversole of the Union Carbide Corporation in the USA, reported the first demonstration of the CVD growth of diamond [28, 29]. This method involved growing diamond on diamond seeds. Substrates were heated between 1200 and 1500 K, where, by a method of thermal decomposition at a pressure of one atmosphere, a gas containing methyl groups was used for the growth of diamond upon the seed. A black carbon (graphite) was reported to develop and periodically, the seed would require cleaning to remove the graphitic layer before the process could be repeated to continue the growth of the diamond. Growth rates were low, typically of the order of 0.1μm per hour and used a hot filament process to activate the methane/hydrogen gas mixture. A step towards making this method commercially viable came in 1968, when research found that the addition of atomic hydrogen into the growth chemistry favoured the formation of the sp^3 bonding structure of diamond over the undesirable sp^2 bonding of graphite [30, 31].

Many methods can be used to activate the gas mixture, the most simple being where a hot filament is placed close to the substrate at 2300 K (HF-CVD). Whilst simple in design, contamination of the film from the filament is significant. A thorough review of the hot-filament CVD method is presented by Argoitia [32].

An alternative method for the activation of the precursors, is by a microwave plasma (MP), first reported by Kamo from the National Institute for Research in Inorganic Materials (NIRIM) in Japan [33]. The possibility of electrode contamination is removed. Whilst the exact set-up of the apparatus may vary between reactors, the essential design has become a widespread technique for diamond growth. As with HF-CVD, MP-CVD is well reviewed in the Handbook of Industrial Diamonds and Diamond Films [34].

Today, MP-CVD is being used to produce electronic and optical-grade single crystal synthetic diamond, when grown on good quality, HPHT synthesised, diamond substrates. Research now focusses on the cost optimisation of the process, source materials and identification of ideal recipes to maximise growth control and rate.

The choice of substrate and its growth direction, has been shown to have an effect on the quality of diamond produced. Best control and highest quality are

achieved on {001}-orientated substrates [35]. The preparation of the substrate is as significant as optimisation of the growth conditions and chemistries involved. Surface roughness and dislocations in the substrate can propagate into the grown structure, reducing the ultimate quality of the product and the resultant properties the sample will have.

In terms of growth parameters, important considerations include the ratio of methane to hydrogen in the growth gasses, the microwave plasma power density, substrate temperature, impurities and gas pressures. These all impact on growth rate, defect density and surface morphology [36–41]. Controlled growth of single-crystal diamond has been achieved at rates of up to 19 µm, when plasma densities in the range of 65–125 $W\,cm^{-3}$ were used [42]. Higher plasma densities require substrates to be cooled (1100-1200 K), to maintain the control over growth and higher concentrations of methane are needed as surface etching of the diamond becomes a significant competitor to diamond growth [41].

2.2.2.1 Dopant control in CVD growth

As with HPHT growth, intentional but also unintentional doping of the growth material needs to be considered. Whilst there is significantly greater atmospheric control with the CVD reactor, the hardware components can act as a source of impurities, which may ultimately become incorporated into the lattice. Nitrogen is an obvious consideration. This may enter as an impurity in source gasses or due to leakage of the reactor. High concentrations of nitrogen present in CVD growth have been shown to have a detrimental effect on the quality of the growth layers [43]. When the majority of CVD grown diamond is for use in optical and electronic applications, the reduction of nitrogen content is essential to maximise the desired properties. Isolated nitrogen concentrations even as low as 1 ppb, can make the grown material unsuitable for its intended purpose [44, 45]. A second substantial consideration are the potential sources of silicon that exist within the chamber, such as the walls or windows. It must therefore be considered as a significant contaminant in CVD grown diamond.

Research with polycrystalline material showed that the incorporation of nitrogen not only changed the properties of the resulting sample but also had a sub-

stantial effect on the surface morphology and growth rates of the diamond [46, 47]. Even the addition of nitrogen of concentrations of 2–10 ppm, led to an increased growth rate of 2.5 times [48].

2.3 Irradiation of diamond

It is well known that specific treatments can be used to enhance gemological characteristics and therefore the value of a sample; for example laser drilling and fracture filling and more specifically colour treatments to improve a white diamond's colour grade or to enhance a white diamond and give it a fancy colour [49, 50]. Government agencies and confederations including the CIBJO (Confédération Internationale de la Bijouterie, Joaillerie et Orfèvrerie) or World Jewellery Confederation, explicitly require the disclosure of diamond treatments at the point of sale. However, enhancement treatments may have a positive influence on the properties of diamond for the industrial market. Therefore, understanding is required to identify key markers of treatments in diamonds. Many processes can be used to treat diamond but this thesis will focus on the effects of irradiation (neutron and electron) and annealing and hence, this will be the focus here.

First experiments on the effects of radiation on diamond were performed by Crookes in 1904 using radium salts [51]. These experiments slowly turned the diamond colour a dark green, although penetration by the α-particles was very shallow and left the diamonds highly radioactive. Today, diamonds are irradiated in four principal ways: proton bombardment by cyclotrons, gamma-ray bombardment by exposure to cobalt-60, neutron bombardment via nuclear reactors and by electron bombardment via Van de Graaf generators.

Diamond is considered a *radiation hard* material [52] but bombarding the diamond lattice with high energy particles will lead to the displacement of carbon atoms from their lattice sites; defects in the form of vacancies and interstitials (defects occupying sites other than those at lattice positions) result. The introduction of these radiation damage centres can substantially change the properties of the lattice, with annealing causing the mobility of these defects and the potential for the formation of complex lattice defects.

Low energy particles bombarding a solid may interact in one of two ways; if charged, they may ionise a lattice atom and if they collide with a lattice atom, they may knock the atom from its lattice site. The result of the collision with sufficient energy will be a cascade of damage in the lattice [53]. The level of damage induced in the lattice is highly dependent upon the irradiating particle, its momentum and charge.

2.3.1 Neutron irradiation

Neutrons have zero charge and therefore their main interaction through the diamond is ballistic. Carbon has a very low cross-section for neutron interaction [54]. As a result, the particle will have a long path length in diamond and be scattered very little when at a low energy. However, scattering is extremely energy dependent.

For neutrons at 1 MeV interacting with carbon, the total cross-section is approximately 2.5 barns[1] [54]. As a consequence, 87.9% of neutrons pass through a 300 µm sample without any interaction, resulting in more uniform damage than electron irradiation which may only penetrate a few millimetres. This leads to a near homogeneous distribution of vacancies in the lattice, at a rate of approximately 44 vacancies cm^{-1} [54].

The majority of the damage in neutron irradiation is not from the interacting neutron but from the cascade of secondary damage from the displaced carbon atoms. The displacement-threshold energies for type IIa diamond are reported as 37.5 ± 1.2 eV in the [100] direction, 45.0 ± 1.3 eV in the [111] direction and 47.6 ± 1.3 eV in the [110] direction [55]. Multiple vacancies and damage clusters will result and hence the concentration of vacancies will increase deeper into the crystal. TRIM (TRansport of Ions in Matter) modelling has calculated the depth profile of vacancies to be constant beyond a depth of 200 nm and a truer average value of vacancy production to be $68 \pm 7\,cm^{-1}$ [54].

[1] A barn (b) is a unit of area commonly used in nuclear physics for expressing the cross-sectional area of nuclei with nuclear reactions. $1b = 10^{-28} m^2$.

2.3.2 Electron irradiation

The dominant effect in irradiation by electrons is the energy loss due to electronic excitation. When the electron is incident upon a lattice atom, the excess kinetic energy transferred to the displaced atom is insufficient for it to cause a secondary effect. The probability is therefore that electrons will form single, isolated vacancy defects during irradiation [54]. For a 1 MeV electron beam, it is calculated that the beam density is 1.5 ± 0.3 electrons cm^{-1} and for a 2 MeV beam, 1.7 ± 0.3 electrons cm^{-1}.

2.3.3 Irradiation damage centres

Prior to irradiation, type IIa diamond shows minimal absorption below the fundamental absorption edge at 5.5 eV. However, following irradiation, sharp absorptions in the 1.6–2.5 eV region are observed, labelled GR1 (General Radiation 1), with an additional absorption at 2.9 eV [56]. This causes the green/blue colouration in samples and was concluded to result from either an isolated vacancy or an interstitial carbon atom. As irradiation dose increases, so too does the intensities of the lines and the intensity of the colouration. On cooling, the GR1 band resolves to a sharp line at 1.673 eV, accompanied by broader side bands at higher energies, labelled GR2–8.

The GR1 defect was identified as having tetrahedral symmetry, with the ZPL (zero phonon line) originating from an $E \rightarrow T$ transition at that defect [57, 58]. It was assigned to the neutral vacancy defect as a result of its stability at temperatures of the order of 900 K and its decaying by second order kinetics [59]. Theory identified the defect to have several possible ground states with similar energies and different multiplicities [60]. The neutral vacancy centre was found to migrate more readily than the negative state, with a migration energy of 2.3 ± 0.3 eV [61]. The ground state of the neutral vacancy is diamagnetic and therefore cannot be detected by EPR (electron paramagnetic resonance). The $^5A_2$ excited state of the neutral vacancy is observed by the illumination of an irradiated sample, indicating an effective electronic spin of the neutral vacancy of $S = 2$ [62]. The negative charge state of the vacancy defect has also been identified by EPR, with an effec-

tive spin $S = 3/2$ [63]. The optical analogue is labelled ND1 with a sharp ZPL at 3.149 eV [64].

A significant number of vacancies will migrate to form new complexes with other defects upon annealing but recombination with the interstitial, simultaneously formed with the vacancy, will account for a substantial decrease in vacancy concentration in the temperature range 600-700℃. Annealing at temperatures of the order of 1100 K leads to the formation of a substantial concentration of di-vacancies [65].

The vacancy defect has been well investigated by optical [58, 64, 66–68] and EPR studies [62, 63] and substantial reports also exist considering interstitial related defects. For every vacancy created upon 1-2 MeV irradiation at 77 K, an equal number of interstitials also exist [69]. However, excitation enhanced migration of the interstitial has been shown when irradiation occurs at higher temperatures, indicating an activation energy of 0.3 eV [70]. This migration can explain the formation of di-interstitial defects upon irradiation at room temperature [71], as opposed to an activation energy for migration calculated at 1.6 eV for annealing post irradiation [70, 71].

Four potential interstitial structures have been proposed in literature, tetrahedral, bond-centred, ⟨100⟩-split interstitial and ⟨110⟩-split interstitial [72]. The only stable structure of the interstitial atom is in the ⟨001⟩-spilt interstitial model (D_{2d} symmetry), irrelevant of the charge state and it is modelled to have the lowest energy configuration [73, 74]. All others were hypothesised to be unstable.

The R2 EPR defect was first observed by Faulkner and Lomer in 1962 and is associated with the ⟨001⟩-spilt interstitial defect [73, 75–77]. This EPR signal is usually the most prevalent in EPR studies of radiation damaged diamond. Optically, the recognised vibronic transition of this defect is the absorption peak at 1.859 eV [78–81]. Additionally, the 1.685 eV feature is also associated with this interstitial defect and the concentration of the defect within diamond can be inferred from the intensity of these features [79].

An upper limit for the migration of this I^0 defect is 1.7 eV [72]. Annealing studies of low temperature irradiated diamond, has proposed that the interstitial is mobile below temperatures of 80 K and furthermore, that the formation of R1

([I–I]^0), improbable by irradiation alone, is formed after irradiation at 300 K [82].

The R1 defect, first observed at room temperature in type IIa irradiated diamond [83], is acknowledged to be the di-interstitial, an aggregate of two ⟨001⟩-spilt interstitials on adjacent lattice sites [71]. Both R1 and R2 as observed by EPR are in the neutral charge state. However, in type Ib diamond, where there is a significant concentration of nitrogen, the nitrogen may act as an electron donor. The result is for these interstitial defects to be in the negative charge state with $S = 0$ and therefore EPR invisible [22].

2.4 Common defects in diamond

The vast array of defects possible within diamond are too numerous for them all to be mentioned here. This thesis will therefore be concerned only with those arising from the presence of nitrogen or hydrogen impurities and the effects of annealing and irradiation on those defects and the diamond lattice. An overview is presented in Figure 2-1.

2.4.1 Nitrogen in diamond

Nitrogen is one of the most dominant impurities in both natural and HPHT synthetic diamond. It has therefore become one of the most important to understand. Neutral single substitutional nitrogen is a deep donor [84]. It is dominant with regards to the optical properties of diamond; nitrogen related defects, specifically N_S^0 and N3 (3N+V) are important in determining the colour of the diamond.

Extensive studies, by both optical and EPR spectroscopy, have been completed with regards to the single substitutional nitrogen N_S^0 centre in diamond, to gain an understanding of its structure and symmetry [85–90]. Subsequently, it is well accepted that nitrogen forms four bonding orbitals with neighbouring carbon atoms of the diamond lattice. However, the extra electron of nitrogen ($1s.2s^2.2p^3$) compared to carbon, occupies a highly localised anti-bonding orbital, directed along one of the N-C bonds. As a result, the length of the N-C′ bond is elongated by approximately 28% compared to other lattice C-C bonds [91]. The neutral defect therefore undergoes a trigonal distortion, with the nitrogen atom and one carbon

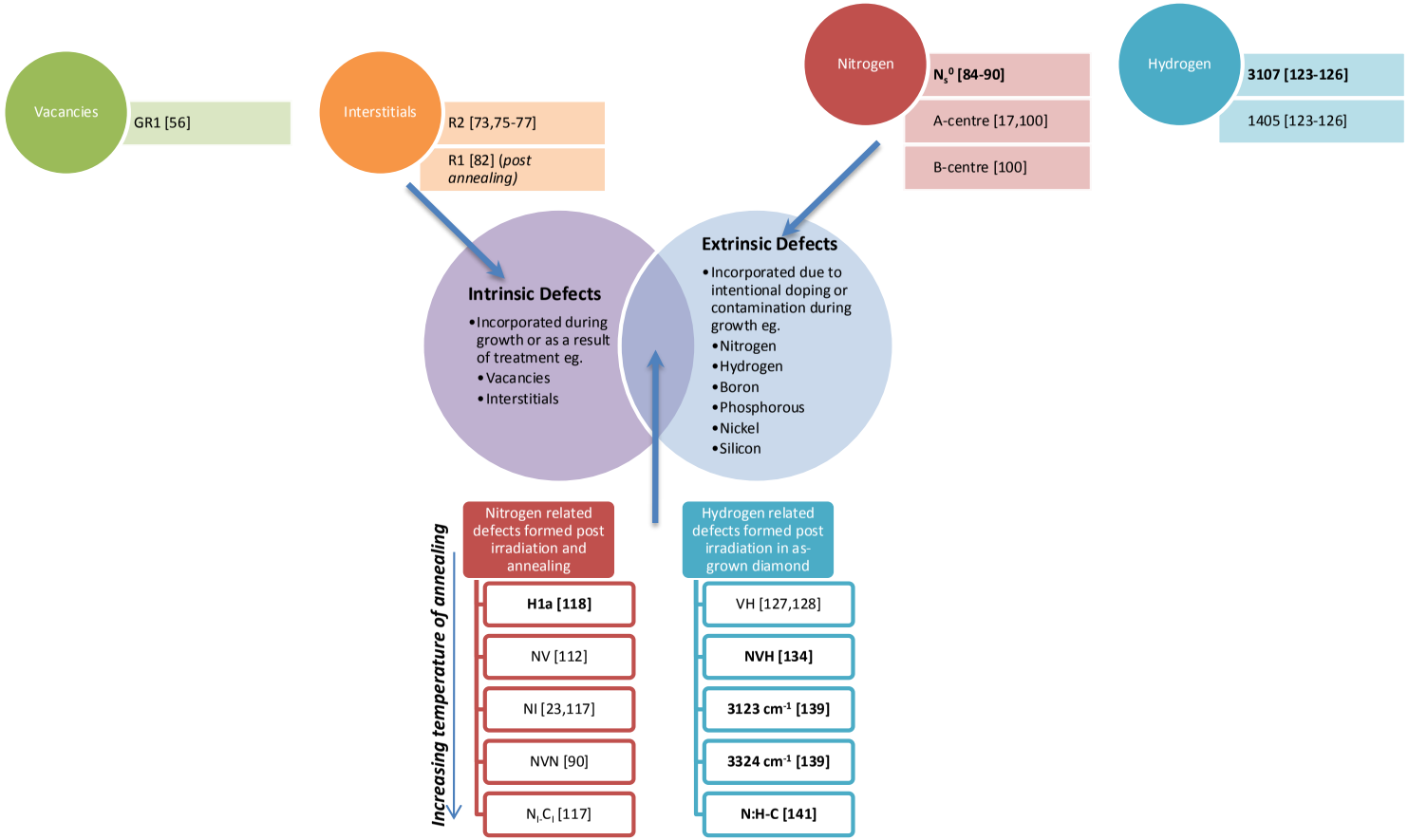

Figure 2-1: The figure outlines key defects in diamond mentioned in this thesis. Those highlighted in bold are discussed as part of the results chapters in more detail. This figure in no way provides a comprehensive outline of irradiation damage defects or extrinsic defects found in diamond.

atom moving away from each other in the ⟨111⟩ direction [90, 92, 93].

The neutral single substitutional nitrogen centre was first identified by Smith *et al.* by EPR [85] and labelled P1. The dispersed nitrogen identified to exist in samples, was also found to produce strong absorption in the infrared one-phonon region of the spectrum and was labelled the C-centre [94–96]. Through the use of vacuum gas analysis, it was shown that the intensity of both of these correlated features [97], represented the concentration of nitrogen within the sample [88].

For type Ib material, two key absorption features, 1344 cm^{-1} and 1130 cm^{-1} were attributed to the centre, showing a reproducible ratio of peak intensities over many samples [98]. ^{15}N isotopic substitution investigations identified a red shift of ≈15 cm^{-1} of the 1130 cm^{-1} with no simultaneous shift in the 1344 cm^{-1} LVM. However, for ^{13}C isotopic enrichment, the 1130 cm^{-1} feature displayed no shift and the 1344 cm^{-1} LVM was seen to shift to 1292 cm^{-1}. The 1130 cm^{-1} mode was therefore assigned to the nitrogen vibration of the N_S^0 defect and the 1344 cm^{-1} LVM to a pure carbon vibration associated with the strengthened carbon bond [99].

In natural samples, nitrogen is present almost completely in one or more non-paramagnetic forms and so can not be detected by EPR. In optical absorption, two additional distinct components to the infrared spectrum were identified and labelled as A and B [100].

2.4.1.1 Aggregation of nitrogen related defects

The A-centre in diamond is a complex of two neighbouring substitutional nitrogen atoms on adjacent lattice sites. It is well established experimentally and results post heat treatment at temperatures greater than 1950 K for extended periods [17]. Simultaneously, the N3 absorption was detected [101, 102].

The rate of aggregation can be enhanced by the inclusion of vacancies into the lattice structure [103, 104]. Vacancies can enhance the migration of substitutional nitrogen centres to form A-centres at lower temperatures. Further aggregation leads to the B-centre (four nitrogen atoms surrounding a vacancy), giving vibrational bands at 1332, 1171, 1093, 1003 and 780 cm^{-1} [105]. It is unknown whether the A-centre migrates as a unit to form the B-centre, or whether it is through the dissociation of the A-centre during annealing that the VN_4 structure forms.

Another prominent nitrogen related defect groups are the vacancy-nitrogen defects. H3 and H4 represent the VN_2 and V_2N_2 centres [90, 106] but most prominent is the NV centre. Irradiation and annealing treatments (at approximately 900 K) give rise to an absorption band at 1.945 eV (637 nm) [107]. The zero phonon line (ZPL) was shown to originate from a defect with trigonal symmetry and more specifically, an $A \rightarrow E$ transition. The vacancy was known to be mobile in diamond at 900 K [61] and hence it was concluded that the defect responsible for the absorption was a vacancy neighbouring a substitutional atom. This was correlated with an EPR defect that presented with the correct symmetry, an electronic spin of 1 and nuclear spin of 1 and near atomic 100% abundance [108].

Under similar conditions, an absorption band at 2.156 eV (575 nm) was observed [109–111], arising from an $E \rightarrow A$ transition from a trigonal defect [111]. Correlation between these two features identified that as there was a sudden decrease in intensity of the 1.945 eV line at high irradiation doses, there was an abrupt increase in the 2.156 eV feature [112]. It was concluded that at lower irradiation doses, there was an excess of the neutral single substitutional nitrogen defect. The nitrogen and vacancy defects could complex to form the NV defect and the N_S^0 defect would donate and electron forming NV^- and N_S^+. At higher irradiation doses, the majority of the N_S^0 defects would be ionised to N_S^+, with the formation of V^- and hence the NV defect would exist in the neutral charge state [112].

$$N_S^0 + V^0 \rightarrow NV^0$$
$$N_S^0 + N_S^0 \rightarrow NV^- + N_S^+$$
$$N_S^+ + V^- \rightarrow NV^0$$

Both forms of the NV defect are observed in as grown CVD diamond [113]. It may be grown into the diamond lattice as a unit or under the conditions of growth, be formed by the diffusion of the vacancy to a N_S^0 centre.

Nitrogen interstitials have been reported in theoretical and experimental studies [22, 114–117]. The knowledge of the fate of interstitial defects and nitrogen is less advanced. As the $\langle 001 \rangle$-split interstitial migrates through the lattice, it can become trapped by the N_S^0 defect, forming a defect where one atom of the

interstitial structure is replaced by a nitrogen atom. This has been identified by EPR studies and labelled WAR9 and shown to be extremely stable [117]. It was detected as occurring only in the low nitrogen sectors of the sample, suggesting the defect to be an electron acceptor existing in the negative charge state in regions of high nitrogen concentration. A secondary nitrogen related interstitial defect is that labelled WAR10, a ⟨001⟩-nitrogen split interstitial ⟨001⟩-carbon split interstitial pair forming under similar conditions to the WAR9 defect [117].

The most prominent defect to arise post irradiation of type I diamond, whether by electrons or neutrons, is the absorption feature at 1450 cm^{-1} labelled the H1a defect [118]. This is also thought to arise from a nitrogen related interstitial defect. The strength of the line is noted as being sample-dependent and linear in intensity with irradiation dose. This defect is reviewed further in Chapter 6.

2.4.2 Hydrogen in diamond

Hydrogen is typically the most abundant atom in the gas phase during diamond growth by CVD. The predominant motivation for the study of hydrogen, is its effect on the electrical properties of diamond as a result of hydrogenation [119]. Hydrogen is a strong reactant with solids due to its strong chemical activity, high lattice mobility and its availability in molecular gasses and liquids. Hydrogen can be present in concentrations up to 1 atomic percent in some natural and polycrystalline samples [120]. However, the defects that form are commonly infrared inactive and paramagnetic, which hinders their detection.

Calculations using Hartree-Fock theory have concluded that hydrogen is more stable at a bond-centred site with a predicted energy difference of 2.7 eV over the tetrahedral location [121]. In comparison, the use of density functional theory has predicted the energy difference to be 1.9 eV [122]. The bond-centred defect leads to a large lattice relaxation, with the C-C bonds extending by 43%. The hydrogen atom positions itself in the centre of the bond, 11 Å away from each carbon atom [91]. As a result, these carbon atoms relax towards the plane of their three nearest neighbours, compressing these bonds by nearly 4% and leading to a change in the bonding configuration from the diamond sp^3 structure to the more stable sp^2 structure [91].

Further theoretical calculations have shown that it is unlikely that single hydrogen atoms would be the final form in diamond, since a complex of two hydrogen atoms has a lower energy than two isolated defects [122]. Like nitrogen, hydrogen can form many new centres by migrating and aggregating with other defects when exposed to treatments such as irradiation or annealing. Lines at 3107 cm^{-1} and 1405 cm^{-1} were the first to be commonly seen and attributed the C–H stretch and bend modes of the same defect and observed in natural as well as some synthetic diamond post annealing [123–126]. These defects will be reviewed further in Chapter 7.

In polycrystalline diamond, EPR has been shown to commonly detect the H1 centre (VH^0) [127, 128], stable up to temperatures of approximately 1200 K [129–131]. This has been correlated to a near trigonal defect [132] and is present in samples of high hydrogen concentration, where the isolated neutral nitrogen defect is absent [131]. In addition, EPR has also identified the H2 defect [131], appearing in samples with a lower concentration of hydrogen and in the presence of the neutral nitrogen P1 signal [131]. For both H1 and H2, it is proposed that the hydrogen atom is not incorporated into the lattice of the bulk diamond and is instead at a distorted region such as a grain boundary [133].

The first conclusively assigned point defect in bulk diamond was the NVH^- defect by EPR [134], a defect with $S = 1/2$ and C_{3v} symmetry. In the model of this defect, the hydrogen atom is bonded to one of the three carbon atoms nearest to the vacancy. This suitably replicated the experimental hyperfine parameters observed [135–137]. This static configuration would result in a defect of C_{1h} symmetry but permitting the hydrogen atom to tunnel between the three equivalent C_{1h} configurations, on a timescale short compared to that of EPR experiments, would result in the observation of a defect with C_{3v} symmetry. The NVH defect is further reviewed in Chapter 7.

Hydrogen may also complex with vacancies in the lattice in single crystal material. The negatively charged hydrogen vacancy defect (VH^-) has been proposed by EPR [127], suggesting the defect to be a complex formed from a hydrogen atom bonded to one of the four carbon atoms at a vacancy. Modelling of the hyperfine parameters for this structure did not agree with the EPR results observed and an

alternative model of a hydrogen di-vacancy complex provides an alternative structure in broad agreement with experimental observations [135, 138]. Contention remains over the true assignment of the EPR defect.

In the C–H stretch region (2750–3300 cm^{-1}), the most commonly detected bands are at 3123 and 3324 cm^{-1}, in addition to those already mentioned [139]. Again these will be more thoroughly discussed in Chapter 7.

Much of the knowledge of hydrogen related defects in diamond comes from the extensive theoretical modelling performed by Goss [136, 140, 141]. Discussed in depth are many of the complexes that hydrogen may form with impurities including boron and nitrogen. Hydrogen will bind with donors to passivate them. In diamond, the acceptor site is likely to be bond-centred and so it is reasonable that in a nitrogen hydrogen pair, the hydrogen will be located in a similar position [142]. Calculation shows that for a N–H–C defect, the hydrogen atom will lie close to the carbon neighbour. The binding energy of such a defect is calculated as 1.49 eV. This complex cannot be described as passivated due to the defect possessing a filled level in the bandgap and modelling places the donor level at 1.1 eV above the valance band. By LDA-DFT (local density approximation - density functional theory) methods, the N-H defect has a binding energy of 4.2 eV and 3.5 eV for the reactions $N - H \rightarrow N^0 + H^0$ and $N - H \rightarrow N^+ + H^-$ respectively, using LDA-DFT calculations [141].

An alternative model is for a defect made from an A-centre with a hydrogen atom placed in the bond-centred position between the two nitrogen atoms. The long bond distance between nitrogen atoms makes this highly attractive, with a bond dilation of 3%. Its formation is theorised to be in the 4–5 eV region. However, in CVD material, nitrogen is typically incorporated as single substitutional centres, with an activation energy for the aggregation of nitrogen of 5 eV [143]. This makes this a less plausible model.

References

[1] S. Tennant, Philosophical Transactions of the Royal Society **87**, 123 (1797).

[2] J. E. Hannay, Proceedings of the Royal Society of London **30**, 188 (1880).

[3] H. Moisson, Comptes Rendus p. 320 (1894).

[4] C. A. Parsons, Proceedings of the Royal Society of London A. **79**, 532 (1907).

[5] C. A. Parsons, Journal of the Institute of Metals **20**, 5 (1918).

[6] C. A. Parsons, Philosophical Transactions of the Royal Society of London A. **220**, 67 (1920).

[7] O. I. Leipunskii, Uspekhi Khimii **8**, 1519 (1939).

[8] R. Liljeblad, Arkiv for Kemi **8**, 423 (1955).

[9] R. Berman and F. Simon, Zeitschrift fur Elektrochemie **59**, 333 (1955).

[10] R. J. Wedlake, in *Properties of Diamond*, edited by J. E. Field (Academic Press, 1979), chap. 16, pp. 501–535.

[11] P. W. Bridgman, Journal of Chemical Physics **15**, 92 (1947).

[12] F. P. Bundy, H. T. Hall, H. M. Strong, and R. H. Wentorf, Nature **176**, 51 (1955).

[13] H. P. Bovenkerk, F. P. Bundy, H. T. Hall, H. M. Strong, and R. H. Wentorf, Nature **184**, 1094 (1959).

[14] G. Muncke, in *Properties of Diamond*, edited by J. E. Field (Academic Press, 1979).

[15] A. T. Collins and S. C. Lawson, Philosophical Magazine Letters **60**, 117 (1989).

[16] R. M. Chrenko, H. M. Strong, and R. E. Tuft, Philosophical Magazine **23**, 313 (1971).

[17] R. M. Chrenko, R. E. Tuft, and H. M. Strong, Nature **270**, 141 (1977).

[18] R. H. Wentorf, Journal of Physical Chemistry **75**, 1833 (1971).

[19] H. M. Strong and R. M. Chrenko, The Journal of Physical Chemistry **75**, 1838 (1971).

[20] H. M. Strong, *Manufacture of diamond products* (1978), US Patent 4082185.

[21] C. V. H. Strömann, F. Tshishikhawe, J. O. Hansen, and R. C. Burns, *Synthesis of diamond* (2006), European Patent WO2006/061672 A1.

[22] G. A. Watt, M. E. Newton, and J. M. Baker, Diamond and Related Materials **10**, 1681 (2001).

[23] Y. V. Babich, B. N. Feigelson, and A. P. Yelisseyev, Diamond and Related Materials **13**, 1802 (2004).

[24] R. C. Burns, V. Cvetkovic, C. N. Dodge, D. J. F. Evans, M. T. Rooney, P. M. Spear, and C. M. Welbourn, Journal of Crystal Growth **104**, 257 (1990).

[25] H. Kanda and T. Sekine, in *Properties and Growth of Diamond*, edited by G. Davies (IEE - Inspec, 1994), vol. 9 of *EMIS Datareviews Series*, chap. 12, pp. 415–424.

[26] Y. Borzdov, Y. Pal'yanov, I. Kupriyanov, V. Gusev, A. Khokhryakov, A. Sokol, and A. Efremov, Diamond and Related Materials **11**, 1863 (2002).

[27] H. Kanda, T. Ohsawa, O. Fukunaga, and I. Sunagawa, Journal of Crystal Growth **94**, 115 (1989).

[28] W. G. Eversole and N. Y. Kenmore, *Synthesis of diamond* (1962), US Patent 3030187.

[29] W. G. Eversole and N. Y. Kenmore, *Synthesis of diamond* (1962), US Patent 3030188.

[30] J. C. Angus, H. A. Will, and W. S. Stanko, Journal of Applied Physics **39**, 2915 (1968).

[31] S. P. Chauhan, J. C. Angus, and N. C. Gardner, Journal of Applied Physics **47**, 4746 (1976).

[32] A. Argoitia, C. S. Kovach, and J. C. Angus, in *Handbook of Industrial Diamonds and Diamond Films*, edited by M. A. Prelas, G. Popovici, and L. K. Bigelow (Marcel Dekker Inc., 1997).

[33] M. Kamo, Y. Sato, S. Matsumoto, and N. Setaka, Journal of Crystal Growth **62**, 642 (1983).

[34] P. K. Bachmann, in *Handbook of Industrial Diamonds and Diamond Films*, edited by M. A. Prelas, G. Popovici, and L. K. Bigelow (Marcel Dekker Inc., 1997).

[35] C. Findeling-Dufour, A. Vignes, and A. Gicquel, Diamond and Related Materials **4**, 429 (1995).

[36] D. G. Goodwin and J. E. Butler, in *Handbook of Industrial Diamonds and Diamond Films*, edited by M. A. Prelas, G. Popovici, and L. K. Bigelow (Marcel Dekker Inc., 1997).

[37] H. Watanabe, D. Takeuchi, S. Yamanaka, H. Okushi, K. Kajimura, and T. Sekiguchi, Diamond and Related Materials **8**, 1272 (1999).

[38] H. Okushi, Diamond and Related Materials **10**, 281 (2001).

[39] H. Okushi, H. Watanabe, S. Ri, S. Yamanaka, and D. Takeuchi, Journal of Crystal Growth **237-239**, 1269 (2002).

[40] M. Kasu and N. Kobayashi, Diamond and Related Materials **12**, 413 (2003).

[41] J. Achard, A. Tallaire, R. Sussmann, F. Silva, and A. Gicquel, Journal of Crystal Growth **284**, 396 (2005).

[42] A. Tallaire, J. Achard, A. Secroun, O. De Gryse, F. De Weerdt, J. Barjon, F. Silva, and A. Gicquel, Journal of Crystal Growth **291**, 533 (2006).

[43] L. Bergman, M. T. McClure, J. T. Glass, and R. J. Nemanich, Journal of Applied Physics **76**, 3020 (1994).

[44] A. Secroun, A. Tallaire, J. Achard, G. Civrac, H. Schneider, and A. Gicquel, Diamond and Related Materials **16**, 953 (2007).

[45] A. Secroun, O. Brinza, A. Tardieu, J. Achard, F. Silva, X. Bonnin, K. D. Corte, A. Anthonis, M. E. Newton, J. Ristein, et al., Phys. Status Solidi A **204**, 4298 (2007).

[46] S. Jin and T. D. Moustakas, Applied Physics Letters **65**, 403 (1994).

[47] W. Muller Sebert, E. Worner, F. Fuchs, C. Wild, and P. Koidl, Applied Physics Letters **68**, 759 (1996).

[48] A. Tallaire, A. T. Collins, D. Charles, J. Achard, R. Sussmann, A. Gicquel, M. E. Newton, A. M. Edmonds, and R. J. Cruddace, Diamond and Related Materials **15**, 1700 (2006).

[49] J. G. Hamilton, T. M. Putnam, and M. L. Ehrmann, American Mineralogist **37**, 941 (1952).

[50] A. T. Collins, Nature **273**, 654 (1978).

[51] W. Crookes, Proceedings of the Royal Society of London **74**, 47 (1904).

[52] S. Han, Review of Scientific Instruments **68**, 647 (1997).

[53] E. W. J. Mitchell, in *Physical Properties of Diamond*, edited by R. Berman (Clarendon Press, 1965), pp. 394–421.

[54] A. Mainwood, Diamond and Related Materials **7**, 504 (1998).

[55] J. Koike, D. M. Parkin, and T. E. Mitchell, Applied Physics Letters **60**, 1450 (1992).

[56] C. D. Clark, R. W. Ditchburn, and H. B. Dyer, Proceedings of the Royal Society of London Series A **234**, 363 (1956).

[57] C. D. Clark and J. Walker, Proceedings of the Royal Society of London Series A **334**, 241 (1973).
[58] G. Davies and C. M. Penchina, Proceedings of the Royal Society of London Series A **338**, 359 (1974).
[59] C. D. Clark, R. W. Ditchburn, and H. B. Dyer, Proceedings of the Royal Society of London Series A **237**, 75 (1956).
[60] C. Coulson and M. Kearsley, Proceedings of the Royal Society of London. Series A, Mathematical and Physical Sciences **241**, 433 (1957).
[61] G. Davies, S. C. Lawson, A. T. Collins, A. Mainwood, and S. J. Sharp, Physical Review B **46**, 13157 (1992).
[62] J. A. van Wyk, O. D. Tucker, M. E. Newton, J. M. Baker, G. S. Woods, and P. Spear, Physical Review B **52**, 12657 (1995).
[63] J. Isoya, H. Kanda, Y. Uchida, S. C. Lawson, S. Yamasaki, H. Itoh, and Y. Morita, Physical Review B **45**, 1436 (1992).
[64] G. Davies, Nature **269**, 498 (1977).
[65] D. J. Twitchen, D. C. Hunt, C. Wade, M. E. Newton, J. M. Baker, T. R. Anthony, and W. F. Banholzer, Physica B: Condensed Matter **273-274**, 644 (1999).
[66] G. Davies and M. H. Nazaré, Journal of Physics C: Solid State Physics **13**, 4127 (1980).
[67] G. Davies and E. C. Lightowlers, Journal of Physics C: Solid State Physics **3**, 638 (1970).
[68] C. D. Clark and R. J. Wedlake, Journal of Physics E: Scientific Instruments **6**, 43 (1973).
[69] D. C. Hunt, D. J. Twitchen, M. E. Newton, J. M. Baker, J. K. Kirui, J. A. van Wyk, T. R. Anthony, and W. F. Banholzer, Physical Review B **62**, 6587 (2000).
[70] M. E. Newton, B. A. Campbell, D. J. Twitchen, J. M. Baker, and T. R. Anthony, Diamond and Related Materials **11**, 618 (2002).
[71] D. J. Twitchen, M. E. Newton, J. M. Baker, O. D. Tucker, T. R. Anthony, and W. F. Banholzer, Physical Review B **54**, 6988 (1996).
[72] S. J. Breuer and P. R. Briddon, Physical Review B **51**, 6984 (1995).
[73] J. P. Goss, B. J. Coomer, R. Jones, T. D. Shaw, P. R. Briddon, M. Rayson, and S. Öberg, Physical Review B **63**, 195208 (2001).
[74] A. Mainwood, F. Larkins, and A. Stoneham, Solid-State Electronics **21**, 1431 (1978).
[75] C. Weigel, D. Peak, J. W. Corbett, G. D. Watkins, and R. P. Messmer, Phys. Rev. B **8**, 2906 (1973).
[76] L. H. Li and J. E. Lowther, Journal of Physics and Chemistry of Solids **58**, 1607 (1997).
[77] D. C. Hunt, D. J. Twitchen, M. E. Newton, J. M. Baker, T. R. Anthony, W. F. Banholzer, and S. S. Vagarali, Physical Review B **61**, 3863 (2000).
[78] H. E. Smith, PhD. thesis, King's College, University of London (2004).
[79] J. Walker, Journal of Physics C: Solid State Physics **10**, 3867 (1977).
[80] H. E. Smith, G. Davies, M. E. Newton, and H. Kanda, Diamond and Related Materials **13**, 705 (2004).
[81] H. E. Smith, G. Davies, M. E. Newton, and H. Kanda, Physical Review B **69**, 045203 (2004).
[82] I. Flint and J. Lomer, Physica B+C **116**, 183 (1983).
[83] E. A. Faulkner and J. N. Lomer, Philosophical Magazine B **7**, 1995 (1962).
[84] R. G. Farrer, Solid State Communications **7**, 685 (1969).

[85] W. V. Smith, P. P. Sorokin, I. L. Gelles, and G. J. Lasher, Physical Review **115**, 1546 (1959).
[86] M. H. Nazaré and A. J. T. Neves, Journal of Physics C: Solid State Physics **20**, 2713 (1987).
[87] G. S. Woods, J. A. van Wyk, and A. T. Collins, Philosophical Magazine B **62**, 589 (1990).
[88] W. Kaiser and W. L. Bond, Physical Review **115**, 857 (1959).
[89] G. S. Woods, G. C. Purser, A. S. S. Mtimkulu, and A. T. Collins, Journal of Physics and Chemistry of Solids **51**, 1191 (1990).
[90] A. Mainwood, Physical Review B **49**, 7934 (1994).
[91] P. R. Briddon and R. Jones, Physica B: Condensed Matter **185**, 179 (1993).
[92] S. A. Kajihara, A. Antonelli, J. Bernholc, and R. Car, Physical Review Letters **66**, 2010 (1991).
[93] P. R. Briddon, R. Jones, and M. I. Heggie, in *International Conference on New Diamond Science and Technology*, edited by R. Messier, J. T. Glass, J. E. Butler, and R. Roy (1991), p. 63.
[94] H. B. Dyer, F. A. Raal, L. D. Preez, and J. H. N. Loubser, Philosophical Magazine **11**, 763 (1965).
[95] J. J. Charette, Journal of Chemical Physics **35**, 1906 (1961).
[96] J. J. Charette, Journal of Chemical Physics **37**, 3014 (1962).
[97] G. B. B. M. Sutherland, D. E. Blackwell, and W. G. Simeral, Nature **174**, 901 (1954).
[98] A. T. Collins and G. S. Woods, Philosophical Magazine B **46**, 77 (1982).
[99] C. D. Clark, A. T. Collins, and G. S. Woods, in *The Properties of Natural and Synthetic Diamond*, edited by J. Field (Academic Press Inc. (London) Ltd., 1992), pp. 35–79.
[100] G. Davies, Journal of Physics C: Solid State Physics **5**, 2534 (1972).
[101] J. P. Goss, R. Jones, S. J. Breuer, P. R. Briddon, and S. Öberg, Physical Review Letters **77**, 3041 (1996).
[102] R. Jones, J. P. Goss, P. R. Briddon, and S. Öberg, Phys. Rev. B **56**, R1654 (1997).
[103] A. T. Collins, Journal of Physics C: Solid State Physics **13**, 2641 (1980).
[104] A. T. Collins, Journal of Physics C: Solid State Physics **11**, L417 (1978).
[105] R. Jones and J. P. Goss, in *Properties, Growth and applications of Diamond*, edited by M. H. Nazaré and A. J. Neves (INSPEC, IEEE, London, 2000), chap. A5.1.
[106] R. Jones, P. R. Briddon, and S. Berg, Philosophical Magazine Letters **66**, 67 (1992).
[107] G. Davies and M. E. R. Hamer, Proceedings of the Royal Society of London Series A **348**, 285 (1976).
[108] J. H. N. Loubser and J. A. van Wyk, Diamond Research **11**, 11 (1977).
[109] J. E. Ralph, Proceedings of the Physical Society **76**, 688 (1960).
[110] G. Davies, Journal of Physics C: Solid State Physics **12**, 2551 (1979).
[111] A. T. Collins and S. C. Lawson, Journal of Physics: Condensed Matter **1**, 6929 (1989).
[112] Y. Mita, Physical Review B **53**, 11360 (1996).
[113] T. A. Kennedy, J. S. Colton, J. E. Butler, R. C. Linares, and P. J. Doering, Applied Physics Letters **83**, 4190 (2003).
[114] G. S. Woods and A. T. Collins, Journal of Physics C: Solid State Physics **15**, L949 (1982).

[115] I. Kiflawi, A. Mainwood, H. Kanda, and D. Fisher, Physical Review B **54**, 16719 (1996).

[116] J. P. Goss, P. R. Briddon, S. Papagiannidis, and R. Jones, Physical Review B **70**, 235208 (2004).

[117] S. Felton, B. L. Cann, A. M. Edmonds, S. Liggins, R. J. Cruddace, M. E. Newton, D. Fisher, and J. M. Baker, Journal of Physics: Condensed Matter **21**, 364212 (2009).

[118] G. S. Woods, Philosophical Magazine B **50**, 673 (1984).

[119] S. M. Myers, M. I. Baskes, H. K. Birnbaum, J. W. Corbett, G. G. DeLeo, S. K. Estreicher, E. E. Haller, P. Jena, N. M. Johnson, R. Kirchheim, et al., Reviews of Modern Physics **64**, 559 (1992).

[120] B. Dischler, C. Wild, W. Mller-Sebert, and P. Koidl, Physica B: Condensed Matter **185**, 217 (1993).

[121] T. L. Estle, S. Estreicher, and D. S. Marynick, Physical Review Letters **58**, 1547 (1987).

[122] P. Briddon, R. Jones, and G. M. S. Lister, Journal of Physics C: Solid State Physics **21**, L1027 (1988).

[123] R. M. Chrenko, R. S. McDonald, and K. A. Darrow, Nature **213**, 474 (1967).

[124] G. S. Woods and A. T. Collins, Journal of Physics and Chemistry of Solids **44**, 471 (1983).

[125] I. Kiflawi, D. Fisher, H. Kanda, and G. Sittas, Diamond and Related Materials **5**, 1516 (1996).

[126] F. De Weerdt and I. Kupriyanov, Diamond and Related Materials **11**, 714 (2002).

[127] C. Glover, M. E. Newton, P. M. Martineau, S. Quinn, and D. J. Twitchen, Physical Review Letters **92**, 135502 (2004).

[128] N. Mizuochi, H. Watanabe, J. Isoya, H. Okushi, and S. Yamasaki, 14th European Conference on Diamond, Diamond-Like Materials, Carbon Nanotubes, Nitrides and Silicon Carbide **13**, 765 (2004).

[129] I. Watanabe and K. Sugata, Japanese Journal of Applied Physics **27**, 1808 (1988).

[130] H. Jia, J. Shinar, D. P. Lang, and M. Pruski, Physical Review B **48**, 17595 (1993).

[131] X. Zhou, G. D. Watkins, K. M. McNamara Rutledge, R. P. Messmer, and S. Chawla, Physical Review B **54**, 7881 (1996).

[132] K. Iakoubovskii, A. Stesmans, K. Suzuki, A. Sawabe, and T. Yamada, Physical Review B **66**, 113203 (2002).

[133] D. Talbot-Ponsonby, PhD. thesis, Oriel College, University of Oxford (1997).

[134] C. Glover, M. E. Newton, P. M. Martineau, D. J. Twitchen, and J. M. Baker, Physical Review Letters **90**, 185507 (2003).

[135] M. J. Shaw, P. R. Briddon, J. P. Goss, M. J. Rayson, A. Kerridge, A. H. Harker, and A. M. Stoneham, Physical Review Letters **95**, 105502 (2005).

[136] J. P. Goss, P. R. Briddon, R. Jones, and S. Sque, Journal of Physics: Condensed Matter **15**, S2903 (2003).

[137] A. Kerridge, A. H. Harker, and A. M. Stoneham, Journal of Physics: Condensed Matter **16**, 8743 (2004).

[138] M. J. Shaw, P. R. Briddon, J. P. Goss, M. J. Rayson, A. Kerridge, A. H. Harker, and A. M. Stoneham, Physical Review Letters **95**, 219901 (2005).

[139] F. Fuchs, C. Wild, K. Schwarz, W. Muller-Sebert, and P. Koidl, Applied Physics Letters **66**, 177 (1995).

[140] J. P. Goss, R. Jones, M. I. Heggie, C. P. Ewels, P. R. Briddon, and S. Öberg, Physical Review B **65**, 115207 (2002).

[141] J. P. Goss, Journal of Physics: Condensed Matter **15**, R551 (2003).
[142] S. P. Mehandru and A. B. Anderson, Journal of Materials Research **9**, 383 (1994).
[143] T. Evans and Z. Qi, Proceedings of the Royal Society of London Series A **381**, 159 (1982).

Chapter 3

Theory

This chapter aims to explain some of the physics relevant to the studies reported in this thesis. The principal focus is the optical study of point defects in irradiated and annealed diamond. Hence, the theory of the optical properties of point defects, uniaxial stress and vibronic coupling will be presented, as well as a brief introduction of the theory of defect migration.

3.1 Sub band gap vibrational optical absorption in diamond

Electromagnetic (EM) radiation can be absorbed by diamond, where the intensity of absorption as a function of energy, is governed by the origin and mechanism of the absorption within the lattice. The absorption of such radiation requires an electric dipole, which can respond to the electric field and acquire or change its dipole moment [1]. States with different energies are orthogonal and do not overlap. Therefore absorption at a static dipole does not occur [2]. For a crystal, the absorption must therefore result from a vibration, transforming the state and giving an overlap with a non-zero value. The rate of vibration, leading to a change in the dipole moment of the defect will therefore determine whether absorption will occur.

There are three different coupling mechanisms that may occur in solids.

- Restrahl - single phonon absorption occurring in ionic crystals [3]

- Defect induced one-phonon absorption - a defect in the lattice introduces strain, destroying the lattice symmetry and permitting the introduction of an electric dipole

- Multi-phonon absorptions - two or more phonons simultaneously interacting to produce an electric dipole

For the intrinsic diamond lattice, all atoms are covalently bonded equally with their four nearest neighbours. These bonds will differ in orientation with the nearest neighbours and be a translation of the second nearest neighbour bonds. For a single phonon, neighbouring atoms will have displacements and induced dipole moments that are equal but opposite and π out of phase, making the wavevector $\underline{k} = 0$. The inversion symmetry of the diamond lattice prevents an induced dipole moment by a single phonon and therefore there is no IR absorption in this region from intrinsic diamond.

The large indirect band-gap of diamond prevents electronic excitation of intrinsic diamond until 5.5 eV. Any absorption occurring at a lower energy is probably a result of a defect present within the diamond lattice, introducing additional states into the band gap and destroying the lattice symmetry.

3.1.1 Defect induced absorption

A defect in the diamond lattice may induce a dipole moment resulting in absorption in two ways:

- electronic absorption

- vibrational absorption

For intrinsic diamond, *electronic absorption* can only occur when the incident radiation has sufficient energy to promote a charge carrier from the valence band to the conduction band. A defect can modify the electronic configuration of the band gap and destroy the periodic boundary structure of the lattice. Electronic transitions can then occur between the states of the defect within the band gap, absorbing a quantum of energy equal to the energy separation of these states and giving sharp absorption features called zero phonon lines (ZPLs).

Alternatively, a defect related bond vibration may couple to the EM wave, providing energy and momentum are conserved and *vibrational absorption* occurs. Even at low temperatures, the nucleus of the atom vibrates around an equilibrium point, producing a deformation of charge with the surrounding electrons and creating a small oscillating electric dipole.

The Raman frequency categorises the maximum frequency at which a phonon can propagate through the lattice. For diamond, this corresponds to when the transverse and longitudinal optical modes are degenerate and the wavevector is zero, giving a maximum allowed phonon frequency of $1332\,\mathrm{cm}^{-1}$ [4, 5]. At higher frequencies, a defect related vibrational mode is localised (LVM) in frequency and space and can involve just a few atoms around the defect [6]. LVMs are typically narrow and they usually occur from light impurities that are strongly bonded, the strong bonding damping vibrations. The linewidth of the mode is determined by the lifetime of the vibration. Lifetimes increase as the temperature is decreased, leading to narrower lines and improved resolution.

Electron-phonon coupling processes are also described as vibronic. An electronic absorption which occurs without the aid of a phonon is labelled as a zero-phonon line and has a minimum linewidth determined by the life-time of the excited state. This can be further broadened by lattice strain [7]. The energy of the state can be lowered with an increase in strain, as it perturbs the electronic orbitals [2]. Movement of the atoms act to reduce the energy of the state and the resulting distortion of the orbital component of the wavefunction subsequently leads to stretching of the bonds and distortion to the surrounding lattice. This leads to an increase in the elastic energy, which varies as the displacement of atoms squared. The result is harmonic motion about the equilibrium, driven by the reduction in energy and electronic states of a defect may be coupled to the vibrations of the centre in this way. Transitions between states can then occur, with the simultaneous absorption of a photon and creation of a phonon. A consequence of this is that vibronic side-bands may be observed at higher energies and at a distance from the ZPL equal to a phonon quantum of energy.

3.1.2 Isotope effects on local vibrational modes

The behaviour of an absorption line with changing isotopes, can reveal a substantial amount of information with regards to the nature of the defect composition.

As revision, the introduction of a defect destroys the translational symmetry. The effect can be quantified by considering a monatomic linear chain, where one atom of mass M is replaced by a smaller mass m [8]. It can be shown that one of the normal modes of the lattice will be localised around the light atom and placing the light atom at the $n = 0$ position, the lattice equations of motion become:

$$m\ddot{u} = k(u_1 + u_{-1} - 2u_0) \tag{3-1}$$

$$M\ddot{u} = k(u_2 + u_0 - 2u_1) \tag{3-2}$$

where u_n is the displacement of the n^{th} atom from its equilibrium position and k is the nearest neighbour force constant. The solution to the perfect linear chain, where a is the nearest-neighbour distance and q the phonon wave number is therefore:

$$\omega = 2\sqrt{\frac{k}{M}}\sin\left(\frac{qa}{2}\right) \tag{3-3}$$

Euler's equation states

$$\sin z = [\exp(iz) - \exp(-iz)]/2i \tag{3-4}$$

The wave number must be considered as complex such that $q = q_R + iq_i$ and hence, $\sin(qa/2) = \sin(q_R a/2)\cosh(q_I a/2) - i\cos(q_R a/2)\sinh(q_I a/2)$. For the frequency to be real, the imaginary part must be equal to zero and hence $q_R = \pi/a$. Therefore the displacement of the n^{th} atom can be given by:

$$\begin{aligned} u_n &= u_0 \exp[i(qan - \omega t)] \\ &= u_0(-1)^n \exp(-q_I an)\exp(-i\omega t) \end{aligned} \tag{3-5}$$

As the distance from $n = 0$ increases, the solution damps exponentially. Substituting this into Equations (3-1) and (3-2):

$$\omega^2 = (k/m)[2 + 2\exp(-q_I a)] \tag{3-6}$$

$$\omega^2 = (k/M)[2 + \exp(-q_I a) + \exp(q_I a)] \tag{3-7}$$

Solving these simultaneous equations yields:

$$\exp(q_I a) = 2(M - m)/m \tag{3-8}$$

and

$$\omega^2 = \omega_{max}^2 \left(\frac{M^2}{2Mm - m^2} \right) \tag{3-9}$$

where $\omega_{max} = (4k/M)^{1/2}$ and is the maximum frequency of the unperturbed linear chain. Therefore, if $m < M$ then a local vibrational mode exists which is above the highest phonon frequency. If $m \ll M$, then $\omega \cong \omega_{max}\sqrt{M/2m}$.

A diatomic model is commonly used to quantify the frequency and isotope shifts of local vibrational modes. In this model, an impurity of mass m is attached by a spring k to a host atom M and to account for the vibration of local host atoms, an additional empirical constant χ is introduced. The vibrational frequency of the diatomic molecule is subsequently given using the reduced mass μ as:

$$\omega = \sqrt{k(1/\chi M + 1/m)} \equiv \sqrt{k/\mu} \tag{3-10}$$

For example, in an isotopic substitution process where hydrogen ($m = 1$ amu) with a frequency of ω_H is replaced by deuterium ($m = 2$ amu) with a frequency of ω_D, the isotopic frequency ratio is given by

$$r = \omega_H/\omega_D = \sqrt{2\frac{\chi M + 1}{\chi M + 2}} \tag{3-11}$$

giving a result of just less than the square root of 2.

The anharmonicity of the potential can reduce the isotopic frequency ratio. For larger displacements, the potential becomes weaker [9]. The anharmonic term is inversely proportional to the reduced mass. Therefore the anharmonic term is greater for lighter isotopes reducing the isotopic frequency ratio.

3.1.3 Measuring defect concentration

For optical absorption, the intensity of the transition line is directly related to the concentration of the defect causing it. Using calculated coefficients, the intensity of a transition can be used to infer the concentration. However, optical spectroscopy is a bulk technique and will not provide detail of the inhomogeneity of the sample. Systematic imaging is required for this information.

Within a spectrum, many lines may originate from the same defect, for example, representing different vibrational modes of the same bond. Annealing is a useful technique for identifying paired transitions, promoting the migration and therefore potential trapping of defects, which will subsequently alter concentration and intensity. The different modes will not anneal independently and hence patterns in intensity changes can be identified.

3.1.4 Symmetry and the effects of stress

As well as the electronic states of a defect being degenerate, so too may the induced directional dipole moment have orientational degeneracy. Strain can interact with the orbital components of electronic states, having the effect of lifting degeneracy and leading to the observation of absorption features splitting. The property of the lattice to show differences in this splitting behaviour with strain of different orientations, indicates the symmetry of the defect and gives information about the nature of the states involved. With the addition of temperature variation, information can be gained about the degeneracy of the ground state; changes in temperature will vary the population of each state and effect the intensity of absorption for each resulting transition.

The amount of strain per unit stress provides information on the elastic constants near to the defect and hence will differ from the bulk. Vacancies are known to *soften* the crystal and interstitials to *harden* the crystal due to the increase in local density. However, splitting of some ZPLs is inherent in as-grown samples, where large amounts of internal strain from defects can arise as a result of the growth process.

3.2 Crystal symmetry and point groups

The symmetry of a defect can place restrictions upon the expected properties of that defect. Diamond is a cubic crystal with tetrahedral (T_d) symmetry [4, 6]. For this point group, there are 24 associated symmetry operations which describe the processes that can be performed and will leave a single point group unaffected [1]. For each symmetry operation, there will be a corresponding symmetry element, a

Table 3-1: Symmetry operations and their symmetry elements [1].

$\boldsymbol{e}$	The identity
$\boldsymbol{C_n}$	An n-fold rotation by $2\pi/n$ around an axis of symmetry
$\boldsymbol{\sigma}$	A reflection in a vertical (σ_{v}), horizontal (σ_{h}) or dihedral (σ_{d}) mirror plane
i	An inversion through the centre of symmetry
$\boldsymbol{S_n}$	The group S_n with n-fold improper rotation

plane, line or point about which the operation is carried out. The point group of a defect identifies the symmetry operations which are associated with it. For this thesis, the Schönflies system of notation will be used. There are 5 primary labels which then subdivide (Table 3-1). Some visual examples are given in Appendix A.

3.2.1 Group theory

A set of elements $a, b, ...$ form a group G if they satisfy the following criteria [1]:

a) The identity element e is an element of G

b) The product ab of any two elements is an element of G

c) The products of the elements are associative

d) For each element, a, there is an inverse element, a^{-1}, which is also a member of G

This mathematical theory of groups can be applied to study the symmetry of molecules and rigourous mathematical treatments of group theory exist in physics. The reader is directed to Ludwig *et al.* and Sternberg for a more thorough analysis [10, 11].

For diamond, with the lattice possessing high symmetry, any defect within the lattice must have equal or lower symmetry and be a subgroup of T_{d}. For example, the $\mathrm{N_S^0}$ defect adopts C_{3v} symmetry which possess 6 members (Figure 3-1).

Symmetry operations can be performed consecutively, although the order of operations is important. A general feature is that the result of a joint symmetry

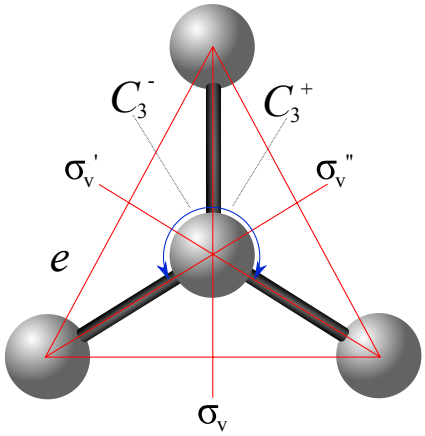

First:	e	C_3^+	C_3^-	σ_v	σ_v'	σ_v''
Second						
e	e	C_3^+	C_3^-	σ_v	σ_v'	σ_v''
C_3^+	C_3^+	C_3^-	e	σ_v'	σ_v''	σ_v
C_3^-	C_3^-	e	C_3^+	σ_v''	σ_v	σ_v'
σ_v	σ_v	σ_v''	σ_v'	e	C_3^-	C_3^+
σ_v'	σ_v'	σ_v	σ_v''	C_3^+	e	C_3^-
σ_v''	σ_v''	σ_v'	σ_v	C_3^-	C_3^+	e

Figure 3-1: The symmetry elements of the C_{3v} group. This projection is looking down the $\langle 111 \rangle$ axis. In addition, the C_{3v} multiplication table is shown, where each product is shown to be equivalent to a single element of the group.

operation will always be equivalent to a single symmetry operation. For example, $C_3^+ C_3^- = e$. The multiplication of symmetry operations is always associative and the outcome for all symmetry operations are presented in a group multiplication table. For C_{3v} symmetry there are 36 products (Figure 3-1).

Symmetry operations are in general non-commutative and hence the matrix representation of a symmetry is generally used. For this, a basis is selected, a set of functions upon which the operation acts. For C_{3v}, a suitable basis set could be (S_N, S_A, S_B, S_C). The dimension of this is therefore 4. The elements of the C_{3v} group can then be represented as:

$$\mathbf{D}^{(4)}(e) = \begin{bmatrix} 1 & 0 & 0 & 0 \\ 0 & 1 & 0 & 0 \\ 0 & 0 & 1 & 0 \\ 0 & 0 & 0 & 1 \end{bmatrix} \quad \mathbf{D}^{(4)}(C_3^-) = \begin{bmatrix} 1 & 0 & 0 & 0 \\ 0 & 0 & 1 & 0 \\ 0 & 0 & 0 & 1 \\ 0 & 1 & 0 & 0 \end{bmatrix} \quad \mathbf{D}^{(4)}(C_3^+) = \begin{bmatrix} 1 & 0 & 0 & 0 \\ 0 & 0 & 0 & 1 \\ 0 & 1 & 0 & 0 \\ 0 & 0 & 1 & 0 \end{bmatrix}$$

$$\chi(\mathrm{e}) = 4 \qquad \chi(\mathrm{C}_3^-) = 1 \qquad \chi(\mathrm{C}_3^+) = 1$$

$$\mathbf{D}^{(4)}(\sigma_v) = \begin{bmatrix} 1 & 0 & 0 & 0 \\ 0 & 1 & 0 & 0 \\ 0 & 0 & 0 & 1 \\ 0 & 0 & 1 & 0 \end{bmatrix} \quad \mathbf{D}^{(4)}(\sigma_v') = \begin{bmatrix} 1 & 0 & 0 & 0 \\ 0 & 0 & 1 & 0 \\ 0 & 1 & 0 & 0 \\ 0 & 0 & 0 & 1 \end{bmatrix} \quad \mathbf{D}^{(4)}(\sigma_v'') = \begin{bmatrix} 1 & 0 & 0 & 0 \\ 0 & 0 & 0 & 1 \\ 0 & 0 & 1 & 0 \\ 0 & 1 & 0 & 0 \end{bmatrix}$$

$$\chi(\sigma_v) = 2 \qquad \chi(\sigma_v') = 2 \qquad \chi(\sigma_v'') = 2 \tag{3-12}$$

Each matrix is the n-dimensional representative of the operation R ($\mathbf{D}^{(n)}(R)$). The set of these representatives corresponding to all the elements of the group is called the matrix representation, Γ. Representation theory aims to reduce any given representation to an irreducible representation, containing all the information about the group without redundancy. This does not though produce a unique representation and the form of an irreducible representation will be dependent upon the original basis set selected. The trace of any representative of an operation will be invariant under a similarity transform of the basis.

The character χ of the operation R is defined as:

$$\chi(R) = \sum_i D_{i_1 i_2 \ldots i_n}(R) = Tr\{\mathbf{D}^{(n)}(R)\} \tag{3-13}$$

All operations R of the same class have the same character. A character table of all possible irreducible representations of a group can then be formed by the Little Orthogonality Theorem (LOT) and can be found in a number of sources (Table 3-2) [1, 10, 11]. In addition, the Great Orthogonality Theorem (GOT) can be used to determine the singlet, doublet or triplet nature of the associated states. The GOT states that for a group of order h, where $\mathrm{D}^{(l)}(R)$ is the representative of the operation R in a d_l-dimensional irreducible representation of symmetry species $\Gamma^{(l)}$ of the group, then:

$$\sum_R D_{ij}^{(l)}(R)^* D_{i'j'}^{(l')}(R) = \frac{h}{d_l}\delta_{ll'}\delta_{ii'}\delta_{jj'} \tag{3-14}$$

Therefore, if you select any location in the matrix of one irreducible representation and any location in a second, same or different irreducible representation of the group and sum the products over all the operations of the group, then the answer is zero unless the locations of the elements are the same in both matrices. If this is the case, then the result of the calculation is h/d_l. By the Mulliken system of notation, A and B electronic states are non-degenerate whilst E and T states and doubly and triply degenerate respectively [7].

The representation Γ of a group can be written as the sum of the irreducible representations $\Gamma^{(l)}$ of the symmetry species l, where a_l is the number of times the irreducible representation appears in the direct sum $\mathbf{D}(R) = \mathbf{D}^{(\Gamma_1)}(R) \oplus \mathbf{D}^{(\Gamma_1)}(R) \oplus \ldots \mathbf{D}^{(\Gamma_n)}(R)$.

$$\Gamma = \sum_i a_l \Gamma^{(l)} \tag{3-15}$$

Table 3-2: The C_{3v} character table. The number of elements or order h equals 6. $g(c)$ illustrates the number of each transformation for the symmetry and $\chi(c)$ the character of the group.

	$\boldsymbol{e}$	$\boldsymbol{2C_3}$	$\boldsymbol{3\sigma_v}$
$\boldsymbol{A_1}$	1	1	1
$\boldsymbol{A_2}$	1	1	-1
$\boldsymbol{E}$	2	-1	0
$g(c)$	1	2	3
$\chi(c)$	4	1	2

The coefficients can be calculated by use of the LOT and since the characters of members of the same class of operations are the same:

$$a_l = \frac{1}{h}\sum_c g(c)\chi^{(l)}(c)^*\chi(c) \tag{3-16}$$

For our example of C_{3v}, the characters for e, $2C_{3v}$ and $3\sigma_v$ are 4, 1 and 2 respectively. Therefore:

$$\begin{aligned} a_{A_1} &= \frac{1}{6}(1\cdot 1\cdot 4 + 2\cdot 1\cdot 1 + 3\cdot 1\cdot 2) = 2 \\ a_{A_2} &= \frac{1}{6}(1\cdot 1\cdot 4 + 2\cdot 1\cdot 1 + 3\cdot (-1)\cdot 2) = 0 \\ a_{E} &= \frac{1}{6}(1\cdot 2\cdot 4 + 2\cdot (-1)\cdot 1 + 3\cdot 0\cdot 2) = 1 \end{aligned} \tag{3-17}$$

Therefore, the orbitals span $\Gamma = 2A_1 + E$.

Initially, the chosen basis set was arbitrary. It is more convenient to find a symmetry-adapted basis set, where the linear combinations of the basis functions transform the original representations into a reducible form. These are referred to as SALCs (symmetry-adapted linear combinations). In order to calculate these SALCs corresponding to any symmetry species l, the projection operator $p^{(l)}$ must be determined. This considers the dimensionality d_l, of the representation of the symmetry specie and the number of operations that can be performed which leave the orbitals unchanged.

$$p^{(l)} = \frac{d_l}{h}\sum_R \chi^{(l)}(R)^* R \tag{3-18}$$

$p^{(l)}$ acts to project the basis functions (f_j) into a SALC that transforms the irreducible representation. For C_{3v}, the SALCs for S_N, S_A, S_B, S_C are highlighted in Table 3-3.

Table 3-3: The transform table for the basis under the symmetry operations for C_{3v}.

	$\boldsymbol{S_n}$	$\boldsymbol{S_A}$	$\boldsymbol{S_B}$	$\boldsymbol{S_C}$
$\mathbf{e}$	S_N	S_A	S_B	S_C
$\mathbf{C_3^+}$	S_N	S_C	S_A	S_B
$\mathbf{C_3^-}$	S_N	S_B	S_C	S_A
$\sigma_\mathbf{v}$	S_N	S_A	S_C	S_B
$\sigma'_\mathbf{v}$	S_N	S_C	S_B	S_A
$\sigma''_\mathbf{v}$	S_N	S_B	S_A	S_C

The character of the corresponding operation can then be calculated by summing the entries for each orbital and multiplying by d/h. For $d = 1$, $\chi(R) = (1,1,1,1,1,1)$,

$$\begin{aligned}
\frac{1}{6}(6S_N) &= S_N \\
\frac{1}{6}(2S_A + 2S_B + 2S_C) &= \frac{1}{3}(S_A + S_B + S_C) \\
\frac{1}{6}(2S_A + 2S_B + 2S_C) &= \frac{1}{3}(S_A + S_B + S_C) \\
\frac{1}{6}(2S_A + 2S_B + 2S_C) &= \frac{1}{3}(S_A + S_B + S_C)
\end{aligned} \tag{3-19}$$

For $d = 2$, $\chi(R) = (2,-1,-1,0,0,0)$:

$$\begin{aligned}
\frac{2}{6}(2\cdot S_N + (-1)\cdot S_N + (-1)\cdot S_N) &= 0 \\
\frac{2}{6}(2\cdot S_A + (-1)\cdot S_C + (-1)\cdot S_B) &= \frac{1}{3}(2S_A - S_C - S_B) \\
\frac{2}{6}(2\cdot S_B + (-1)\cdot S_A + (-1)\cdot S_C) &= \frac{1}{3}(2S_B - S_A - S_C) \\
\frac{2}{6}(2\cdot S_C + (-1)\cdot S_B + (-1)\cdot S_A) &= \frac{1}{3}(2S_C - S_B - S_A)
\end{aligned} \tag{3-20}$$

Since the number of SALCs must equal the dimensionality, one of the SALCs is taken arbitrarily and an orthogonal combination constructed of the other two. The result is therefore:

$$\begin{aligned}
A_1 &\left\{ \quad S_1 = S_N \right. \\
A_1 &\left\{ \quad S_2 = \tfrac{1}{\sqrt{3}}(S_A + S_B + S_C) \right. \\
E &\left\{ \begin{array}{l} S_3 = \tfrac{1}{\sqrt{6}}(2S_A - S_C - S_B) \\ S_4 = \tfrac{1}{\sqrt{2}}(S_B - S_C) \end{array} \right.
\end{aligned} \tag{3-21}$$

Table 3-4: The C_{3v} product table.

	A_1	A_2	E
A_1	A_1	A_2	E
A_2		A_1	E
E			$A_1 + A_2 + E$

3.2.2 Calculation of many electron states

Once the linear orbitals and their dimensionality have been calculated, the states can be populated. Consider the NV^- defect; there are 6 available electrons. Considering the Pauli exclusion principal, A is a singlet and hence may contain up to 2 electrons; E is a doublet and therefore may contain up to 4. The possible configurations, considering it has C_{3v} symmetry and therefore 2 A states and 1 E state give:

$$a_1^2 a_1^2 e^2 \quad a_1^2 a_1^1 e^3 \quad a_1^2 e^4 \quad a_1^1 a_1^2 e^3 \quad a_1^1 a_1^1 e^4 \tag{3-22}$$

Here a_1 transforms as A_1 and e as E. The direct product for each configuration permits the calculation of the symmetry of each configuration. For the C_{3v} example used here, the product table can be found in Table 3-4.

By the direct product table, $a_1^2 a_1^2 e^2$ is:

$$A_1 \otimes A_1 \otimes A_1 \otimes A_1 \otimes E \otimes E = A_1 + [A_2] + E \tag{3-23}$$

The two a_1 states transform identically and can be simplified such that $x^{\alpha+\beta} = a_1^\alpha a_1^\beta$. Additionally, the maximum number of electrons that can be in the e state is 4 and since holes transform as electrons, $x^3 e^3$ is equivalent to $x^1 e^1$. Simplifying the possible configurations reduces the inequivalent configurations to:

Configuration	**Symmetry of resultant states**
$x^2 e^4$	${}^1A_1$
$x^3 e^3$	${}^1E + {}^3E$
$x^4 e^2$	${}^1A_1 + {}^3A_2 + {}^1E$

Here the superscripts of each energy level define the spin multiplicity $(2S + 1)$. This defines the type of the state; superscript value of 1 denotes a spin singlet.

The application of group theory can be used to determine optical selection rules, gain information on the states that degenerate electrons possess in a crystal and by bringing all this information together, provide an understanding of the effect stress has on the perturbation of states and the resultant changes in spectroscopy. It cannot determine the order of states or their relative energies.

3.3 Uniaxial stress spectroscopy

3.3.1 Absorption

Despite the great efforts in cataloguing defects as they arise, as Collins states in 1999 and is still true today, "*...the things we still don't know about optical centres in diamond still greatly exceeds those which have been established with a reasonable degree of certainty*" [12]. A key task of this thesis is to extend our understanding by identifying the structure and symmetry of defects that arise from the treatments of diamond. With the information on symmetry properties, it is then possible to postulate about the atomic structure, electronic states and constrain the expected properties.

For defect centres, many degeneracies may exist. For example, the trigonal centre, aligned along the $\langle 111 \rangle$ axes of the crystal [6], has four possible orientations: [111], [11$\bar{1}$], [1$\bar{1}\bar{1}$], [$\bar{1}\bar{1}\bar{1}$]. The number of equivalent orientations n, can be calculated by the number of symmetry elements of the tetrahedral point group G, divided by the number of symmetry elements of the defect centre g. For C_{3v}, $n = G/g = 24/6 = 4$. However, this is not always the case; for example, when considering nickel centres in diamond, the defect is shown to grow preferentially into certain crystallographic sectors at the expense of others [13].

A perturbation is often required to allow optical techniques to distinguish between different orientations of a defect. Many techniques can be used to achieve this; polarised luminescence will preferentially excite the centres. Alternatively, techniques utilising the Zeeman effect (the splitting of a spectral line in the presence of a static magnetic field), can provide information as to the shift of energy levels [14, 15]. Typically, the effects are weak in diamond, as the perturbation is small compared with the linewidth. Perturbation from the magnetic field is

therefore difficult to observe.

The most successful method of perturbation is by uniaxial stress, applying a stress to the principal axis of a defect and observing resultant changes to spectral lines. Seminal work was completed by Kaplyanskii and many of the relations used today were derived during those studies [16, 17]. This work was amended and extended by research by Hughes, Runciman, Ludlow, Davies, Nazaré and Mohammed, who together have made contributions considering defects of trigonal symmetry, spin-orbit coupling, crystal misorientation and its contributing effect and tabulation of the possible values of the effect of sub-bandgap generated luminescence, gradually expanding the knowledge of the technique and its capabilities [18–22].

Uniaxial stress is therefore a well advanced and understood technique in terms of the theory and application. To illustrate, a defect of C_{3v} will be considered and a method shown for the calculation of the perturbation to the Hamiltonian, the resultant transition frequencies and the expected intensities when stressed.

3.3.2 The application of stress to a defect of C_{3v} symmetry

Original workings dealt only with orientational degeneracy, i.e. an optical transition between two A states. However, $A \rightarrow E$ transitions are very common. This example will consider the $A \rightarrow E$ transition for a C_{3v} symmetry defect.

For the trigonal centre, the principal axis is orientated along the [111] direction, Z. The X and Y axes are therefore chosen as being along the $[1\bar{1}0]$ and $[11\bar{2}]$ directions respectively and *not* the crystallographic axes, x, y, and z (Figure 3-2). Careful consideration needs to be given to ensure that the axes set used is consistent throughout.

The stress induced perturbation ($\mathscr{H}_1$) is written as:

$$\mathscr{H}_1 = \sum_{ij} a_{ij}\sigma_{ij} \tag{3-24}$$

where a_{ij} and σ_{ij} are the electronic operators and components of the stress tensor for a force applied to the i^{th} face in the j^{th} direction. Therefore, σ_{ij} is the projection of the stress tensor to the specific (i, j) direction.

$$\sigma_{ij} = \sigma \cos(\theta_i)\cos(\theta_j) \tag{3-25}$$

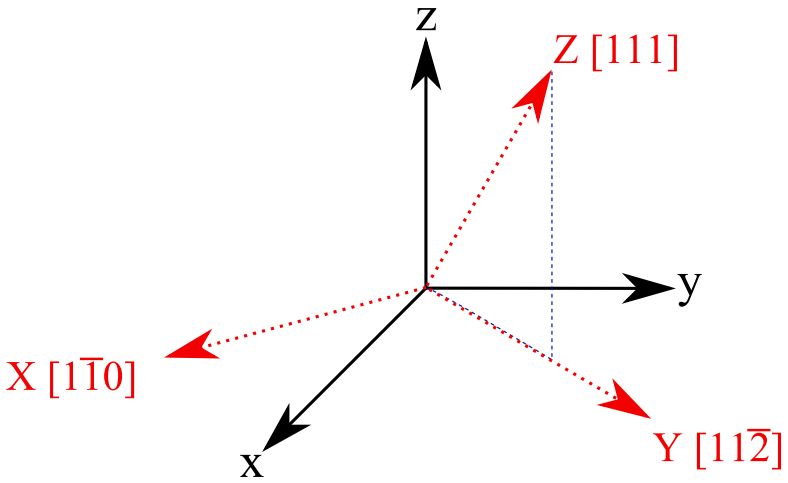

Figure 3-2: Orientation of the trigonal defect in diamond with respect to the crystallographic axes. The solid black lines represent the crystal axes, labelled with lower case letters. The dotted red lines, indicate the defect axes, labelled by capital letters.

$\boldsymbol{\sigma}$ is symmetric. Stresses where $i = j$ represent compressive stresses, whereas $i \neq j$ characterise shear stresses. In application, when directed along $\langle 001 \rangle$, symmetric σ_{ii} stress is generated and when along $\langle 111 \rangle$, shear σ_{ij} stress is induced. Stressing along the $\langle 110 \rangle$ direction applies both forms and can act as a consistency check.

Therefore, since the stress matrix is symmetric, for the site shown in the Figure 3-2:

$$\begin{aligned} \sigma \parallel [001]: &\quad \sigma_{xx} = \sigma_{yy} = \sigma_{xy} = \sigma_{xz} = 0 \text{ and } \sigma_{zz} = \sigma \\ \sigma \parallel [111]: &\quad \text{all } \sigma_{ij} = \sigma/3 \\ \sigma \parallel [110]: &\quad \sigma_{xx} = \sigma_{yy} = \sigma_{xy} = \sigma/2 \text{ and } \sigma_{zz} = \sigma_{xz} = \sigma_{yz} = 0 \end{aligned} \tag{3-26}$$

For purely orientational degeneracy, only non-degenerate terms will contribute to the perturbation of the Hamiltonian. However, for a centre with electronic as well as orientational degeneracy, the Hamiltonian for the perturbation of a C_{3v} centre is [18]:

$$\begin{aligned} \mathscr{H} = \mathscr{H}_0 &+ c_{A_1}(\sigma_{xx} + \sigma_{yy} + \sigma_{zz}) + c'_{A_1}(\sigma_{xy} + \sigma_{yz} + \sigma_{zx}) \\ &+ c_{E_\theta}(\sigma_{xx} + \sigma_{yy} - 2\sigma_{zz}) + \sqrt{3}c_{E_\epsilon}(\sigma_{xx} - \sigma_{yy}) \\ &+ c'_{E_\theta}(\sigma_{yz} + \sigma_{zx} - 2\sigma_{xy}) + \sqrt{3}c'_{E_\epsilon}(\sigma_{yz} - \sigma_{zx}) \end{aligned} \tag{3-27}$$

where the electronic operators $c_{A_1} \ldots c'_{E_\epsilon}$ transform as indicated by their subscripts. $(\sigma_{xx} + \sigma_{yy} + \sigma_{zz})$ represents the hydrostatic stress.

For the C_{3v} symmetry, there are four symmetry related sits which are characterised by the site rotation matrices:

$$
\begin{aligned}
{}^1\mathbf{R}_{C_{3v}} = e = \begin{bmatrix} 1 & 0 & 0 \\ 0 & 1 & 0 \\ 0 & 0 & 1 \end{bmatrix} \quad {}^2\mathbf{R}_{C_{3v}} = \begin{bmatrix} \bar{1} & 0 & 0 \\ 0 & \bar{1} & 0 \\ 0 & 0 & 1 \end{bmatrix} \\
{}^3\mathbf{R}_{C_{3v}} = \begin{bmatrix} 1 & 0 & 0 \\ 0 & \bar{1} & 0 \\ 0 & 0 & \bar{1} \end{bmatrix} \quad {}^4\mathbf{R}_{C_{3v}} = \begin{bmatrix} \bar{1} & 0 & 0 \\ 0 & 1 & 0 \\ 0 & 0 & \bar{1} \end{bmatrix}
\end{aligned}
\tag{3-28}
$$

Therefore the components of stress for each symmetry site (n) can be calculated as follows, using the general stress matrix $\boldsymbol{\sigma}$:

$$
{}^n\mathbf{R}^T_{C_{3v}} \boldsymbol{\sigma} {}^n\mathbf{R}_{C_{3v}} \tag{3-29}
$$

3.3.2.1 Calculation of transition shifts for stress in the $\langle 001 \rangle$ direction

For stress applied in the $\langle 001 \rangle$ direction, it has been shown that all elements of the stress matrix are equal to zero excepting σ_{zz}. Therefore, for all sites:

$$
\boldsymbol{\sigma} = \begin{bmatrix} \bar{1} & 0 & 0 \\ 0 & \bar{1} & 0 \\ 0 & 0 & 1 \end{bmatrix} \begin{bmatrix} 0 & 0 & 0 \\ 0 & 0 & 0 \\ 0 & 0 & \sigma \end{bmatrix} \begin{bmatrix} \bar{1} & 0 & 0 \\ 0 & \bar{1} & 0 \\ 0 & 0 & 1 \end{bmatrix} = \begin{bmatrix} \bar{1} & 0 & 0 \\ 0 & \bar{1} & 0 \\ 0 & 0 & 1 \end{bmatrix} \begin{bmatrix} 0 & 0 & 0 \\ 0 & 0 & 0 \\ 0 & 0 & \sigma \end{bmatrix} = \begin{bmatrix} 0 & 0 & 0 \\ 0 & 0 & 0 \\ 0 & 0 & \sigma \end{bmatrix} \tag{3-30}
$$

From this, the Hamiltonian for each site can be evaluated by taking the values for the various σ_{ij} components. For sites 1–4, only the σ_{zz} components return non-zero values and the perturbed Hamiltonian for all four sites is:

$$
\mathscr{H} = \mathscr{H}_0 + c_{A_1}(\sigma) + c_{E_\theta}(-2\sigma) \tag{3-31}
$$

This has the form:

$$
\begin{array}{lccc}
 & |a_1\rangle & |\theta\rangle & |\epsilon\rangle \\
\langle a_1| & \hbar\omega_0 + \langle a_1|c_{A_1}|a_1\rangle\sigma & & \\
\langle \theta| & & (\langle\theta|c_{A_1}|\theta\rangle - 2\langle\theta|c_{E_\theta}|\theta\rangle)\sigma & \\
\langle \epsilon| & & & (\langle\epsilon|c_{A_1}|\epsilon\rangle - 2\langle\epsilon|c_{E_\theta}|\epsilon\rangle)\sigma
\end{array}
\tag{3-32}
$$

The vanishing integrals in the above matrix can be identified by application of the Wigner-Eckart theorem [23]. This states that "*basis functions that span irreducible representations of different symmetry species are orthogonal*".

The Eigenvalues of this Hamiltonian help quantify the shift of the transitions upon the application of stress to a C_{3v} centre in the $\langle 001 \rangle$ direction. Using the identities that:

$$\mathrm{A}_1 = \langle a_1 | c_{\mathrm{A}_1} | a_1 \rangle - \langle \theta | c_{\mathrm{A}_1} | \theta \rangle \tag{3-33}$$

and

$$-\mathrm{B} = \langle \theta | c_{\mathrm{E}_\theta} | \theta \rangle \tag{3-34}$$

$$\begin{aligned} E_1 &= \hbar\omega_0 + \langle a_1 | c_{\mathrm{A}_1} | a_1 \rangle \sigma \\ E_2 &= (\langle a_1 | c_{\mathrm{A}_1} | a_1 \rangle + 2\mathrm{B})\sigma \\ E_3 &= (\langle \epsilon | c_{\mathrm{A}_1} | \epsilon \rangle - 2\mathrm{B})\sigma \end{aligned} \tag{3-35}$$

and therefore:

$$\begin{aligned} \hbar\omega_{12} &= E_1 - E_2 = \hbar\omega_0 + [\mathrm{A}_1 - 2\mathrm{B}]\sigma \\ \hbar\omega_{13} &= E_1 - E_3 = \hbar\omega_0 + [\mathrm{A}_1 + 2\mathrm{B}]\sigma \end{aligned} \tag{3-36}$$

3.3.2.2 Calculation of transition shifts for stress in the $\langle 111 \rangle$ and $\langle 110 \rangle$ directions

A similar method can be used for analysing the $\langle 111 \rangle$ and $\langle 110 \rangle$ directions. Now, the general stress matrices for site 1 are as follows:

$$\sigma_{\langle 111 \rangle} = \begin{bmatrix} \sigma/3 & \sigma/3 & \sigma/3 \\ \sigma/3 & \sigma/3 & \sigma/3 \\ \sigma/3 & \sigma/3 & \sigma/3 \end{bmatrix} \quad \sigma_{\langle 110 \rangle} = \begin{bmatrix} \sigma/2 & \sigma/2 & 0 \\ \sigma/2 & \sigma/2 & 0 \\ 0 & 0 & 0 \end{bmatrix} \tag{3-37}$$

The Hamiltonians for each are subsequently calculated by Equation (3-29) (Table 3-5) and using the additional identities that:

$$\mathrm{A}_2 = 1/2 \langle a_1 | c'_{\mathrm{A}_1} | a_1 \rangle - \langle \theta | c'_{\mathrm{a}_1} | \theta \rangle \tag{3-38}$$

and

$$\mathrm{C} = -\langle \theta | c'_{\mathrm{E}_\theta} | \theta \rangle = \langle \epsilon | c'_{\mathrm{E}_\theta} | \epsilon \rangle \tag{3-39}$$

the shift rates can be calculated (Table 3-6).

Table 3-5: Perturbed Hamiltonians for a defect of C_{3v} symmetry with $\sigma \parallel \langle 111 \rangle$ and $\sigma \parallel \langle 110 \rangle$.

Site	**Hamiltonians for** $\langle 111 \rangle$
1	$\mathscr{H}_0 + c_{\mathrm{A}_1}(\sigma) + c'_{\mathrm{A}_1}(\sigma)$
2	$\mathscr{H}_0 + c_{\mathrm{A}_1}(\sigma) + c'_{\mathrm{A}'_1}(-\sigma/3) + c'_{\mathrm{E}_\theta}(-4\sigma/3)$
3	$\mathscr{H}_0 + c_{\mathrm{A}_1}(\sigma) + c'_{\mathrm{A}'_1}(-\sigma/3) + c'_{\mathrm{E}_\theta}(-2\sigma/3) + c'_{\mathrm{E}_\epsilon}\sqrt{3}(2\sigma/3)$
4	$\mathscr{H}_0 + c_{\mathrm{A}_1}(\sigma) + c'_{\mathrm{A}'_1}(-\sigma/3) + c'_{\mathrm{E}_\theta}(-2\sigma/3) + c'_{\mathrm{E}_\epsilon}\sqrt{3}(-2\sigma/3)$
Site	**Hamiltonians for** $\langle 110 \rangle$
1, 2	$\mathscr{H}_0 + c_{\mathrm{A}_1}(\sigma) + c'_{\mathrm{A}'_1}(\sigma/2) + c'_{\mathrm{E}_\theta}(\sigma) - c'_{\mathrm{E}_\theta}(\sigma)$
3, 4	$\mathscr{H}_0 + c_{\mathrm{A}_1}(\sigma) - c'_{\mathrm{A}'_1}(\sigma/2) + c'_{\mathrm{E}_\theta}(\sigma) + c'_{\mathrm{E}_\theta}(\sigma)$

Table 3-6: Frequency transitions of a defect of C_{3v} symmetry under stress in the $\langle 111 \rangle$ and $\langle 110 \rangle$ directions. Each transition is attributed to a site from which it originates, correlating with the site rotation matrices (Equation (3-28)).

Transition$_{\langle 111 \rangle}$	**Site**	**Transition**$_{\langle 110 \rangle}$	**Site**
$\hbar\omega_0 + [\mathrm{A}_1 + 2\mathrm{A}_2]\sigma$	1	$\hbar\omega_0 + [\mathrm{A}_1 + \mathrm{A}_2 + \mathrm{C} - \mathrm{B}]\sigma$	1,2
$\hbar\omega_0 + [\mathrm{A}_1 - \frac{2}{3}\mathrm{A}_2 + \frac{4}{3}\mathrm{C}]\sigma$	2,3,4	$\hbar\omega_0 + [\mathrm{A}_1 + \mathrm{A}_2 - \mathrm{C} + \mathrm{B}]\sigma$	1,2
$\hbar\omega_0 + [\mathrm{A}_1 - \frac{2}{3}\mathrm{A}_2 - \frac{4}{3}\mathrm{C}]\sigma$	2,3,4	$\hbar\omega_0 + [\mathrm{A}_1 - \mathrm{A}_2 + \mathrm{C} + \mathrm{B}]\sigma$	3,4
		$\hbar\omega_0 + [\mathrm{A}_1 - \mathrm{A}_2 - \mathrm{C} - \mathrm{B}]\sigma$	3,4

This method can be applied for any symmetry to identify the equations characterising the rate of frequency shift of a transition when perturbed by an applied stress.

3.3.2.3 Calculation of stress split transition intensities for a C_{3v} symmetry defect

The intensities of the stress split lines can be obtained by consideration of the polarisations of light with respect to the direction of stress for the various transitions. As before, care needs to be taken when moving between the crystallographic directions used for defining the application of stress and the axes defined for the defect (Figure 3-2).

For an $A \rightarrow A$ transition at a trigonal defect, the dipole will be in the Z

direction. For an $A \rightarrow E$ transition at a trigonal centre, the dipole is in the (X,Y) plane. For a defect with C_{3v} symmetry, consideration of the $\langle 001 \rangle$ and $\langle 110 \rangle$ directions is trivial since there is no mixing between the $|\theta\rangle$ and $|\epsilon\rangle$ basis functions labelling the E state. However, for stress applied along the $\langle 111 \rangle$ direction, the solution is more complex and shall therefore be examined here.

Considering the trigonal C_{3v} defect, stressed along the $\langle 111 \rangle$ direction, sites 1 and 2 for the $\langle 111 \rangle$ stress direction still present no difficulties, with only terms in the leading diagonal of the Hamiltonian matrix and therefore non-mixed eigenvectors. Sites 3 and 4 introduce mixing between the states (Table 3-5).

Using the identities previously mentioned (Equations (3-33),(3-34),(3-38),(3-39)), the following matrix for site 3 results (ignoring the a_1 state):

	$\|\theta\rangle$	$\|\epsilon\rangle$
$\langle\theta\|$	$\hbar\omega_0 + \langle\theta\|c_{A_1}\|\theta\rangle\sigma - \langle\theta\|c'_{A_1}\|\theta\rangle(\sigma/3)$ $-(2C\sigma/3)$	$(2C\sigma/\sqrt{3})$
$\langle\epsilon\|$	$(2C\sigma/\sqrt{3})$	$\hbar\omega_0 + \langle\epsilon\|c_{A_1}\|\epsilon\rangle\sigma - \langle\epsilon\|c'_{A_1}\|\epsilon\rangle(\sigma/3)$ $+(2C\sigma/3)$

Let $\langle\theta|c_{A_1}|\theta\rangle\sigma - \langle\theta|c'_{A_1}|\theta\rangle(\sigma/3) = \langle\epsilon|c_{A_1}|\epsilon\rangle\sigma - \langle\epsilon|c'_{A_1}|\epsilon\rangle(\sigma/3) = \eta\sigma$. To calculate the Eigenvalues (λ) and Eigenvectors:

$$\begin{vmatrix} (\hbar\omega_0 + \eta - (2C/3)) - \lambda & 2C/\sqrt{3} \\ 2C/\sqrt{3} & (\hbar\omega_0 + \eta + (2C/3)) - \lambda \end{vmatrix} = 0 \qquad (3\text{-}40)$$

Therefore, $\lambda = \eta \pm 4C/3$ and we arrive at the solutions for the transitions as quoted in Table 3-6.

For a matrix $\mathbf{A}$, there exists vectors $\underline{v}$, which when transformed by $\mathbf{A}$, will be a multiple of themselves.

$$\mathbf{A}\underline{v} = \lambda\underline{v} \qquad (3\text{-}41)$$

$\underline{v}$ represents an Eigenvectors of the matrix $\mathbf{A}$ where $\underline{v_1} = \alpha|\theta\rangle + \beta|\epsilon\rangle$ and $\underline{v_2} = -\beta|\theta\rangle + \alpha|\epsilon\rangle$. α and β are related by terms of a single parameter ($\alpha = \cos\phi$ and $\beta = \sin\phi$).

Hence:

$$(\eta - (2C/3) - \lambda_1)\cos\phi + (2C/\sqrt{3})\sin\phi = 0 \tag{3-42}$$

$$(\eta + (2C/3) - \lambda_1)\sin\phi + (2C/\sqrt{3})\cos\phi = 0 \tag{3-43}$$

$$-(\eta - (2C/3) - \lambda_2)\sin\phi + (2C/\sqrt{3})\cos\phi = 0 \tag{3-44}$$

$$(\eta + (2C/3) - \lambda_2)\cos\phi - (2C/\sqrt{3})\sin\phi = 0 \tag{3-45}$$

Multiplying (3-42) by $\sin\phi$ and subtracting (3-44) multiplied by $\cos\phi$, gives

$$\begin{aligned} \tan(2\phi) &= -\sqrt{3} \\ \phi &= -30^\circ \end{aligned} \tag{3-46}$$

Considering a polarised beam of light with an electric vector defined by $\underline{E}$, a centre orientated with the dipole along the symmetry axis $\underline{Z}$ of the defect (i.e. representing and $A \rightarrow A$ transition at a defect with C_{3v} symmetry), will give an absorption from $\underline{E}$ equal to the resolved component along $\underline{Z}$. The loss of energy of the beam, or the level of absorption will be proportional to the square of the projection of $\underline{E}$ on $\underline{Z}$. Therefore the absorption at the centre, summing over all the possible states (i), $\mu_1 \propto \sum_{\mathrm{i}}(\underline{E}\cdot\underline{Z_{\mathrm{l}}})^2$. For an $A \rightarrow E$ transition with the dipole orientated in the (X,Y) plane, the transition $a_1 \rightarrow v_l$ can be calculated by:

$$\mu \propto \sum_i [\alpha_i \underline{E}\cdot\underline{Y}_i + \beta_i \underline{E}\cdot\underline{X}_i]^2 \tag{3-47}$$

3.4 Defect migration

Many mechanisms allow a defect to move through the lattice of the material. They belong to two classes, depending on whether the defect is substitutional or interstitial. Possible methods may be for defects to migrate by jumping from their original sites into a vacant site or by an exchange mechanism with neighbouring atoms.

Jump probability and migration energy can be considered through the Born-Oppenheimer approximation, giving information as to the energy of an atom as a function of its atomic position. Qualitatively, the Born-Oppenheimer approximation rests on the fact that the nuclei are much more massive than the electrons, allowing it to be said that the nuclei are nearly fixed with respect to electron

motion. The application of rate theory and dynamical theory, can then be applied to determine the activation for the migration. Rate theory assumes that between the initial and final states, an activated state exists; dynamical theory treats the displacement as a superposition of phonons in a harmonic crystal, such that when the cumulative local displacements of the defect are sufficiently large and neighbouring atoms can move sufficiently to reduce the repulsion between them, a jump may occur.

The identification of a specific migration mechanism is a complex problem. Information with regards to this can only be gained indirectly since it is not possible to observe and individual atom inside the crystal. A more thorough review of defect migration and diffusion is presented by Lannoo and Bourgoin [24, 25].

3.5 Annealing

This thesis utilises two experimental methods of heat treatment. The first results in the permanent change of a defect by heating and shall be referred to as annealing. The second induces a change in the defect concentration due to charge transfer process which is reversible and shall be referred to as heat treatment. This chapter will refer to processes of annealing but similar principles can be applied to heat treatments.

Changes to concentrations under annealing occur when the defect concentration is not at an equilibrium for a specific temperature. The concentration of a defect may be reduced as a result of migration towards a sink with which it can combine, such as a vacancy, dislocation or another defect, *or* the dissociation of complexes into two new defects.

The optical *activity* of a defect can also be modified by the charge state in which it exists. This can be modified by heat treatment processes causing the transfer of charge between defects at relatively low temperatures, less than those required for the break-up or migration of the defect.

The more stages that are involved in the formation of a new defect, i.e. the requirement of the dissociation of one or more other defects, the greater the energy required to for the process to occur. This therefore acts as the rate determining

step for the process.

3.5.1 First order kinetics

For a first order reaction where [N] → [M], the rate of change of a defect concentration in a period t is given by Equation (3-48).

$$\frac{d[\mathrm{N}]}{dt} = -K[\mathrm{N}] \tag{3-48}$$

K the rate constant. The solution to this will depend upon the order of the reaction. For a first order reaction, the solution is given by the Arrhenius equation:

$$[\mathrm{N}] = [\mathrm{N_0}]\exp(-Kt) \tag{3-49}$$

The number of defects which will disappear per unit time is proportional to the number of defects present at that time and the rate constant.

$$K = \nu_0 \exp\left(\frac{-E_a}{\mathrm{k_B T}}\right) \tag{3-50}$$

in units per time. ν_0 is the characteristic attempt frequency and E_a the activation energy for the process.

The sample is considered as homogeneous in terms of the distribution of the defects involved and it is assumed that the sink concentration will remain constant and much greater than that of the defect. The sink is therefore not a limiting factor in the formation of the new defect. A further assumption is that as $t \to \infty$, [N]→ 0 and therefore the forward reaction will dominate.

3.5.2 Second order kinetics

If instead [N]+[N] → [M] the rate of reaction is dependent upon the concentrations of both reactants, then second order kinetics are appropriate.

$$[\mathrm{N}] = \frac{1}{[\mathrm{N_0}]^{-1} + Kt} \tag{3-51}$$

Second order kinetics may be appropriate for the direct recombination of two randomly distributed defects. An example of this is with vacancies (V) and interstitials (I). They are formed in equal concentrations as a product of irradiation

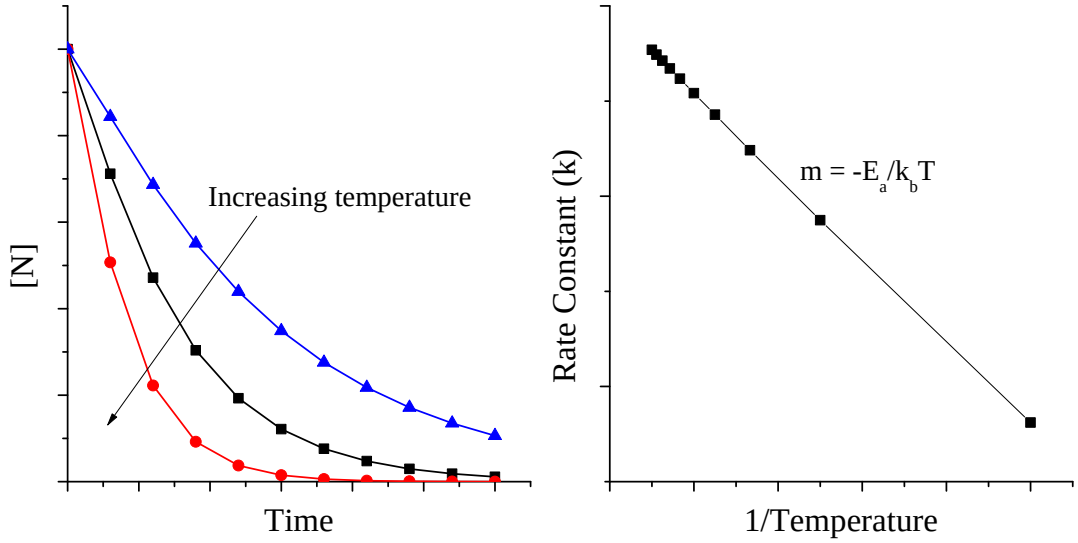

Figure 3-3: Isothermal annealing curves. Annealing experiments are performed at the same temperature for increasing periods of time. When repeated at different temperatures, this produces a set of curves from which the activation energy can be calculated. For first order kinetics, $K \propto 1/T$.

and can recombine by a single jump.

$$\frac{d\mathrm{N_I}}{dt} = \frac{d\mathrm{N_V}}{dt} = -K\mathrm{N_I}\mathrm{N_V} \tag{3-52}$$

Since $\mathrm{N_I} = \mathrm{N_V}$

$$\frac{d\mathrm{N_I}}{dt} = -K\mathrm{N_I}^2 \tag{3-53}$$

For other instances, where reactions are of a higher order, a system of coupled differential equations exist. The problem is more complex and will not be considered here.

3.5.3 Iso- thermal/chronal annealing

Two ways of determining the activation energy of a defect's migration process is by isothermal (same temperature) or isochronal (same time) annealing. For isothermal annealing, consideration is given to a changing defect concentration as annealing time increases at a set temperature (Figure 3-3). Repeating this for a series of temperatures results in a set of annealing curves. For first order kinetics, K is proportional to 1/T with a gradient of $-E_a/\mathrm{k_B}$ (Equation (3-50)). Hence the activation energy for the process can be established.

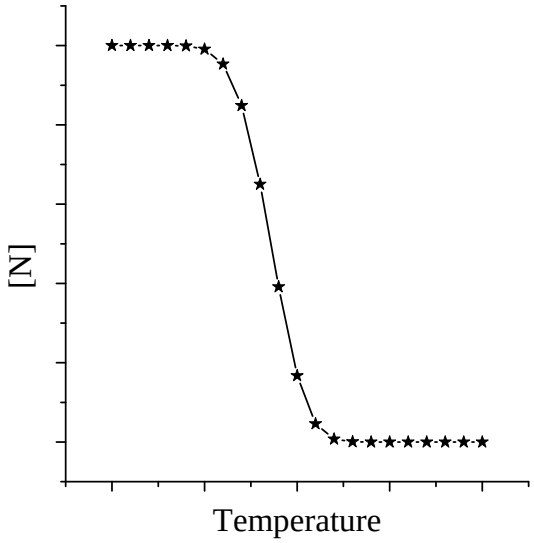

Figure 3-4: Isochronal annealing curve. As the temperature of annealing increases, there is a sudden change in concentration. From this, the activation can be estimated.

For the isochronal annealing of a first order process (Figure 3-4), E_a and K can be estimated a single isochronal annealing curve (Equation (3-49)). The sample is heated for a fixed time (t) at successive, increasing temperatures. Isochronal annealing provides a rapid method of estimating the activation energy but for the determination of accurate values, isothermal annealing is necessary.

References

[1] P. W. Atkins and R. S. Friedman, *Molecular Quantum Mechanics* (Oxford University Press, 2003), 3rd ed.

[2] H. E. Smith, PhD. thesis, King's College, University of London (2004).

[3] M. Lax and E. Burstein, Physical Review **97**, 39 (1955).

[4] C. V. Raman, Proceedings of the Indian Academy of Science **A19**, 189 (1944).

[5] S. A. Solin and A. K. Ramdas, Physical Review B **1**, 1687 (1970).

[6] G. Davies, *Optical Measurements of Point Defects* (Academic Press, 1998), vol. 51B of *Semiconductors and Semimetals*, chap. 1, pp. 1–92.

[7] J. Walker, Reports on Progress in Physics **42**, 1605 (1979).

[8] C. Kittel, *Introduction to Solid State Physics* (John Wiley & Sons, 1976).

[9] M. D. McCluskey, Journal of Applied Physics **87**, 3593 (2000).

[10] W. Ludwig and C. Falter, *Symmetries in Physics* (Springer-Verlag Berlin Heidelberg New York, 1988).

[11] S. Sternberg, *Group theory and physics* (Cambridge University Press, 1994).

[12] A. T. Collins, Diamond and Related Materials **8**, 1455 (1999).

[13] A. T. Collins, Journal of Physics: Condensed Matter **1**, 439 (1989).

[14] P. Zeeman, Philosophical Magazine Series 5 **43**, 226 (1897).

[15] P. Zeeman, Nature **55**, 347 (1897).

[16] A. A. Kaplyanskii, Optics and Spectroscopy **16**, 329 (1963).

[17] A. A. Kaplyanskii, Optics and Spectroscopy **16**, 557 (1963).

[18] A. E. Hughes and W. A. Runciman, Proceedings of the Physical Society **90**, 827 (1967).

[19] I. K. Ludlow, Journal of Physics C: Solid State Physics **1**, 1194 (1968).

[20] G. Davies, Journal of Physics C: Solid State Physics **8**, 2448 (1975).

[21] G. Davies and M. H. Nazaré, Journal of Physics C: Solid State Physics **13**, 4127 (1980).

[22] K. Mohammed, G. Davies, and A. T. Collins, Journal of Physics C: Solid State Physics **15**, 2779 (1982).

[23] M. Tinkham, *Group Theory and Quantum Mechanics* (McGraw-Hill Book Company, 1964).

[24] J. Bourgoin and M. Lannoo, *Point Defects in Semiconductors I - Theoretical Analysis*, Springer Series in Solid-State Sciences (Springer-Verlag Berlin Heidelberg New York, Germany, 1981).

[25] J. Bourgoin and M. Lannoo, *Point Defects in Semiconductors II - Experimental Aspects*, Springer Series in Solid-State Sciences (Springer-Verlag Berlin Heidelberg New York, Germany, 1983).

Chapter 4

Experimental Techniques

This chapter will outline the main techniques used in the work reported in this thesis. These will include: high-pressure high-temperature (HPHT) and vacuum/atmosphere annealing, optical absorption spectroscopy, uniaxial stress, electron paramagnetic resonance spectroscopy (EPR) and general sample preparation.

4.1 Annealing

Annealing of a semiconductor material can lead to substantial changes in structural, mechanical and electronic properties. The intended purpose of annealing may be to reduce the concentration of unwanted defects or to promote the diffusion of impurities. For semi-conductor materials, a combination of the two is generally desired, to process the material to anneal out unwanted defects, whilst minimising the diffusion of other dopants.

The work of this thesis uses two techniques for annealing diamond. Since diamond is not the stable allotrope of carbon at atmospheric pressure, there is a requirement for stabilising pressure before it can be annealed at high temperatures (>1600℃). The equilibrium phase boundary between the graphitic and diamond phases is outlined in Figure 4-1 and Equation (4-1), where P is the applied pressure and T, the environmental temperature. [1].

$$\mathrm{P\,(kbar)} = 17 + 0.021\mathrm{T\,(K)} \tag{4-1}$$

Annealing at atmosphere at temperatures less than 800℃ can be done, al-

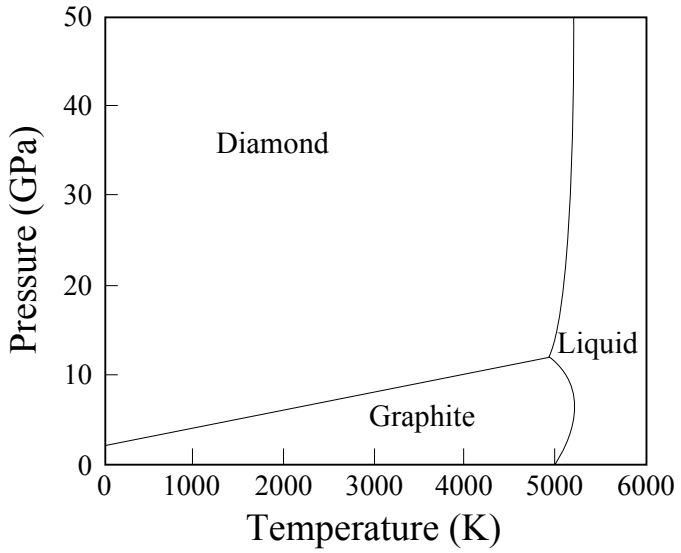

Figure 4-1: The pressure, temperature phase and transition diagram for carbon as presented evaluated by experiments of Bundy *et al.* [2]. Lines represent the equilibrium phase boundaries.

though caution must be taken to minimise environmental oxygen. Oxygen can behave in a catalytic manner, leading to surface graphitisation and sample damage [3].

4.1.1 The high-pressure high-temperature press

DB1, the HPHT press used, was originally built by Vector S.A. for the synthesis of diamond. It was refurbished and modified for the Diamond Trading Company, to be used for research into the effects of HPHT annealing on defects in diamond. It was then donated to the University of Warwick to continue this work. The system is comprised of three elements:

- The 500 tonne hydraulic press
- The electrical power system
- The pressure and power feedback control

4.1.1.1 The hydraulic system

The hydraulic system controls both the pressure and flow of hydraulic fluid within a closed loop circuit. These two parameters are controlled by an electronic amplifier card and via a pressure transducer, oil pressure and flow values are transmitted

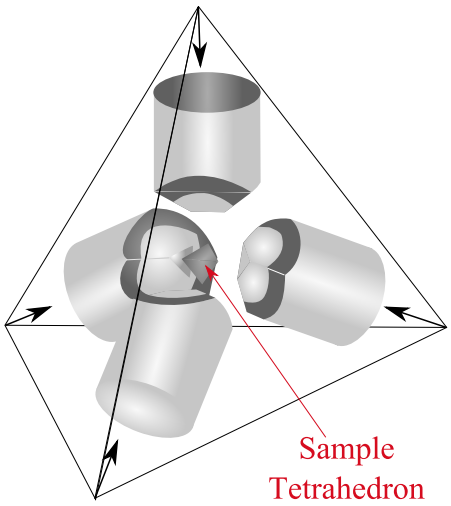

Figure 4-2: Configuration of four anvils.

as voltage feedback values to the system. A valve acts as a flow controller when the set point value is in excess of the current pressure and a regulator when the desired set point has been achieved. A Bosch radial piston pump is pressure and flow compensated, with the pump delivery responding to system parameter changes as required. A high pressure relief valve protects the system, ensuring that the piston pump will compensate at high pressure loads. An accumulator, located in the main pressure line, helps to cushion any shock changes.

The ram is driven by supplying a voltage to the pressure and flow controls at the proportional valve. The speed of movement is governed by the signal from the flow controller, until the point where contact is made and pressure begins to build. The load, provided by the ram, is then governed by the pressure build up. The load will remain at a constant value until the voltage governing the load is changed. In order for the ram to drop, the system pressure must be slowly released.

4.1.1.2 The anvils

Anvils are formed from tungsten carbide, held in a steel binding ring with a hollow steel ring surrounding for the purpose of water cooling. Two of the four anvils have an electrical terminal attached, to provide an electrical circuit when contacted with the sample cell. This was used for the resistive heating of the sample. Three of the anvils were machined to fit inside the *gun barrel* cone with an inclined angle

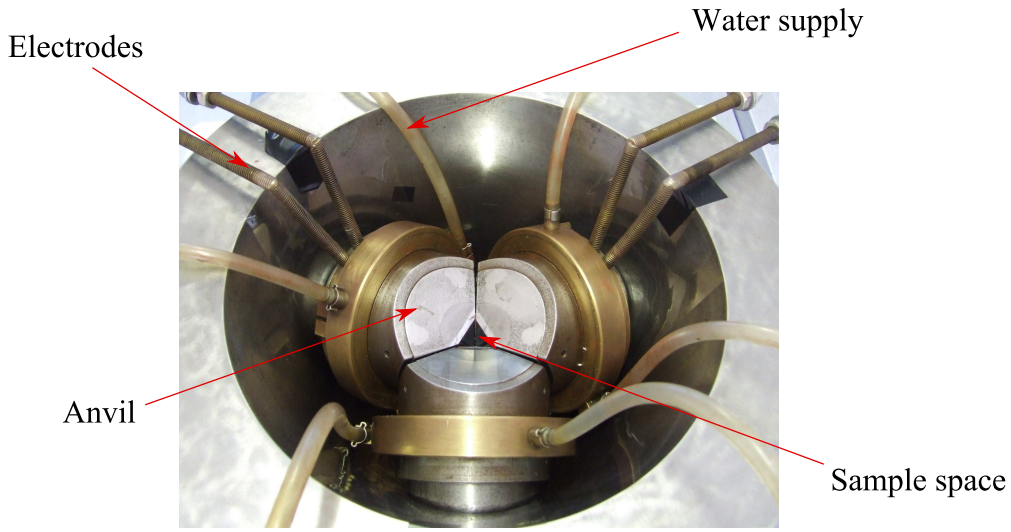

Figure 4-3: Configuration of the lower three anvils within the gun barrel. Labelled are the electrodes and the water supply tubes for the cooling of the anvils.

of 18.5°, with the fourth top anvil having a flat face for planar contact with the load plate (Figure 4-3).

In preparation for running, the gun barrel was lined with Teflon and Melinex sheeting to electrically insulate the anvils from the gun barrel and provide a surface of reduced friction and the smooth and even displacement of the anvils under pressure. Teflon buttons 0.25 cm thick, were placed in four places evenly around one face of the three base anvils and all three faces of the top anvil to prevent contact between them. These were mounted using double-sided adhesive tape. The slanting faces, 0.5 cm from the flat triangular face, were painted with ferric oxide to increase the friction between the extruding pyrophyllite and the tungsten carbide anvil face and encourage the formation of gaskets. In experiments where a thermocouple was used, the non-electrode connected base anvil had additional Teflon sheeting on the uppermost face, over which the thermocouple wires passed.

4.1.1.3 The high pressure cell

The sample cell was machined from pyrophyllite (Figure 4.4(b)), an easily machinable material with excellent thermal stability. It is widely used in high pressure experiments as both a pressure transmitting medium and a gasket material. In this system, it fulfills both functions.

Pyrophyllite undergoes several phase changes when heated, which would cause

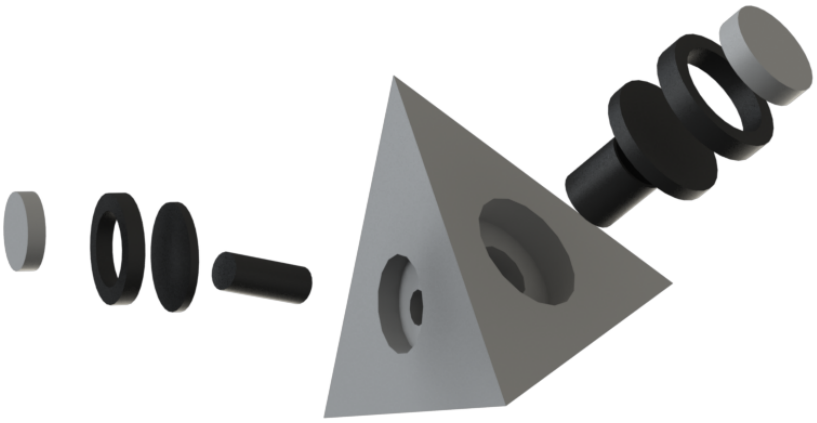

(a)

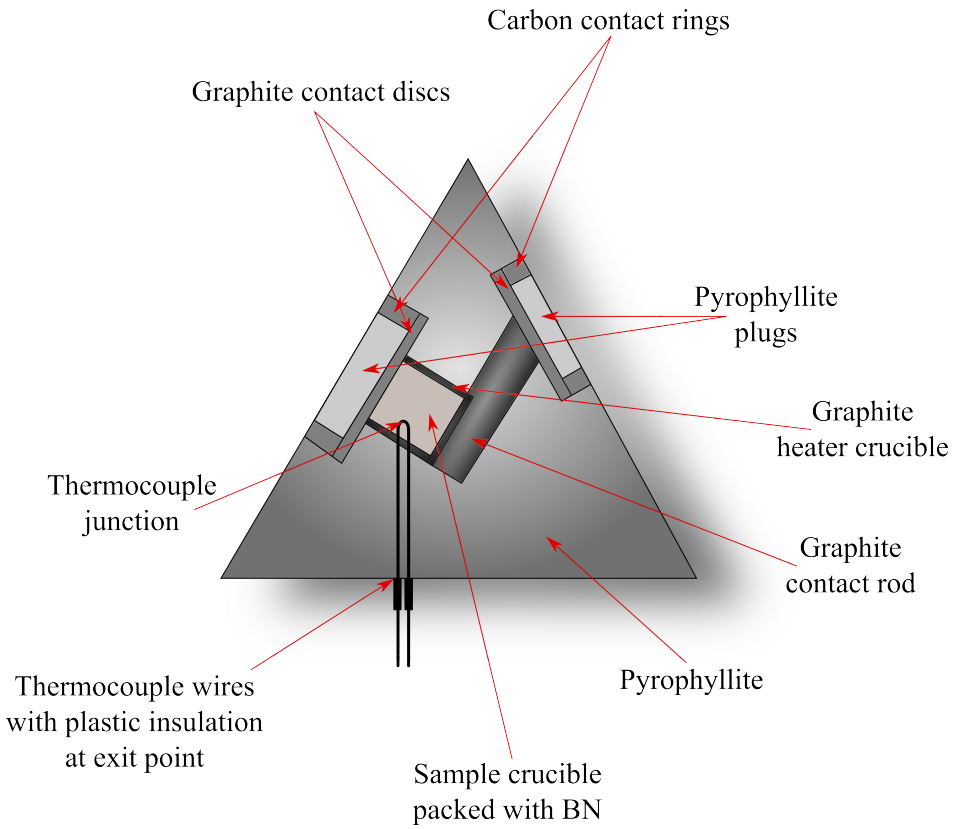

(b)

Figure 4-4: The design of the tetrahedral sample cell for HPHT annealing. (a) shows an exploded view of the tetrahedron, highlighting the graphite contact rings, discs and pyrophyllite plugs. (b) shows a cross section through the tetrahedron, indicating the positioning of the thermocouple junction and the graphite heating rod and crucible [4].

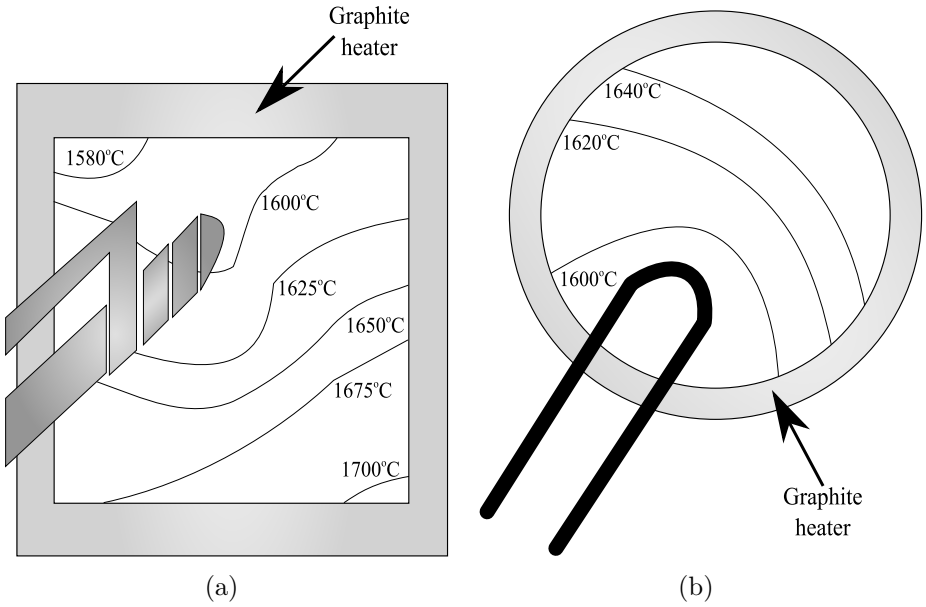

Figure 4-5: Estimates of the heat dissipation across a sample chamber [6]. (a) illustrates a vertical cross section of the graphite heater crucible with a set point of 1600℃ for 10 minutes. (b) indicates the circular cross section under the same environmental parameters.

large pressure variations within the sample region. Therefore, before use, the pyrophyllite was baked at 500℃ for 8 hours and then kept in a furnace at 80℃ until required, to stabilise its properties and minimise its water content.

Two chambers are drilled into the tetrahedron. One is filled with a solid graphite rod and the other with a crucible style graphite sample holder. This creates the conductive path for resistive heating of the sample. A graphite disc and ring with a pyrophyllite plug seal the crucible once the sample has been inserted.

Within the sample crucible, the sample is placed centrally and packed with hexagonal boron nitride powder. The low shear strength of boron nitride allows it to flow freely around the material and there is no reported evidence of any interaction between boron nitride and diamond [5].

A thermocouple was frequently used within the chamber. A tungsten iridium thermocouple was originally chosen, which had the benefit of a small EMF below 50℃ and so did not require a cold junction calibration. However, at high pressures, the wires were often damaged by compression from the anvils. Thinner K-type thermocouples were subsequently used, which had an upper operating temperature

limit of 1250℃. Extrapolation of the input electrical power with temperature permitted conversions at higher powers.

It has been shown that the presence of a thermocouple within a chamber can act as a heat sink, creating a temperature gradient across the sample region (Fig. 4-5) [6]. This was measured by finding the ratio of luminescence of the 2.464 (H3 defect) and 1.945 eV (NV^- defect) sidebands which provided an indication of temperature at various points across a compacted diamond powder at 9.5 GPa. A similar temperature gradient would be expected for boron nitride.

4.1.1.4 The controllers

The existing hardware controllers of the press system were outdated and required replacement. Two new Eurotherm 2704 controllers were installed, providing the user interface with the hydraulic and power systems. These controllers were soft and hard wired to suit our requirements, providing control over output commands, feedback controls, PID settings and permitted the integration of a number of safety features based upon inputs from various hardware components.

Within the power controller, a power demand (set point) was made, which by a micropower control card, was separated into distinct current and voltage values according to internal settings. Via a transformer, these were then transmitted to anvil electrodes, producing a sufficient voltage to resistively heat the sample to the desired temperature. A monitor on the feedback current and voltage, communicated a process variable (working value) via a multiplier, so as to display a power value to the user.

A number of hardware monitors and the input and output variables of the controllers were integrated into the safety system, controlled by the Eurotherm controllers. Optical sensors detected the current height of the ram which then was used to identify a *fast approach* and *slow approach* regimes as the ram approached the load plate. These two states then throttled the flow voltage between maximum and half maximum to control the speed of the ram. Check signals identified if water flow was present around the anvils before heating was permitted and communication between the two controllers using the soft wiring options, ensured that pressure ramping was completed before heating could begin and that the

power programme had reach an *end state* before the pressure would ramp down. A final safety check was the introduction of Hall sensors in the hardware to detect the feedback current and voltage. On occasion, where a short circuit had developed, normally due to contacting anvils, the current would rise rapidly with no associated resistance. From a number of successful experiments across the operating range of the press, it was noted that the current would never rise above 300 A. Therefore, if the Hall sensor detected a current greater than 300 A, a signal was sent to the controller, soft wired to be understood as an abort command and would end the power ramping programme.

To preserve the anvils, load ramping was limited to 3 tonnes per minute and unloading to 1 tonne per minute. For heating, this was limited to 50 Watts per minute to prevent excessive heating strains to the sample cell.

4.1.1.5 Calibration of sample cell environment

Thermometry with this system proved difficult. The pressure exerted on the wires by the extruding gasket was sufficient that wires frequently fractured. Thicker thermocouples did not fracture so easily but were too large to form a neat, non–shorting join in the graphite sample chamber or alternatively were pinched and fractured by the compressing anvils. Lower pressure thermometry at temperatures less than 1250℃ was possible (<4 GPa), which could then be extrapolated for higher temperatures.

An EMF is generated along the length of the two dissimilar metals that are subjected to a temperature gradient. For most metals used for thermocouples, the output voltage increases linearly with temperature difference. The EMF of the thermocouple was recorded and was translated into a temperature value based upon the materials of the thermocouple. The resulting calibration equation was calculated as:

$$\text{Temperature}\,(^{\circ}\text{C}) = \text{Power}\,(\text{W}) \times 1.53(4) \tag{4-2}$$

The cell pressure versus the applied load was calibrated by measuring the change in electrical resistance of several well known phase transitions of bismuth [7, 8]. At room temperature, load was applied to the system at a rate of 1 tonne per minute and the resistance of the bismuth wire measured. The re-

Table 4-1: Phase transitions of bismuth under pressure [7, 8].

Transition	**Pressure (GPa)**
I→II	2.54
II→III	2.7
High Bismuth	7.7

sistance data were correlated to the process variable and set point data from the pressure controller, to find a resistance versus load relation and therefore a conversion factor between the two quantities. Observing the high bismuth transition was not possible, resulting in having only two points at similar pressures to form the calibration from. Repeated calibrations using this technique have resulted in similar relations between load and pressure such that:

$$\text{Pressure (GPa)} = 0.037(4) \times \text{Load (T)} \tag{4-3}$$

Hysteresis is evident in the system. As the load is applied, the tetrahedra cell is compressed to a volume approximately half of its original. Therefore, as load is removed, the relative pressure is substantially higher. Experiments performed at a range of pressures were completed sequentially as load on the cell was increased.

4.1.2 The horizontal tube furnace

Annealing experiments utilised an Elite Thermal Systems Ltd. horizontal tube furnace, with a hot zone of 180 mm and a maximum temperature of 1600℃. The furnace tube was constructed of re-crystallised alumina tube surrounded by heating elements. Alumina radiation shields were inserted at either end of the work tube to ensure that heat was focused in the central hot zone by radiation reflection. A diagram of the tube furnace is shown in Figure 4-6.

The horizontal thermal profile for the furnace was measured at different temperatures (for example Figure 4.7(a)). This profiling permitted reproducibility of sample positioning in the optimum location within the tube. Temperature variation over the sample region of the boat (2 cm) was minimal, providing a homogeneous environment during annealing. The calibration between the furnace

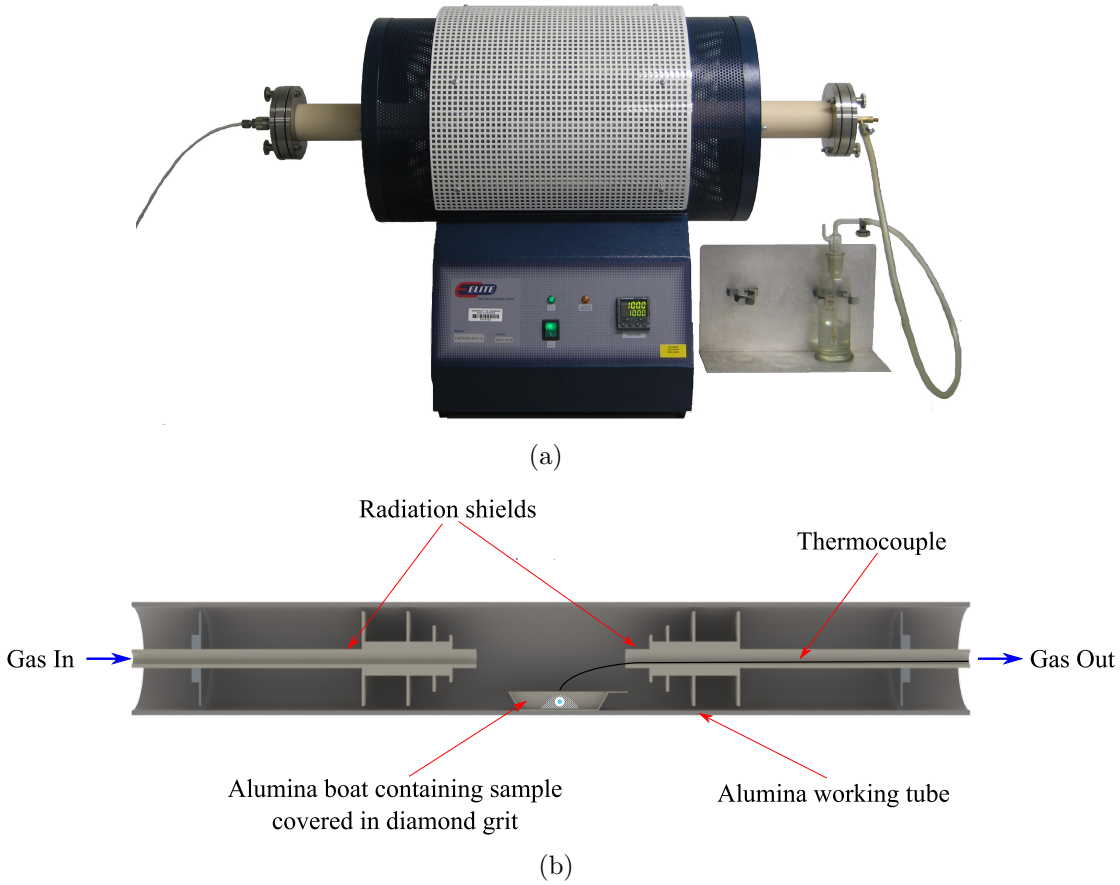

Figure 4-6: (a) Photograph of the Elite Thermal Systems Ltd. tube furnace. Forming gas enters from the left through the alumina tube and exits through the bubbler. A thermocouple can be inserted in the right-hand end through the T-junction. Samples were always inserted from the right, so that a gas flow could be maintained. (b) A cross section through the alumina working tube illustrating the radiation shields and sample positioning.

set point and the sample temperature (Figure 4.7(b)) was calculated as:

$$T_{\text{sample}}(^{\circ}\text{C}) = 0.95(1) \times T_{\text{set point}}(^{\circ}\text{C}) + 45(7) \tag{4-4}$$

Throughout every anneal, a continuous flow of forming gas was maintained to slightly over pressure the annealing chamber and minimise oxygen content. The flow rate was monitored by a bubbler. A T-junction ensured that the thermocouple could be inserted whilst allowing the gas to continue to flow through the system. All anneals using the tube furnace were performed at ambient pressure with the sample centrally located and covered with sacrificial diamond grit.

For anneals at temperatures less than 1000℃, the sample was inserted once the hot zone had reached the desired temperature. A small temperature decrease

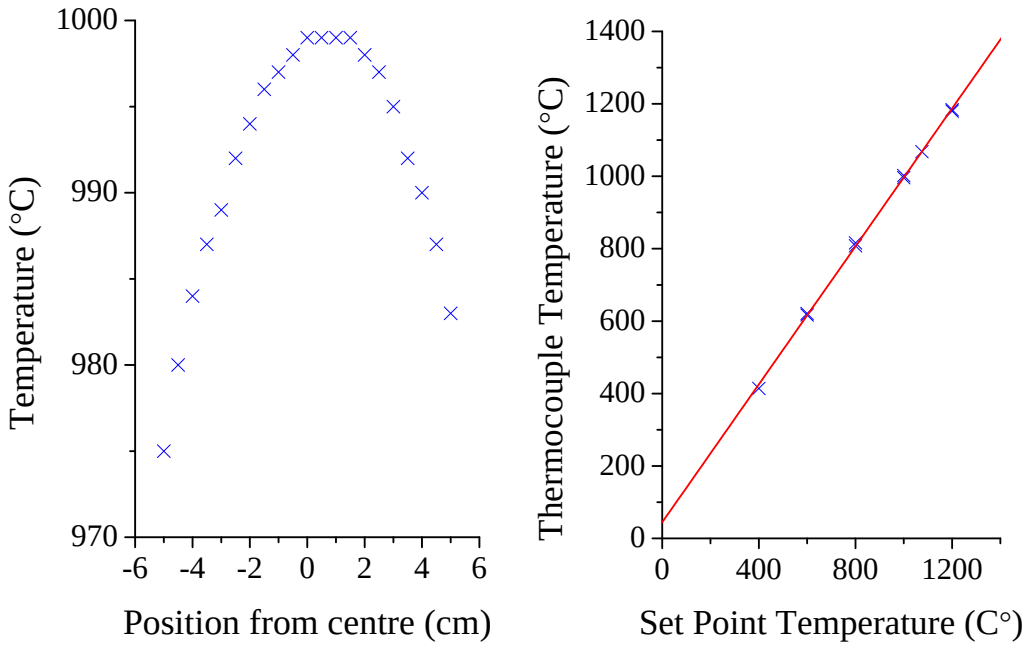

Figure 4-7: (a) represents the horizontal profile of the tube furnace across the region between the two radiation shields. The profile was taken with the furnace set point = 1000℃. (b) illustrates the calibration profile for the tube furnace plotting data points attained during ramping up and down of the temperature. A linear fit of this data provides a gradient of 0.95(1) with an intercept of 45(7).

was noted during the insertion period but was not of significance. For annealing at temperatures greater than 1000℃, the sample was inserted once the furnace temperature had reached 800℃ and the furnace ramped to the desired temperature with the sample *in situ*. Considering the length of annealing periods, the contribution from the additional temperature ramping was minimal. In all cases, the flow of forming gas was increased slightly as the sample was inserted. Once annealing was completed, the set temperature was reduced back to 800℃ and the sample slowly withdrawn from the centre under increased forming gas flow. The sample was then left at the edge of the working tube to cool, with a continuing flow of forming gas.

For experiments where a lower set point was required and rapid cooling desired, a Carbolite MTF (mini tube furnace) was used. This was a smaller unit with a maximum temperature of 1000℃ and a quartz working tube replacing the alumina. The benefit of this was that samples could be rapidly inserted and removed without risk of material shock. Samples were inserted directly onto the quartz

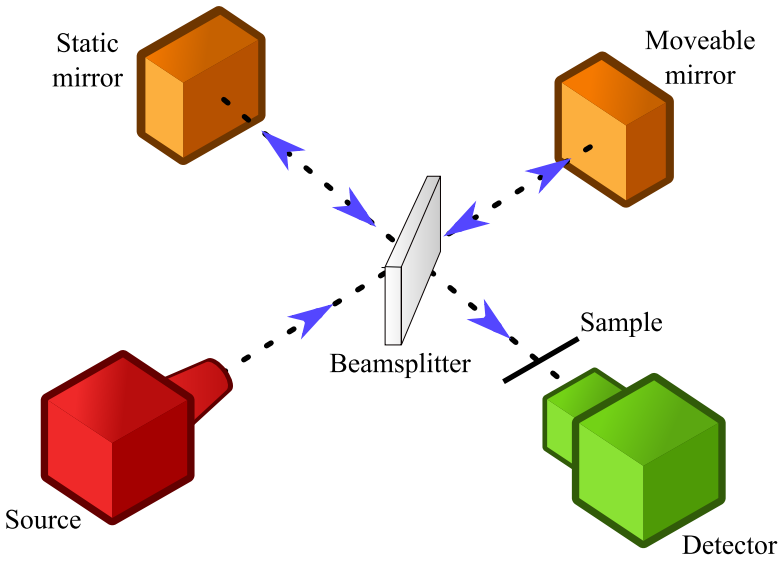

Figure 4-8: A block diagram of the primary components of an interferometer.

tube and were not covered with sacrificial grit. When treatment was complete, the sample was immediately removed and quenched to *lock–in* defect concentrations. Generally these treatments were for charge transfer experiments and hence treatment and removal were performed in the dark.

4.2 Fourier transform infrared absorption spectroscopy

The Fourier Transform InfraRed (FTIR) spectrometer is a Michelson Interferometer (Figure 4-8). A beam of light from a broad band source is split into two by a beam splitter and directed towards two mirrors; one mirror is held in a fixed position, the other swept. The two beams are then recombined and passed through the sample. At the detector, an interferogram is measured as a function of path difference. This signal is digitised before a process of Fourier transformation provides the resultant absorbance/transmission spectrum.

Background atmospheric absorption can prove an inconvenience in generating the interferogram. Changes in water and carbon dioxide concentration can introduce undesired absorption bands in the spectrum. Consequently, the spectrometer is continually purged with nitrogen gas, a diatomic, symmetrical molecule which does not have a vibrational absorption in the infrared region. Additionally, the

analysis software has a method of CO_2 and H_2O suppression, removing their characteristic absorption features.

The degree of tolerable divergence of the two beams is dependent upon the resolution set; the higher the resolution, the lower the divergence. This can be controlled by restricting the beam size by a variable aperture, the J-stop. On returning to the beam splitter, the two beams must be superimposed exactly. Any tilt or shear can have distortion effects on the final spectrum. Since the mirror has a finite distance it can move, reversal of direction can often introduce an oscillation, leading to a distorted spectrum at the high and low ends of the scan.

In comparison to a more common dispersive spectrometer, the FTIR spectrometer has two advantages; firstly, all wavelengths are measured simultaneously as opposed to successively (Felgett or multiplex advantage) and secondly, a series of slits are not required to limit the light input (Jacquinot or throughput advantage). Together, this means that spectra can be obtained more rapidly with an improved signal-to-noise ratio.

The processor acts as a frequency analyser, producing a recognisable spectrum. The interferogram is sampled at intervals equal to half the shortest wavelength of the source. Radiation at shorter wavelengths will be sampled but may appear in the wrong place. This effect is called *aliasing*.

The apparatus used for this thesis, is a PerkinElmer Spectrum-GX FTIR Spectrometer with the components as summarised in Table 4-2. Two beam splitters are used. For the mid-infrared, the beam splitter is formed from a plate of potassium bromide (KBr) with a germanium coating. This covers a range of 7800-370 cm^{-1}. The near infrared scans utilises a quartz beamsplitter, over a range from 15000-2700 cm^{-1}. A beam condenser is used to reduce the diameter of the beam at the sample, from approximately 6 mm to 2 mm. The beam source is a voltage stabilised, air cooled, wire coil operated at 1350 K for MIR measurements or a voltage stabilised, air cooled, tungsten source in a quartz envelope for scans in the NIR.

The software providing the interface between the apparatus and the user was "Spectrum", a PerkinElmer application designed to provide complete control over

Table 4-2: Summary of the appropriate components of the Spectrum-GX spectrometer for investigations in the mid and near infrared regions.

Region	**Range**	**Light Source**	**Detector**	**Beam Splitter**
MIR	370 - 7800 cm^{-1}	Glow Bar	Deuterated TriGlycine Sulphate	Optimised KBr
NIR	2000 - 15000 cm^{-1}	Halogen Lamp	Deuterated TriGlycine Sulphate	Quartz

the system. All settings and scan parameters could be set through the software interface and full initialisation and alignment completed.

Low temperature infrared spectroscopy was possible through the installation of a home-built cryostat into the beam path. The sample was surrounded by indium and mounted into the aperture of a copper block. This in turn was mounted onto a larger copper arm. The temperature was measured using a silicon diode semiconductor resistor and a Oxford Instruments Intelligent Temperature Controller (ITC). The cryostat contained windows made from calcium fluoride, transparent over the region 1000-20000 cm^{-1} (Figure 4-9).

4.2.1 Analysis of IR spectra

The intensity of absorption by an optically active centre is proportional to the number of absorbing centres present. The absorption coefficient is proportional to the square of the effective electric dipole moment $|p|^2$.

Calculation of the absorption coefficient can therefore be made using Equation (4-5), where t is the path length through the sample and I_0 and I are the dipole intensities before and after passing through the sample.

$$\mu = \frac{2.3}{t} \log_{10}\left(\frac{I_0}{I}\right) \tag{4-5}$$

Alternatively, for diamond, the intrinsic multi-phonon absorption at 2000 cm^{-1} can be used to calibrate the absorption coefficient. The data are baselined and normalised such that at 2000 cm^{-1} the absorption coefficient is equal to 12.3 cm^{-1} [9]. This calibration eliminates error in measuring small thicknesses and considers any

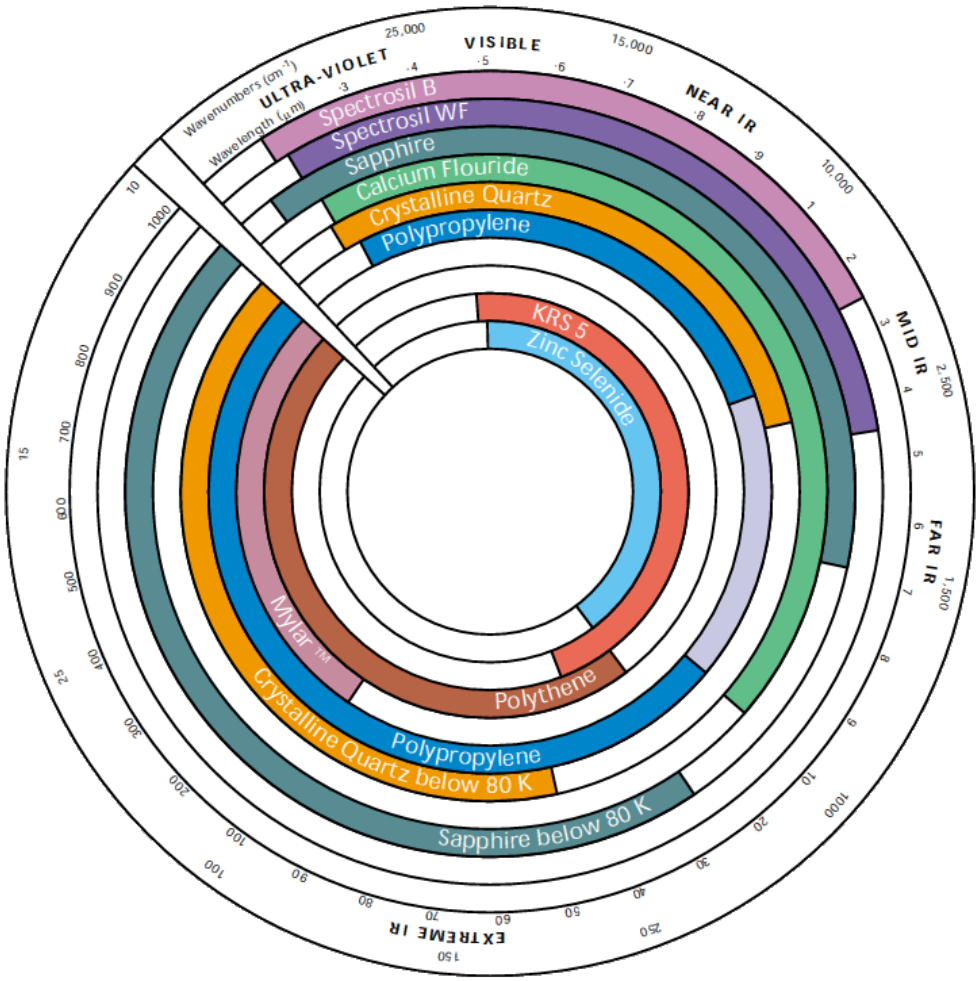

Figure 4-9: The type of window material chosen whether for cryostats of polarisers is dependent upon the wavelength an intensity of the radiation used. The diagram illustrates the spectral range over which the material is optimum. (Spectrosil is a synthetic vitreous silica, the *WF* variant being a water free version of *B*, KRS 5 is a thallium bromide-thallium iodide compound and Mylar™a polyester film.) Taken from material published by Oxford Instruments - Windows for Cryogenic Environments.

multiple reflections from within the sample.

For convolved lineshapes, once the spectra have been baselined and normalised, any number of Lorentzian lineshapes can be fitted to the spectrum to replicate the lineshape observed.

4.2.1.1 Nitrogen Fitting

Several common nitrogen related defects give rise to well characterised infrared absorption spectra in the one-phonon region. Although specific calibration factors have been determined relating absorption coefficients at a specific energy to defect

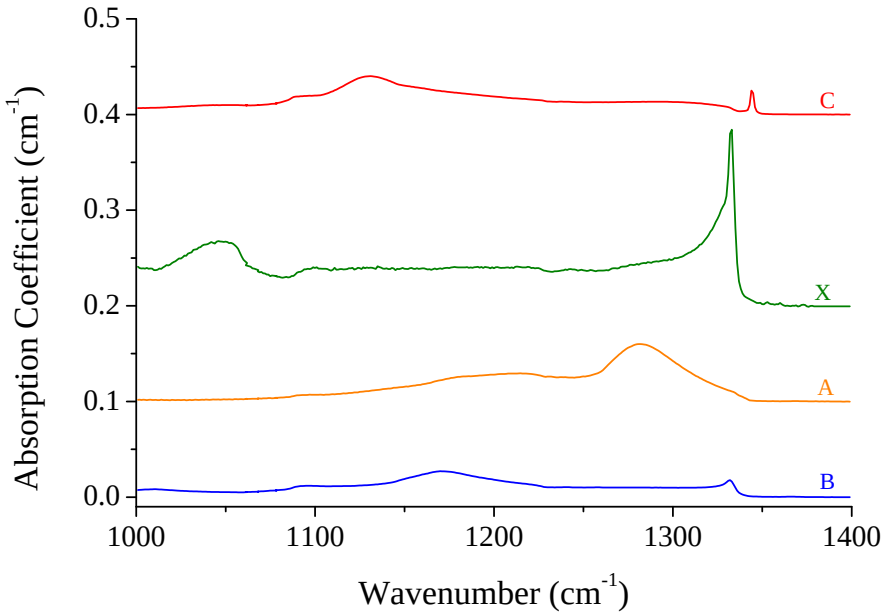

Figure 4-10: Characteristic spectra of ^{14}N-related centres in the one-phonon region at room temperature. Each has been scaled to represent the absorption from 1 ppm of the defect. The C spectrum is representative of absorption from the C-centres (N_S^0 defects) in diamond, X, the absorption from the N_S^+ defect and A and B, characteristic absorption of the A- and B- centres of aggregated nitrogen.

concentration, when more than one defect is present, the experimental data must first be deconvolved into the component spectra.

Common nitrogen related defects in diamond and their concentration correlation values are given below [10–13].

$$\text{C-centre } (^{14}N_S^0)\text{: } \mu(1130) = 25(5)\ \text{ppm per cm}^{-1} \tag{4-6}$$

$$\text{X-centre } (^{14}N_S^+)\text{: } \mu(1332) = 5.5(9)\ \text{ppm per cm}^{-1} \tag{4-7}$$

$$\text{A-centre: } \mu(1282) = 16.5(9)\ \text{ppm per cm}^{-1} \tag{4-8}$$

$$\text{B-centre: } \mu(1282) = 79.4(9)\ \text{ppm per cm}^{-1} \tag{4-9}$$

The spectral region from 1000–1400 cm^{-1} is extrapolated and fitted using multiples of the characteristic absorption spectra for the C (N_S^0), A (N–N), B (4N+V), X (N_S^+) and D (platelet) absorption centres (Figure 4-10). The multiplying factor used to obtain a realistic fit of the experimental data is then used in conjunction with the correlation factors to identify the concentration of substitutional nitrogen in each nitrogen-related centre.

When the concentration of N_S^0 is low, fitting by the 1130 cm^{-1} peak is not

possible. Instead, the intensity of the 1344 cm^{-1} local vibrational mode is used [14]. This absorption feature is resolution dependent and hence the correct correlation factor must be used [15].

4.3 Uniaxial stress

The effect of uniaxial stress on optical transitions can be used to determine the symmetry of the defect responsible for the mode and the nature of the associated electronic and vibrational transitions. The theoretical interpretation of uniaxial stress spectroscopy is discussed in Chapter 3. A brief description of the experimental details and sample preparation follows.

4.3.1 The stress cell

Samples were prepared such that they were free from cracks and inclusions, from which fractures could propagate when under pressure. The crystal face orientation was identified by EPR. The accuracy of the face plane orientation was to within ±1°, confirmed by the use of Laue X-ray back-reflection diffraction.

Stress measurements were then completed using a custom built stress cell (Fig. 4-11), and samples prepared such that stress could be applied in a specific direction. The components of the uniaxial stress cell are as follows:

A. Screw cap - this ensures that a seal is maintained once the system is under pressure

B. Inlet plate - includes a rubber O-ring. An integrated Swagelok fitting permits quick connection of the nitrogen gas line. The gas line is a narrow diameter tube to minimise the volume of gas held in the system at any one time.

C. Adjuster plate - sets the ram position when no pressure is applied

D. Cell Body - manufactured from thick stainless steel to manage the stored energy from the pressurised gas. It contains the piston (area = 0.0038(1) m^2) and the ram

E. Ram rod

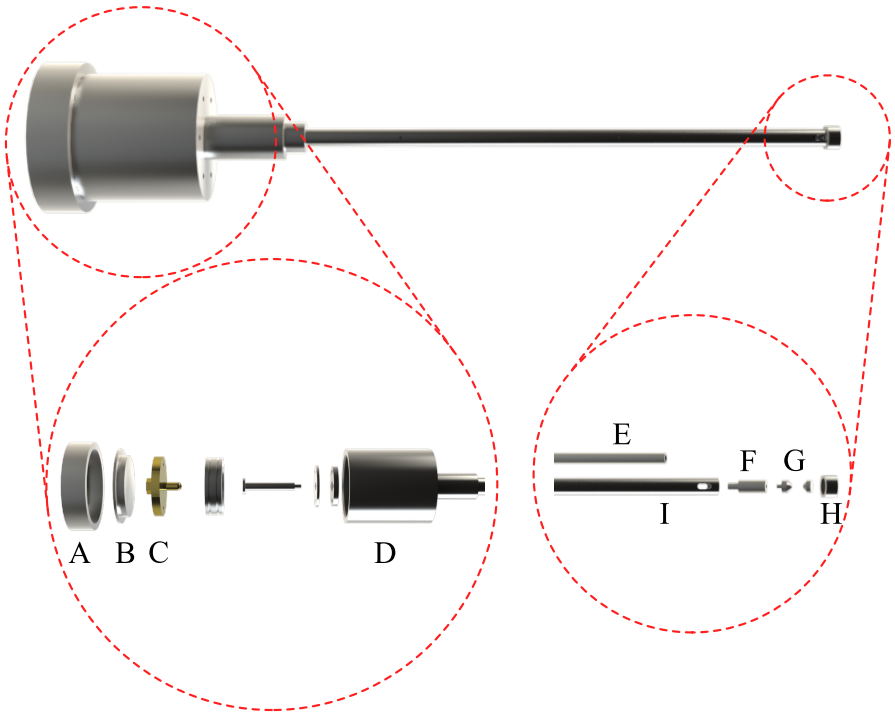

Figure 4-11: An exploded image of the custom built stress cell

F. Slug - manufactured from stainless steel, it sits between the anvil and the ram rod

G. Anvils

H. Screw cap - holds the anvils in place and acts as a resistance plate for the building of pressure

I. External casing - includes apertures to allow a beam path to the sample and small holes for pressure release in the event of failure

The anvils and samples were prepared in a specific, reproducible manner. Gaskets made from thin 0.02 mm gauge aluminium foil were cut and attached using GE varnish to the polished and clean surfaces of the steel anvils. Cleanliness throughout the mounting procedure was paramount, as the presence of grit could lead to inhomogeneous application of stress and fracture propagation points. The sample itself had foil wings applied to the non-illuminated and non-stress loaded faces to minimise the light arriving at the detector, which had not been transmitted through the sample. These were also attached using GE varnish and had to

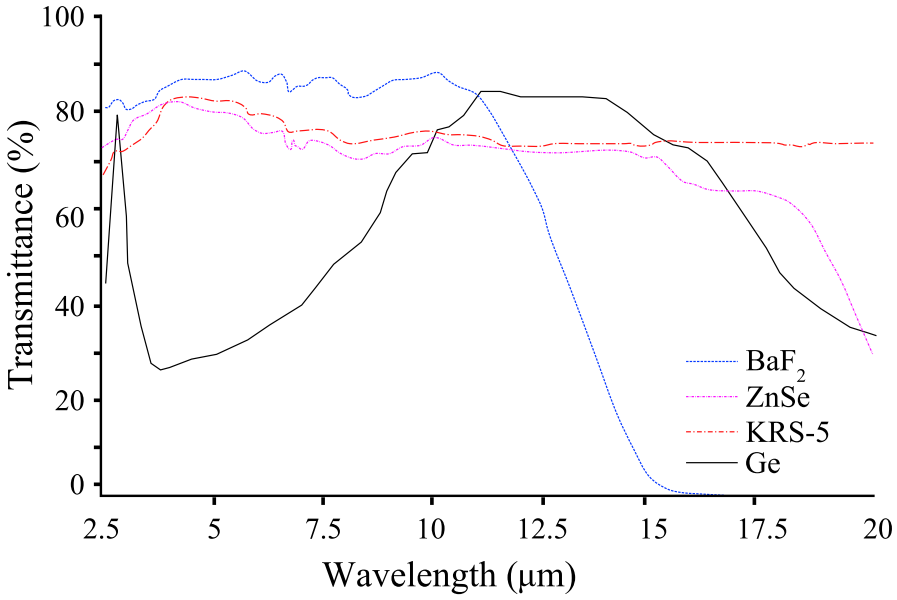

Figure 4-12: Transmittance profile of the Edmund Optics zinc selenide holographic wire grid polariser for four principal materials: barium fluoride (BaF_2), zinc selenide (ZnSe), thallium bromoiodide (KRS-5) and germanium (Ge). Whilst the KRS-5 polariser is best in terms of its overall performance, balancing cost and the principal spectral range used, the zinc selenide polariser best suits the requirements of this investigation. This figure has been adapted from the promotional material of Edmund Optics.

be carefully sized to match the sample length and not interfere with the seating of the sample on the prepared anvil.

Pressurised nitrogen gas was used, monitored by a 10" pressure gauge (S.M. Gauge Company) which could withstand a range of 0 - 350 psi at room temperature. Acting on the ram rod and subsequently the anvils, the diamond was compressed in a uniaxial direction defined by the orientation of the sample. The incident electric field vector was polarised parallel and perpendicular to the direction of stress by an Edmund Optics zinc selenide holographic wire grid polariser. This has an extinction ratio[1] of 150:1 at 3 μm and 300:1 at 10 μm. The transmittance profile can be seen in Figure 4-12. Spectra were collected for each orientation before the pressure on the sample was increased.

[1]Extinction ratio: the ratio of the power of a plane-polarised beam transmitted through a polariser placed with its polarising axis parallel to the beam's plane compared with the transmitted power when the polariser's axis is perpendicular to the beam's plane.

4.3.2 Modelling defect structures

Modelling of defect structures was performed by Dr. Jonathan Goss of the University of Newcastle. Candidate structures for defects can be modelled using density-functional calculations with the local density approximation. This is implemented in the AIMPRO (Ab Initio Modelling Program) code.

4.3.2.1 The fundamentals of AIMPRO

In order to determine the structure of an assembly of atoms, it is required that the Schrödinger equation be solved, only achievable by the application of a set of approximations. The first is that the Schrödinger equation can be reduced to an equation involving only electrons moving in a potential of fixed nuclear sites, since the nuclear masses are so much greater than those of the electrons. This is a result of the Born-Oppenheimer approximation. The solution provides the structural potential energy and for dynamical quantities, the classical problem of nuclei moving in a force field needs to be solved. However, an exact solution is still not possible due to inter-electronic coulomb terms. If these terms are ignored, an exact wavefunction can be written but this extreme approximation hinders the power of this method. Various modifications have been proposed to include these interactions: the Hartree-Fock theory (HFT) and density functional theory (DFT).

These modifications use an average electrostatic potential over the positions of other electrons rather than summing the specific interactions between two electrons. The Schödinger equation is thus separable and the effective potential is composed of the Hartree potential, the electrostatic potential due to the electron density of charge at a point and the exchange-correlation potential. The definition of the exchange-correlation potential differentiates the two theories; it is determined either by all of the orbitals, as in the HFT, or only by the electron density, as with DFT. However, the precise dependence of density is unknown except for a homogenous gas. Therefore, it is assumed that at a point r, the exchange-correlation potential is given by a homogenous gas value involving the density $n(r)$ at the same point r. This is local density functional theory (LDFT). For high electron densities, it can be shown that the exchange-correlation potential is proportional to $n^{\frac{1}{3}}$ and therefore this is also applicable for the potential at a

given r. AIMPRO uses LDFT and therefore the electron density is a fundamental quantity.

The problem is now simplified to a situation considering one electron and that electron's interaction with all other ions. Core electrons are bound close to ions and do not contribute to bonding. These can therefore be removed from the calculation by the use of pseudopotentials which will have no core states. Pseudopotentials due to Bachelet, Hamann and Schlüter (BHS) are utilised in AIMPRO [16].

The simplified Schrödinger equation can then be expanded in terms of a basis chosen as either plane waves of Cartesian Gaussian orbitals. For the work presented here, the wave function basis consists of atom-centred Gaussians. In practice, they are centred at the nuclei. If $n_i = 0$, the orbitals are called s-Gaussian orbitals and are simply spherical; if one is unity and the others zero, then the functions are p-Gaussian orbitals and if the sum of n_i is 2, the set of six orbitals generate five d-orbitals and one s-orbital. Solution of the Hamiltonian then generates the output charge density. From this, the structural energy can be calculated and the forces on each atom found. Through small movements in the atoms, a minimum energy can be calculated, called the relaxation of the assembly of atoms.

For the use of AIMPRO, the following is required:

- the positions of the atoms in the cluster
- the basis to be used for the wavefunction and charge density
- the electronic configuration
- the identities of the atoms that are to be relaxed

The output of such modelling can provide the structure energy, electronic levels and positions of the atoms.

4.3.2.2 AIMPRO specifics for the modelling of the defects of this work

In this work, carbon is treated using fixed linear-combinations of s- and p-orbitals with the addition of d-orbitals to allow for polarisation effects to be computed. This gives a total of thirteen functions per atom. Nitrogen is treated using independents sets of s-, p- and d-orbitals with four widths and yielding forty functions per atom. The charge density is Fourier-transformed, using plane-waves with a

cut-off of 350 Ry. The defects are represented using periodic boundary conditions with cells of 64 host sites in a simple cubic arrangement, with a periodic length of $2a_0$. The Brillouin-zone is sampled using the Monkhorst-Pack scheme with a uniform mesh of $2 \times 2 \times 2$ special k-points. When a denser sample of $4 \times 4 \times 4$ was considered, very small quantitative differences (< 0.2 meV/atom) was observed suggesting the $2 \times 2 \times 2$ representation to sufficiently converge.

Deformation of the supercell under strain, representing the application of stress to the defect, assumed an isotropic, homogeneous elastic medium. This was characterised by Young's Modulus, for which a value of 1223 GPa [17] was used and the Poisson ratio, with a value of 0.1 [18]. For varying strains, force constants were obtained by displacing atoms in each of the x, y and z directions by 0.026 Å and evaluating the forces on each of the atoms in the cell. Therefore, second derivatives of the energy with respect to displacement can be obtained employing a finite difference formula using the analytic forces and the quasi-harmonic dynamical matrix. Diagonalisation yielded vibrational frequencies as a function of strain or as a function of stress, using the Young's Modulus.

4.4 Electron paramagnetic resonance (continuous wave)

Quantitative electron paramagnetic resonance (EPR) experiments were completed using the Bruker EMX and EMX-E X-band systems at 9.7 GHz. These two systems are very similar, made up of a number of components which work to guide microwaves generated from a source with a fixed frequency into a resonant cavity. The magnetic field is then swept over a range to stimulate absorption by specific defects. The fundamental components of the EPR spectrometer are outlined in Figure 4-13.

4.4.1 The microwave bridge

The microwave bridge (Figure 4-14) houses the source, a Gunn diode, the output power of which is controlled accurately by a variable attenuator. Most EPR sys-

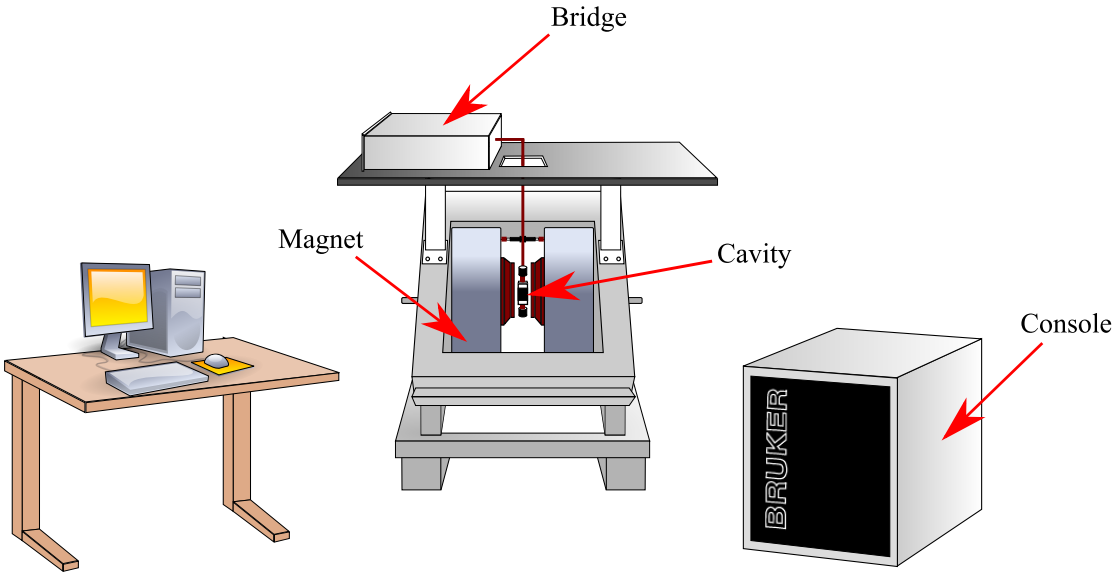

Figure 4-13: A block diagram of a Bruker EPR spectrometer. Detailed views of the components and bridge can be seen in Figure 4-14. This diagram is based upon that provided in the Bruker EMX User's Manual [19].

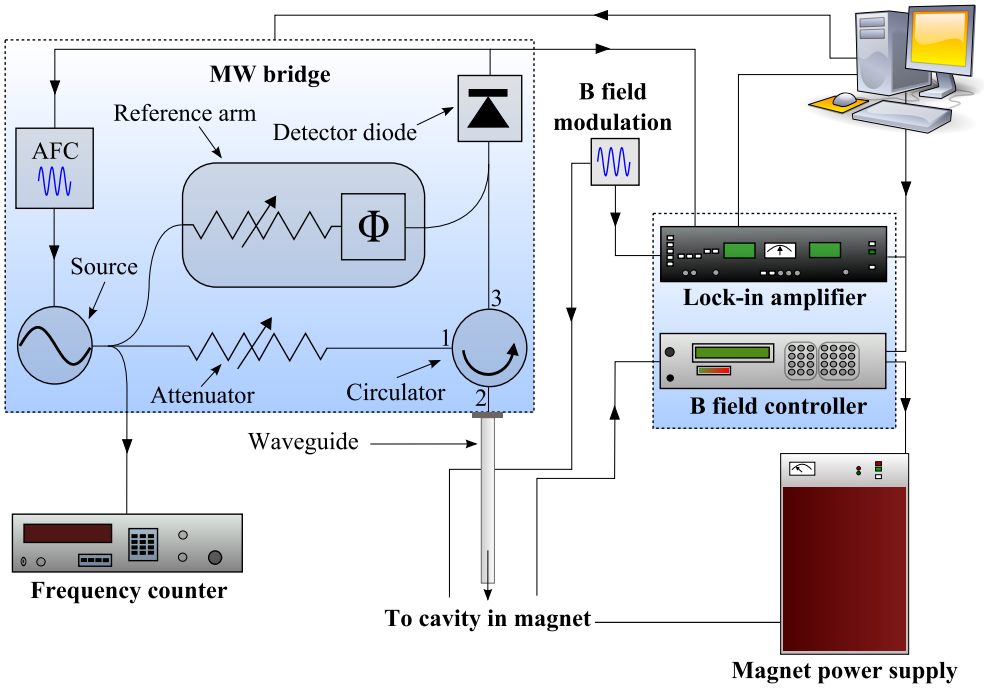

Figure 4-14: The principal components of an EPR spectrometer. This is representative of the typical spectrometers used for this research.

tems are reflection spectrometers, measuring changes in the reflected power from a cavity housing the sample. The circulator is therefore a critical component, ensuring that microwaves entering at port 1 are directed only towards the cavity and reflected microwaves from the cavity can then be directed only through port 3 to the detector. The reflected microwave signal is detected by a Shottkey barrier diode, which is biased by approximately 1 mW power from the reference arm, such that the diode output is linearly proportional to the reflected power/EPR signal.

For the EMX system, a Bruker ER041XG bridge was used which has a maximum attenuation of 60 dB (2×10^{-4} mW). For the EMX-E system, it was usual for a 90 dB (2×10^{-7} mW) bridge to be employed (ER041XG-H). The latter was essential for defects which easily saturated (had long T_1 such that the Boltzmann population distribution was not maintained), even at low microwave powers.

For all systems, frequency monitoring was performed by an EIP Microwave Inc. 545A microwave frequency counter. Experiments monitoring frequency fluctuations over long periods (days), indicated a typical drift of less than 150 kHz (< 0.05 G).

4.4.2 The cavity

The cavity design is critical to amplify weak signals from a sample. It may vary in shape and construction, each design having specific properties and sensitivities. At a resonant frequency, no microwaves are reflected back from the cavity and the system is said to be *critically coupled*. At this point, the impedance of the waveguide and cavity are matched. This is achieved by modifying the iris size between the cavity and the waveguide, controlling the amount of reflected microwaves. When off resonance, it is important to diminish any sources of reflected power.

To remain coupled, it is essential that the microwave source remains matched to the resonant frequency of the cavity. Changes in environmental temperature and other local factors can cause the frequency to drift from its optimum position for a given cavity. An automatic frequency control (AFC) unit is therefore utilised to counteract this drift, employing a feedback loop to lock the frequency at its optimum value at the centre of the cavity mode.

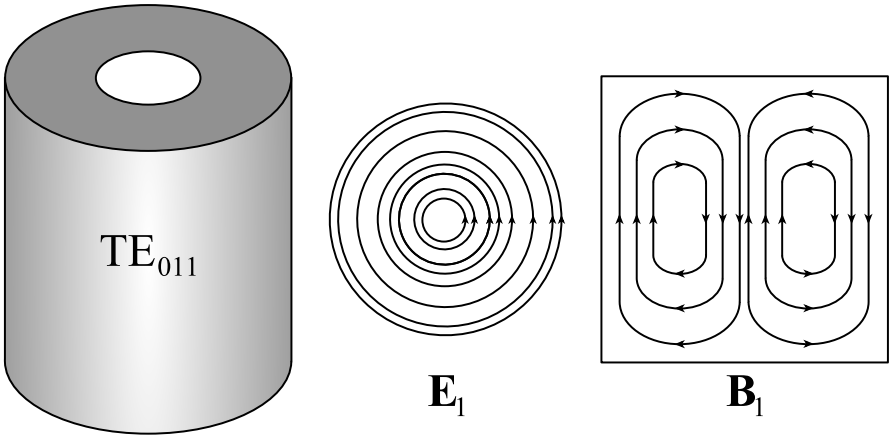

Figure 4-15: A schematic of the cylindrical TE_{011} cavity highlighting the electric and magnetic fields ($\mathbf{E}_1$ and $\mathbf{B}_1$).

A cavity is characterised by how efficiently microwave energy is stored, giving it its *Q factor*. Sensitivity increases with Q, which can be defined as:

$$Q = \frac{2\pi \text{ (energy stored)}}{\text{energy dissipated per cycle}} \tag{4-10}$$

Energy is commonly lost through the side walls of the cavity; microwaves generate electrical currents in the side walls which in turn create heat.

The sample is positioned in the cavity at a point where the magnetic field component of the microwave field is at a maximum and the electric field is at a minimum. This is in order to efficiently drive the magnetic-dipole transitions and minimise the dielectric losses, which have a significant negative effect on the resulting signal-to-noise ratio.

Cavities can vary greatly in design. The naming convention is according to the mode that the cavity supports.

- TE - transverse electric
- TM - transverse magnetic

In addition, subscript numbers are used to denote the number of half wavelengths along the three dimensions. Most commonly used in this thesis are the Bruker super-high Q (SHQ) ER4122 spherical TE_{011} cavity, a Bruker ER4105DR TE_{104} rectangular cavity and an EX-102 TE_{011} cylindrical cavity (Figure 4-15).

Within the cavity, the sample is mounted on either a single or dual axis rod within a goniometer as illustrated in Figure 4-16. These combinations of sample

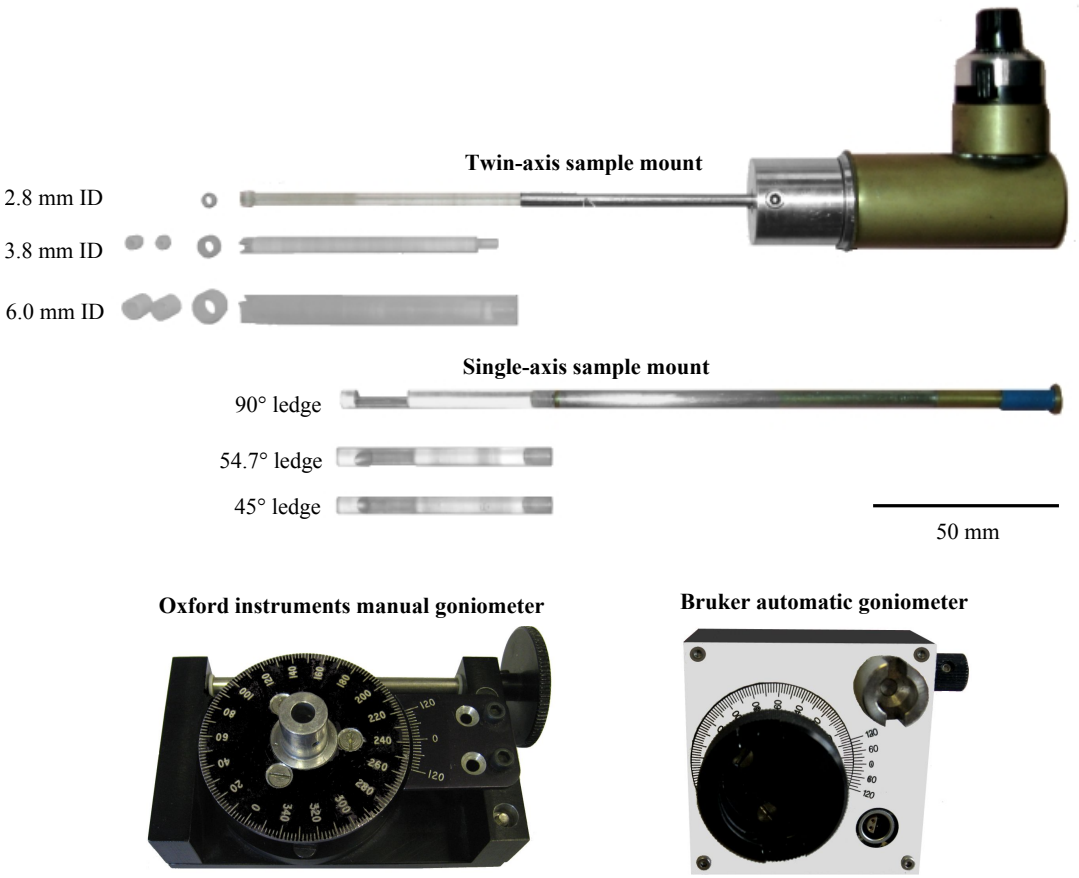

Figure 4-16: An illustration of the goniometers and sample mounts used in conjunction with cavities for the EPR experiments of this thesis.

rods and goniometers permit the manipulation of samples into any desired plane relative to the magnetic field. The single axis rods are formed from a German silver[2] and brass rod with detachable Rexolite[3] end piece, with varying ledge angles. The dual axis rods formed of the same material, with a variety of wheels attached to the Rexalite rod by a thin piece of cotton. Variations in wheel size permitted a range of sample sizes to be easily inserted. Samples greater than 5 mm required the use of the single axis system. Samples were attached to the single axis rods and held in the dual axis wheels by a thin layer of vacuum grease, which produces no EPR signal in the regions of interest.

[2]German silver is an alloy of copper, silver and nickel with varying percentage contributions with a low thermal conductivity.

[3]Rexalite is a cross linked polystyrene microwave plastic, with a constant dielectric constant of 2.53 through to 500 GHz. Extremely low microwave dissipation factors make it ideal for use in microwave environments.

4.4.3 Magnetic field modulation and recording a spectrum

When the resonance condition is met for a defect, reflected microwaves are returned to the bridge and directed towards the detector. The detector is biased with 1 mW power by the reference arm and a phase shifter ensures that the microwaves from the reference arm are in-phase with the reflected microwaves from the cavity.

Phase sensitive detection enhances the signal-to-noise ratio. The magnetic field is modulated with an amplitude B_m at a frequency ν_m. A small amplitude magnetic field modulation, typically at a frequency of 100 KHz, is superimposed onto the large Zeeman field. This modulation is transferred to the microwave signal observed upon detection of an EPR transition (Figure 4-17).

Modulation broadening can occur when the modulation field is greater than the linewidth of the signal. Intentional over modulating can have the benefit of reducing saturation effects by spreading the same number of spins over a larger field and reducing the number of spins per Gauss (Figure 4.17(b)). However, the signal strength may subsequently fall below the detection level and hence an appropriate balance must be found.

Defect concentration can be determined from the resulting spectrum. The concentration of a particular paramagnetic defect is proportional to the integrated intensity of all the EPR absorption lines that originate from that defect. A specific sample acts as a reference for all EPR experiments, having a known defect concentration. For a given experiment, the integrated intensity for that number of spins can be found and compared to the unknown defect signal. A number of factors can effect the intensity of a given centre including: spin (S) and electronic g factor, incident microwave power ($P_{\mu W}$), microwave detector gain (G), acquisition time (t_{aq}), modulation amplitude (B_m), cavity Q-factor, cavity filling factor and the number of scans acquired (N).

In the absence of power saturation, the EPR signal intensity is proportional to the incident microwave power. Both the reference and the sample spectra must be taken at powers which do not saturate the signal. The concentration of a defect in a sample, [C], can be calculated from the concentration of a known defect in the reference sample, [ref] by Equation (4-11), where I is the integrated intensity

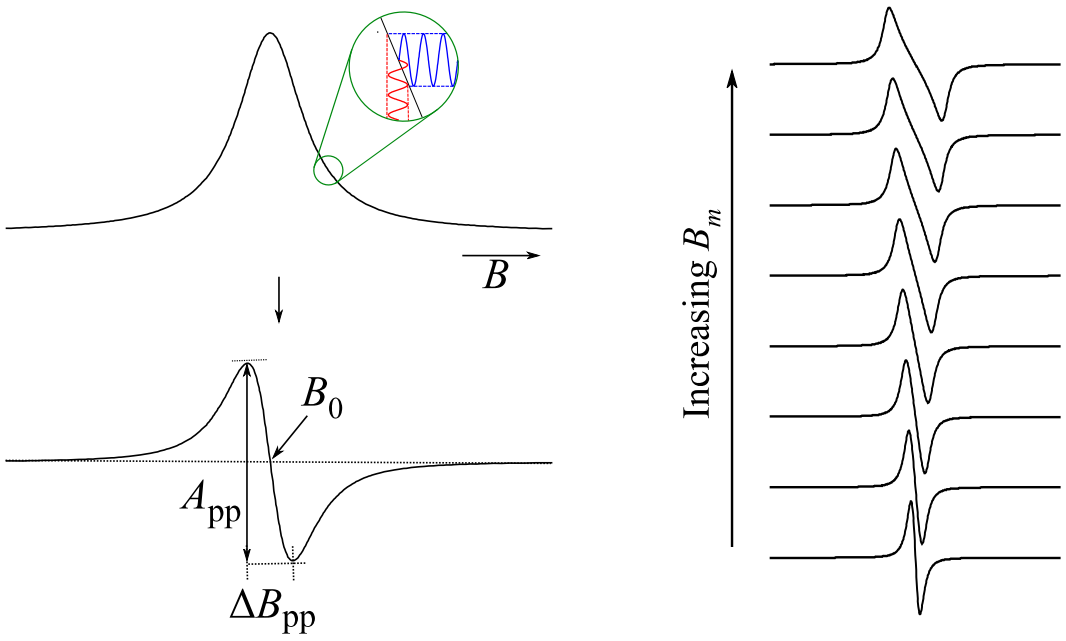

Figure 4-17: (a) Resonant microwave absorption and the resultant derivative spectrum. As the signal is sampled at different points, the resultant gradient changes, leading to the first derivative lineshape. (b) An excessive field modulation amplitude leads to distortions of the signal.

of the signal. It is assumed that the Q-factor and the filling factor do not vary between the reference and sample scans.

$$[\mathrm{C}] = [\mathrm{ref}]\,\frac{I_\mathrm{C}}{I_\mathrm{ref}}\sqrt{\frac{(P_{\mu\mathrm{W}})_\mathrm{ref}}{(P_{\mu\mathrm{W}})_\mathrm{C}}}\,\frac{M_\mathrm{ref}}{M_\mathrm{C}}\,\frac{(B_m)_\mathrm{ref}}{(B_m)_\mathrm{C}}\,\frac{g^2_\mathrm{ref}}{g^2_\mathrm{C}}\,\frac{S(S+1)_\mathrm{ref}}{S(S+1)_\mathrm{C}}\,\frac{(t_{aq})_\mathrm{ref}}{(t_{aq})_\mathrm{C}}\,\frac{G_\mathrm{ref}}{G_\mathrm{C}}\,\frac{N_\mathrm{ref}}{N_\mathrm{C}} \tag{4-11}$$

The reference sample used for the studies of this thesis was an HPHT grown, type Ib single sector sample, with a total nitrogen concentration of 240(10) ppm. This had been determined by FTIR measurements.

4.5 Photoluminescence spectroscopy

Photoluminescence (PL) experiments were performed using a Renishaw Raman In-Via Microscope system that utilised an argon laser excitation at 514.5 nm. Using liquid helium to cool the system, measurements were made at temperatures from 4 K, implementing a continuous flow microstat from the Oxford Instruments range (Figure 4-18). This could be employed for Raman and PL experiments.

Figure 4-18: Photograph of the Oxford Instruments continuous flow liquid helium microstat.

Temperature control was made using a Rh-Fe thermocouple and connected to a calibrated Oxford Instruments Intelligent Temperature Controller (ITC-4). In addition, gas flow was regulated by an Oxford Instruments Gas Flow Controller (VC30). Together, these instruments maintained the optimum conditions for Helium flow, to maintain a controlled and steady temperature with minimal liquid usage.

Samples were mounted by silver dag, attaching them to a copper sample holder. This was in turn attached a copper block, permitting good conductivity of heat between the sample, the internal heater and the thermocouple. For low temperature measurements, a heat shield was installed around the sample arm, to reflect incident radiation and before cooling, the microstat was evacuated and the sample region purged with a helium gas for heat exchange.

In processing, spectra are normalised with respect to the Raman line, the intensity of which varies linearly with the laser power being employed. A series of laser wavelengths are available between two spectrometers: 325 (HeCd), 442 (HeCd), 514 (Ar^+), 633 (HeNe) and 785 nm (solid state). Light from the laser is directed by a series of mirrors through the lens of a confocal microscope. This focuses the laser onto the mounted sample. The resulting emitted light is then collected by the objective and collimated, passing through a notch filter (the characteristics of which are dependent upon the exciting laser wavelength) and focussing onto the entrance slit of the spectrometer and the detector (Figure 4-19).

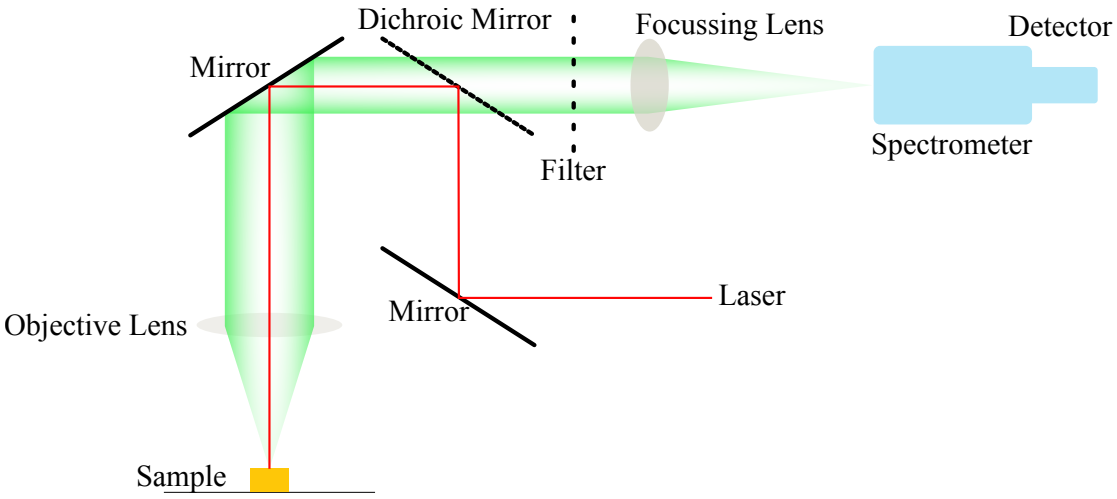

Figure 4-19: Schematic of the optics within the Renishaw PL spectrometers.

4.6 UV-Vis optical absorption spectroscopy

Ultraviolet-visible / near infrared (UV-Vis/NIR) optical absorption measurements were taken using a PerkinElmer Lambda 1050 spectrophotometer, over a range of 175–3300 nm. The spectrophotometer included a 3-detector module, permitting the use of photomultiplier tube (PMT), Peltier-cooled Indium Gallium Arsenide (InGaAs) and Peltier-cooled Lead Sulphide (PbS) detectors.

Experiments were carried out at either 4 K or 77 K, cooled by liquid Helium. An Oxford Instruments continuous flow cryostat with a silicon diode thermocouple calibrated by the ITC, were used. Samples were mounted by compacting indium around the sample in the aperture, maximising the light throughput and examining the entire sample.

A helium exchange gas surrounded the sample, acting to efficiently exchange heat with the liquid helium circulating the cryostat. This also purged the air, removing moisture which would otherwise cause condensation on the optical windows when the cryostat was cooled. Before experiments began, the system was left for 30 minutes once at temperature, to reach an equilibrium.

For investigations, spectra were collected between 1050 nm and 200 nm at an interval of 0.2 nm. Detector changes were set to occur at wavelengths away from key absorption features. In order to best balance the reference beam and sample beam, apertures of a size comparable to the sample were used with no additional attenuation of the beam intensity. The gain and response times of the detectors

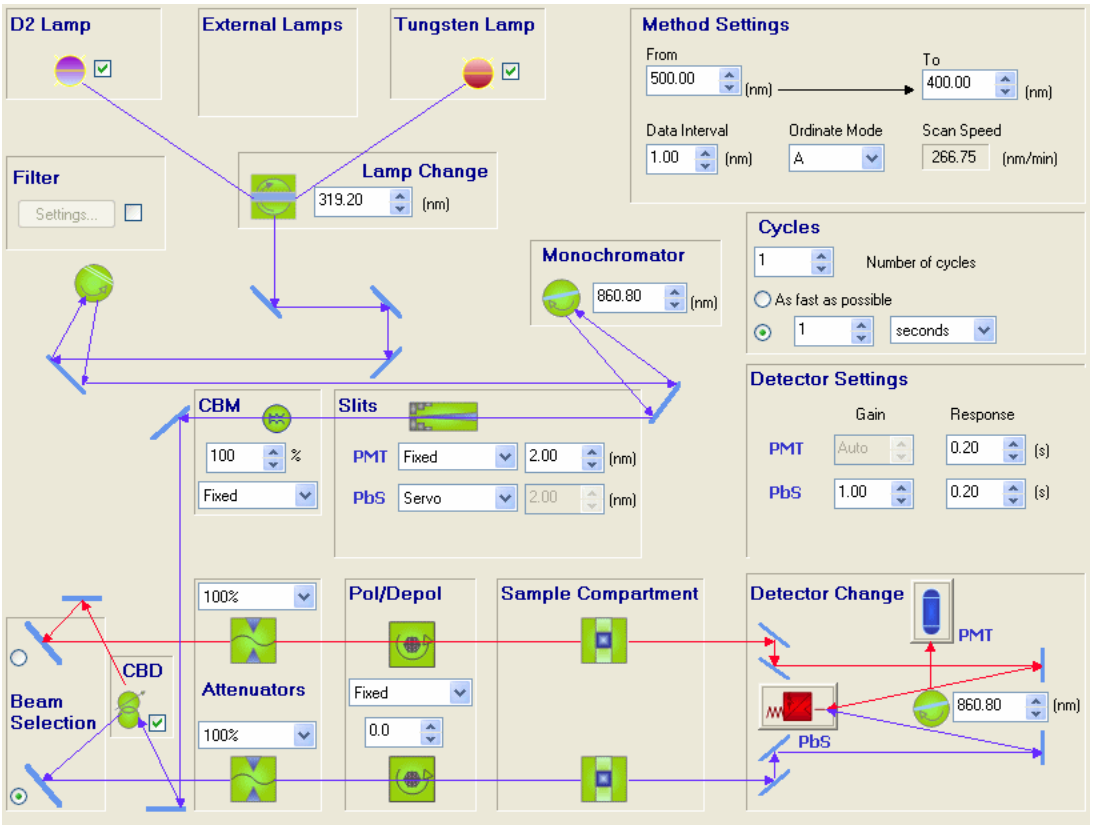

Figure 4-20: Generic settings and schematic of the beam path for the Lambda 1050 Spectrometer [20].

were set so as to optimise the spectra recorded with regards to noise and sensitivity.

4.7 Irradiation

During this thesis, both electron and neutron irradiation experiments are performed.

4.7.1 Electron irradiation

Electron irradiation was carried out the Isotron facility in South Marston, Wiltshire. Isotron provided two sources, 3 mA and 30 mA with experiments being completed at room temperature.

Using the 1.5 MeV source, electron irradiation doses could be calculated from previous calibration experiments (Table 4-3). At the facility, the samples to be irradiated were mounted in indium on a copper block cooled by circulating mains

Table 4-3: A table outlining the exposure conditions for specific doses. From this, other similar doses can be calculated. These calibration experiments have been completed by the DTC Research Centre.

Dose ($e^{-}cm^{-2}$)	**Source**	**Exposure Time**
1×10^{15}	3 mA	2 minutes 30 seconds
1×10^{17}	30 mA	28 minutes 17 seconds
5×10^{17}	30 mA	2 hours 21 minutes 25 seconds

water. This ensured that the sample temperature was not greater than 200℃.

4.7.2 Neutron irradiation

Neutron irradiation experiments were performed at that Hoger Onderwijs Reactor at the Delft University of Technology in the Netherlands. The BigBeBe facility was employed, which has a fast flux of 5.9×10^{12} neutrons per cm^2 per second over an energy range of 1 keV to 30 MeV, with the peak at approximately 1 MeV.

Samples were thoroughly cleaned and checked prior to irradiation, removing any surface impurity and ensuring that they were inclusion free. Samples were mounted within a quartz ampoule, which was then sealed and entered into the reactor. The atmosphere within the ampoule was ambient air. The ampoule was irradiated for 24 hours to achieve a dose of 5×10^{17} neutrons per cm^2 at room temperature. However, the local sample temperature was likely to have been approximately 200℃ due to localised heating from neutron collisions.

4.8 Sample preparation

4.8.1 Sample cleaning

Samples were cleaned by heating in a supersaturated solution of concentrated sulphuric acid and potassium nitrate to a temperature of 300℃, allowed to cool and washed in a heated solution of sulphuric acid to remove any excess potassium nitrate crystals. They were rinsed in de-ionised water and stored between sheets of lint-free cloth in a membrane box.

When samples were indium mounted for optical spectroscopy, sample faces

were washed with acetone once mounted, to minimise the presence of grease that may have subsequently been deposited since cleaning. In some instances this left a residue on the surface of the sample, observable in PL spectroscopy.

After preparation for uniaxial stress experiments, samples were scrutinised under a microscope to identify and remove with a scalpel any evidence of GE varnish on the sample faces. GE varnish is strongly absorbing in the infrared. Faces were also washed with acetone to remove grease also strongly absorbing in the IR region.

4.8.2 Sample cutting and polishing

Laser cutting and polishing were used to prepare the samples for HPHT annealing. Post annealing, polishing was also performed to remove etched surfaces prior to optical spectroscopy measurements. Diamond polishing was carried out using a conventional diamond sceife. Samples with carefully orientated parallel faces were prepared for uniaxial stress studies from the diamonds supplied for this research. For these samples, the face plane orientation was required to be less than $\pm 1^{\circ}$ off of the desired plane. This was confirmed by Laue back-reflection of X-ray diffraction. By assessing the diffraction pattern attained from the crystal, adjustments to the tang mounting of the sample were made, ensuring that the polishing was parallel to the desired plane. All samples were polished such that they were free from inclusions, cracks and chips as apparent by $\times 10$ magnification.

For all other samples, a near parallel orientation, as judged by eye, was sufficient. The surface was polished so as to achieve a mirror finish but the removal of all polishing marks was not essential.

References

[1] F. P. Bundy, H. P. Bovenkerk, H. M. Strong, and R. H. Wentorf, The Journal of Chemical Physics **35**, 383 (1961).

[2] F. P. Bundy, W. A. Bassett, M. S. Weathers, R. J. Hemley, H. U. Mao, and A. F. Goncharov, Carbon **34**, 141 (1996).

[3] V. R. Howes, Proceedings of the Physical Society **80**, 648 (1962).

[4] T. Evans and Z. Qi, Proceedings of the Royal Society of London Series A **381**, 159 (1982).

[5] Z. Qi, PhD. thesis, University of Reading (1981).

[6] T. Evans, S. T. Davey, and S. H. Robertson, Journal of Materials Science **19**, 2405 (1984).

[7] A. Yoneda and S. Endo, Journal of Applied Physics **51**, 3216 (1980).

[8] S. Nichols, Journal of Physics D: Applied Physics **4**, 783 (1971).

[9] E. D. Palik, *Handbook of Optical Constants of Solids* (Academic Press Inc., 1985).

[10] G. S. Woods, J. A. van Wyk, and A. T. Collins, Philosophical Magazine B **62**, 589 (1990).

[11] S. C. Lawson, D. Fisher, D. C. Hunt, and M. E. Newton, Journal of Physics: Condensed Matter **10**, 6171 (1998).

[12] S. R. Boyd, I. Kiflawi, and G. S. Woods, Philosophical Magazine Part B **69**, 1149 (1994).

[13] S. R. Boyd, I. Kiflawi, and G. S. Woods, Philosophical Magazine Part B **72**, 351 (1995).

[14] A. T. Collins, G. Davies, H. Kanda, and G. S. Woods, Journal of Physics C: Solid State Physics **21**, 1363 (1988).

[15] D. Hunt, PhD. thesis, St. Peter's College, University of Oxford (1999).

[16] G. B. Bachelet, D. R. Hamann, and M. Schlüter, Phys. Rev. B **26**, 4199 (1982).

[17] S.-F. Wang, Y.-F. Hsu, J.-C. Pu, J. C. Sung, and L. G. Hwa, Materials Chemistry and Physics **85**, 432 (2004).

[18] R. Jones, J. P. Goss, and P. R. Briddon, Physical Review B **80**, 033205 (2009).

[19] R. T. Weber, J. Jang, and D. B. Barr, *EMX User's Manual*, Brucker, EPR Division Bruker Instruments, Inc. Billerica MA USA, 2nd ed. (1998), *Emx user's manual*.

[20] PerkinElmer, *UV WinLab Software Guide*, PerkinElmer, 6th ed. (2009), *UV WinLab Software Guide*.

Chapter 5

Substitutional Nitrogen in Diamond

This chapter will present the uniaxial stress work performed to identify the symmetry and nature of two local vibrational modes in diamond attributed to single substitutional nitrogen defects. Also presented are absorption spectra for $^{15}N_S^+$ and $^{15}N_S^0$.

5.1 Introduction and motivation

Nitrogen is the most common impurity found in diamond and is a constituent of many commonly observed defects. It is such a significant impurity, that classification of diamond stems from the inclusion of nitrogen in the lattice. Owing to its prominence, it is essential to understand its influence on the properties of the material, its behaviour under a range of treatments and its interaction with other potential defects in the lattice. This chapter focuses on furthering the understanding of the 1344 cm^{-1} and 1332 cm^{-1} local vibrational modes (LVMs), characteristic of single substitutional nitrogen.

5.2 A review of substitutional nitrogen in diamond

Nitrogen in diamond is an extensively studied area owing to its common incorporation in natural, CVD and HPHT synthesis processes, usually as a result of atmospheric gasses or impurities of the source materials. Nitrogen incorporates in

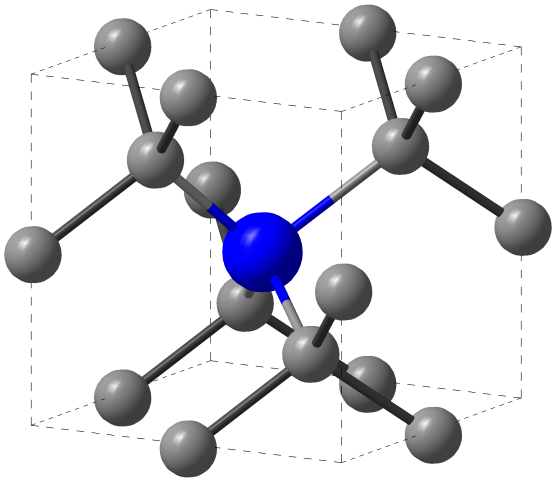

Figure 5-1: An illustration of the structure of N_S^0.

an atomically dispersed state in diamond during growth (Figure 5-1). For natural diamond, the long period located sub-surface in high temperature and pressure environments, leads to the migration and aggregation of nitrogen into clusters (type Ia). For CVD-grown synthetic samples, the combination of temperatures and time required for growth is often insufficient to lead to substantial aggregation of the dispersed nitrogen atoms and hence it is more common that samples will be of type Ib. However, for HPHT synthesis at higher temperatures, aggregation during growth may occur.

A *nitrogen getter* [1–3] may be included with the source materials of HPHT growth to reduce the concentration of nitrogen taken into the diamond. The disadvantage is that some part of the getter material may become incorporated into the final diamond. For CVD growth, nitrogen incorporation is easier to control, by maximising the purity of source gases and purging the growth chamber to remove atmospheric gasses.

5.2.1 Detection by electron paramagnetic resonance (EPR)

It was by EPR that the presence of nitrogen in diamond was first identified [4, 5]. Several characteristics make nitrogen an easy defect to recognise by EPR. The odd number of electrons creates a source of unpaired electrons, making the centre paramagnetic and the near 100% abundance of ^{14}N with a nuclear spin of 1 and provides a distinct signature for this defect [4, 6]. Much of the structural

information concerning N_S^0 has been established by EPR studies.

For N_S^0, the g factor is isotropic at 2.0024 ± 0.0005. There are four equally abundant C–N bonds and the donor electron occupies an anti-bonding orbital on a nitrogen atom and a nearest neighbour carbon atom [4]. The result is a significant bond distortion, an elongation of 28%, identified by theory and experiment [6, 7]. Subsequently, measurements of nitrogen rich and deficient regions of diamond, indicate a 40% increase in volume occupied by the N_S^0 defect [8]. An elongation in one of the $\langle 111 \rangle$ direction results, giving the C_{3v} symmetry identified by EPR [4]. The relaxation of this bonding from T_d to C_{3v} results in nitrogen being a deep donor [9–13].

For a given site of the nitrogen atom, there are four different relaxations available. Each of the orientations of the centre can be uniquely identified by EPR by their different hyperfine interactions with the central nitrogen nucleus. If no lattice strain or additional interactions from impurities exist, the four defect orientations are equivalent in energy and will occur with equal probability. At temperatures greater than 600 K, motional averaging occurs of the N_S^0 centre. The unpaired electron hops between the four N–C bonds and at 1200 K, the hopping is so rapid that an average of all possible sites is observed. The reorientation activation energy is reported as 0.7(1) eV [14].

Additionally, the application of external stress to the diamond can lift degeneracy, inducing an alignment of the centres [15]. Studies by Ammerlaan showed that the application of 2 GPa of stress in the $\langle 110 \rangle$ direction at 142 K, resulted in the increase in concentration of energetically favourable directions over the higher energy configurations by up to 50% [15]. Two processes were identified as governing the reorientation; at high temperatures, the reorientation was thermally activated, whereas low temperatures saw a tunnelling mechanism determining the reorientation rate.

5.2.2 Detection by optical spectroscopy

The presence of nitrogen induces characteristic absorption in the infrared, visible and ultraviolet regions [16]. The addition of the nitrogen impurity destroys the lattice symmetry, permitting absorption in the one-phonon region and for a di-

amond of natural abundance of nitrogen, a maximum at 1130 cm^{-1} is observed, with a sharp peak at 1344 cm^{-1}. The intensity of these lines has been shown to be related and to originate from the same defect [17], although their relative intensities depend substantially upon the resolution of the spectrum [18]. Isotopic substitution experiments identified a red shift of 15 cm^{-1} of the 1130 cm^{-1} absorption feature upon substitution of ^{14}N with ^{15}N in the diamond [17]. The frequency ratio (0.99) is very close to that expected for a C–N vibration. No shift in the 1344 cm^{-1} absorption feature is observed upon isotopic substitution of nitrogen. However, for diamond enriched with ^{13}C, there is a shift of the 1344 cm^{-1} mode to 1292 cm^{-1} [19], suggesting the 1344 cm^{-1} mode to originate from a pure carbon vibration. The intensity of these features can be used to characterise the concentration of nitrogen within the diamond. 1 cm^{-1} absorption at 1130 cm^{-1} is produced by 25±2 ppm of N_S^0 centres [20]. The first overtone of the 1344 cm^{-1} vibrational mode is detected at 2688 cm^{-1} [17].

N_S^0 can donate an electron if the diamond contains a suitable acceptor. A diamagnetic centre results (N_S^+), sitting on the lattice site, forming four identical bonds to the neighbouring carbon atoms. In a spectral scan of 1 cm^{-1} resolution, 1 cm^{-1} absorption at 1332 cm^{-1} from the N_S^+ centre is produced by 5.5±1 ppm of N_S^+ centres. The sharp 1332 cm^{-1} mode is accompanied by further features at 1115, 1046 and 950 cm^{-1} [21].

In the visible region of the spectrum, absorption is observed from 1.7 eV, rising continuously to the band edge [22]. The concentration of N_S^0 is correlated to the integrated intensity of a broad feature at 4.6 eV (270 nm) [16] resulting from mainly vibronic transitions at this defect [18], although background absorption can increase inaccuracy in calculation. The onset of the optical absorption and photoconductivity measurements, have placed the deep nitrogen donor level at 1.7 eV below the conduction band [9]. Further measurements on CVD-grown diamond suggest a photoionisation energy of N_S^0 of 2.2 eV [23].

5.2.3 Migration and aggregation of nitrogen

A plethora of defects resulting from the migration and aggregation of nitrogen are observed in diamond. At temperatures greater than 1700℃, nitrogen atoms

can migrate through the lattice leading to aggregation and the formation of A-centres [24]. By heating at 1900℃ under a stabilising pressure of 6 GPa for 1 hour, an 80% conversion of single nitrogen atoms to A-centres can be achieved [25]. The effect of irradiation introduces vacancies and interstitials into the lattice, leading to the donation of an electron from N_S^0, forming N_S^+ and the negatively charged vacancy (V^-) and possible interstitial defects. The presence of vacancies within the lattice can also lead to vacancy enhanced migration and aggregation of nitrogen (Equation (5-1)). The process involves the multiple release and re-trapping of vacancies, permitting the nitrogen atom to more readily migrate through the lattice and for A-centres to form at lower temperatures, of the order of 1500℃ [26].

$$\begin{aligned} N + V &\rightarrow NV \\ NV &\rightarrow VN \\ VN &\rightarrow V + N... \\ ...NV + N \rightarrow VN + N &\rightarrow V + N - N \end{aligned} \tag{5-1}$$

In a similar way to the calculation for the concentration of N_S^0 and N_S^+, the defect induced one-phonon region of the infrared spectrum can be deconvolved to isolate the absorptions resulting from the A-centres in the diamond lattice [24, 27]. $1\,cm^{-1}$ absorption at $1282\,cm^{-1}$ for ^{14}N diamond, results from a concentration of 17.5 ppm of nitrogen in A-centre form [28]. The $1282\,cm^{-1}$ absorption feature in ^{14}N diamond is common to both A-centre and B-centre aggregates. For the spectrum of B-centres, there is commonly the addition of the $1370\,cm^{-1}$ absorption peak, indicative of platelets which is not present in the A-centre spectrum.

5.2.4 Sector dependence of nitrogen uptake

Synthetic diamond can grow with concentrations of several hundreds of parts nitrogen per million carbon atoms. In general, synthetic diamond grows with a morphology that is cubo-octahedral [2], although variations in growth temperature and solvent/catalyst chemistries can modify this [29]. The uptake of nitrogen is greatest in the ⟨111⟩ sectors, although at low temperatures, the concentration of nitrogen in the ⟨001⟩ sectors can exceed that of the ⟨111⟩ [30]. Since the majority of techniques investigate the bulk average properties, consideration may need to

be given to the specific environment of a defect and whether it has some sector dependence. An example of this is with the WAR9 and WAR10 defects which are only observed in low nitrogen sectors. In high nitrogen regions, the defects are thought to be in their negative charge state.

5.3 Experimental detail

For uniaxial stress experiments investigating the N_S^0 absorption feature, two HPHT grown ^{15}N samples (samples A and B) were used. The single substitutional nitrogen concentration was 160 ppm and 150 ppm respectively, as determined by EPR and each sample had similar dimensions (1.0 mm by 1.1 mm by 2.1 mm). Sample A was cut such that stress could be applied along the $\langle 001 \rangle$ and $\langle 110 \rangle$ directions, with sample B cut for stress along the $\langle 111 \rangle$ direction. The experimental detail considering uniaxial stress experiments is outlined in Chapter 4.

The accuracy of the face plane orientation for all these samples prepared for stress was to within $\pm 1^\circ$. Accuracy in the face plane was observed by Laue X-ray back-reflection diffraction. Samples were polished such that they were free from inclusions, cracks and chips, as apparent by $\times 10$ magnification. This minimised the risk of cleaving or fracture of the samples under stress. Uniaxial stress experiments were conducted at room temperature at an infrared absorption spectroscopy resolution of $1\,cm^{-1}$ resolution.

For investigation of the LVM attributed to the N_S^+ defect, two CVD grown ^{14}N samples were used (samples C and D). Each had an approximate concentration of N_S^0 of 15 ppm and N_S^+ of 5 ppm. The low N_S^0 concentration ensured clarity in distinguishing the shift of N_S^+ under stress from the $1344\,cm^{-1}$ absorption band.

To consider the isotopic substitution behaviour of N_S^+, a further sample (sample F) approximately 95% enriched with ^{15}N was irradiated with a dose of 1.5×10^{18} 1.5 MeV electrons per cm^2 to form the N_S^+ defect and compared to sample E of natural abundance of ^{14}N, irradiated with 1×10^{18} 1.5 MeV electrons per cm^2.

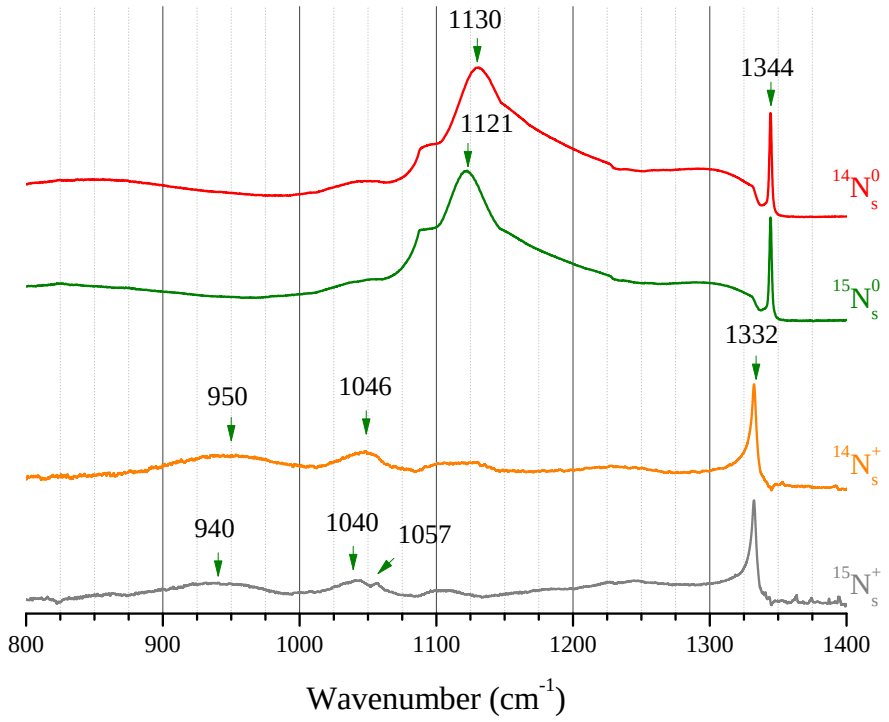

Figure 5-2: A comparison of substitutional nitrogen component spectra. The figure highlights the absorption spectra which result wholly from either N_S^0 or N_S^+ and in addition, shows spectra for a sample with nitrogen in natural abundance and sample enriched with ~95% ^{15}N. These spectra have been scaled to have an intensity of 1 by their most prominent feature (either 1344 cm^{-1} or 1332 cm^{-1}) and offset for clarity.

5.4 Results and analysis

5.4.1 Isotopic substitution effects on substitutional nitrogen absorption features

The absorption spectrum attributable to the N_S^+ defect has been identified by the subtraction of the characteristic N_S^0 and two-phonon features from a post irradiation spectrum. Figure 5-2 shows the variation in spectra for the N_S^0 and N_S^+ defects in the one-phonon region for samples enriched with ^{14}N and ^{15}N. The result for N_S^0 agrees with isotopic shifts published in the literature [17] and provides new information with regard to the N_S^+ defect.

The observed shift in the absorption features of the spectra result from the change in mass directly influencing the vibrational frequency of the bond. The effect of isotopic substitution on vibration frequency is discussed in Chapter 2.

Upon isotopic substitution, the shift in the vibration frequency can be estimated using $\omega_1/\omega_2 = \sqrt{m_2/m_1}$, considering the atoms as masses on a spring. If the effective mass is equal to the mass of nitrogen, resultant vibrational frequency would be $\omega_1/\sqrt{m_2/m_1}$. If the atoms in the diamond bond *into* the lattice, this value becomes an upper limit for the change of the vibrational frequency. For vibrations in the one-phonon region, the shift is therefore seen to be less than that predicted by this model.

Figure 5-2 highlights the relative complexity of the N_S^+ spectra compared to that of the N_S^0 defect. In addition to the sharp mode at 1332 cm^{-1}, attributed to a pure carbon vibration, it is apparent that several weaker features shift to a lower wavenumber. The broad absorption at 950 cm^{-1} becomes centred at 940 cm^{-1} in the ^{15}N enriched sample and a further broad absorption at 1046 cm^{-1} is seen to shift to 1040 cm^{-1}.

Whilst literature discusses the presence of N_S^+ and its associated spectrum, no previous record exists of the influence of isotopic substitution on these features. The complexity of the spectrum and isotope shifts of these nitrogen defects is now evident but further work is required.

5.4.1.1 Developments in quantification of nitrogen in isotopically enriched samples

Deconvolution of the one-phonon region of the diamond spectrum has permitted the development of a more accurate way to assess the nitrogen content of samples and the various forms.

A fitter program is set with normalised spectra of all components. The relation is known between the intensity at a particular wavenumber and the concentration of each defect, such that the total concentration can be calculated. These values can be found in the literature for the ^{14}N defects of diamond in the one-phonon region [20, 21, 31, 32].

$$\begin{aligned} ^{14}N_S^0\text{: } & \mu(1130) = 25(5)\ \text{ppm per cm}^{-1} \\ ^{14}N_S^+\text{: } & \mu(1332) = 5.5(9)\ \text{ppm per cm}^{-1} \\ \text{A-centre: } & \mu(1282) = 16.5(9)\ \text{ppm per cm}^{-1} \\ \text{B-centre: } & \mu(1282) = 79.4(9)\ \text{ppm per cm}^{-1} \end{aligned} \tag{5-2}$$

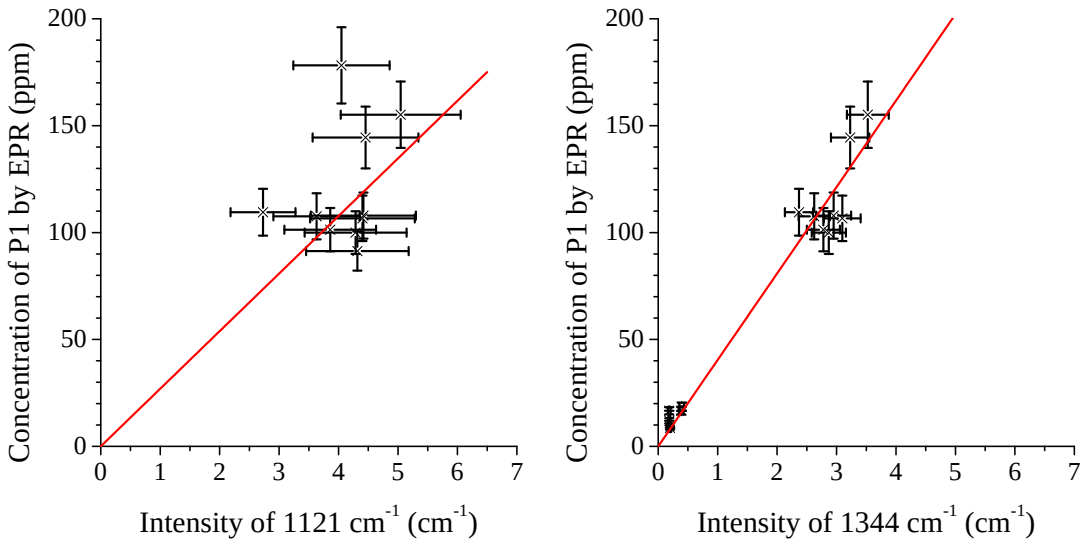

Figure 5-3: A comparison of the concentration of ^{15}N in diamond with the intensity of the 1121 cm^{-1} and 1344 cm^{-1} vibrational modes attributed to the N_S^0 defect. A linear correlation is expected in both instances as illustrated. A linear fit passing through the origin provides a relation between the absorption coefficient of the mode and the concentration of N_S^0 which is calculated as 27(2) ppm per cm^{-1} and 42(3) ppm per cm^{-1} for 1121 cm^{-1} and 1344 cm^{-1} respectively. Spectra were collected at room temperature and at a resolution of 1 cm^{-1}.

Noting that the primary absorption feature for both the A-centre and B-centre forms of aggregated nitrogen are at 1282 cm^{-1}, care must be taken in the assignment of concentration values. In order to develop the fitter to also include ^{15}N defects, it must first be assessed whether the isotopic substitution alters the relative intensity of the vibrational modes.

The concentration of paramagnetic $^{15}N_S^0$ can be easily determined by EPR. $^{15}N_S^0$ is a I=$\frac{1}{2}$ defect compared to I= 1 for $^{14}N_S^0$, resulting in a two line spectrum from the hyperfine splitting as opposed to three. In comparing this to the intensity of the 1121 cm^{-1} line from the one-phonon region spectra of a near-100% ^{15}N diamond, it is possible to assess the effect of the changed mass on the oscillator strength and spring constant of the defect.

This study has found, considering the ^{15}N equivalent defect, a correlation factor of 27(2) ppm per cm^{-1} between the intensity of 1121 cm^{-1} absorption feature and the concentration of nitrogen atoms in the P1 (N_S^0) EPR centre (Figure 5.3(a)). This is within error of the correlation value published for $^{14}N_S^0$ (Equation 5-2). Results of lower concentrations are determinable from the 1344 cm^{-1} LVM as a

Table 5-1: Concentration relation of N_S^0 and the 1344 cm^{-1} local vibrational mode. The absorbance of the 1131 cm^{-1}absorption peak (in ^{14}N diamond) has been shown to correlate with that of the 1344 cm^{-1} band and it can now been seen that the resolution of the spectrometer has a significant effect on the calculation of the concentration result [33].

Resolution cm^{-1}	μ_{1130}/μ_{1344}	$[N_S^0]$ **per cm^{-1} absorbance at 1344 cm^{-1}**
0.5	1.2(1)	30
1	1.5(1)	37
2	1.7(1)	42
4	2.6(2)	65

result of its sharper lineshape. The 1344 cm^{-1} LVM is better resolved at low concentrations compared to the 1121 cm^{-1} mode (^{15}N). The broad lineshape of the 1121 cm^{-1} also leads to greater error in the quantification of its intensity.

The 1344 cm^{-1} LVM correlates with the absorption at 1130/1121 cm^{-1}. Since it is significantly sharper and its lineshape clearer to fit, this would be a more accurate method of calculation. Hunt notes that the linewidth of this absorption band varies significantly with experimental resolution of the infrared spectrometer (Table 5-1) [33].

It is substantially more difficult to assess the concentration correlation value for $^{15}N_S^+$ and ^{15}A-centre. In order to generate significant concentrations of the N_S^+ centre, it would be required for the sample to be irradiated. This will introduce vacancies and interstitials into the lattice and whilst the vacancy can act as a charge acceptor for the electron, generating N_S^+, other defects involving nitrogen may form, such that the sum of nitrogen in the N_S^+ and N_S^0 defects is not representative of the total. Since N_S^+ is diamagnetic, it cannot be detected by EPR measurements; nor can A-centres. However, infrared spectra can be deconvolved through the subtraction of N_S^0 to identify the A-centre spectrum for ^{15}N samples (Figure 5-4).

The result of this study is that the substitution of ^{14}N with ^{15}N atoms does not lead to a substantial change in the oscillator strength of the defect for N_S^0. Therefore, in this thesis, the values published in literature for all the ^{14}N defects will be used for the calculation of the concentrations of the ^{15}N variants.

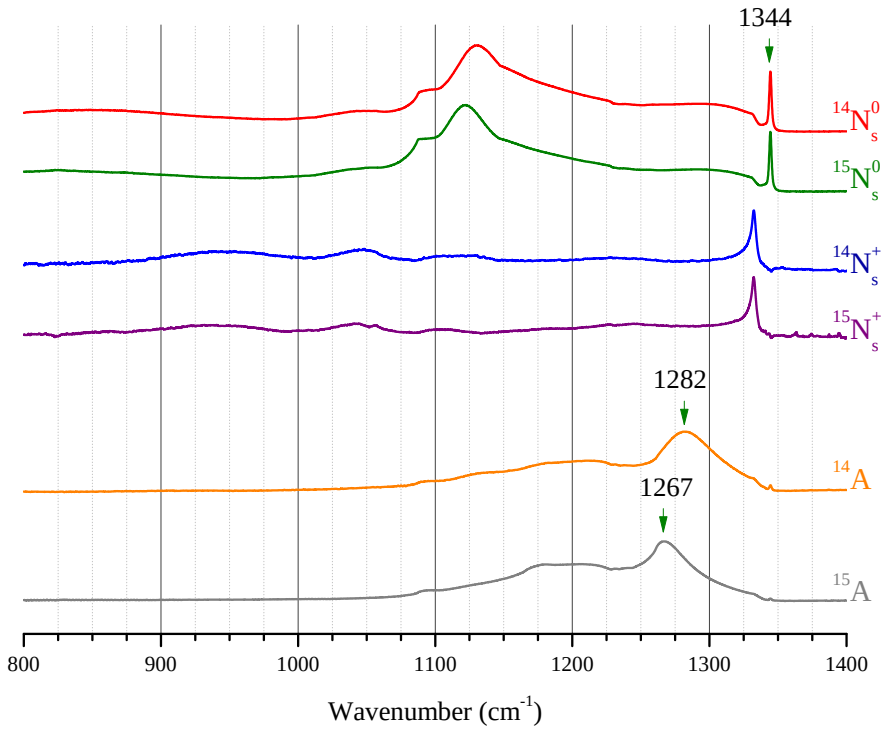

Figure 5-4: A comparison of the component spectra at room temperature of nitrogen-related defects in the infrared one-phonon region. The figure highlights the absorption spectra which result wholly from N_S^0, N_S^+ and the A-centre in both the ^{14}N and ^{15}N forms. These samples have either natural abundance ratios of ^{14}N and ^{15}N or have been enriched with approximately 95% ^{15}N. These spectra have been scaled to have an intensity of 1 cm^{-1} by their most prominent feature and offset for clarity.

5.4.2 The effect of uniaxial stress on single substitutional nitrogen

5.4.2.1 The neutral single substitutional nitrogen defect

The uniaxial stress experiments of this study have highlighted the need for the application of stress at >3 GPa, for the effects of stress, noted by the resolvable shift and split of absorption features, to be apparent and quantifiable. This is higher than previously reported, where no apparent shift in the 1344 cm^{-1} absorption band was observed when the applied stress was of the order of 1.2 GPa [35]. The absence of any detectable shift was concluded to be a result of the vibrational nature of the absorption band being observed, rather than electronic, which previous stress studies had probed. Vibrational lines would still split, lifting the vibrational and orientational degeneracy of the centre but would require a signif-

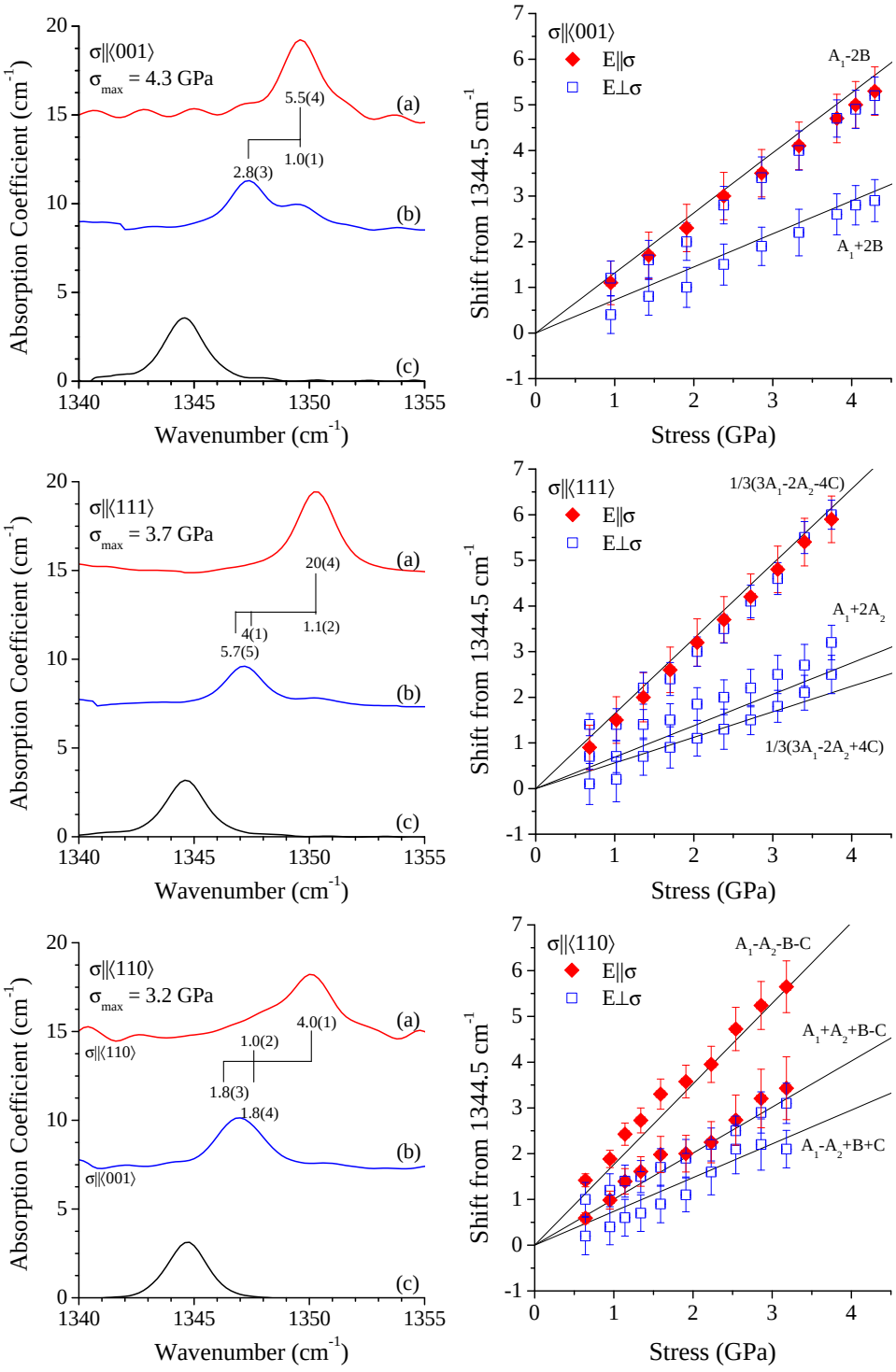

Figure 5-5: The effect of stress upon the local vibrational mode at 1344 cm^{-1}, attributed to single substitutional nitrogen in ^{15}N type Ib diamond. The left column illustrates spectra taken at room temperature and attained at 4.3 GPa, 3.7 GPa and 3.2 GPa for $\sigma \parallel \langle 001 \rangle$, $\langle 111 \rangle$ and $\langle 110 \rangle$ directions respectively. These have been baselined, corrected to 12.3 cm^{-1} at 2000 cm^{-1} and offset for clarity. Spectra (a) and (b) in each represent the sample under stress resulting from (a) parallel and (b) perpendicular polarisation of the electric-field vector and spectrum (c) represents the unperturbed sample. The relative intensities of the transitions is indicated. The right column illustrates the transition frequencies as a function of stress compared to the best fit parameters from all the data for an $A \rightarrow E$ transition at a C_{3v} centre (Table 5-2).

Table 5-2: Tabulated shift and splitting patterns for a C_{3v} centre displaying an $A \rightarrow E$ transition [34]. See also Appendix B.

Direction	**Transition Energy**	$\mathbf{E_{\parallel}}$**:**$\mathbf{E_{\perp}}$
[001]	$\hbar\omega + (A_1 - 2B)\sigma$	4:1
	$\hbar\omega + (A_1 + 2B)\sigma$	0:3
[111]	$\hbar\omega + (A_1 + 2A_2)\sigma$	0:6
	$\hbar\omega + \frac{1}{3}(3A_1 - 2A_2 - 4C)\sigma$	16:1
	$\hbar\omega + \frac{1}{3}(3A_1 - 2A_2 + 4C)\sigma$	0:9
		$\mathbf{E_{110}}$**:**$\mathbf{E_{001}}$**:**$\mathbf{E_{1\bar{1}0}}$
[110]	$\hbar\omega + (A_1 + A_2 - B + C)\sigma$	0:0:3
	$\hbar\omega + (A_1 + A_2 + B - C)\sigma$	1:2:0
	$\hbar\omega + (A_1 - A_2 + B + C)\sigma$	0:2:1
	$\hbar\omega + (A_1 - A_2 - B - C)\sigma$	3:0:0

icantly greater stress to permit any shifting and splitting to be resolved beyond the linewidth of the band.

Under the application of stress, a splitting and linear stress induced shifting of the 1344 cm^{-1} absorption band is observed with an applied stress of the order of 4 GPa. Experimental spectra of the splitting and shifting of transitions are illustrated in Figure 5-5. Spectra are overlayed with the experimentally calculated relative intensities of the deconvolved absorption bands (Table 5-2). In addition, the peak positions of the transitions are plotted as a result of increasing stress.

The 1344 cm^{-1} absorption band is observed to split into two unique transitions when stressed along the $\langle 001 \rangle$ direction, three when stressed in the $\langle 111 \rangle$ direction and three with stress applied in the $\langle 110 \rangle$ direction. The number of transitions resolved in each polarisation of the electric dipole vector and the relative intensities of the resolved transitions, are indicative only of an $A \rightarrow E$ transition of a defect with C_{3v} symmetry.

The transition energy equations outlined in Table 5-2, characteristic of this specific transition, were assigned to the deconvolved absorption bands based upon their polarisation and relative intensities. From this assignment, considering both polarisations of the electric dipole vector and all directions of stress, a method of least squares fitting comparing experimental and theoretical transition frequencies was used to calculate the piezospectroscopic parameters of the transition energy

Table 5-3: Experimental and theoretical piezospectroscopic parameters for the N_S^0 defect

Parameter	**Experimental Value**	**Theoretical Value**
A_1	+1.02(8)	+0.92
A_2	-0.23(9)	-0.17
B	-0.16(7)	-0.13
C	-0.30(10)	-0.18

equations. These experimental values are listed in Table 5-3.

The line-shift data fit exceptionally well to the theoretical model for an $A \rightarrow E$ transition at a trigonal centre. The intensity data, however, does not fit this model well and will be discussed shortly. The complexity of the C_{3v} symmetry results in the response to stress being described by four parameters: A_1, A_2, B and C, calculable from the plots illustrated in Figure 5-5.

The 1121 cm^{-1} absorption feature (^{15}N diamond) in these samples, does not show a resolvable stress induced splitting at stresses up to 4 GPa. The magnitude of the shift in the $\langle 001 \rangle$ direction measured 7.4(3) cm^{-1} in the parallel polarisation an 4.6(3) cm^{-1} in the perpendicular polarisation but the number of transitions could not be concluded. For the $\langle 111 \rangle$ direction, the magnitude of the shift is greater in the perpendicular polarisation, measuring 7.4(3) cm^{-1} and 5.6(3) cm^{-1} in the parallel polarisation. The overtone of the 1344 cm^{-1} absorption feature at 2688 cm^{-1} is weak in intensity and below detectable limits.

Theoretical calculations for the predicted stress reaction of this N_S^0 mode have been made. The C_{3v} structure of the N_S^0 defect (Figure 5-1) was modelled by Goss of Newcastle University using density-functional calculations within the local-density approximation [36], as implemented in the AIMPRO (Ab Initio Modelling Program) code (see also §4.3.2.) [37, 38]. His modelling predicts theoretical piezospectroscopic parameters as outlined in Table 5-3.

Due to the nature of the calculation and the absorption band's proximity to the bulk-phonon in terms of its frequency, it would seem reasonable for these values to have significant error from state mixing. However, both results are in exceptional agreement and both the experimental results and theoretical calculations predict the N_S^0 defect to be most sensitive to hydrostatic stresses.

In these data, significant band bending is not observed and as a result, it seems unlikely that there is evidence of state mixing and therefore forbidden transitions becoming allowed under the presence of stress.

5.4.2.2 Reorientation of the N_S^0 defect

Whilst the rate of stress induced shifting and splitting of the 1344 cm^{-1} LVM is in excellent agreement with that for an $A \rightarrow E$ transition originating from a defect of C_{3v} symmetry, the relative intensities of the transitions from the polarised spectra are not (comparing the indicated relative intensities from the spectra (Figure 5-5) with the theoretical relative intensities from tables (Table 5-2)). The reorientation of the N_S^0 defect has been discussed previously in literature and is reviewed in §5.2.1. In the absence of stress, the defect is reorientating both by tunnelling and thermal excitation between the thermally populated excited vibrational states, the temperature regime governing which is dominant. The application of stress then modifies the energetic favourability of some of these states, increasing the concentration of the energetically favourable orientations, at the expense of the higher energy configurations. This is illustrated schematically in Figure 5-6. For stress in the $\langle 110 \rangle$ direction as illustrated, the bonds in the b and c directions are compressed and those in the a and d directions elongated. As a result, the energy of the centres in orientations b and c is increased relative to the a and d orientations.

For compression along the $\langle 111 \rangle$ direction, stress is applied along one of the bond directions, the three remaining bonds being equivalent in energy. This gives two states, one with $g = 1$ and the other $g = 3$, where g is the degeneracy of the state. The probability (p_i) that the system occupies one of these states is given by Equation (5-3), where $Z = \sum_i g_i e^{-\beta E_i}$ defines the partition function, β the inverse temperature ($1/k_B T$) and E_i the energy level of the state.

$$p_i = \frac{g_i}{Z} \exp^{-\beta E_i} \tag{5-3}$$

The increase in stress increases the energy difference between the two states and modifies the probabilities of their occupancy. This is reflected in the intensity seen for that specific transition in the infrared spectrum. Application of stress

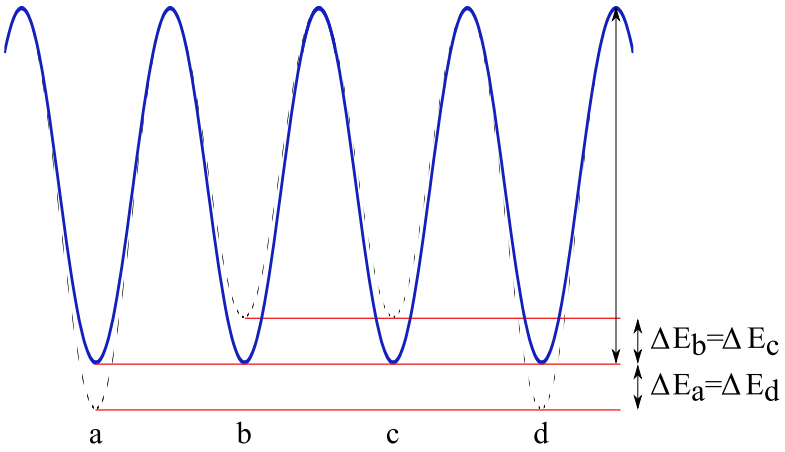

Figure 5-6: Schematic representation of the potential barriers separating the nitrogen centre in the orientations a, b, c, d. The solid line represents the potential barriers without the application of stress and the dotted line, with stress in the ⟨110⟩ direction. This is adapted from a paper by Ammerlaan *et al.* [39].

along the ⟨001⟩ direction, gives transition intensities which match theory, since all the bond angles of the N_S^0 defect under stress remain equivalent.

For the application of stress to the N_S^0 defect in the ⟨111⟩ direction, near complete reorientation away from the bond parallel to the direction of stress could be attained with an applied stress of approximately 3 GPa. This could be simulated through modelling, by applying a hypothetical energy difference between the degenerate states of 22(5) meV GPa^{-1}. This has the effect of adjusting the energetic favourability of the different states and consequently the probability of occupation when under stress by Equation 5-3, a result reflected in the intensity of the associated transitions for the excited and ground states (as predicted by Table 5-2), as observed in infrared spectroscopy. Applying this energetic offset to the modelled stress induced shifting and splitting of the transitions lines (based on Table 5-2), provided an accurate representation of the experimentally observed intensities (Figure 5-7). For the application of stress in the ⟨110⟩ direction, a smaller offset of 11(2) meV GPa^{-1} was sufficient to correct for the intensity mismatch.

A predicted value for the ratio of energy differences can be calculated from the derivation of piezospectroscopic parameters as demonstrated in Chapter 3. For

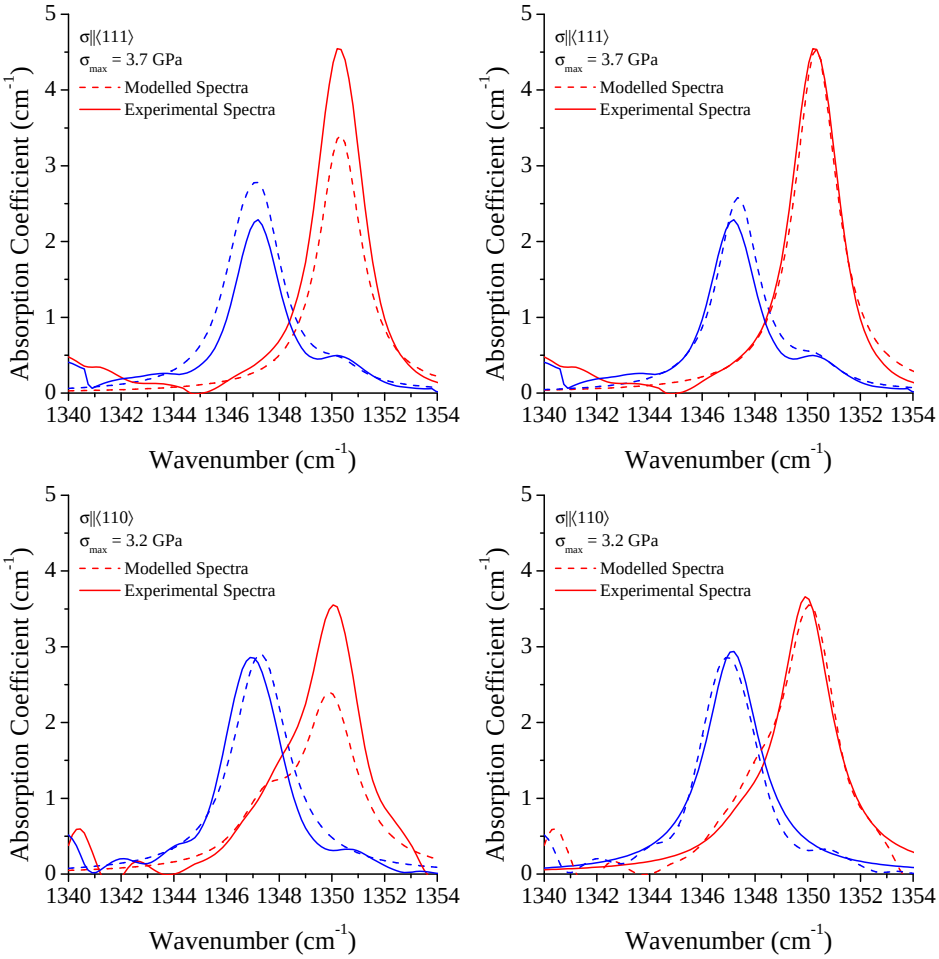

Figure 5-7: The graphs on the left illustrate the error in the transition intensities of the experimental spectra (solid lines) compared to the model for a defect with C_{3v} symmetry (dotted line) (Table 5-2), for stress applied in the $\langle 111 \rangle$ and $\langle 110 \rangle$ directions. The spectra on the right, illustrate the experimental data overlayed with a model based on that of Table 5-2 but with consideration to the population adjustment occurring when the degeneracy is removed by the application of stress.

$\sigma \parallel \langle 111 \rangle$, where E_{GS} is the ground state energy,

$$\text{Site 1: } E_{GS} = \left[\langle a_1|c_{A_1}|a_1\rangle + \langle a_1|c_{A_1'}|a_1\rangle\right]\sigma_{111} \tag{5-4}$$

$$\text{Site 2,3,4: } E_{GS} = \left[\langle a_1|c_{A_1}|a_1\rangle - \frac{1}{2}\langle a_1|c_{A_1'}|a_1\rangle\right]\sigma_{111} \tag{5-5}$$

$$\Delta E_{GS} = \frac{4}{3}\langle a_1|c_{A_1}|a_1\rangle\sigma_{111} \tag{5-6}$$

For $\sigma \parallel \langle 110 \rangle$:

$$\text{Site 1.2: } E_{GS} = \left[\langle a_1|c_{A_1}|a_1\rangle + \langle a_1|c_{A_1'}|a_1\rangle\right]\frac{\sigma_{110}}{2} \tag{5-7}$$

$$\text{Site 3,4: } E_{GS} = \left[\langle a_1|c_{A_1}|a_1\rangle - \langle a_1|c_{A_1'}|a_1\rangle\right]\frac{\sigma_{110}}{2} \tag{5-8}$$

$$\Delta E_{GS} = \langle a_1|c_{A_1}|a_1\rangle\sigma_{110} \tag{5-9}$$

Table 5-4: Tabulated shift and splitting patterns for a tetragonal centre displaying an $A_1 \rightarrow T_2$ transition [40]. For stress applied in the $\langle 001 \rangle$ and $\langle 111 \rangle$ directions, the triplet splits into a singlet and doublet. The transition energies marked with * are the transitions of the doublet.

Direction	**Transition Energy**	$\mathbf{E_\parallel}$**:**$\mathbf{E_\perp}$
[001]	$^*\hbar\omega + [(A_e - A_1) - B_e]\sigma$	0:1
	$\hbar\omega + [(A_e - A_1) + 2B_e]\sigma$	1:0
[111]	$^*\hbar\omega + [(A_e - A_1) - C_e/3]\sigma$	0:1
	$\hbar\omega + [(A_e - A_1) + 2C_e/3]\sigma$	1:0
		$\mathbf{E_{110}}$**:**$\mathbf{E_{001}}$**:**$\mathbf{E_{1\bar{1}0}}$
[110]	$\hbar\omega + [(A_e - A_1) + (B_e + C_e)/2]\sigma$	1:0:0
	$\hbar\omega + [(A_e - A_1) - B_e]\sigma$	0:1:0
	$\hbar\omega + [(A_e - A_1) + (B_e - C_e)/2]\sigma$	0:0:1

Therefore

$$\frac{\Delta E_{GS_{111}}}{\Delta E_{GS_{110}}} = \frac{(4/3)\sigma_{111}}{\sigma_{110}} \tag{5-10}$$

The expected ratio of the energy difference between energy states at the maximum experimental stress for each direction is 1.5(1). Considering the values for the energy differences predicted by fitting the experimental intensities of the stress induced transitions, a factor of 2.0(5) is calculated, within error of the expected ratio.

5.4.2.3 The 1332 cm^{-1} mode, N_S^+

In a similar manner, sensitivity to stress of the mode attributed to N_S^+ at 1332 cm^{-1} has been assessed. The results for this appear significantly more complicated than for the N_S^0 defect. The added complication arises from the 1332 cm^{-1} frequency being the Raman frequency of diamond, the highest atomic vibration frequency of the lattice corresponding to the degenerate vibration of the Bravais lattice of carbon atoms with respect to one another [41].

Grimsditch *et al.* reported on the effect of uniaxial stress on the first-order Raman phonon line of diamond, calculating the corresponding deformation potentials. Under uniaxial stress, the Raman shift line was seen to deform under the

following parameters [42]:

$$\begin{aligned} A = (A_e - A_1) &= 1.47\,cm^{-1}GPa^{-1} \\ B = B_e &= 0.27\,cm^{-1}GPa^{-1} \\ C = C_e &= 2.8\,cm^{-1}GPa^{-1} \end{aligned} \tag{5-11}$$

In diamond and in the absence of strain, the $\overrightarrow{k} = 0$ optical phonons are triply degenerate due to the cubic symmetry of the diamond lattice [43]. The application of stress therefore removes the symmetry and splits the triplet state with a shift induced as a result of the hydrostatic component of stress. For uniaxial stress in the [001] or [111] directions, the triplet is split into a singlet and a doublet. The Eigenvectors of these components are parallel and perpendicular to the direction of stress respectively.

Experiments using infrared spectroscopy have shown that stressing of the $1332\,cm^{-1}$ LVM leads to an increase in energy of the transitions which split in a resolvable way at stresses greater than 3 GPa (Figure 5-8). By overlaying the model outlined by Grimsditch *et al.* and Cerdeira *et al.* for an $A_1 \rightarrow T_2$ transition at a centre with tetragonal symmetry, it can be clearly noted that the $1332\,cm^{-1}$ LVM of the N_S^+ defect is not behaving in the same manner as that of the Raman line of diamond (Figure 5-9).

The experimental data are not well represented by this model. Not only are the predicted number of transitions wrong comparing the experimental spectra with the model for the predicted transition and symmetry (Figure 5-8) but so too are the rates at which the band is seen to shift with the application of stress (Figure 5-9). The vibration of the $1332\,cm^{-1}$ mode does not therefore behave as the bulk lattice does in its response to stress. Instead, the influence of the positively charged nitrogen atom in this defect is dominating the resulting response to the application of uniaxial stress.

It is expected that the N_S^+ defect would have T_d, tetrahedral symmetry. However, the number of splittings that are seen and the relative rate at which they split, cannot be easily characterised by any of the models for cubic symmetry defects. The influence of stress may be two-fold for this local vibrational mode; there may be some contribution from the effect of stress on the diamond lattice and in addition, an effect from the N_S^+ defect producing the local vibrational mode

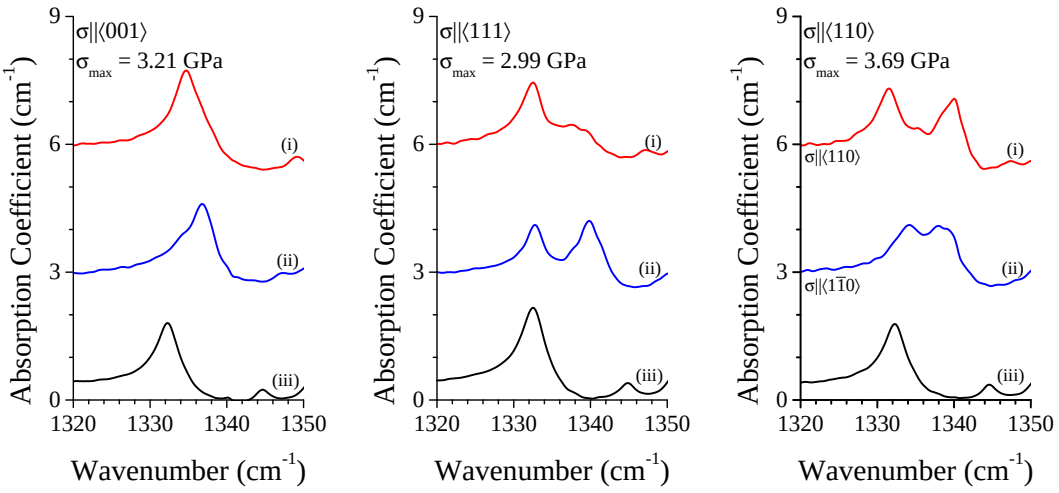

Figure 5-8: Graphs indicate the experimental effects of uniaxial stress on the local vibrational mode labelled 1332 cm^{-1}. Spectra were taken for $\sigma \parallel \langle 001 \rangle$, $\langle 111 \rangle$ and $\langle 110 \rangle$ directions at 3.21 GPa, 2.99 GPa and 3.69 GPa respectively at room temperature. In each figure the electric field vector is orientated (i) parallel to stress and (ii) perpendicular to stress. (iii) is the unstressed spectra. These have been offset for clarity.

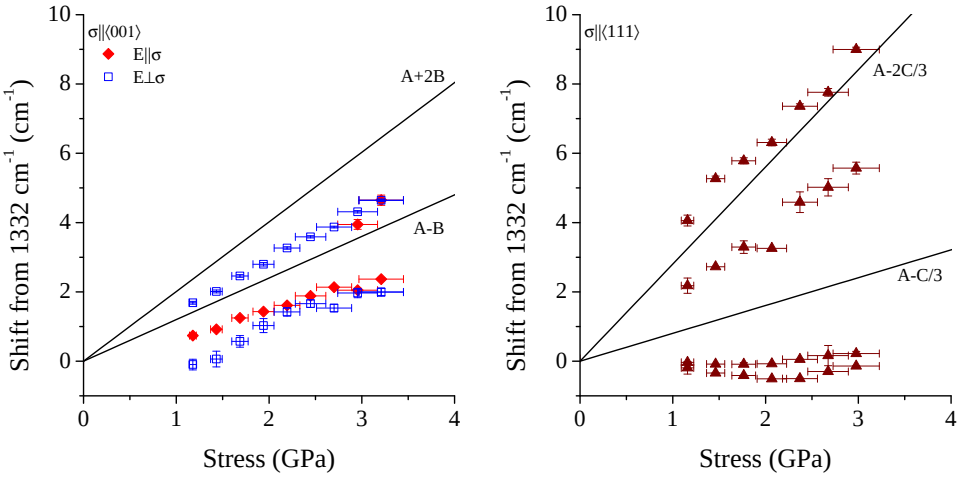

Figure 5-9: These graphs compare the experimental data seen for the shift of the 1332 cm^{-1} LVM with stress, as observed by infrared spectroscopy and the model formulated by Grimsditch *et al.* and Cerdeira *et al.*. They consider the results from stress applied in the $\langle 001 \rangle$ and $\langle 111 \rangle$ directions resulting from hydrostatic and shear stress respectively. For $\sigma \parallel \langle 111 \rangle$, the average shift considering common transitions in the results from the electric vector orientated parallel and orientated perpendicular are plotted for clarity.

at 1332 cm^{-1}. Alternatively, the LVM at 1332 cm^{-1} may result from a combination of defects, each of which are responding differently to the application of stress.

5.5 Conclusions

This chapter has furthered the understanding of substitutional nitrogen defects in diamond. An isotopic study using ^{15}N and ^{14}N enriched diamond, irradiated diamond and annealed diamond has permitted the deconvolution of the spectra attributed to N_S^0, N_S^+ and A-centres. This study has identified that several features are present in the N_S^+ spectrum. The lines are weak in intensity relative to the 1332 cm^{-1} mode, introducing large errors when adding a baseline over this region. The ^{15}N variant of the A-centre spectrum has also been presented. A shift of 14 cm^{-1} was observed for the principal peak at 1282 cm^{-1} to 1267 cm^{-1} but no further resolvable shifts could be identified for other spectral components.

A comparison between the calculated concentration by EPR and the intensity of the 1121 cm^{-1} absorption feature in infrared spectroscopy has identified there to be no difference in the oscillator strengths of the $^{15}N_S^0$ defect compared to the $^{14}N_S^0$ centre. A similar comparison could not be completed for the N_S^+ or A-centre defects, since neither are paramagnetic. Experiments assaying the nitrogen concentration post sample treatment, either irradiation or annealing, are required but care must be taken to consider other nitrogen related defects that may be forming simultaneously.

Uniaxial stress has identified the C_{3v} symmetry of the defect attributed to the 1344 cm^{-1} mode, identifying that stresses greater than 3 GPa are required to induce a resolvable shifting and splitting of the associated transitions. The mode was identified as originating from an $A \rightarrow E$ transition. Piezospectroscopic parameters for this centre were subsequently calculated, indicating the centre to be highly sensitive to hydrostatic, compressive stress. Theoretical modelling of the N_S^0 defect by Goss, independently calculated parameters that were in excellent agreement with those found experimentally for the 1344 cm^{-1} LVM [44], confirming its identity to originate from the N_S^0 defect and highlighting the power of the uniaxial stress technique. The success of the unified result between experimental analysis

and theoretical modelling, encourages the calculation of piezospectroscopic of vibration modes arising from other defects that are commonly found in diamond. An approach such as this could permit the assignment of vibrational modes, which originate from defects of the same symmetry but have substantially different stress parameters, to the correct atomistic model, something which can not be achieved by uniaxial stress experiments alone. Furthermore, theoretical modelling may be able to identify other optically or Raman active modes not previously identified, expanding the catalogue of identified transition lines observed in spectroscopy.

Reorientation of the N_S^0 defect was observed by a mismatch in the relative intensities of the stress induced transitions compared to that expected for this transition type and symmetry. Modelling a perturbation to the probability of occupation of the sites of the defect, considering energetic equivalence with respect to the direction of applied stress, suitably predicted the mismatch that was observed. At 3.7 GPa stress applied in the $\langle 111 \rangle$ direction, near complete reorientation of the defect away from the bond parallel to the direction of stress was observed.

The application of uniaxial stress to the defect responsible for the 1332 cm^{-1} LVM, produced no conclusive identification of symmetry. The N_S^+ defect is expected to have T_d symmetry but the pattern and rate of splitting of the associated transitions did not comprehensively match any recorded cubic defect symmetry. Reported models for the influence of stress on the bulk diamond lattice, did not suitably replicate the data observed experimentally. Under stress, this mode may be displaying a complex behaviour resulting from both the effect of stress on the N_S^+ defect and the effect of stress on the bulk diamond lattice or even from an additional defect contributing intensity to the 1332 cm^{-1} LVM. The results of this study are inconclusive.

5.6 Further work

The outcomes of this chapter suggest several further investigations. With regards to the deconvolution of the ^{15}N one-phonon spectrum into N_S^0 and N_S^+ component spectra, further work is required for the $^{15}N_S^+$ spectrum to confirm the identification of constituent transitions and their assignment to carbon and nitrogen

vibrations. Samples with a higher concentration of N_S^+ are desirable to strengthen the modes in the spectrum. A potential method for comparing the intensity of the A-centre to its concentration could be by EPR. It would require ionising the A-centre and observing the ionised A-centre spectra, a experimental procedure outlined by Tucker [45]. The lifetime of the ionised A-centre is a few hundred seconds and hence high concentrations would be required such that only a few IR scans would be needed. A change in the intensity of the A-centre absorption could then be compared to the change in ionised A-centre concentration as detected by EPR. The distribution of A-centres tends to be highly inhomogeneous, so total sample illumination would be required. As with all these experiments, sample inhomogeneity will be the biggest concern and challenge.

Further investigation of the stress induced splitting and shifting of the N_S^+ centre is also required, using samples with higher concentrations of this defect.

References

[1] R. H. Wentorf, Journal of Physical Chemistry **75**, 1833 (1971).

[2] H. M. Strong and R. M. Chrenko, The Journal of Physical Chemistry **75**, 1838 (1971).

[3] H. M. Strong, *Manufacture of diamond products* (1978), US Patent 4082185.

[4] W. V. Smith, P. P. Sorokin, I. L. Gelles, and G. J. Lasher, Physical Review **115**, 1546 (1959).

[5] J. H. N. Loubser and L. D. Preez, British Journal of Applied Physics **16**, 457 (1965).

[6] A. Cox, M. E. Newton, and J. M. Baker, Journal of Physics: Condensed Matter **6**, 551 (1994).

[7] P. R. Briddon and R. Jones, Physica B: Condensed Matter **185**, 179 (1993).

[8] A. R. Lang, M. Moore, A. P. W. Makepeace, W. Wierzchowski, and C. M. Welbourn, Philosophical Transactions: Physical Sciences and Engineering **337**, 497 (Dec. 15, 1991).

[9] R. G. Farrer, Solid State Communications **7**, 685 (1969).

[10] S. A. Kajihara, A. Antonelli, J. Bernholc, and R. Car, Physical Review Letters **66**, 2010 (1991).

[11] C. F. O. Graeff, E. Rohrer, C. E. Nebel, M. Stutzmann, H. Guttler, and R. Zachai, Applied Physics Letters **69**, 3215 (1996).

[12] P. Gonon, S. Prawer, and D. Jamieson, Applied Physics Letters **68**, 1238 (1996).

[13] M. H. Nazaré, in *Properties and Growth of Diamond*, edited by G. Davies (INSPEC, 1994), no. 9 in EMIS Datareviews Series, chap. 3.2, pp. 85–87.

[14] J. H. N. Loubser and W. P. van Ryneveld, British Journal of Applied Physics **18**, 1029 (1967).

[15] C. A. J. Ammerlaan and E. A. Burgemeister, Physical Review Letters **47**, 954 (1981).

[16] H. B. Dyer, F. A. Raal, L. D. Preez, and J. H. N. Loubser, Philosophical Magazine **11**, 763 (1965).

[17] A. T. Collins and G. S. Woods, Philosophical Magazine B **46**, 77 (1982).

[18] M. H. Nazaré and A. J. T. Neves, Journal of Physics C: Solid State Physics **20**, 2713 (1987).

[19] C. D. Clark, A. T. Collins, and G. S. Woods, in *The Properties of Natural and Synthetic Diamond*, edited by J. Field (Academic Press Inc. (London) Ltd., 1992), pp. 35–79.

[20] G. S. Woods, J. A. van Wyk, and A. T. Collins, Philosophical Magazine B **62**, 589 (1990).

[21] S. C. Lawson, D. Fisher, D. C. Hunt, and M. E. Newton, Journal of Physics: Condensed Matter **10**, 6171 (1998).

[22] M. E. Newton, in *Properties, Growth and Applications of Diamond*, edited by M. H. Nazaré and A. J. T. Neves (INSPEC, London, 2000), chap. A5.4, pp. 136–141.

[23] J. Rosa, M. Vaněček, M. Nesldek, and L. M. Stals, Diamond and Related Materials **8**, 721 (1999).

[24] R. M. Chrenko, R. E. Tuft, and H. M. Strong, Nature **270**, 141 (1977).

[25] B. P. Allen and T. Evans, Proceedings of the Royal Society of London Series A **375**, 93 (1981).

[26] A. T. Collins, Journal of Physics C: Solid State Physics **13**, 2641 (1980).

[27] W. Kaiser and W. L. Bond, Physical Review **115**, 857 (1959).

[28] G. S. Woods, G. C. Purser, A. S. S. Mtimkulu, and A. T. Collins, Journal of Physics

and Chemistry of Solids **51**, 1191 (1990).
[29] H. Kanda, T. Ohsawa, O. Fukunaga, and I. Sunagawa, Journal of Crystal Growth **94**, 115 (1989).
[30] R. C. Burns, V. Cvetkovic, C. N. Dodge, D. J. F. Evans, M. T. Rooney, P. M. Spear, and C. M. Welbourn, Journal of Crystal Growth **104**, 257 (1990).
[31] S. R. Boyd, I. Kiflawi, and G. S. Woods, Philosophical Magazine Part B **69**, 1149 (1994).
[32] S. R. Boyd, I. Kiflawi, and G. S. Woods, Philosophical Magazine Part B **72**, 351 (1995).
[33] D. Hunt, PhD. thesis, St. Peter's College, University of Oxford (1999).
[34] K. Mohammed, G. Davies, and A. T. Collins, Journal of Physics C: Solid State Physics **15**, 2779 (1982).
[35] W. A. Runciman and T. Carter, Solid State Communications **9**, 315 (1971).
[36] J. P. Perdew, K. Burke, and M. Ernzerhof, Physical Review Letters **77**, 3865 (1996).
[37] P. Briddon and R. Jones, Physica Status Solidi (b) **217**, 131 (2000).
[38] M. Rayson and P. Briddon, Computer Physics Communications **178**, 128 (2008).
[39] C. A. J. Ammerlaan and E. A. Burgemeister, Industrial Diamond Review **40**, 128 (1980).
[40] K. Mohammed, PhD. thesis, King's College, University of London (1982).
[41] R. S. Krishnan, Nature **155**, 171 (1945).
[42] M. H. Grimsditch, E. Anastassakis, and M. Cardona, Physical Review B **18**, 901 (1978).
[43] F. Cerdeira, C. J. Buchenauer, F. H. Pollak, and M. Cardona, Physical Review B **5**, 580 (1972).
[44] J. Goss, *Private communication*, email (2009).
[45] O. D. Tucker, M. E. Newton, and J. M. Baker, Physical Review B **50**, 15586 (1994).

Chapter 6

The H1a Absorption Band - Assignment to the di-nitrogen split interstitial defect

This chapter will discuss the experimental and theoretical evidence used to conclusively assign the H1a absorption band observed in irradiated and annealed diamond, to the di-nitrogen split interstitial structure. The formation and stability of the H1a band was studied using isochronal annealing and the constituents confirmed by isotopic substitution. The structure of the defect responsible for the H1a absorption band has been debated for some considerable time. Through the comparison of stress splitting parameters determined from experiment and those calculated by DFT, the di-nitrogen ⟨001⟩-split interstitial structure is confirmed.

6.1 Introduction and motivation

Diamond can be treated in a variety of ways, annealing and irradiation to name just two methods but these treatments can have a dramatic effect on the properties of the material, e.g. optical, mechanical and electrical. In the commercial world, the understanding of these effects is essential to maintaining consumer confidence, since in some cases, treatments can be used to *artificially* enhance the visible beauty of the diamond and claim it to be something that is rare in nature.

It is therefore important to identify the characteristic features that are telltale signs of these treatments. H1a is one such example. The absorption band observed at 0.181 eV (1450 cm^{-1}) was first reported by Clark, Ditchburn and

Dyer in 1956 [1]. This line was not observed in as-grown natural diamond but found by infrared absorption in type Ib, synthetic diamonds post irradiation and annealing at 900℃. Additionally, lines labelled H1b, H2 (NVN^-), H3 (NVN^0) and H4 were also observed, at energies ranging from 0.6 eV to 2.7 eV [1]. Initial discussion proposed that these lines were due to vacancies and interstitials which had become *anchored* on some form of crystal imperfection that was present only in type I diamond. These defects are further discussed in Chapters 2 and 8.

6.2 A review of previous studies on the H1a absorption band

The H1a defect is observed predominantly in type I samples that have been irradiated and annealed [2, 3], although there is some evidence of electron-irradiated type Ia diamonds showing the 1450 cm^{-1} line characteristic of the H1a defect immediately after irradiation [3]. An absorption band forms at 1450 cm^{-1}, when synthetic material is bombarded with high energy electrons and heated for a couple of hours at temperatures of the order of 800℃ [4]. For natural type Ia material, a similar behaviour has been observed [5] but the 1450 cm^{-1} absorption band is not seen in similarly treated type IIa diamond, suggesting the involvement of nitrogen in its formation.

In type Ia samples, the 1450 cm^{-1} band appears at 250℃ compared to 650℃ in type Ib [3]. The H1a absorption begins to weaken at 1100℃ but survives annealing at 1400℃. Studies by Kiflawi *et al.* using synthetic type Ia and type Ib diamond, concluded that it was only the aggregated state of nitrogen that caused this difference in the production of the band [2]. Furthermore, investigations involving type IaA and type IaA/B diamonds concluded that there was no relation between the intensity of the H1a mode and the concentration of nitrogen in B-centre form and that the absorption of the H1a centre correlated only with the A-centre nitrogen concentration [2].

In some instances, the H1a band has been seen directly post irradiation. It was proposed that this is the result of localised heating potentially in the range of 300-500℃, due to the large number of inelastic collisions from a high charged-

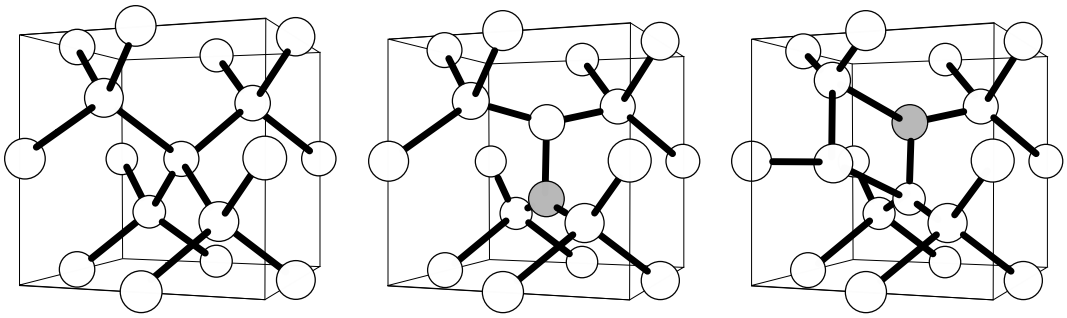

Figure 6-1: Atomic models of the (a) the unperturbed diamond lattice, (b) the WAR9 ⟨001⟩-nitrogen split interstitial defect and (c) WAR10 the ⟨001⟩-nitrogen split interstitial – ⟨001⟩-carbon split interstitial pair defect. The unfilled circles indicate the carbon atoms and the filled, the nitrogen atoms. This is adapted from the paper by Felton *et al.* [13].

particle flux [1, 6]. For neutron irradiated samples, annealing at temperatures greater than 250℃ is required for the absorption feature to be produced and the intensity of H1a is seen to vary linearly with irradiation dose [7].

Concerning the involvement of vacancies in the production of H1a, the threshold temperature of vacancy migration is approximately 600℃ [8]. Since the H1a defect is seen to develop at temperatures as low as 250℃, it seems improbable that vacancies are directly involved. The interaction of vacancies formed from irradiation with nitrogen in diamond has been thoroughly studied [9–12]. At high temperatures, there is the possibility of vacancy enhanced aggregation of nitrogen, leading to the recycling of the vacancy in multiple reactions [4]. However, whilst much is now understood concerning the self-interstitial (labelled R2), the knowledge of the general behaviour of the interstitial is limited. The simple interstitial related defects are reviewed in Chapter 2.

Woods and Collins initially proposed that a carbon interstitial (R2) was involved in the production of H1a [7]. Having formed this interstitial during irradiation, it may be a possibility that upon annealing, the substitutional nitrogen atom is displaced by the interaction with a carbon interstitial into an interstitial position itself, leaving the carbon on the lattice site. However, Woods and Collins were unable to determine from their investigations whether it was simply a nitrogen interstitial that was responsible for the H1a absorption. It is also highly probable that there are alternative sinks for the carbon interstitial which do not

directly result in the formation of a nitrogen interstitial.

The di-interstitial, labelled R1, is not produced in diamonds where the concentration of nitrogen present in the lattice is far greater than the concentration of interstitials produced as a result of irradiation [14]. Recent work has identified two new spin one-half defects which have been identified by EPR as being consistent with the ⟨001⟩-nitrogen split interstitial (N_I, Figure 6.1(b)) and the ⟨001⟩-nitrogen split interstitial – ⟨001⟩-carbon split interstitial pair (N_I–I_{001}) (Figure 6.1(c)) [13].

It is known that the incorporation of nitrogen in HPHT grown diamonds is sector dependent, with ⟨111⟩ sectors showing the highest N_S concentrations and ⟨110⟩ sectors substantially less [15]. The two EPR detected defects were both observed in *lightly* nitrogen doped sectors and were suggested to be electron traps. In *heavily* doped material, where the concentration of substitutional nitrogen is much greater than that of vacancies or interstitials, it was proposed that these defects would exist in the negative charge state and hence be undetectable by EPR.

Theory and experiment surrounding these defects is in good accord [13]. The activation energy for migration of the I_{001} is 1.6 eV but radiation enhanced interstitial migration is known to exist [16]. Once mobile, it is postulated that the I_{001} defect is trapped by N_S^0, leading to the formation of neutral nitrogen interstitials (N_I^0).

$$\begin{aligned} I_{001} + N_S^0 &\rightarrow N_I^0 \\ N_I^0 + N_S^0 &\rightleftharpoons N_I^- + N_S^+ \end{aligned} \tag{6-1}$$

It is unlikely that N_I^0 would revert back to I_{001} and N_S^0, since this is energetically expensive but instead, migrate as a single unit. Theory predicts that the barrier to migration for N_I^- is substantially lower than that for N_I^0 [17] with the capture of I_{001} by N_I producing an R1 like defect, with one of the three fold co-ordinated carbon atoms being replaced by a nitrogen atom.

$$I_{001} + N_I^0 \rightarrow (N_I\text{–}I_{001})^0 \tag{6-2}$$

In the higher nitrogen concentration regions, charge transfer processes could occur.

$$(N_I\text{–}I_{001})^0 + N_S^0 \rightleftharpoons (N_I\text{–}I_{001})^- + N_S^+ \tag{6-3}$$

Capture of N_I by N_S would produce N_{2I}, which is the defect proposed to be responsible for the infrared H1a absorption band (Figure 6.2(c)) [17]. Here, both dumbbell atoms of the interstitial are replaced by nitrogen atoms.

$$N_I + N_S \rightarrow N_{2I} \tag{6-4}$$

It is speculated that the barrier to formation of Equation (6-4) could be reduced if the reactants were in the negative and positive charge states respectively, permitting the migration of the nitrogen interstitial and the formation of the H1a band at 650℃ in type Ib materials. For example,

$$N_I^- + N_S^+ \rightarrow N_{2I} \tag{6-5}$$

It was suggested from the thermal stability of the defect identified as N_I^0, that the neutral charge state is much less mobile than the negatively charged state [13]; there is support from theory for this proposal [17].

Goss *et al.* proposed that N_{2I} could be produced by capture of the I_{001} by an A-centre such that

$$I_{001} + N_S\text{–}N_S \rightarrow N_{2I} \tag{6-6}$$

which could occur at 300℃, where the formation of the H1a band is seen in type Ia diamond. This could explain the different temperatures required to produce the H1a absorption band in type Ia diamond, since only the mobility of I_{001} is required, whereas in type Ib diamond, it is the mobility of N_I^- that is the key factor [17].

6.2.1 Potential Structures for the H1a defect

Two proposals existed for the structure of the defect responsible for H1a but neither appear at first inspection to satisfy both the isotopic evidence for H1a and its annealing behaviour. Isotopic substitution studies of H1a have been reported previously [2, 7]. Comparative work between ^{14}N and ^{15}N doped diamonds has shown that the defect responsible for the H1a band involves the vibration of a

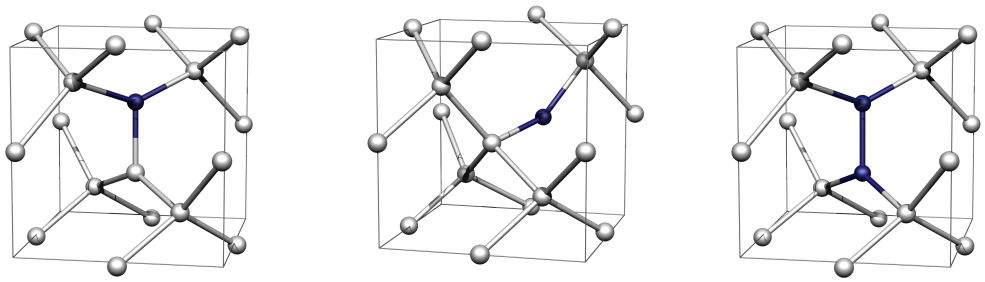

(a) (b) (c)

Figure 6-2: Potential interstitial structures involving nitrogen in diamond. Figure (a) is a schematic of the simple nitrogen interstitial defect structure in diamond; (b) represents the puckered bond-centred nitrogen interstitial proposed as the source of the H1a absorption band by Kiflawi *et al.* [2]; (c) is the alternative structure of the di-nitrogen split interstitial as originally proposed by Goss *et al.* [17].

single nitrogen atom. Two sharp peaks at 1450.3(1) cm^{-1} and 1426.0(1) cm^{-1} were recorded for a sample with approximately equal concentrations of ^{14}N and ^{15}N (Figure 6.3(a)) [7]. The immediate conclusion from this would be that the vibration involves a single nitrogen atom, since no mode from a defect of mixed isotopic composition was identified.

In addition, work with ^{12}C and ^{13}C enriched diamond has indicated the involvement of two equivalent carbon atoms in the H1a local vibrational mode (LVM) (Figure 6.3(b)) [2]. Spectra from a range of samples doped with various percentages of ^{13}C, identified the 1450 cm^{-1} peak to shift to 1424 cm^{-1} in the 97% enriched ^{13}C sample. For samples of mixed isotopic composition, three absorption peaks were identified to be associated to H1a, with the additional band occurring at 1438.3 cm^{-1}. Throughout annealing studies made by Kiflawi *et al.*, the relative intensities of the three peaks remained constant, confirming them to originate from the same centre.

It must though be noted that a minor peak at 1438 cm^{-1} has been previously identified with alternative annealing behaviour and hence is attributable to a different defect [3]. Care must therefore be taken not to confuse this with evidence of a mixed isotope sample. This feature is seen to arise post electron and neutron irradiation and annealing in type Ia and Ib samples and is often hidden by the

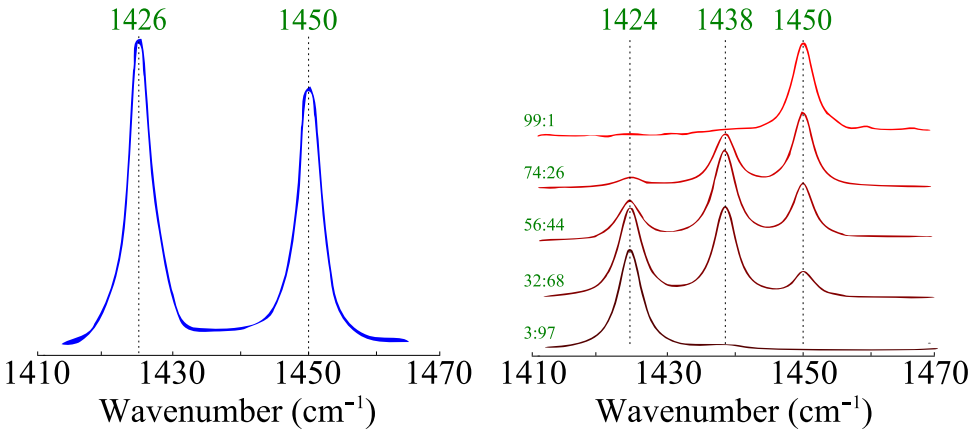

Figure 6-3: Spectra from the isotopic substitution investigations of the H1a defect. (a) illustrates the 50:50 ^{14}N:^{15}N enriched sample spectra for the H1a defect (adapted from a paper by Woods *et al.* [7]) and (b) illustrates results considering a range of isotopic ratios of ^{12}C:^{13}C. This is adapted from a paper by Kiflawi *et al.* [2].

strong 1450 cm^{-1} absorption. During annealing at increasing temperature, the intensity is seen to decrease, at a different rate to that of the 1450 cm^{-1} line but is still present post 4 hours annealing at 1400°C [3].

The results of Woods led to the initial proposal for H1a to originate from a nitrogen interstitial defect of the ⟨001⟩-split site form [3]. However, upon the understanding of the isotopic work for ^{12}C and ^{13}C enriched diamond, indicating that two equivalent carbon atoms are involved in the vibration, theoretical modelling based upon semi-empirical Hartree-Fock theory, led to the hypothesis that the nitrogen atom was occupying a position midway between the two nearest neighbour carbon atoms, displaced off the axis between them at a bond angle of 115° with the carbon-nitrogen bond having a length of 1.47 Å (Figure 6.2(b)) [2]. The proposed formation mechanism in type Ia material requires that an approaching self-interstitial interacts with the N-pair allowing it to dissociate at relatively low temperatures into N_I and N_S. The different behaviour in type Ib material was tentatively explained by the role of charge state effects not present in Ia material (Equations (6-5) and (6-6)).

Calculations by density-functional theory of the potential interstitial nitrogen structures and a range of associated complexes, cast doubt on this model [17]. Indeed, the puckered bond-centred structure was found to be unstable relative

to the formation of a ⟨001⟩-oriented split-interstitial, where nitrogen is three fold co-ordinated, consistent with simple chemical principles. In addition, the stability of H1a at high temperatures was viewed as inconsistent with the calculated migration barrier of the simple nitrogen interstitial. The calculations showed N_I to be mobile at the production temperature of 300℃ in type Ia material, which would contradict the stability of the absorption feature at 1400℃. Furthermore, recent EPR studies [13] have identified, as discussed, the N_I to adopt an ⟨001⟩-split nitrogen interstitial configuration, thus rebutting the claim by Kiflawi *et al.* [2], that the nitrogen interstitial adopts a bond-centred configuration.

It was proposed that the H1a defect was a complex of two nitrogen atoms sharing a single ⟨001⟩-split configuration (Figure 6.2(c)) [17]. This explains both the thermal stability and vibrational properties seen experimentally but superficially contradicts the lack of additional bands in ^{14}N-^{15}N mixed-isotope doped material, which was seen as evidence of just one N atom present in the H1a centre [2]. However, the calculated vibrational modes exhibit negligible interaction between the nitrogen atoms for the degenerate pair of modes in the vicinity of H1a, so in any given mode, only one of the nitrogen atoms is involved, leading to the nitrogen isotopic effects observed. Investigations by electron paramagnetic resonance have to date not revealed any analogue to the H1a feature. In light of this, the proposal of H1a to be a di-nitrogen interstitial seems reasonable due to its non-paramagnetic nature in the neutral charge state.

The equilibrium structure of N_{2I} is tetragonal, transforming under the D_{2d} point-group. The proposed structure is illustrated in Figure 6.2(c) with the principal axis vertically aligned. The predicted high symmetry of the defect and the degeneracy of the local-vibrational mode, lends this centre to a convincing assignment using the splitting patterns and rates under uniaxial-stress along high-symmetry crystallographic directions.

6.3 Experimental details

Isotopic shift studies were made using two samples. Sample M, a ^{14}N enriched, HPHT-grown type Ib sample, was irradiated to a dose of 1.0×10^{18} 1.5 MeV electrons per cm^2

Table 6-1: A summary of the samples used for the investigations of the H1a defect. All irradiation experiments were performed with a sample temperature of less than 200℃ and all annealing experiments were performed in forming gas.

Sample	**Description**	**Treatment**	**Use**
M	HPHT-grown ^{14}N enriched with $[N_S^0] = 150\,\text{ppm}$	Irradiated to 1.0×10^{18} 1.5 MeV e^- per cm^2	Isotopic investigation
N	HPHT-grown 95% ^{15}N enriched with $[N_S^0] = 150\,\text{ppm}$	Irradiated to 1.5×10^{18} 1.5 MeV e^- per cm^2	Isotopic investigations and uniaxial stress in the ⟨001⟩ and ⟨110⟩ directions
P	HPHT-grown 95% ^{15}N enriched with $[N_S^0] = 150\,\text{ppm}$	Irradiated to 1.0×10^{18} 1.5 MeV e^- per cm^2	Annealing study
Q	HPHT-grown 95% ^{15}N enriched with $[N_S^0] = 150\,\text{ppm}$	Irradiated to 1.0×10^{18} 1.5 MeV e^- per cm^2	Isotopic investigations and uniaxial stress in the ⟨111⟩ directions

at a temperature less than 200℃ and annealed at 1000℃ for 1 hour in forming gas. The line position of the H1a absorption band was compared to that in a 95% ^{15}N enriched HPHT-grown type Ib sample[1] (sample N), irradiated to a dose of 1.5×10^{18} 1.5 MeV electrons per cm^2 and annealed similarly. Observation of isotopic shift was made by room temperature infrared spectroscopy at $1\,cm^{-1}$ resolution.

For the investigation of annealing behaviour of the H1a defect, an irradiated type Ib sample (sample P) was annealed at 200℃ intervals from 800℃ to 1400℃ and 100℃ thereafter for 4 hours in forming gas. The intensity of the H1a absorption band was measured after each anneal by infrared spectroscopy. All measurements were taken at room temperature and using a resolution of $1\,cm^{-1}$.

Two HPHT-grown type Ib samples, each enriched with 95% ^{15}N, were polished such that sample N had faces suitable for the application of stress along the ⟨001⟩ and ⟨110⟩ directions and sample Q prepared for the application of stress along the ⟨111⟩ direction. The accuracy of the face plane orientation was to within ±1°, confirmed by Laue X-ray back-reflection. Samples were polished such that under ×10

[1] All ^{15}N samples were grown using a modified HPHT synthesis method. Atmospheric gasses were removed from the growth capsule containing the solvent/catalyst and carbon source and at lower than growth temperatures, the capsule was purged with > 95% ^{15}N enriched gas [18].

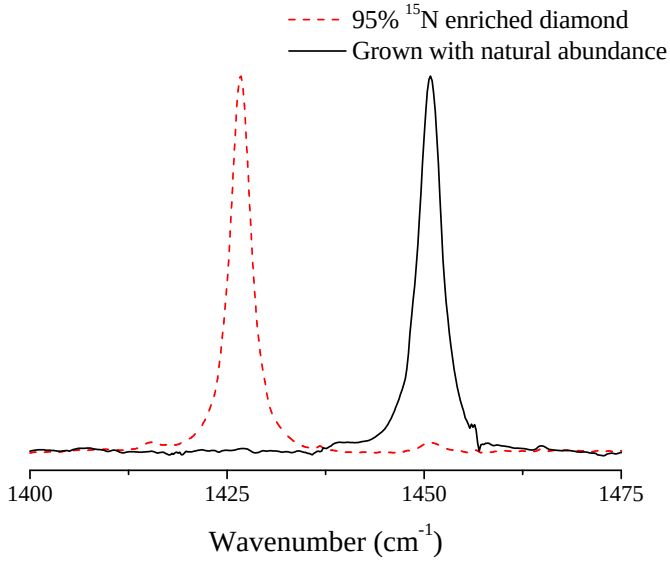

Figure 6-4: Overlayed spectra showing the ^{14}N to ^{15}N isotopic shift of the H1a absorption band. Intensities here have been scaled to give the same peak height for both spectra.

magnification, they were free from inclusions, cracks and chips which could act as fracture propagation sites. Both samples were of the approximate size $1 \times 1 \times 2$ mm. Irradiation was performed to a dose of 1.5×10^{18} 1.5 MeV electrons per cm^2 for sample N and 1.0×10^{18} 1.5 MeV electrons per cm^2 for sample Q. During irradiation, the sample block was water cooled, with the sample temperature being less than 200℃. Irradiation treatment was followed by annealing in an oxygen free environment at a temperature of 1000℃.

Stress investigations were performed using a custom built stress cell in conjunction with the aforementioned FTIR spectrometer. Spectra were taken for stress applied along the three principle directions with the electric-field vector polarised both parallel and perpendicular to the direction of stress using an Edmund Optics zinc selenide holographic wire grid polariser, described in Chapter 4.

6.4 Results and analysis

6.4.1 Isotopic substitution behaviour of H1a

Two similar samples (samples M and N), both irradiated and annealed similarly, were compared to assess the validity of previous claims with regards to the iso-

topic influence on nitrogen on the vibrational mode. For these samples, the H1a absorption feature was recorded to occur at 1450.8(2) cm^{-1} for the ^{14}N doped sample which was observed to shift to 1426.7(2) cm^{-1} for a ≈95% ^{15}N doped diamond (Figure 6-4), in agreement with previously published data. A shift of 24.1 cm^{-1} is comparable in magnitude to that seen for the 1502 cm^{-1} defect under nitrogen isotope substitution experiments. For the 1502 cm^{-1} absorption band, a shift to 1479.1 cm^{-1} (23 cm^{-1}) is observed. The 1502 cm^{-1} line has been interpreted as the vibration of a C–N bond and is evident in type Ib synthetic diamonds. It is tentatively assigned to the stretching mode of such a bond [3]. The 1502 cm^{-1} absorption feature may represent a transitional configuration in the formation of the nitrogen interstitial. Considering its annealing behaviour, annealing in at 650℃ with the H1a defect in type Ib diamond, maximising in intensity at approximately 750℃ and annealing out at 850℃ as the H1a defect continues to grow in intensity.

6.4.2 Annealing behaviour of H1a

Mid infrared (MIR) spectra collected at room temperature, have been taken of a type Ib diamond at various stages of annealing, shown in Figure 6-5. These spectra highlight the growth of H1a defect in ^{15}N enriched diamond to a maximum at 1400℃. In addition, it can be seen that A-centres, causing absorption at 1267 cm^{-1} in ^{15}N doped diamond (*cf.* with 1280 cm^{-1} in ^{14}N enriched diamond), appear post annealing at 1400℃. The reduced temperature of annealing required for A-centre formation has been reported to be due to vacancy enhanced migration [4, 19]. Measurements on both natural and synthetic diamond, indicate that the rate at which A-centres are formed is increased by at least a factor of 50 when first irradiated with approximately 1×10^{18} 2 MeV electrons per cm^2. Isolated nitrogen atoms were concluded to be more efficient at trapping vacancies than A-centres and the resulting NV centre would then migrate through the lattice to form the NVN defects which, when the vacancy broke away would result in an A-centre.

For sample P used in this investigation, the intensity of the resulting H1a defect has been measured post annealing at a range of temperatures (Figure 6-6). The additional absorption feature seen at 1479 cm^{-1}, the ^{15}N variant of the 1502 cm^{-1} absorption band, completely anneals out post the 800℃ treatment,

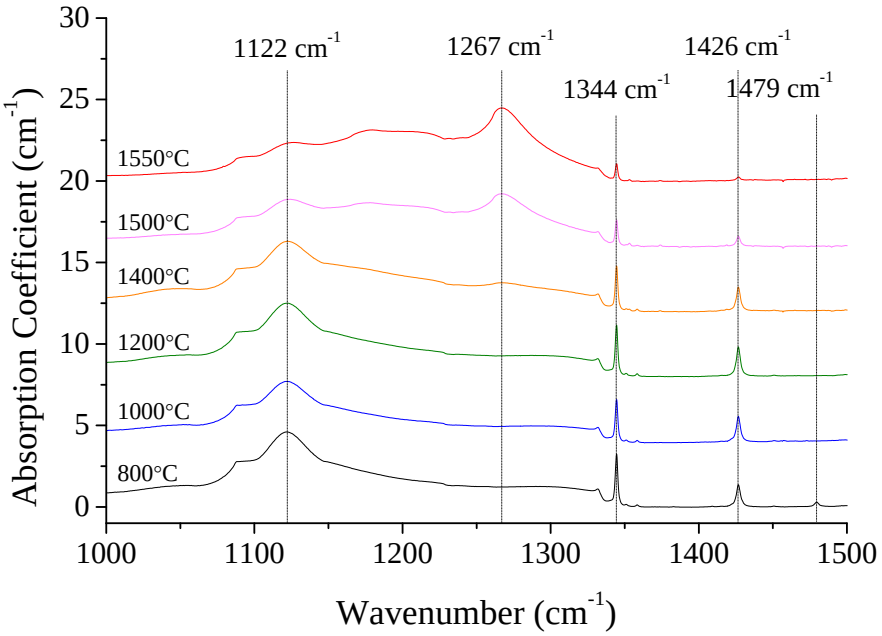

Figure 6-5: Infrared annealing spectra highlighting the growth and loss of H1a in a ^{15}N enriched diamond, with varying annealing temperatures as indicated. Each anneal was performed for four hours in a tube furnace in an oxygen free environment. For this sample, spectra pre irradiation and pre annealing at 800℃ are not available. Spectra have been offset for clarity.

broadly consistent with Figure 6-7[2].

Whilst it is generally accepted that the H1a absorption feature is seen to begin to anneal out at 1100℃ and to have completely annealed out by 1400℃, these experiments suggest values of 1200℃ and 1600℃ to be more appropriate. Near maximum intensity of the H1a defect is easily achievable without risk of graphitisation or sample damage at a temperature of 1000℃. The irradiated samples were subsequently annealed at this temperature to create the H1a defect for the uniaxial stress experiments.

Sample P used in the annealing treatment of Figure 6-6, had an initial single nitrogen concentration of 150 ppm. As the figure shows, over the period of annealing, there is deviation in the total concentration of nitrogen in the sample if the total contributions from N_S^0, N_S^+ and A-centres are considered. A near maximum

[2]Despite this data by Woods (Figure 6-7) having been presented some 26 years ago, this is the original observation of the annealing behaviour of the H1a defect, an experimental result that has not been revisited since. It is therefore important to note this result as a benchmark but also to acknowledge that in the years which have passed, developments have been made to improve the resolution of the techniques employed, the sample preparation prior to investigation and the instrumentation. Therefore, deviation from these results may exist, with new findings potentially being of improved resolution and accuracy.

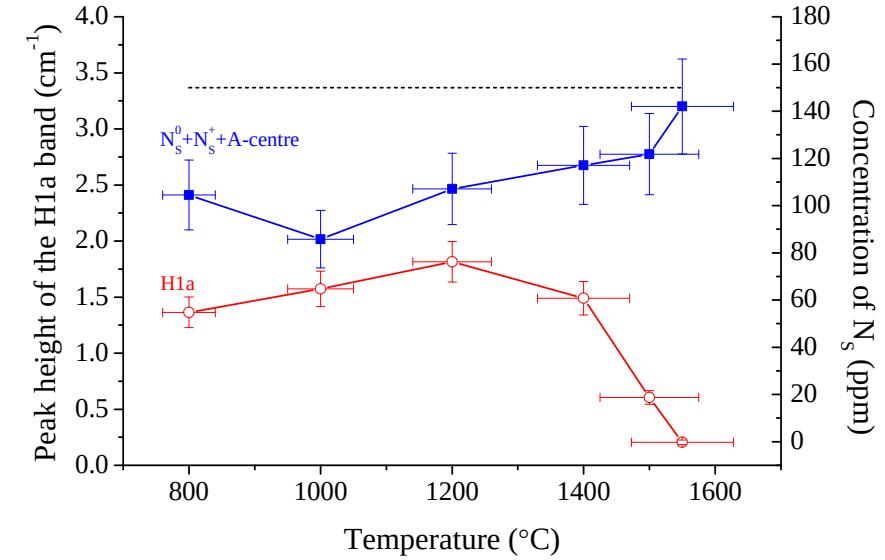

(a)

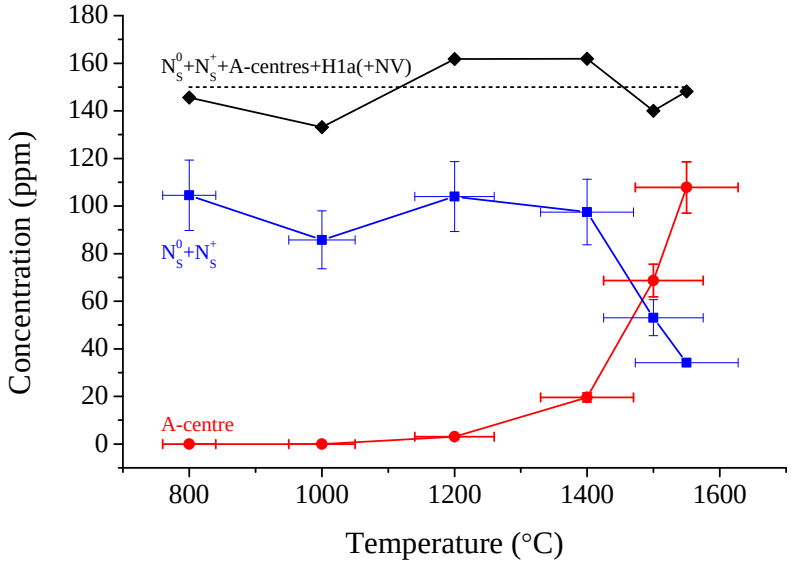

(b)

Figure 6-6: Isochronal annealing study of the H1a absorption in ^{15}N doped type Ib electron irradiated diamond (1×10^{18} 1.5 MeV). The sample was annealed for periods of four hours at increasing temperatures. H1a was stable to approximately 1200℃ after which it decreases in intensity and anneals out at approximately 1600℃. (a) illustrates the changing concentration of total nitrogen in the sample when considering only the N_S^0, N_S^+ and A-centres. The dotted line highlights the as-grown N_S^0 concentration of the sample of 150 ppm. Plotted also is the changing peak height of the H1a LVM with annealing temperature. (b) shows the increase in concentration of A-centres with a decrease in the concentration of single substitutional nitrogen centres, the rise of which is similar in shape to the decrease in the H1a LVM peak height. In addition, the total nitrogen present, considering contributions from H1a and NV is illustrated in comparison to the as-grown N_S^0 concentration (dotted line).

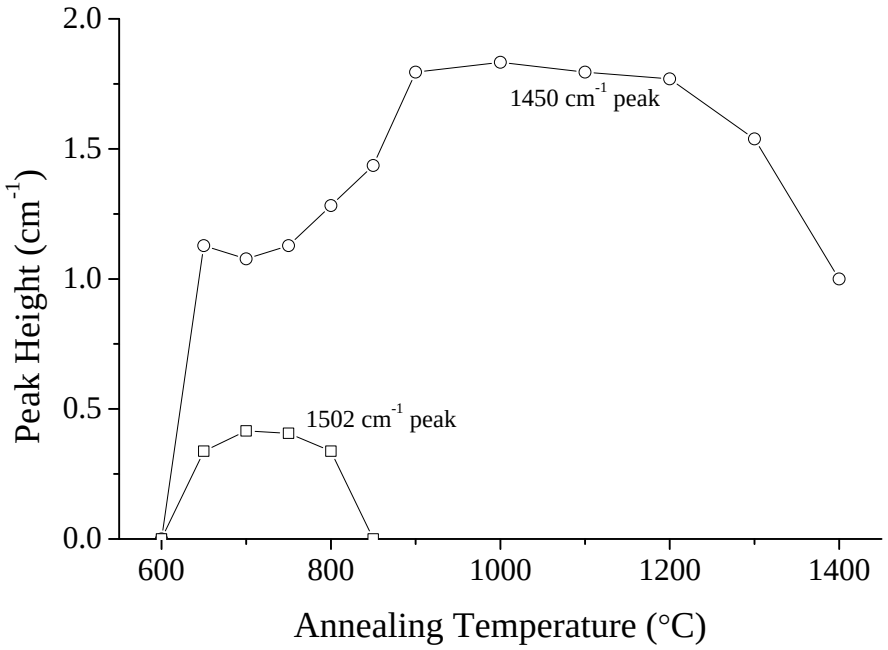

Figure 6-7: Isochronal annealing of four-hour periods of neutron irradiated type Ib synthetic diamond showing the growth and loss of the H1a defect and the 1502 cm^{-1} absorption band. The growth of the 1502 cm^{-1} band is seen to balance the initial dip in the 1450 cm^{-1} growth. This figure has been adapted from the paper by Woods [3].

value of nitrogen concentration (150 ppm) is achieved once the H1a defect has annealed out.

The irradiation of the sample will introduce equal concentrations of vacancies and interstitials into the lattice. Substitutional nitrogen will act as a sink for both these defects, leading to the formation of the nitrogen interstitial (N_I) which can then migrate and be trapped by a further substitutional nitrogen defect, forming the di-nitrogen interstitial defect (N_{2I}). Additionally, the substitutional nitrogen centre can trap a vacancy to form the nitrogen vacancy defect (NV). The annealing behaviour of the H1a and NV defects are very similar, forming at approximately 600-800℃ and annealing out at approximately 1500℃.

$$\begin{aligned} &I_{001} + N_S \rightarrow N_I \text{ and } N_I + N_S \rightarrow N_{2I} \\ &V + N_S \rightarrow NV \end{aligned} \tag{6-7}$$

It is postulated here that upon annealing between 800 and 1500 ℃, the total concentration of nitrogen, $[N]_T$, will be distributed such that:

$$[N]_T = [N_S^0] + [N_S^+] + [\text{A-centre}] + [\text{H1a}] + [\text{NV}] \tag{6-8}$$

If it is assumed that all the nitrogen present in the sample is in one of the forms quoted in Equation (6-8), the *missing* nitrogen highlighted in Figure 6.6(a) must be present in the H1a and NV defects.

By assaying the changing concentration of nitrogen with the changing intensity of H1a and NV defects, calculation of the oscillator strength of the H1a LVM can be made. It is assumed that for every interstitial created by irradiation, one H1a centre is formed containing two nitrogen atoms and that for every vacancy simultaneously produced, one NV centre containing a single nitrogen atom is created. The results indicate that for $1\,\mathrm{cm}^{-1}$ in absorption of the H1a LVM, there are 20 ppm of nitrogen in the H1a defect and a further 10 ppm in the NV defect. This would therefore indicate that the irradiation dose of 1×10^{18} 1.5 MeV electrons per cm^2 has introduced 10 ppm of vacancies and 10 ppm of interstitials into the lattice. This is slightly higher than the value published by Hunt of 7 ppm of V^0 by a dose of 1×10^{18} 2 MeV electrons per cm^2 [20]. For these irradiation conditions at a slightly lower electron energy and therefore lower production rate, the increased concentration of vacancies could be due to a reduced probability of spontaneous recombination of the vacancies and interstitials compared to a pure type IIa lattice and therefore a higher resultant concentration. It is postulated that the H1a and NV defects trap vacancies and N_S^0 defects, leading to the direct formation of A-centres.

$$\begin{aligned} \mathrm{NV} + \mathrm{N_S} &\rightarrow \text{A-centre} + \mathrm{V} \\ \mathrm{N_S} + \mathrm{V} &\rightarrow \mathrm{NV} \end{aligned} \tag{6-9}$$

$$\mathrm{N_{2I}} + \mathrm{V} \rightarrow \text{A-centre} \tag{6-10}$$

6.4.3 Uniaxial Stress Investigations of H1a

Figure 6-8 shows the experimental stress splitting data with the applied stress along the ⟨001⟩, ⟨111⟩ and ⟨110⟩ directions and also illustrates the magnitude of the shifts that result from the application of stress. The solid lines of the plot show a least squares fit of the data to the proposed transitions as determined by Kaplyanskii, Hughes and Runciman (Table 6-2) [21, 22]. In all cases, the experimentally determined features could be fitted with Lorentzian lineshapes

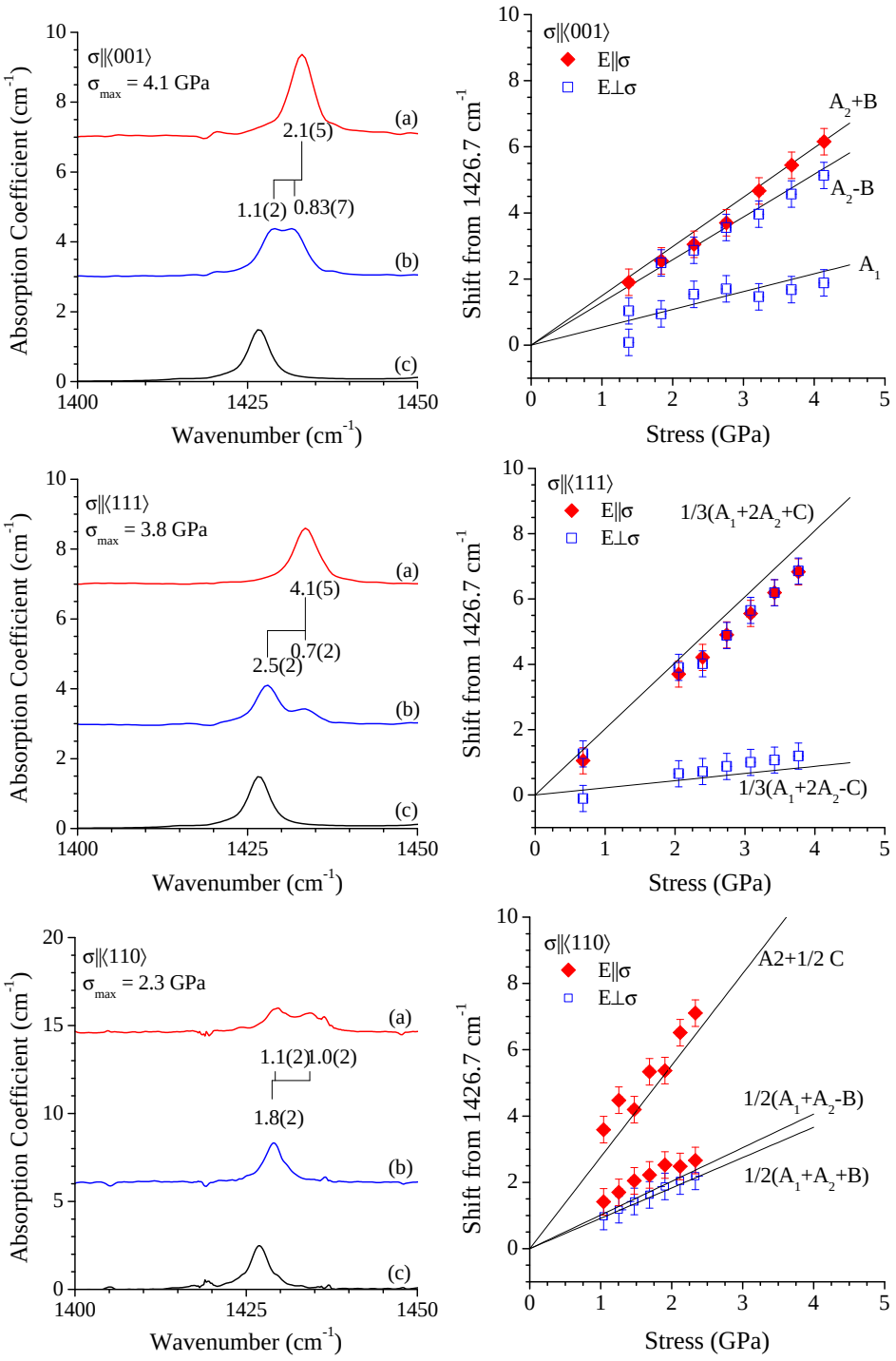

Figure 6-8: Stress induced shifting and splitting at room temperature of the H1a LVM in ^{15}N irradiated and annealed diamond (samples N and Q). The left column illustrates spectra attained at 4.1 GPa, 3.8 GPa and 2.3 GPa for $\sigma\|$ $\langle 001\rangle$, $\langle 111\rangle$ and $\langle 110\rangle$ directions respectively which have been offset for clarity. Spectra (a) and (b) in each represent the sample under stress resulting from (a) parallel and (b) perpendicular polarisation of the electric-field vector and spectrum (c) represents the unperturbed sample. The right column shows the transition frequencies as a function of stress compared to the best fit parameters from all the data for an $A \rightarrow E$ transition at a D_{2d} centre.

Table 6-2: Tabulated shifting and splitting patterns for the D_{2d} centre displaying an $A \rightarrow E$ transition, for each direction of applied stress. See also Appendix B.

Direction	**Transition Energy**	$E_{\parallel}$:$E_{\perp}$
$\sigma \parallel [001]$	$\hbar\omega + A_1\sigma$	0:1
	$\hbar\omega + (A_2 + B)\sigma$	0:1
	$\hbar\omega + (A_2 - B)\sigma$	2:0
$\sigma \parallel [111]$	$\hbar\omega + \frac{1}{3}(A_1 + 2A_2 + C)\sigma$	4:1
	$\hbar\omega + \frac{1}{3}(A_1 + 2A_2 - C)\sigma$	0:3
		E_{110}:E_{001}:$E_{1\bar{1}0}$
$\sigma \parallel [110]$	$\hbar\omega + \frac{1}{2}(A_1 + A_2 + B)\sigma$	0:2:0
	$\hbar\omega + \frac{1}{2}(A_1 + A_2 - B)\sigma$	1:0:1
	$\hbar\omega + (A_2 + \frac{1}{2}C)\sigma$	1:0:0
	$\hbar\omega + (A_2 - \frac{1}{2}C)\sigma$	0:0:1

Table 6-3: Experimental and theoretical piezospectroscopic parameters for the H1a defect compared with those found theoretically for the di-nitrogen interstitial.

Parameter	**Experimental Value**	**Theoretical Value**
A_1	+0.54(9)	+0.5(1)
A_2	+1.39(5)	+1.5(3)
B	-0.10(9)	-0.15(3)
C	+2.75(9)	+2.1(4)

and the relative intensities of these transitions for each direction of applied stress, considering both polarisations, calculated. The number, intensity and polarised absorption behaviour of the resulting transitions post the application of stress, show that the H1a absorption band is an $A \rightarrow E$ transition at a centre with D_{2d} symmetry.

For this transition at this symmetry of centre, the action of stress upon the defect can be characterised by four parameters A_1, A_2, B and C. These values are determined from the plots of the changing transition frequency with stress (Figure 6-8) and the experimental parameters are presented in Table 6-3. The most substantial experimental parameters ($^{exp}A_2$ and ^{exp}C) represent the response

Table 6-4: Calculated linear shift-rates for the E and A_1 LVMs of the ^{14}N and ^{15}N di-nitrogen interstitial model. All values are presented in units of cm^{-1} per percent strain for an [001] oriented di-nitrogen centre and are obtained using a least-squares fit to the calculated data. The errors in the fits are estimated to be less than $1\,cm^{-1}$ per percent strain.

	E		**A_1**	
Direction	**^{14}N**	**^{15}N**	**^{14}N**	**^{15}N**
[001]	−6	−6	−15	−14
[100]	−15	−15	−9	−10
	−18	−18		
[110]	−2	−2	−7	−7
	−33	−31		
[101]	−10	−10	−14	−13
	−12	−12		
[111]	−3	−3	−10	−10
	−23	−22		

and sensitivity to pseudo-hydrostatic and shear forces on the system.

6.4.3.1 Theoretical modelling of the di-nitrogen split interstitial

The experimental evidence would indicate that the H1a LVM originates from an $A \rightarrow E$ transition at a defect with D_{2d} symmetry and therefore supports the model that the H1a band originates from the di-nitrogen split interstitial. Theoretical modelling of the di-nitrogen interstitial can be used to calculate the piezospectroscopic response of the N_{2I} defect for comparison to those observed experimentally for the H1a mode.

Potential structures for the H1a centre were modelled by Goss of Newcastle University, using density-functional calculations within the local-density approximation as implemented in the AIMPRO (Ab Initio Modelling Program) code. The Brillouin-zone is sampled using the Monkhorst-Pack scheme [23], with core-electrons being eliminated using pseudo potentials. Defects are represented by periodic boundary conditions.

Deformation of the supercell under strain assumed an isotropic, homogeneous

elastic medium, characterised by Young's Modulus. For varying strains, atoms were displaced in the x, y and z directions by 0.026 Å and the resulting forces on each atom in the cell were then evaluated. The two-fold degeneracy under zero strain is raised for all strain directions except the [001] direction, for centres orientated parallel to the strain. Additional splittings occur for differently orientated centres as illustrated in Figure 6-9.

A degenerate IR active vibrational mode was calculated to occur at an energy of 1442 cm^{-1} for the $^{14}N_{2I}$ defect and at 1418 cm^{-1} for the $^{15}N_{2I}$ variant. These are in good agreement with the experimental values of 1450 cm^{-1} in ^{14}N diamond and 1426 cm^{-1} in ^{15}N diamond reported in this work for the H1a absorption band.

The strain response was subsequently calculated for the di-nitrogen split interstitial, two-fold degenerate model and shift rates evaluated (Table 6-4).

From these strain parameters, theoretical piezospectroscopic parameters can be calculated for the di-nitrogen split interstitial structure (Table 6-3). Theoretical and experimental parameters are in excellent agreement. This therefore presents the di-nitrogen interstitial model (Figure 6.2(c)) to be the most plausible structure for the H1a LVM at 1450 cm^{-1} for ^{14}N diamond (1426 cm^{-1} in ^{15}N enriched diamond).

In addition to the E-mode attributed to the H1a vibration, theory also predicts other vibrational modes associated with this structure. Of these, the only one calculated to lie above the diamond zone centre optical phonon at 1332 cm^{-1} is an A_1-mode, related to a stretch along the N–N axis (Figure 6.10(c)). This A_1-mode is IR inactive, such that the vibrational mode is not associated with changes in the induced electric-dipole. In contrast to the H1a vibrational mode, the A_1-mode would display a mixed-isotope splitting, characteristic of two nitrogen atoms (1830 cm^{-1} : 1800 cm^{-1} : 1768 cm^{-1} ≡ ^{14}N–^{14}N : ^{14}N–^{15}N : ^{15}N–^{15}N) [17]. Detection of these vibrational modes may be possible by Raman spectroscopy. Neutron irradiation and annealing could maximise the intensity of these transitions, potentially making them strong enough to observe. The predicted parameters associated to these modes are listed in Table 6-4.

Other modes may exist for the di-nitrogen split interstitial. For example, a mode representing the two nitrogen atoms vibrating in union, B_2, would be IR ac-

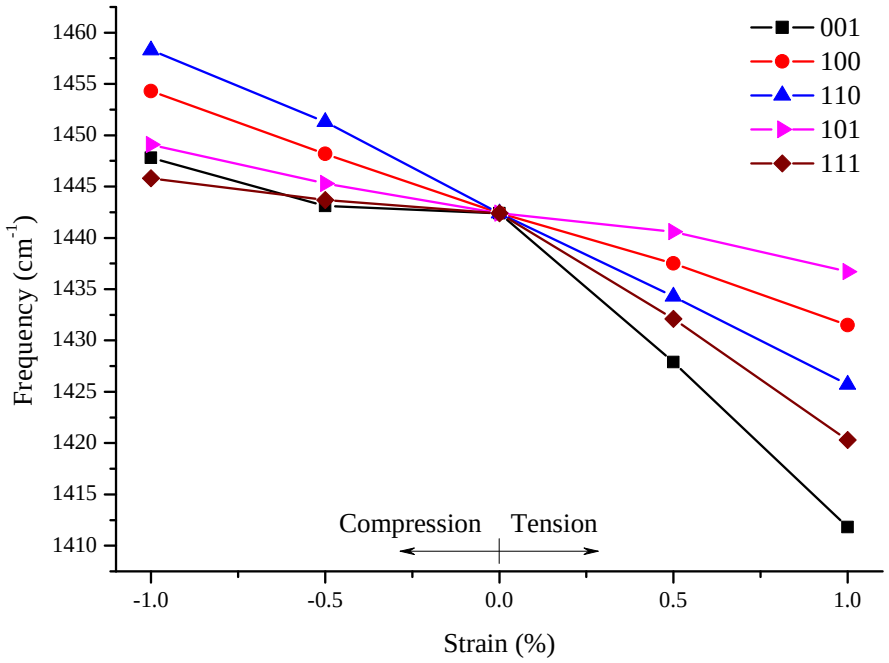

(a)

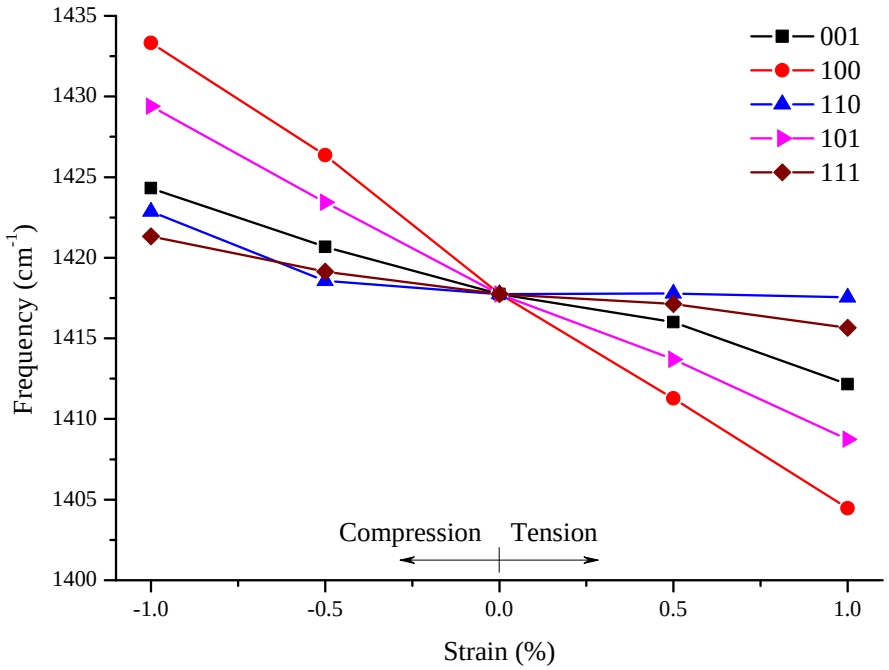

(b)

Figure 6-9: Theoretical frequency shifts of the di-nitrogen interstitial as a function of strain along high symmetry directions for the interstitial N_{2I} for (a) ^{14}N and (b) ^{15}N enriched diamond.

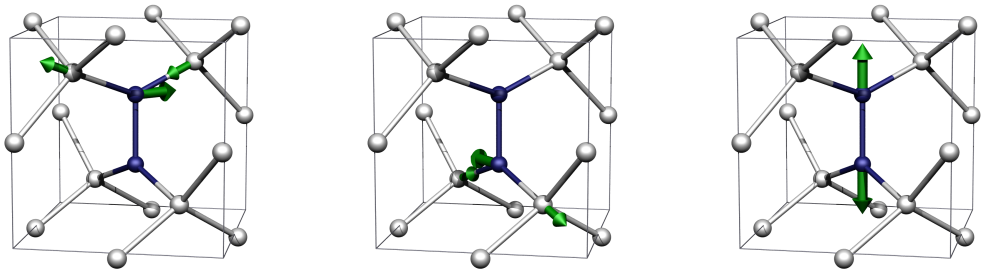

(a) (b) (c)

Figure 6-10: Proposed normal modes of the di-nitrogen split-interstitial [24]. (a) and (b) show the two components of the E-mode assigned to H1a, and (c) the A_1, IR-inactive mode. The central two blue atoms are nitrogen and the cube of side length a_0, indicates the lattice cubic direction. The arrow shows the displacements during the modes of vibration, their lengths indicating relative amplitude on different atom sites.

tive. Modelling however, predicts this to occur at a frequency less than 1332 cm^{-1}, which would therefore be resonant with the one-phonon band and subsequently broad and undetectable.

6.5 Conclusions

The structure and stability of the mode of vibration attributed to H1a has been reviewed here. Isotopic substitution studies have confirmed the previous results that nitrogen is in involved is the defect giving rise to the 1450 cm^{-1}/1426 cm^{-1} LVM in ^{14}N/^{15}N enriched diamond. This supports data previously presented in literature, which have to date, caused confusion in the assignment of the structure attributed to H1a. In addition, the annealing behaviour has been reviewed and it is the conclusion of this work that H1a has been shown to anneal in in irradiated synthetic type Ib diamond at a temperature between 600 and 800℃, maximising at 1200℃ and anneal out at temperatures greater than 1550℃.

Annealing studies have also identified a significant deficit between the total concentration of nitrogen initially measured in the sample and that measured post each annealing stage between 800 and 1550℃. This has identified the H1a defect to be an important sink for nitrogen during annealing. Considering nitrogen as a major sink for vacancies and interstitials, it is the conclusion of this work that

the H1a and NV centres will be the prominent defects accounting for this nitrogen deficit. By assaying the concentration of nitrogen and considering the contribution from these defects, it is calculated that 1 cm^{-1} absorption at the H1a LVM is equal to 20 ppm of nitrogen in the di-nitrogen interstitial centre.

There may be a number of mechanisms responsible for the annealing out of the H1a defect and it is postulated that there is a direct contribution of H1a to the growth of A-centres during annealing.

$$\begin{aligned} N_{2I} + NV &\rightarrow N_S + [N_S - N_S] \\ N_{2I} + V &\rightarrow [N_S - N_S] \\ N_{2I} &\rightarrow N_S + N_S \\ N_{2I} &\rightarrow N_S + N_I \end{aligned} \tag{6-11}$$

Energetically, it seems unlikely that the H1a defect would dissociate into two substitutional nitrogen atoms because of the strain energy required to accommodate the electron in the anti-bonding orbital. More probable and in agreement with evidence of this research, is that a vacancy migrates to the H1a defect, relaxing the di-nitrogen interstitial structure into an A-centre, with both nitrogen atoms occupying lattice sites.

A combination of atomistic modelling and experimental uniaxial stress studies have been used to probe the vibrational nature of the defect and gain an insight into its structure. The data presented here indicates the H1a absorption band to originate from a doubly degenerate local vibrational mode ($A \rightarrow E$ transition) with D_{2d} symmetry. Stress splitting parameters have been calculated and presented, which highlight the centre's sensitivity to shear forces.

Atomistic modelling has permitted the simulation of the di-nitrogen split interstitial defect under strain. The energy of the E-mode of this centre and that seen experimentally for both the ^{15}N and ^{14}N combinations of this defect, are in excellent agreement. From this, theoretical parameters characterising the centre's piezospectroscopic behaviour have been calculated, which have been shown to be in excellent agreement with those determined experimentally. This leads to the conclusion that the $\langle 001 \rangle$ di-nitrogen split interstitial (N_{2I}) defect, is the only plausible model for the centre responsible for the H1a mode, where the mode of vibration is as illustrated in Figure 6.10(a) and Figure 6.10(b). In addition, the-

ory has proposed an infra-red inactive but Raman active A_1 N_I–N_I stretch mode for the N_{2I} defect. It is predicted that this will display mixed-nitrogen isotope splitting and stress induced splitting resolvable under uniaxial stress.

The result of this work encourages the calculation of piezospectroscopic parameters for other vibrational modes of a plethora of defects in diamond. This is essential in associating vibrational modes originating from different transitions of the same defect, to the correct atomistic model. From the study of this defect specifically, it is now a challenge to identify and probe the other associated modes of this centre with photoluminescence spectroscopy.

This work has been published in Physical Review B [24].

6.6 Further work

The research presented here could be extended to investigate a number of areas. Greater information is required with regards to the nitrogen deficit that is observed in samples when annealing between 800 and 1500℃ and additional techniques are required to identify and quantify the nitrogen content of NV. Simultaneously, evidence of any other nitrogen related defects should be watched for.

An alternative investigation would be to substantially increase the damage caused by irradiation. If the concentration of vacancies became comparable to the concentration of nitrogen in the diamond, for example by neutron irradiation, maximising the formation of the H1a defect into what complexes do the remaining irradiation damage defects migrate?

Thirdly, investigations could be performed to identify the A_1 Raman active mode. Work could consider locating a transition which displayed comparable annealing behaviour to the H1a IR mode and demonstrating a mixed-isotope splitting of a transition in ^{15}N enriched diamond.

References

[1] C. D. Clark, R. W. Ditchburn, and H. B. Dyer, Proceedings of the Royal Society of London Series A **237**, 75 (1956).

[2] I. Kiflawi, A. Mainwood, H. Kanda, and D. Fisher, Physical Review B **54**, 16719 (1996).

[3] G. S. Woods, Philosophical Magazine B **50**, 673 (1984).

[4] A. T. Collins, Journal of Physics C: Solid State Physics **13**, 2641 (1980).

[5] W. A. Runciman and T. Carter, Solid State Communications **9**, 315 (1971).

[6] C. D. Clark, R. W. Ditchburn, and H. B. Dyer, Proceedings of the Royal Society of London Series A **234**, 363 (1956).

[7] G. S. Woods and A. T. Collins, Journal of Physics C: Solid State Physics **15**, L949 (1982).

[8] G. Davies, S. C. Lawson, A. T. Collins, A. Mainwood, and S. J. Sharp, Physical Review B **46**, 13157 (1992).

[9] G. Davies and M. E. R. Hamer, Proceedings of the Royal Society of London Series A **348**, 285 (1976).

[10] G. Davies, Journal of Physics C: Solid State Physics **12**, 2551 (1979).

[11] S. Felton, A. M. Edmonds, M. E. Newton, P. M. Martineau, D. Fisher, and D. J. Twitchen, Physical Review B **77**, 081201 (2008).

[12] S. Felton, A. M. Edmonds, M. E. Newton, P. M. Martineau, D. Fisher, D. J. Twitchen, and J. M. Baker, Physical Review B **79**, 075203 (2009).

[13] S. Felton, B. L. Cann, A. M. Edmonds, S. Liggins, R. J. Cruddace, M. E. Newton, D. Fisher, and J. M. Baker, Journal of Physics: Condensed Matter **21**, 364212 (2009).

[14] G. A. Watt, M. E. Newton, and J. M. Baker, Diamond and Related Materials **10**, 1681 (2001).

[15] R. C. Burns, V. Cvetkovic, C. N. Dodge, D. J. F. Evans, M. T. Rooney, P. M. Spear, and C. M. Welbourn, Journal of Crystal Growth **104**, 257 (1990).

[16] M. E. Newton, B. A. Campbell, D. J. Twitchen, J. M. Baker, and T. R. Anthony, Diamond and Related Materials **11**, 618 (2002).

[17] J. P. Goss, P. R. Briddon, S. Papagiannidis, and R. Jones, Physical Review B **70**, 235208 (2004).

[18] C. V. H. Strömann, F. Tshishikhawe, J. O. Hansen, and R. C. Burns, *Synthesis of diamond* (2006), European Patent WO2006/061672 A1.

[19] B. P. Allen and T. Evans, Proceedings of the Royal Society of London Series A **375**, 93 (1981).

[20] D. Hunt, PhD. thesis, St. Peter's College, University of Oxford (1999).

[21] A. Kaplyanskii, Optics and Spectroscopy **16**, 329 (1964).

[22] A. E. Hughes, Proceedings of the Physical Society **87**, 535 (1966).

[23] H. J. Monkhorst and J. D. Pack, Physical Review B **13**, 5188 (1976).

[24] S. Liggins, M. E. Newton, J. P. Goss, P. R. Briddon, and D. Fisher, Physical Review B **81**, 085214 (2010).

Chapter 7

Hydrogen Related Defects in Diamond

The aim of this chapter is to further the understanding of the incorporation of hydrogen into diamond and the influence of annealing on these defects. Of key interest are the 3107, 3123 and 3324 cm^{-1} absorption features.

7.1 Introduction and motivation

Like nitrogen, hydrogen is a common impurity in synthetic, chemical vapour deposition (CVD) grown diamond. It is typically the most abundant atom in the gas phase for CVD growth. Hydrogen can be present in concentrations up to 1 at.% in some natural [1, 2] and polycrystalline CVD diamond [3] and whilst optical and magnetic spectroscopic techniques can be used to assign spectra to specific hydrogen related structures such as the 3107, 3123 and 3324 cm^{-1} absorption bands, conclusive results regarding structure have yet to be achieved.

7.2 A review of hydrogen related defects

7.2.1 The 3107 cm^{-1} absorption band

One of the most commonly reported hydrogen related defects is the absorption band at 3107 cm^{-1} (and bending mode at 1405 cm^{-1}), first observed by Chrenko *et al.* [4–13]. Seen in natural and high-temperature annealed synthetic (high-pressure high-temperature (HPHT) and CVD) type I diamond, this centre is exceptionally stable, requiring HPHT conditions for its formation and remaining stable at tem-

peratures greater than 1700℃ [8, 12, 14]. The distribution of these defects has been found to be inhomogeneous in natural type Ia diamond [8, 15] and furthermore, in natural diamond, similar HPHT annealing conditions can both generate and remove the absorption band, indicating its strong sensitivity to other defects present within the lattice [8].

The strength of this absorption band has also been shown to correlate with the concentration of nitrogen present in the lattice [7, 13, 16]. ^{12}C:^{13}C isotopic substitution experiments confirm that the 3107 cm^{-1} absorption band originates from a C–H stretch vibration, indicating a shift in the absorption band to 3098 cm^{-1} [6, 17]. No shift is seen when similar experiments are performed with ^{14}N and ^{15}N enriched samples [7, 10]. It is generally acknowledged in the literature that the band arises from a C–H vibration and it is assumed that nitrogen is involved in the defect but the dependence of the 3107 cm^{-1} LVM's intensity on a particular aggregate of nitrogen is still debated.

Uniaxial stress investigations by Runciman *et al.* and Davies *et al.* had been unable to resolve any sensitivity of the 3107 cm^{-1} transition to the application of uniaxial stress, therefore failing to propose a model for the symmetry of the associated defect. Cruddace observes a resolvable and sizable splitting of the transition by infrared spectroscopy [18]. At 1.35 GPa in the ⟨001⟩ direction, a single transition is observed, which shifts very little when stressed but under stress applied in the ⟨111⟩ direction, the transition splits into two when the electric field vector is polarised parallel to the direction of stress and remains a single line when polarised perpendicular. This result is indicative of the 3107 cm^{-1} band arising from an $A \rightarrow A$ transition at a trigonal centre.

The 1405 cm^{-1} absorption band is a secondary line found to accompany the 3107 cm^{-1} mode in spectra. Attributed to a C–H bending mode, it sits close to the one-phonon frequency of diamond and subsequently has a weak interaction with the one-phonon modes [17]. Correlation between the 3107 cm^{-1} and 1405 cm^{-1} absorption intensities has been noted, resulting in the assignment of the two absorption bands to the same defect [6]. Uniaxial stress experiments by Cruddace, concluded this mode to originate from an $A \rightarrow E$ transition at a trigonal centre.

7.2.2 The 3123 cm^{-1} absorption band and the NVH defect

The 3123 cm^{-1} band is routinely observed in nitrogen doped, CVD grown diamond [19, 20]. Isotopic substitution experiments with deuterium identified the centre to involve one hydrogen atom. The transition *disappeared* in the deuterium enriched sample, the conclusion being that the absorption band shifted to beneath the strong two-phonon absorption of diamond, resulting in lifetime broadening of the line [10, 21]. Experiments considering isotopic substitution with ^{15}N and ^{14}N enriched samples, gave no evidence of a shift in the transition frequency, concluding there to be no involvement of nitrogen in the vibration. Finally, substitution of ^{12}C with ^{13}C, induced a red frequency shift of 6 cm^{-1} and confirmed the assignment of the vibration to a C–H mode.

Cruddace correlated the 3123 cm^{-1} absorption band with the NVH^- defect observed by EPR [18] and by uniaxial stress, identified the mode to originate from an $A \rightarrow A$ transition at a monoclinic I defect. The NVH^- defect is commonly observed in single crystal CVD diamond but no reports exist of its observation in natural or HPHT synthetic material. EPR has identified the defect to have C_{3v} symmetry [22] and it has been shown that in the NVH^- EPR centre, the hydrogen atom tunnels between configurations where it is bonded to one of the three carbon atoms surrounding the vacancy (Figure 7-1) [23]. On the EPR timescale, the motion can be observed but it is sufficiently slow on the timescale of optical absorption measurements that C_{1h} (monoclinic I) symmetry is observed. Thus, the 3123 cm^{-1} local vibrational mode has the correct symmetry to be assigned to the NVH defect but with these data alone, it could be attributed to either the neutral NVH^0 (IR active, EPR inactive) or negative NVH^- (IR inactive, EPR active) charge state. It must be noted that NVH^+ is not expected in nitrogen doped diamond but could be present in material with a high concentration of shallow acceptors.

Charge transfer investigations highlighted that after heat treatment at 850 K, the absorption line at 3123 cm^{-1} was no longer visible and yet it was maximised post illumination with UV light [24]. The inverse was seen with the concentration of the NVH^- EPR defect. The intensity of the 3123 cm^{-1} absorption line was seen to fall with increasing treatment temperature between 300 K and 850 K as

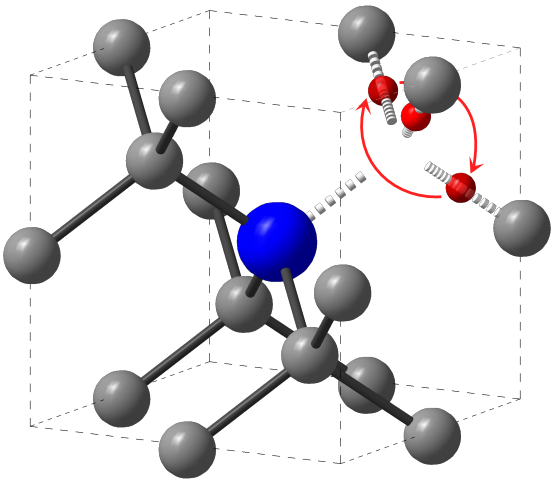

Figure 7-1: A schematic of the NVH defect. The largest, blue atom represents the presence of nitrogen in the defect structure. The smallest, red atom tunnels between the three potential monoclinc I configurations, with a lifetime in each position of τ. The time averaged position of these three is therefore one with the hydrogen atom in plane with the nitrogen atom and carbon atom, giving C_{1h} symmetry.

the concentration of NVH^- increased. This suggested a correlation between the change in the concentration of NVH^- and a change in the intensity of the 3123 cm^{-1} line. Cann concluded that based on the assumption that $\Delta NVH^- = -\Delta NVH^0$ and that the NVH^0 defect was the only contributor to the 3123 cm^{-1} line, a correlation for the concentration of NVH^0 from the intensity (I) of the 3123 cm^{-1} could be made (Equation (7-1)).

$$[NVH^0]_{ppb} = 330(30)\ \text{ppb cm}^2\ \times I_{3123\,\text{cm}^{-1}} \tag{7-1}$$

Cann was unable to identify which of the additional absorption features in the C–H stretch mode region of the infrared spectrum were attributable to the NVH^- defect [24]. Kerridge *et al.* predicted through modelling that the properties of the hydrogen-like nucleus of the defect would remain largely unchanged by a change in its charge state and hence the local electron density would remain constant [25]. Therefore, the symmetry of both charge states would be the same and the tunnelling rates for the two defects should be similar.

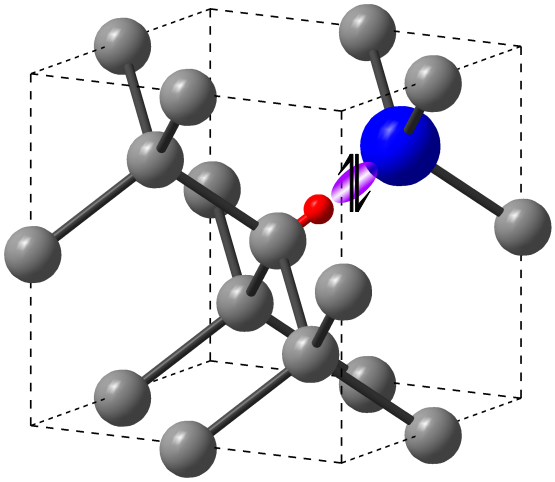

Figure 7-2: A schematic of the proposed 3107 cm^{-1} defect, N:H–C.

7.2.3 The hypothesised N:H–C defect

One final defect to note in preparation for the results of this chapter, is the N:H–C defect (Figure 7-2). In Goss's review of hydrogen in diamond, he proposes a hydrogen-nitrogen complex with a stretch mode at 3324 cm^{-1} [26]. This mode should shift by 6 cm^{-1} upon the substitution of ^{12}C with ^{13}C and by 910 cm^{-1} in deuterium doped samples. There would be a negligible shift upon the substitution of ^{14}N with ^{15}N. It is concluded therefore that the vibration arises from the hydrogen and carbon bond. The complex possesses a filled level in the band gap and therefore is electrically stable and will not display photochromic behaviour.

The proposed method of formation is by N_S^0 acting as a trap for hydrogen. The relaxed structure in the N_S^0 defect results in one very long N–C bond, of the order of 1.9 Å [27]. The hydrogen atom may then insert itself into this N–C bond and as it does, the interactions between this orbital and the hydrogen 1s orbital overlap, forming the C–H bond. The hydrogen electron pairs with the dangling orbital on the carbon atom and the nitrogen lone-pair electrons destabilise because of the interaction between the C–H σ bond and the nitrogen lone pair. This results in a doubly filled band-gap orbital [27]. Studies in similar materials such as silicon, have identified that hydrogen will bind to the host atom rather than the donor impurity [28].

Tentative assignment of the N:H–C defect to the observed 3107 cm^{-1} mode, as a result of thermal stability investigations has been made [18]. However, both the

3107 cm^{-1} and 3324 cm^{-1} features in the C–H stretch region of the IR spectrum have the correct trigonal symmetry for the assignment to the N:H–C structure. Therefore, this assignment needs to be questioned.

This chapter aims to answer the following:

- What is the annealing behaviour for the production of the 3107 cm^{-1} defect in CVD diamond and how does the initial concentration of nitrogen in the diamond influence its intensity?
- Does theoretical modelling of the N:H–C defect match the experimental evidence for the 3107 cm^{-1} defect or is this an inaccurate assignment? If the proposal is incorrect, what is the true structure of this defect and is the 3324 cm^{-1} band the true optical analogue for the N:H–C defect?
- Having identified the 3123 cm^{-1} absorption feature as the NVH^0 defect, what is its oscillator strength and can an optical analogue for the NVH^- defect be found?

7.3 Experimental detail

Experimental work for this chapter has taken a number of forms, many of which are outlined in Chapter 4. In addition and discussed below, are the processes of charge transfer experiments and HPHT annealing.

7.3.1 Charge transfer experiments between defects

A SC-CVD grown diamond, with a concentration of 2.6(4) ppm of N_S^0 as determined by EPR was used. The change in concentration of the NVH^- defect, as detected by EPR, was compared to the change in intensity of the 3123 cm^{-1} absorption band, as observed in IR spectroscopy at 4 cm^{-1} resolution. The change in concentration of these defects was stimulated through isochronal heat treatments in the range of 450 K to 800 K, at 50 K intervals.

The sample was first illuminated for 10 minutes with a 200 W HgXe arc lamp. IR and EPR spectra were then taken. The sample was then treated at incremental temperatures for 10 minutes. After heating, the sample was rapidly quenched to

lock the defect concentrations. From the initial heat treatment, until the final heat treatment at 800 K, the sample was kept in a dark environment.

For the correlation between intensity and concentration, additional SC-CVD and HPHT grown samples were considered.

7.3.2 HPHT annealing

A series of SC-CVD samples were used, all cut from the same original diamond. The total concentration of N_S^0, as measured by EPR for these samples, was of the order of 12(2) ppm. Each sample was annealed for 30 minutes with a stabilising pressure of 6.6 GPa at temperatures of 1500, 1700, 1900, 2100 and 2300℃. Samples were then removed, cleaned and analysed by infrared spectroscopy.

Further details of HPHT treatments can be found in §4.1.1.

7.4 Results and analysis

7.4.1 The 3123 cm^{-1} absorption line and the NVH defect

Figure 7-3 shows how the complex EPR spectrum attained over the g=2 region for this sample can be deconvolved. The component spectra are from the N_S^0 and the NVH^- defects, the latter of which has been modelled to consider the effects of the motional averaging of the hydrogen atom. Figure 7-4 shows that as the isochronal annealing temperature is increased, the intensity of the 3123 cm^{-1} absorption feature decreases. The concentration of NVH^- is seen to increase, calculated from the doubly integrated intensity of the deconvolved NVH^- spectrum observed by EPR.

The 3123 cm^{-1} absorption band shows a significant change in the intensity from a maximum post illumination, to an intensity indeterminable by infrared spectroscopy after heating at 800 K for 10 minutes. The intensities of lines at 2727, 2807 and 2916 cm^{-1}, are also seen to increase on annealing at 800 K.

The relation between the variations with isochronal annealing temperature in the intensity of the 3123 cm^{-1} band and the concentration of the NVH^- defect are shown in Figure 7-5. The solid curves show simultaneous fits to the intensity of

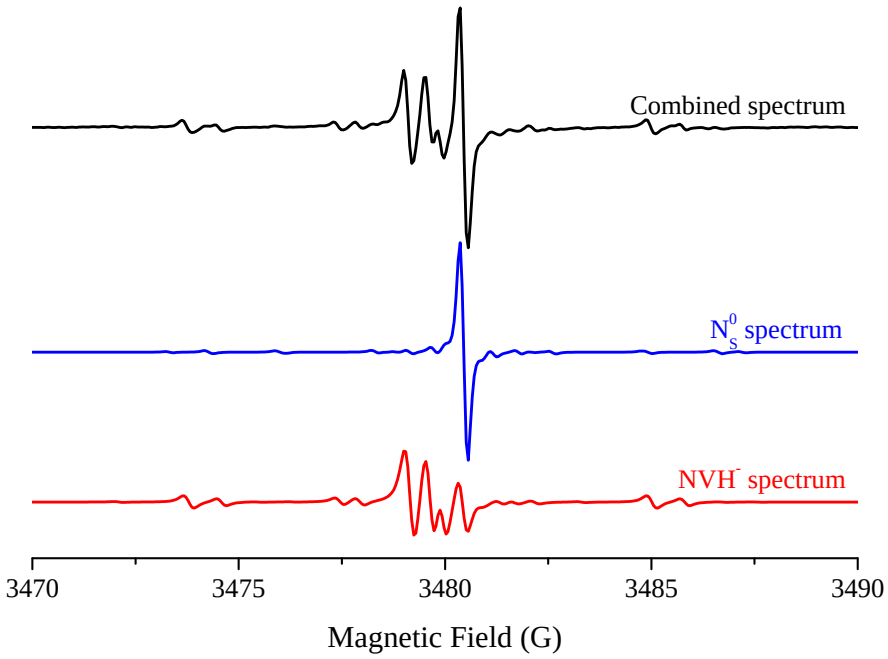

Figure 7-3: A deconvolution of the room temperature EPR spectrum taken post heat treatment at 700 K. The upper spectrum indicates the combined theoretical spectrum, the central spectrum, the contribution from the P1 (N_S^0) defect and the lower spectrum, the contribution of the NVH^- defect considering motional averaging of the hydrogen atom.

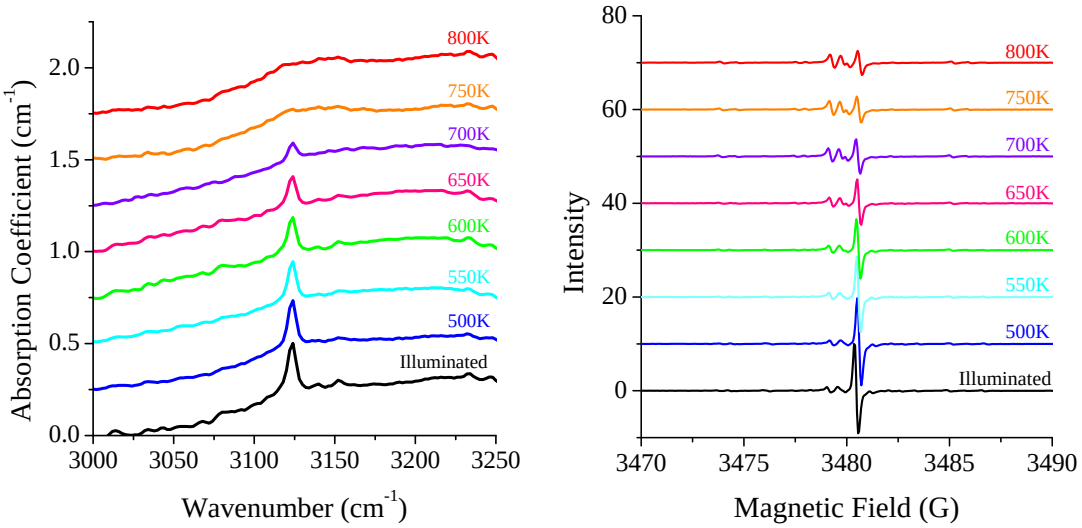

Figure 7-4: A graphical illustration of (a) the decay of the 3123 cm^{-1} absorption band with increased isochronal annealing temperature and (b) the growth in the intensity of the NVH^- spectrum. A clearer insight into the contribution to the EPR spectra from the NVH^- defect can be seen in Figure 7-3. All spectra were collected at room temperature and have been offset for clarity. The lowest of the lines represents the results post illumination with temperature increasing with higher stacked spectra from 500 K to 800 K at 50 K intervals.

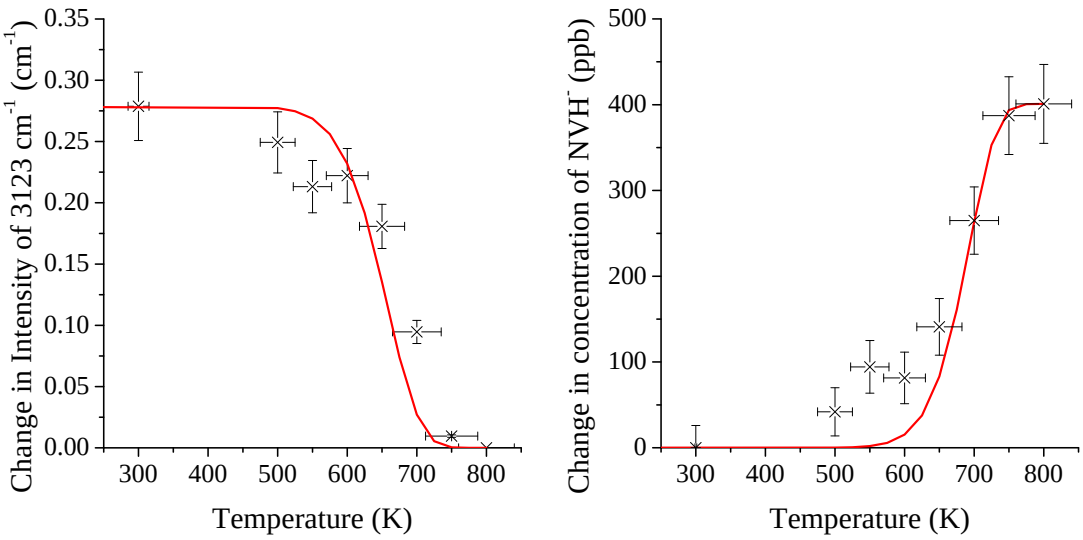

Figure 7-5: Graphs illustrating a change in (a) the 3123 cm^{-1} absorption band and (b) the concentration of the NVH^- defect with treatment temperature. The lines of fit represent a process following first order kinetics.

the 3123 cm^{-1} LVM and the concentration of NVH^- defect. This assumes that one is converted into the other in a process governed by first order kinetics.

Comparing the change in intensity of the 3123 cm^{-1} absorption band using spectra taken at 4 cm^{-1} resolution, with the increase in concentration (Figure 7-6), this work proposes a new correlation value of:

$$[NVH^0]_{ppb} = 200(15)\,ppb\,cm^2 \times I_{3123\,cm^{-1}} \quad (7\text{-}2)$$

$$= 1400(150)\,ppb\,cm \times H_{3123\,cm^{-1}} \quad (7\text{-}3)$$

where $I_{3123\,cm^{-1}}$ is the integrated intensity of the 3123 cm^{-1} LVM and $H_{3123\,cm^{-1}}$ is the peak height of the LVM. This number is significantly less than that reported by Cann [24]. The values presented here are the result of a study using more samples and a greater number of data points from each, in terms of the number of heat treatments performed. It is therefore considered to be more accurate.

As Figure 7-7 shows, changing resolution has a significant effect on the peak height of the 3123 cm^{-1} absorption band. The intensity of the band remains constant within error but if the correlation for height is used, the additional conversion factor illustrated in Table 7-7, needs to be considered.

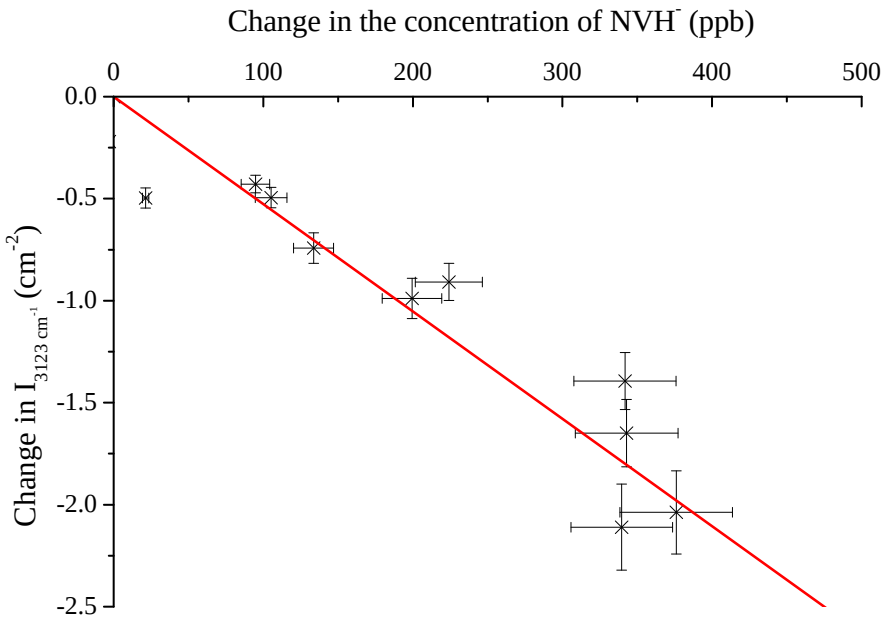

Figure 7-6: Graphical illustration of the relation between the 3123 cm^{-1} defect and NVH^- showing an inverse correlation. Assuming $\Delta\mathrm{NVH}^- = -\Delta\mathrm{NVH}^0$ and that the NVH^0 defect is the only contributor to the 3123 cm^{-1} LVM, then $[\mathrm{NVH}^0]_{\mathrm{ppb}} = 200(15)\,\mathrm{ppb\,cm^2} \times I_{3123\,\mathrm{cm}^{-1}}$ at 4 cm^{-1} resolution.

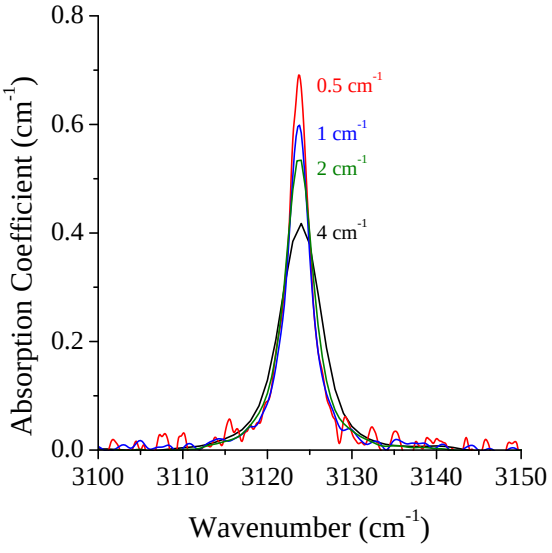

Resolution (cm^{-1})	Factor
0.5	0.64(9)
1	0.73(10)
2	0.79(11)
4	1.00(13)

Figure 7-7: The effect of changing resolution on the 3123 cm^{-1} LVM. The graph indicates how significantly a change in resolution effects the lineshape, with the table stating correction factors for the calculation of concentration. For example, a scan made at 1 cm^{-1} resolution indicates a peak height of 3 cm^{-1} at 3123 cm^{-1} indicating a concentration of $0.73 \times 3 \times 1400 = 3$ ppm.

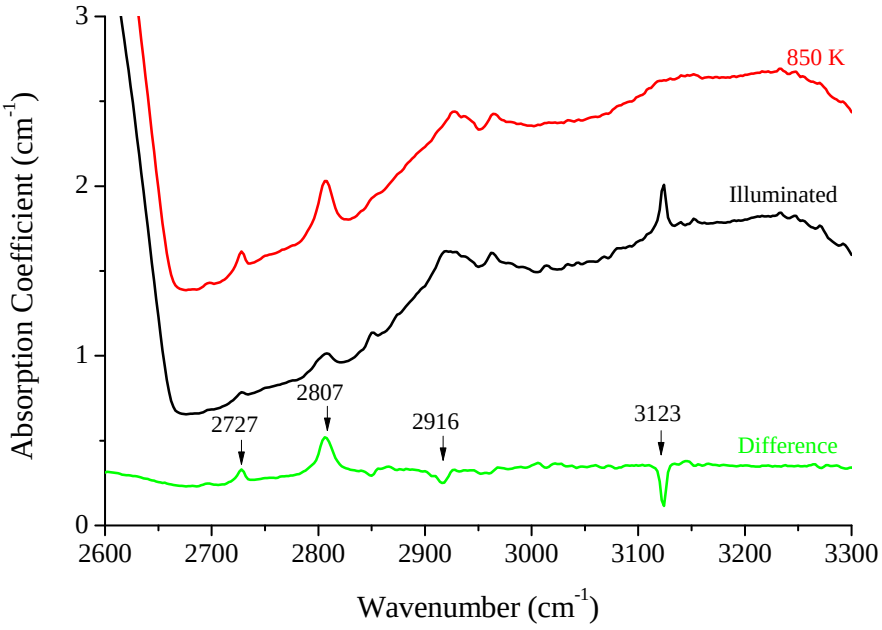

Figure 7-8: Absorption bands in the C–H stretch region of the infrared spectrum which demonstrate photo-/thermo- chromic effects. Key bands to note are the 2727, 2807, 2916 and the 3123 cm^{-1} absorption lines.

7.4.1.1 Possible optical analogues of the NVH^- defect

Identification of the 3123 cm^{-1} local vibrational mode with the NVH^0 defect, now leaves the challenge of identifying the optical analogue of the local vibrational mode associated with the NVH^- centre. Two significant lines which display appropriate photo-/thermo- chromic behaviour occur at 2727 and 2807 cm^{-1} (Figure 7-8).

Figure 7-9 illustrates the relation between the peak heights of both the 2727 and 2807 cm^{-1} absorption features and the concentration of the NVH^- defect as determined by EPR. Both graphs are fitted with a linear relation which passes through the origin, in an attempt to derive an oscillator strength for the transition. For the 2727 cm^{-1} mode, a relation of 5400(370) ppb per cm^{-1} was calculated, compared to 1800(100) ppb per cm^{-1} for the 2807 cm^{-1} absorption line. This result is not sufficient to identify which correlates best with the NVH^- defect.

In addition, it is known that NVH^- and NVH^0 will have the same symmetry [25]. Uniaxial stress spectra of the 2727 cm^{-1} and 2808 cm^{-1} lines are inconclusive (Figure 7.10(b)). Neither absorption line shows a resolvable stress induced splitting or shifting at stresses of the order of 3 GPa. No conclusive assignment

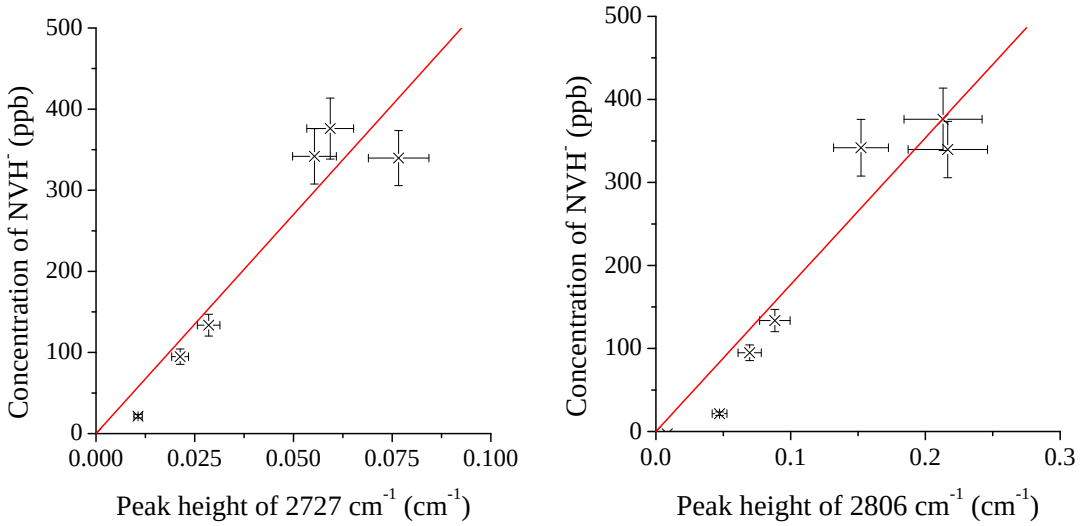

Figure 7-9: The intensity of potential optical analogues with regards to the concentration of the NVH^- defect as observed in EPR. (a) displays the relation for the absorption line at 2727 cm^{-1} and (b) the relation for the 2807 cm^{-1} line. Both graphs have been fitted with a linear relation passing through the origin, to derive a potential oscillator strength for the transition. (a) gives a gradient of 5400(370) ppb per cm^{-1} and (b) a gradient of 1800(100) ppb per cm^{-1}.

can therefore be made based on the evidence of this investigation.

7.4.2 HPHT treatment of the 3107 cm^{-1} absorption band

The 3107 cm^{-1} absorption band has been shown in this work to anneal in at temperatures greater than 1700℃ (Figure 7-11). With the annealing programme completed here, the band is continuing to grow even after annealing at 2300℃.

As well as a significant growth in the intensity of the 3107 cm^{-1} absorption band, there are several other changes in this region of the mid-infrared spectrum. The as-grown CVD material initially shows substantial intensity at 3123 cm^{-1} and 3324 cm^{-1}. As these two lines anneal out, lines at 3033 and 3395 cm^{-1} appear. The 3033 cm^{-1} band appears to be relatively stable to high temperatures, annealing out at 2300℃, where as the 3395 cm^{-1} line disappears after annealing at 1700℃. Lines at 3107 cm^{-1} and 3313 cm^{-1} begin to grow post annealing at 1700℃, with 3107 cm^{-1} continuing to grow after higher temperature anneals (Figure 7-11). The 3313 cm^{-1} feature appears to reach a maximum at 2100℃ but is still present at 2300℃.

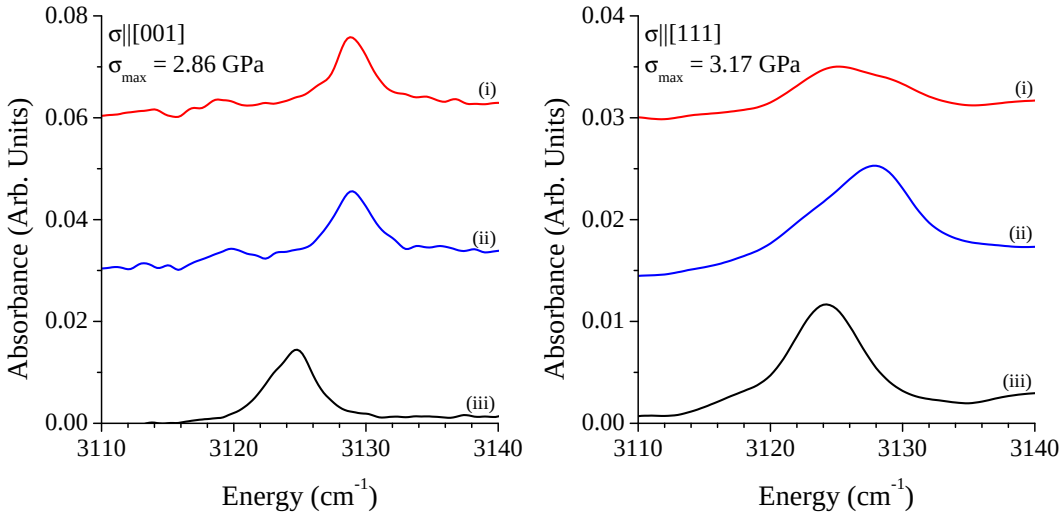

(a)

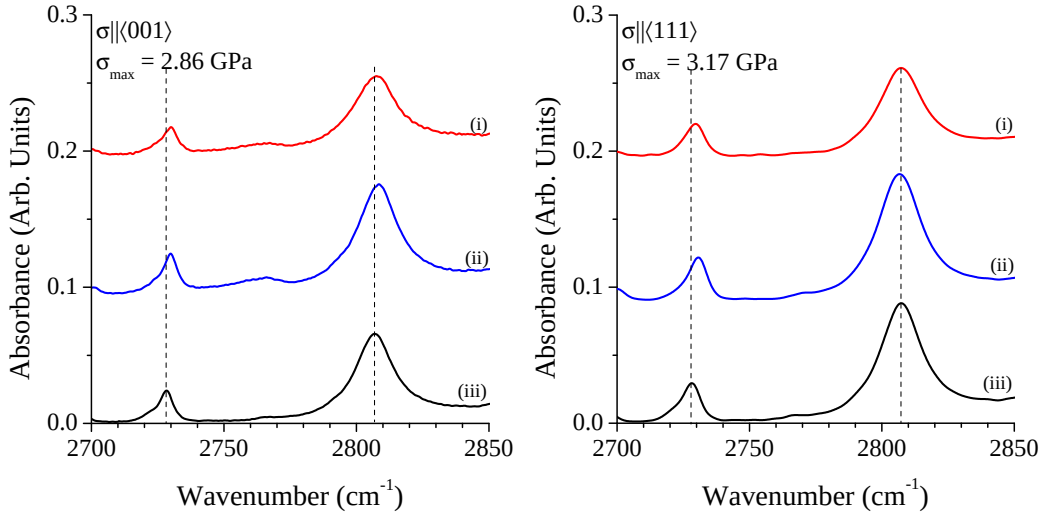

(b)

Figure 7-10: Uniaxial stress splitting spectra for the (a) 3123 cm^{-1} and (b) 2727 cm^{-1} and 2808 cm^{-1} lines. In each, the electric vector is polarised (i) parallel and (ii) perpendicular to the direction of stress. (iii) illustrates the unstressed spectrum. In (a), relative intensities of transitions for a monoclinic I symmetry have been labelled. Spectra have been offset for clarity.

Of particular interest is the relation between the presence of nitrogen within the lattice of the diamond sample and its influence on the growth and intensity of the 3107 cm^{-1} absorption line. Initial investigations observe the changing concentration of nitrogen in the sample with annealing (Figure 7.12(b)). As the 3107 cm^{-1} line begins to grow, there is an initial increase in the concentration of N_S^0 but decrease in the concentration of N_S^+. As the 3107 cm^{-1} absorption band continues to grow, there is a net decrease in the total concentration of single ni-

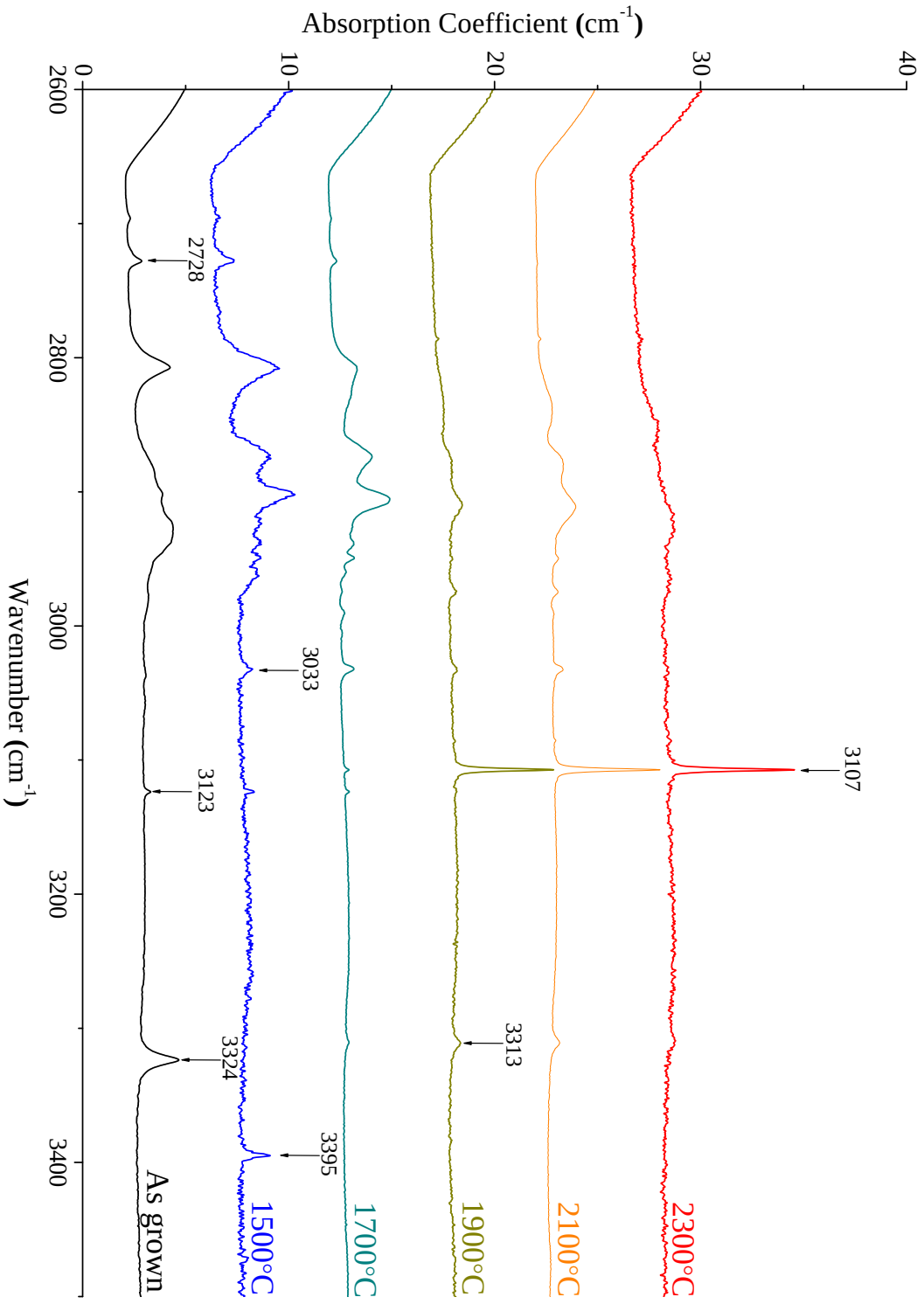

Figure 7-11: Mid-infrared spectra of the C-H stretch region after different HPHT anneals. All samples were annealed for 30 minutes under 6.6 GPa of pressure. Spectra were collected at room temperature and have been offset for clarity.

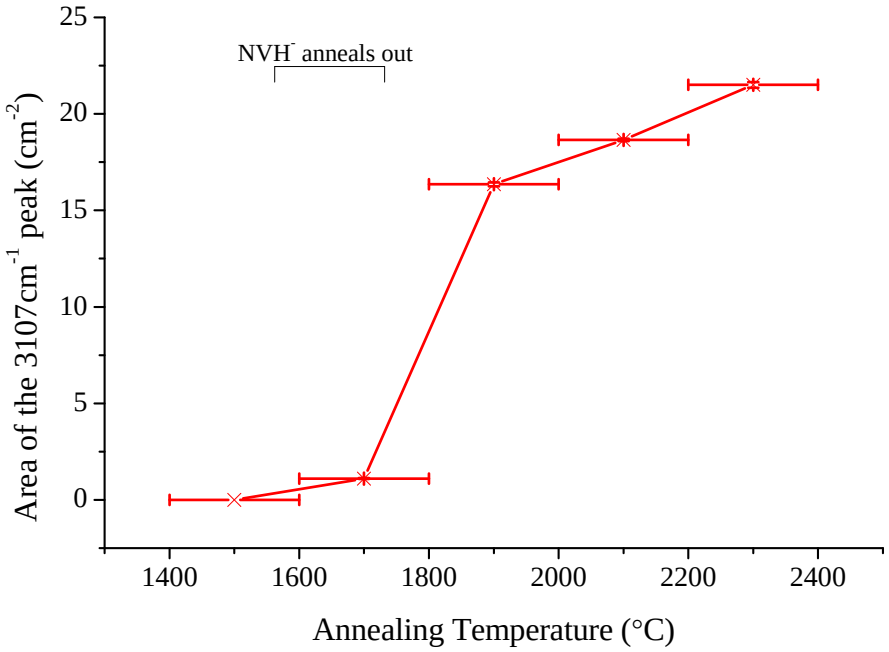

(a)

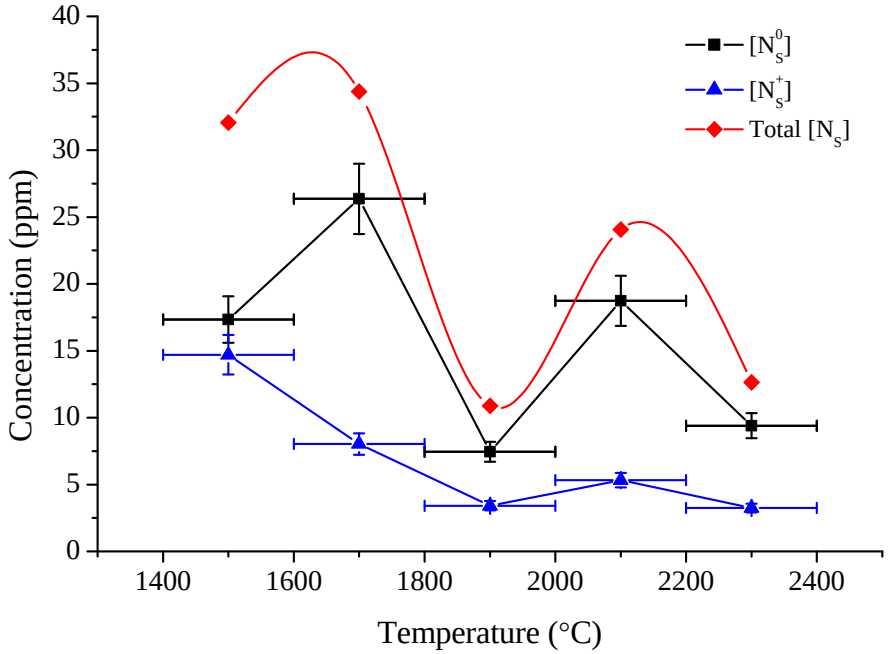

(b)

Figure 7-12: The effect of HPHT annealing on the growth of the 3107 cm^{-1} absorption band and subsequent change in the concentration of nitrogen. (a) shows the increase in absorption intensity of the 3107 cm^{-1} absorption band with increasing annealing temperature, reaching towards a maximum post annealing at 2300℃. (b) plots the simultaneous changing concentration of the N_S^+ and N_S^0 defects with annealing temperature. Plotted also is the changing total single substitutional nitrogen concentration ($[N_S^0]+[N_S^+]$). The concentration of A-centres in this sample was below detectable limits. The trendline illustrating the changing total $[N_S]$ is to guide the eye.

trogen in the sample. At these temperatures, the A-centre could be forming but the concentration of this defect, if present, was below the detectable limits of IR spectroscopy.

The fastest increase in the intensity of the 3107 cm^{-1} defect occurs in a temperature range where the NVH^-/NVH^0 defects are annealing out (Figure 7-11). Since the concentration of single substitutional nitrogen does not increase in the same period, this may be indicative of a direct conversion from NVH^- to the defect responsible for the 3107 cm^{-1} absorption band.

Collecting data from a range of HPHT experiments at 2100(200)℃ for 60 minutes, a relation between the total concentration of single substitutional nitrogen and the intensity of the 3107 cm^{-1} feature, has been found (Figure 7-13). A best fit is obtained when the peak height of the 3107 cm^{-1} line is proportional to the square of the total concentration of nitrogen. This is in contrast to the data presented by Kiflawi *et al.*, who identified the intensity of the 3107 cm^{-1} defect to be directly proportional to the concentration of nitrogen in HPHT samples [7]. For their sample suite, concentrations of nitrogen were orders of magnitude greater than seen here.

7.4.3 Symmetry and structure analysis of C–H stretch modes

Investigation of an absorption line's response to stress is a powerful technique to gain information on the symmetry and therefore potential structure of a defect. With annealing behaviour and isotopic substitution information alone, conclusive assignment of structure cannot be made.

The 3107 and 3324 cm^{-1} lines are characterised as $A \rightarrow A$ transitions originating from trigonal centres, with derived piezospectroscopic parameters characterising the shift rates of the defects (Table 7-1).

Based on the symmetry of these two absorption bands, there are a number of possibilities for the structure of these defects. The defect is known to include hydrogen, proposing a number of trigonal defects including N:H–C, H_2^*, hydrogen in an anti-bonding site or bond-centred position or possibly an A-centre with a hydrogen bonded in an anti-bonding configuration.

N:H–C was originally proposed to be the most probable structure for the

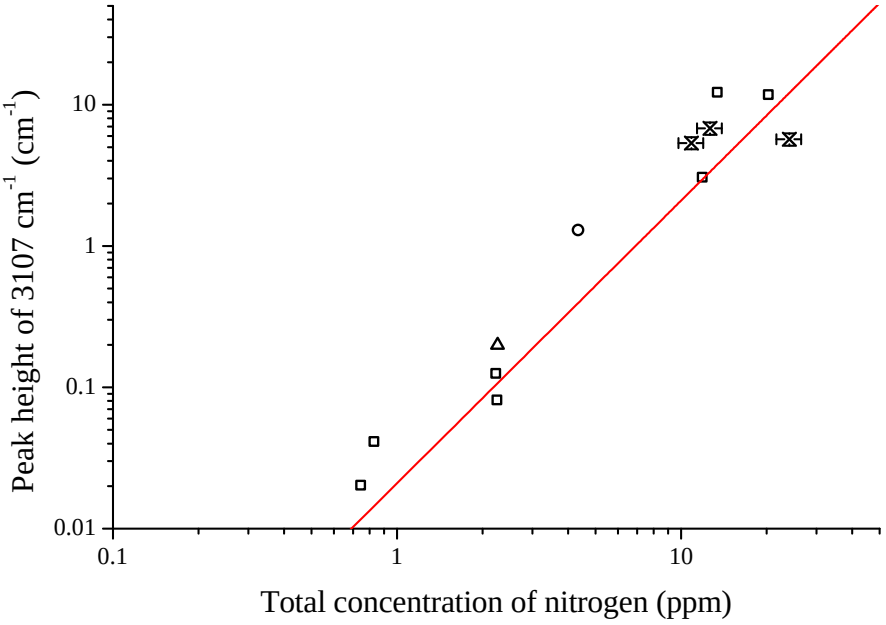

Figure 7-13: A graph indicating the relation between the peak height of the 3107 cm^{-1} line and the concentration of single substitutional nitrogen in diamond post annealing at 2100℃ for 60 minutes. The trend line models the behaviour predicted for a second order kinetic process with $h_{3107} \propto [N_S^0]^2$. Data has been collected from a number of HPHT experiments under similar conditions. □ data markers represent data from DTC, △ datum marker represents a result presented by Charles *et al.* [12], ∘ datum marker represents a result presented by Wang *et al.* [29] and × data markers, data collected during this study.

Table 7-1: Experimental piezospectroscopic parameters for the 3107, 3123 and 3324 cm^{-1} absorption bands and theoretical parameters for the N:H–C defect.

Parameter	**3107 cm^{-1}**	**3324 cm^{-1}**	**N:H–C**	**3123 cm^{-1}**
A_1	0.5(3)	1.4(5)	1.7	-1.7(3)
A_2	0.9(2)	1.0(4)	1.2	1.8(3)
A_3				0.9(3)
A_4				0.1(3)

3107 cm^{-1} transition. As Table 7-1 and Figure 7.14(a) show, the experimental uniaxial stress data are not well matched with that calculated theoretically for the N:H–C defect. Instead, the parameters are significantly closer to the experimental results gained for the 3324 cm^{-1} defect. Given the success in relating theory and experiment for the 1344 cm^{-1} LVM of the N_S^0 defect (Chapter 5) and the H1a defect (Chapter 6), it is proposed that the 3324 cm^{-1} LVM originates from the

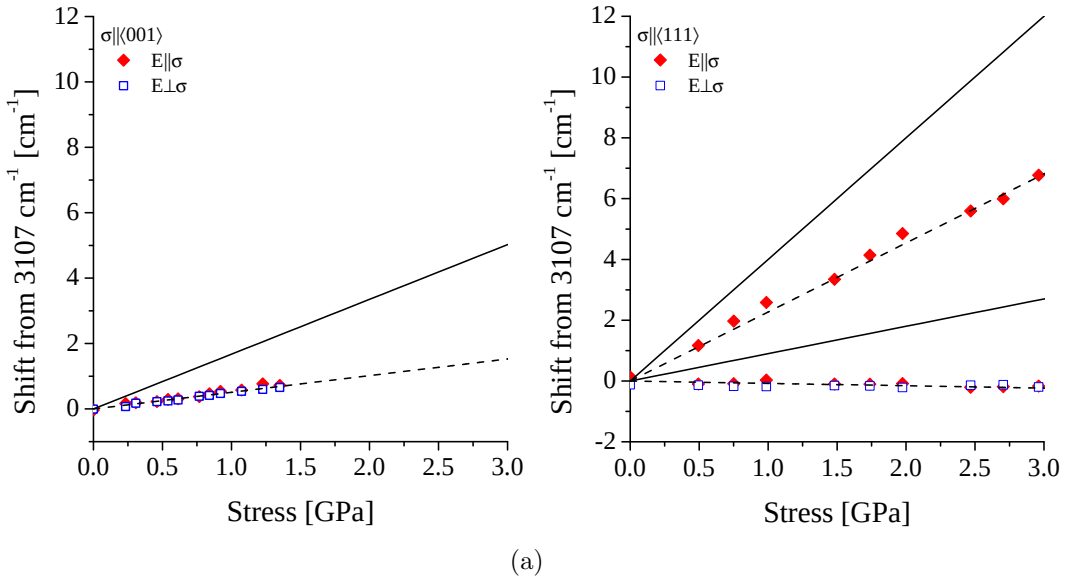

(a)

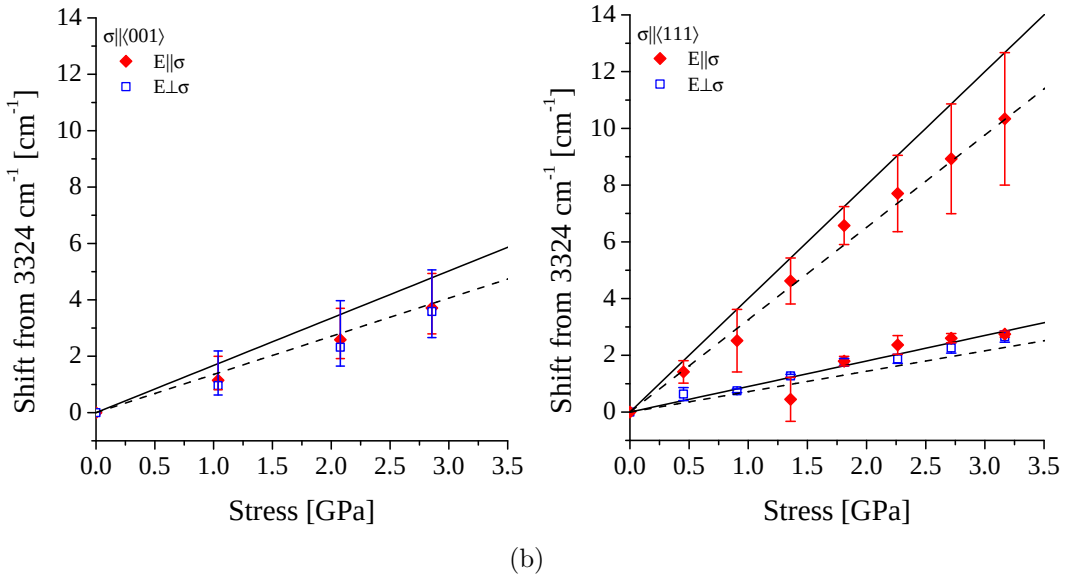

(b)

Figure 7-14: Graph depicting the experimental shift of the (a) 3107 cm^{-1} and (b) 3324 cm^{-1} absorption bands under uniaxial stress in the ⟨001⟩ and ⟨111⟩ directions. Each graph is overlayed with the theoretical transition shift for the N:H–C defect with the solid line indicating the predicted shift of N:H–C and the dashed line the least squares fit model from the experimental data.

N:H–C defect.

Experimentally, for ^{13}C:^{12}C isotopic substitution, a shift of 6 cm^{-1} is observed for the 3324 cm^{-1} line [10, 21]. For ^{14}N:^{15}N isotopic substitution, no shift is seen in the transition but this does not preclude the involvement of nitrogen in the associated defect [10, 21]. There is also a strong influence on the transition from the presence of hydrogen in the defect, although the precise isotopic shift with

deuterium enrichment is unknown. It is suspected to shift the transition to under the two-phonon absorption of the mid-infrared spectrum [10, 21]. Theoretical modelling calculates the stretch mode of the N:H–C defect to be at 3324 cm^{-1} and has been shown to red shift by 6 cm^{-1} and 910 cm^{-1} with the substitution of ^{13}C and ^{2}H respectively and be unaffected by the isotopic substitution of ^{14}N with ^{15}N [30]. Comparing the shifts seen experimentally with those predicted theoretically, excellent agreement is observed, substantiating the assignment of the 3324 cm^{-1} LVM to the N:H–C defect.

Further evidence supporting the assignment of the N:H–C defect to the 3324 cm^{-1} transition is its annealing behaviour. The 3324 cm^{-1} line is stable to approximately 1000℃ in samples and anneals out by approximately 1100℃. Isochronal annealing at 1100℃, 1125℃ and 1150℃ revealed the 3324 cm^{-1} line to display second order kinetic trends, with first order models failing to provide a satisfactory representation of the data [18] and an activation energy of 4.6(2) eV. In comparison, using LDA-DFT techniques, Goss calculates that for the dissociation of the N:H–C defect, $N - H \rightarrow N^0 + H^0$ would have a binding energy of 4.2 eV. $N - H \rightarrow N^+ + H^-$ would instead have a binding energy of 3.5 eV. The dissociation path to two neutral components, provides a value in reasonable agreement with that derived from experiment.

Finally, the 3324 cm^{-1} line does not display any change in intensity when subjected to photo-/thermo- chromic experiments (Figure 7-15), complementing the electrical inactivity and stability of the N:H–C model.

7.5 Conclusions

This chapter has furthered the understanding of three key C–H stretch modes seen in infrared spectroscopy. The 3123 cm^{-1} absorption band assigned to the NVH^0 defect has been quantified. By comparison of the change in intensity of the 3123 cm^{-1} line and the change in concentration of the NVH^- defect as determined by EPR over a wide sample range, a correlation factor of 200(15) ppb cm^2 has been concluded for scans at 4 cm^{-1} resolution. Conversion factors for other resolution scans have been presented.

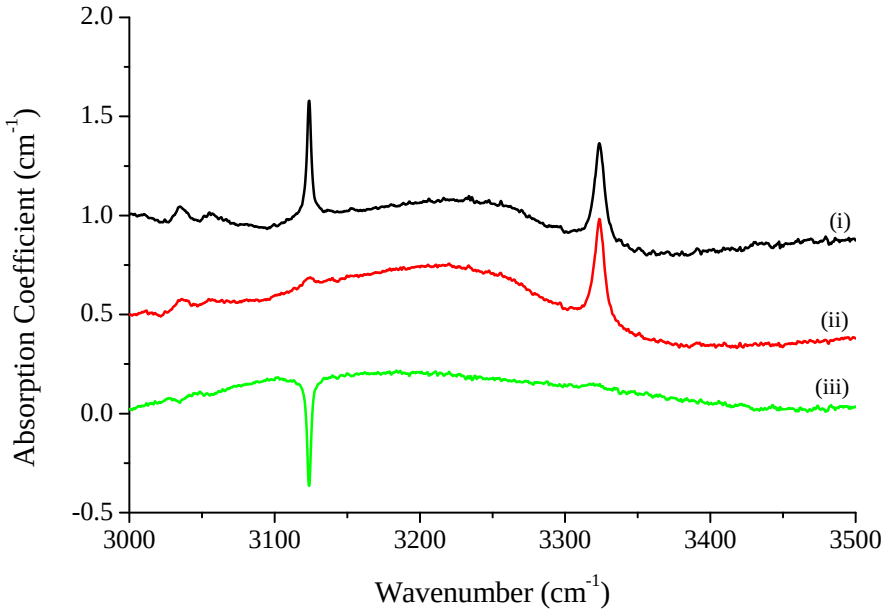

Figure 7-15: A graph illustrating the photo-/thermo- chromic behaviour of the 3324 cm^{-1} transition. (i) indicates the spectrum post illumination for 5 minutes with the 200 W HgXe arc lamp. (ii) represents the spectrum taken post treatment for 60 minutes at 850 K with the sample treated, mounted and scanned in the dark. (iii) represents the difference between these two spectra, indicting a maximum change in the 3123 cm^{-1} line and no change in the 3324 cm^{-1} line.

Potential optical analogues for the NVH^- defect have been considered. Two candidates highlighted by this work are lines occurring at 2727 and 2807 cm^{-1}, which both display the correct photo-/thermo- chromic behaviour and occur at lower energies compared to the NVH^0 defect. Both these lines show a linear trend between their change in intensity and the change in concentration of the NVH^- defect. Under uniaxial stress, the response of these two modes differs slightly, although neither demonstrate a resolvable stress induced splitting to categorically identify the associated defect as having monoclinic I symmetry. The 2727 cm^{-1} mode gives the greatest suggestion of splitting, which at first sight, appears very similar to the stress induced splitting patterns of the 3123 cm^{-1} absorption band. It is therefore the suggestion of this work that the 2727 cm^{-1} transition is a more plausible candidate for the NVH^- defect.

The previous assignment of the 3107 cm^{-1} absorption feature to the N:H–C defect has been rebutted. Theoretical modelling of the N:H–C defect does not replicate accurately the experimental data seen for the 3107 cm^{-1} absorption feature with regards to its sensitivity to stress, despite having the correct symmetry.

Piezospectroscopic parameters highlight the 3324 cm^{-1} mode to be a better match to the theoretical N:H–C defect. The splitting patterns and shift rates are comparable and this claim is substantiated by further evidence. The 3324 cm^{-1} line does not display sensitivity to photo-/thermo- chromic experiments, suggesting there to be no unfilled electronic states in the band structure and complementing the electrical inactivity predicted for the N:H–C defect. Furthermore, the isotopic substitution behaviours with ^{13}C, deuterium and ^{15}N enriched samples compared to samples of natural abundance, are identical, comparing experiment and theory.

Samples have been annealed to temperatures of 2300℃, with no evidence of the 3107 cm^{-1} absorption feature reaching a turning point in its intensity. This work has also identified the relation that, in CVD-grown samples with a low concentration of substitutional nitrogen, there is a squared dependence between the concentration of nitrogen and the peak height of the 3107 cm^{-1} absorption feature. It has previously been presented in literature that a linear relation between these two quantities exists in HPHT-grown samples, with concentrations of substitutional nitrogen greater than 200 ppm [7]. Could this be indicative of two formation mechanisms dependent upon lattice impurities and defects or more simply, considering the lack of isotopic substitution evidence, that nitrogen's role in the growth of the 3107 cm^{-1} defect is purely concerned with the uptake of hydrogen, with higher concentrations of nitrogen leading to faster growth rates and an increased uptake of hydrogen into the diamond lattice? It is known that the growth rate shows a dependence to the square root of the concentration of nitrogen. Therefore, is the concentration of hydrogen related to the fourth power of nitrogen concentration?

It had been proposed that the 3107 cm^{-1} defect involves an A-centre and hydrogen. To maintain the correct trigonal symmetry, an A-centre would sit in a location along the $\langle 111 \rangle$ direction on the next position to the carbon atom, with an anti-bonding hydrogen attached. This would mean that a very large distance between the nitrogen and carbon atoms would exist, making the sensitivity of the C–H mode to the presence of the A-centre weak.

7.6 Further work

Whilst this work reports many advances in the understanding of C–H stretch modes in infrared spectroscopy, there are many areas which can be furthered to strengthen the assignments made here.

For the 3123 cm^{-1} line, it is important that further data are added to improve the estimation of the oscillator strength and therefore the quantification of the concentration of the NVH^0 defect in diamond. Ideally samples with more extreme concentrations are required to extend the plot. In addition to this, significant work is required to identify the optical analogue of the NVH^- defect. Two proposals have been made here but the lack of resolution of the uniaxial stress data, prevents secure assignment of the symmetry of the defect from which it originates.

The revised assignment of the N:H–C defect to the 3324 cm^{-1} line has now meant that uncertainty exist as to the structure of the 3107 cm^{-1} defect. What role does nitrogen play in the defect and more generally, what effect does nitrogen have on the uptake of hydrogen during CVD growth?

References

[1] P. R. W. Hudson and I. S. T. Tsong, Journal of Materials Science **12**, 2389 (1977-12-01).

[2] J. P. F. Sellschop, S. H. Connell, C. C. P. Madiba, E. Sideras-Haddad, M. C. Stemmet, K. Bharuth-Ram, H. Appel, W. Kundig, B. Patterson, and E. Holzschuh, Nuclear Instruments and Methods in Physics Research Section B: Beam Interactions with Materials and Atoms **68**, 133 (1992).

[3] B. Dischler, C. Wild, W. Mller-Sebert, and P. Koidl, Physica B: Condensed Matter **185**, 217 (1993).

[4] Y. Borzdov, Y. Pal'yanov, I. Kupriyanov, V. Gusev, A. Khokhryakov, A. Sokol, and A. Efremov, Diamond and Related Materials **11**, 1863 (2002).

[5] R. M. Chrenko, R. S. McDonald, and K. A. Darrow, Nature **213**, 474 (1967).

[6] G. S. Woods and A. T. Collins, Journal of Physics and Chemistry of Solids **44**, 471 (1983).

[7] I. Kiflawi, D. Fisher, H. Kanda, and G. Sittas, Diamond and Related Materials **5**, 1516 (1996).

[8] F. De Weerdt and I. Kupriyanov, Diamond and Related Materials **11**, 714 (2002).

[9] W. A. Runciman and T. Carter, Solid State Communications **9**, 315 (1971).

[10] F. Fuchs, C. Wild, K. Schwarz, and P. Koidl, Diamond and Related Materials **4**, 652 (1995).

[11] J. Chevallier, F. Jomard, Z. Teukam, S. Koizumi, H. Kanda, Y. Sato, A. Deneuville, and M. Bernard, Diamond and Related Materials **11**, 1566 (2002).

[12] S. J. Charles, J. E. Butler, B. N. Feygelson, M. E. Newton, D. L. Carroll, J. W. Steeds, H. Darwish, C. S. Yan, H. K. Mao, and R. J. Hemley, Physica Status Solidi (a) **201**, 2473 (2004).

[13] F. De Weerdt and A. T. Collins, Diamond and Related Materials **15**, 593 (2006).

[14] I. Kiflawi, A. Mainwood, H. Kanda, and D. Fisher, Physical Review B **54**, 16719 (1996).

[15] G. Davies, A. T. Collins, and P. Spear, Solid State Communications **49**, 433 (1984).

[16] K. Iakoubovskii and G. J. Adriaenssens, Diamond and Related Materials **11**, 125 (2002).

[17] F. De Weerdt, Y. N. Pal'yanov, and A. T. Collins, Journal of Physics: Condensed Matter **15**, 3163 (2003).

[18] R. J. Cruddace, PhD. thesis, University of Warwick (2007).

[19] W. Wang, T. Moses, R. C. Linares, J. E. Shigley, M. Hall, and J. E. Butler, Gems and Gemology **39**, 268 (2003).

[20] P. M. Martineau, S. C. Lawson, A. J. Taylor, S. J. Quinn, D. J. F. Evans, and M. J. Crowder, Gems and Gemology **40**, 2 (2004).

[21] F. Fuchs, C. Wild, K. Schwarz, W. Muller-Sebert, and P. Koidl, Applied Physics Letters **66**, 177 (1995).

[22] C. Glover, M. E. Newton, P. M. Martineau, D. J. Twitchen, and J. M. Baker, Physical Review Letters **90**, 185507 (2003).

[23] A. M. Edmonds, PhD. thesis, University of Warwick (2008).

[24] B. L. Cann, PhD. thesis, University of Warwick (2009).

[25] A. Kerridge, A. H. Harker, and A. M. Stoneham, Journal of Physics: Condensed Matter **16**, 8743 (2004).

[26] J. P. Goss, Journal of Physics: Condensed Matter **15**, R551 (2003).

[27] S. P. Mehandru and A. B. Anderson, Journal of Materials Research **9**, 383 (1994).

[28] K. Bergman, M. Stavola, S. J. Pearton, and J. Lopata, Phys. Rev. B **37**, 2770 (1988).

[29] W. Wang, P. Doering, R. Tower, J. Lu, S. Eaton-Magaña, P. Johnson, E. Emerson, and T. M. Moses, Gems and Gemology **46**, 4 (2010).

[30] J. P. Goss, R. Jones, M. I. Heggie, C. P. Ewels, P. R. Briddon, and S. Öberg, Physical Review B **65**, 115207 (2002).

Chapter 8

Neutron Irradiation Effects in Diamond

Diamond is perceived as a radiation hard material but the extent of the damage that high energy particles have on the lattice is not well understood. The isolated vacancy and self interstitial have been identified but many questions remain as to the formation of complexes once these primary products of radiation damage become mobile. Furthermore, neutron irradiation and ion implantation produce a cascade of secondary damage not found for electron irradiation and the defects produced under such complex conditions are not well understood.

This chapter will consider the mechanisms and induced defects resulting from neutron radiation damage, characterising the resulting key absorption features.

8.1 Introduction

As a radiation hard material, proposals have been made to use diamond as a semiconductor device for detectors in high-radiation environments, such as in the Large Hadron Collider (LHC) at CERN [1–6]. In addition to the practical reason for testing a diamond's response to radiation, there is the growing concern that a significant number of gem diamonds are being irradiated to improve their colour and value. For example, electron irradiation of type Ib diamond can turn an unattractive brown diamond rich in substitutional nitrogen, a red colour when annealed between 600 and 800°C and a colourless type IIa diamond, blue-green. The artificial enhancement of the colour properties of a gem diamond is something which is of great concern to the gem industry and hence needs to be identifiable

and understood.

8.2 Review of irradiation studies on diamond

The act of bombarding a sample with high energy particles, can significantly change its properties. The momentum and the electronic charge of an irradiating particle determines the damage it can produce. As the particles pass through the lattice, they may participate in a number of collisions with the constituent atoms. The number of collisions will depend upon their energy. If a collision transfers enough energy, the interaction may be sufficient to displace an atom from its lattice site, forcing it into an interstitial position and introducing vacant sites into the lattice. If the material is then annealed such that the new vacancy and interstitial defects are mobile, they may migrate and form complexes with themselves or other point defects in the lattice, further modifying the properties of the diamond.

Neutrons, since electronically neutral, have a small interaction cross section with carbon and the majority (at 1 MeV) will pass through the diamond lattice without effect [7]. However, if a 1 MeV neutron collides with a carbon atom, of the order of 300 keV may be imparted to the carbon atom in the inelastic collision. The carbon atom, recoiling post collision, may then collide with other atoms, leading to secondary collisions and a cascade of further damage throughout the lattice. By electron microscopy, the threshold energy for the displacement of atoms from their lattice sites in natural type IIa diamond was found to be 37.5±1.2 eV for irradiation incident in the [100] direction, 45.0 ± 1.3 eV in the [111] direction and 47.6 ± 1.3 eV in the [110] direction [8]. The threshold energy was defined as the maximum recoil energy which corresponded to the minimum incident electron energy for the observation of defect cluster formation. Collision displacement occurs most easily in the close-packed direction, permitting interstitials to form away from vacancies and giving the variation in threshold energy for different angles of incidence of the bombarding particle [9]. When the incident energy is large or if temperature is increased, the atom displacement may occur in random directions [8].

In diamond, it is theoretically modelled that primary damage due to 1 MeV

neutrons produces of the order of 70 vacancies per neutron per cm [10]. However, the energy imparted to the lattice during irradiation means that many of these vacancies recombine with the displaced interstitials almost immediately, leading to an observed damage of only half this number of vacancies [10]. The recombination volume generally has an extended shape in the close-packed direction as a result of the rigid tetrahedral bonding of diamond, which increases the probability of spontaneous recombination [11, 12].

8.2.1 Neutron irradiation

A dominant effect of radiation damage is to produce the 'GR' vibronic bands, the lowest energy of which occurs at 1.673 eV (741 nm) and is attributed to the V^0 defect [13, 14]. In addition, the I_{001} defect (R2) is a prominent feature at 1.856 eV (668 nm) [15]. The vacancy is mobile at temperatures greater than 600℃ where it can combine with other point defects, vacancies and interstitials in the lattice. The formation of vacancy related defects and additional interstitial related defects, is reviewed in Chapter 2.

Much is known about the interaction of single vacancies produced during irradiation and the diamond lattice but less is reported about the effects of neutron irradiation producing significantly larger concentrations of vacancies. The higher momentum involved in collision leads to a higher probability for multiple vacancy clusters and chains, which may have a significant effect on the optical and electronic properties of diamond.

8.2.1.1 Absorption features in the two phonon region

Woods' study on neutron irradiated (3.6×10^{16} neutrons per cm^2) type IIa diamond, identified a line at 1531.0(5) cm^{-1} with additional minor absorptions at 1570 cm^{-1} and 1420 cm^{-1} [16]. The 1531 cm^{-1} absorption peak annealed out after treatment at 450℃. A second close peak at 1570.3(1) cm^{-1}, at near maximum intensity between 300 and 350℃, annealed out at 650℃. At higher anneals, the only observation was the steady decrease of the lattice absorption, which vanished at 1100℃.

In type Ia diamond, the 1531 cm^{-1} absorption band was again observed but was

weak in intensity, annealing out at 300℃. In addition, a line at 1574.2(2) cm^{-1} annealed in, maximised in intensity at 1100℃ but did not anneal out until treatment at 1400℃.

An absorption band at 1856 cm^{-1} has been reported as a vibrational absorption peak, superimposed on the tail of the two-phonon lattice band [17]. The absorption feature is induced in natural type Ia diamond when bombarded with neutrons (typically 5×10^{17} cm^{-2} fast neutrons) and annealed [17]. The growth of the feature has two annealing stages at 500℃ and 900℃. Annealing of irradiated type Ib diamond does not produce the same absorption system upon low temperature annealing. Instead, annealing at temperatures of the order of 1400℃ is required, the temperature required for the vacancy-enhanced aggregation of nitrogen [18]. The annealing results are similar to those observed for the H1a defect discussed in Chapter 6. In both instances, there are two different temperatures at which the defect may form, depending upon the initial form of the incorporated nitrogen of the sample; potentially, one may be where the impurity is in an isolated form and a second where it is in an already aggregated form.

Isotopic substitution experiments concluded that the 1856 cm^{-1} feature split into three isotopically related transitions in a sample with a relative concentration of ^{14}N:^{15}N of 70:30 [17]. This implied that the absorption resulted from a defect formed of two equivalent nitrogen atoms (a di-nitrogen centre), although the configuration was not determined. Again, this is comparable to the H1a defect (see Chapter 6).

The H1a defect which has a local vibrational mode (LVM) absorption at 1450 cm^{-1} in ^{14}N diamond, has been identified in neutron irradiation type Ib samples [16, 19]. The 1450 cm^{-1} peak increased in intensity linearly for low neutron doses but saturated at 2×10^{17} neutrons per cm^2 and became independent of dose [19].

8.2.1.2 Near infrared (NIR) absorption features

The electronic zero phonon line (ZPL) transition at 4935 cm^{-1} is labelled H1b. A vibronic sideband associated with this ZPL has not been observed and hence it is assumed that the coupling to the diamond lattice vibrations must be very

small [20]. Previously reported correlations between the H1b defect and H3 were disproved by Collins *et al.* as were correlations between H1c and H4 [20].

Uniaxial stress measurements, identified the H1b defect to originate from a defect of monoclinic I symmetry, showing distinct resolvable linear shifting and splitting of the transitions at stresses of the order of 2 GPa [20]. The intensities of the transitions were found to be independent of the magnitude of stress, indicating that the transitions arise from electronic, non-degenerate states. A monoclinic I point centre has a C_{1h} point group with a normal to its reflection plane along the [110] axis of the crystal. The perturbation of the Hamiltonian is shown in Equation (8-1), where s_{ij} are the components of the stress tensor and A_i represents the difference in the perturbation of the excited and ground states of the optical transition per unit stress [21].

$$\mathscr{H}_1 = \mathrm{A}_1 s_{zz} + \mathrm{A}_2(s_{xx} + s_{yy}) + 2\mathrm{A}_3 s_{xy} + 2\mathrm{A}_4(s_{yz} - s_{zx}) \tag{8-1}$$

The intensity of each stress split component will be a function of the orientation of the dipole in the {110} reflection plane, with a component D along the [001] axis and E along $[1\bar{1}0]$. The orientation of the dipole was calculated as $\theta = \tan^{-1}(E/D) = 21(1)^\circ$ for the H1b defect. However, the exact nature of the H1b centre has not been determined.

The 4397 cm^{-1} absorption line is commonly observed in type Ib diamond following neutron radiation and annealing at temperatures greater than 1400℃ [22]. This centre was observed to be stable to temperatures greater than 1700℃ and not observed in type IIa material (Figure 8.1(a)), leading to the presumption that this defect was associated with nitrogen or an aggregate thereof. Instead, in type IIa diamond, four ZPLs at 4066, 4113, 4139 and 4168 cm^{-1} could be identified [23]. The intensity of the 4397 cm^{-1} absorption was shown to be related to the neutron dose and not observed in samples exposed to a dose of less than 8×10^{16} electrons per cm^2 [22].

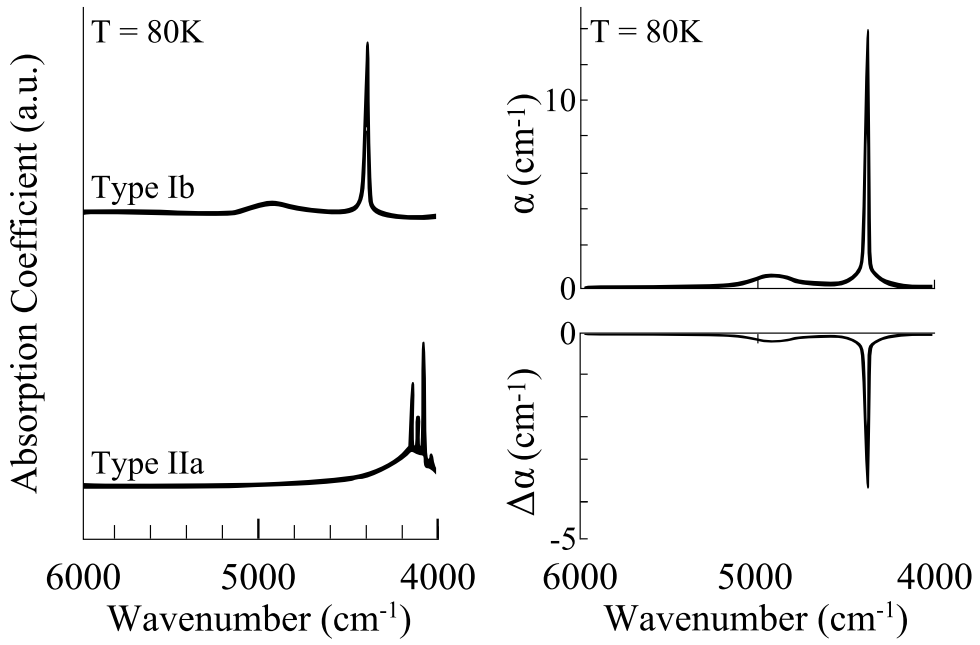

Figure 8-1: Absorption spectra of the H1b defect at 4935 cm^{-1} at 80 K. (a) illustrates the NIR absorption spectra for neutron irradiated type Ib and IIa diamonds annealed at 1700℃. The type Ib spectrum illustrates the ZPL at 4397 cm^{-1} and its one phonon sideband at 4935 cm^{-1}, whereas four ZPLs were observed in the type IIa diamond. (b) illustrates the strong photochromic behaviour of the 4397 cm^{-1} line under excitation by 514.5 nm argon ion laser. The upper figure represents the spectrum prior to illumination and the lower, the difference spectrum under excitation. These figures have been adapted from a paper by Mita *et al.* [22].

8.3 Experimental detail

A series of samples were prepared and neutron irradiated at the Hoger Onderwijs Reactor at the Delft University of Technology in the Netherlands. This suite included natural and synthetic (CVD and HPHT grown) diamonds that were characterised as type IIa and Ib. Two type IIa samples were isotopically enriched with 10% and 50% ^{13}C and one of the type Ib samples was enriched with ~ 95% ^{15}N. The total dose of neutrons was 5×10^{17} neutrons per cm^2. All these samples were prepared as outlined in §4.7.2 and confirmed to be inclusion free. The local sample temperature was estimated to be in the region of 200℃ and irradiation was completed in atmospheric conditions.

Post irradiation, two type IIa CVD samples of natural abundance of ^{13}C (1.1%) were annealed at 400, 600, 800, 1000, 1200, 1400 and 1500℃ for 15 hours in

forming gas in the horizontal tube furnace (§4.1.2). Infrared spectroscopy was then performed at room temperature and liquid nitrogen temperature.

The ^{15}N enriched and the ^{14}N HPHT type Ib samples, both prepared for uniaxial stress applied in the ⟨001⟩/⟨110⟩ and ⟨111⟩ directions respectively, were annealed at 1500℃ for 15 hours in forming gas in the tube furnace. Uniaxial stress experiments (§4.3) in conjunction with infrared spectroscopy, were then performed. All spectra were collected at room temperature and at a resolution of $1\,\mathrm{cm}^{-1}$.

8.4 Results and analysis

8.4.1 Neutron irradiation studies of type IIa diamond

8.4.1.1 Annealing effects on neutron irradiation type IIa diamond

Infrared spectra show substantially more damage from neutron irradiation than was evident in electron irradiation, highlighted by the strong absorption in the one-phonon region (Figure 8-2). Following neutron irradiation, the type IIa samples were opaque in the visible region. Neutron irradiation damage introduced significant absorption in the one-phonon spectral region and a ramp in the absorption was introduced to higher energies (Figure 8-2). It was assumed that annealing at approximately 200℃ was taking place during the 24 hour irradiation period.

The one-phonon irradiation damage induced absorption, completely anneals out by 1500℃. The annealing kinetics fit to a first order kinetic model (see Equations (3-48)-(3-50)). However, the best fit is only achieved with a very small activation energy (~110 meV) and a very low (non-physical) attempt frequency ($\sim 10^{-6}$ Hz). The effective rate constant varies slowly with temperature, $< \times 10$ over the range 200–1500℃.

Figure 8-3 illustrates the comparison between the annealing behaviour of the vacancy and interstitial and that of the radiation induced one-phonon absorption. The profiles are clearly very different and indicate that the recovery of the intrinsic diamond properties does not simply depend on the migration of isolated vacancies and interstitials. The neutron dose is below that expected for bulk amorphisation

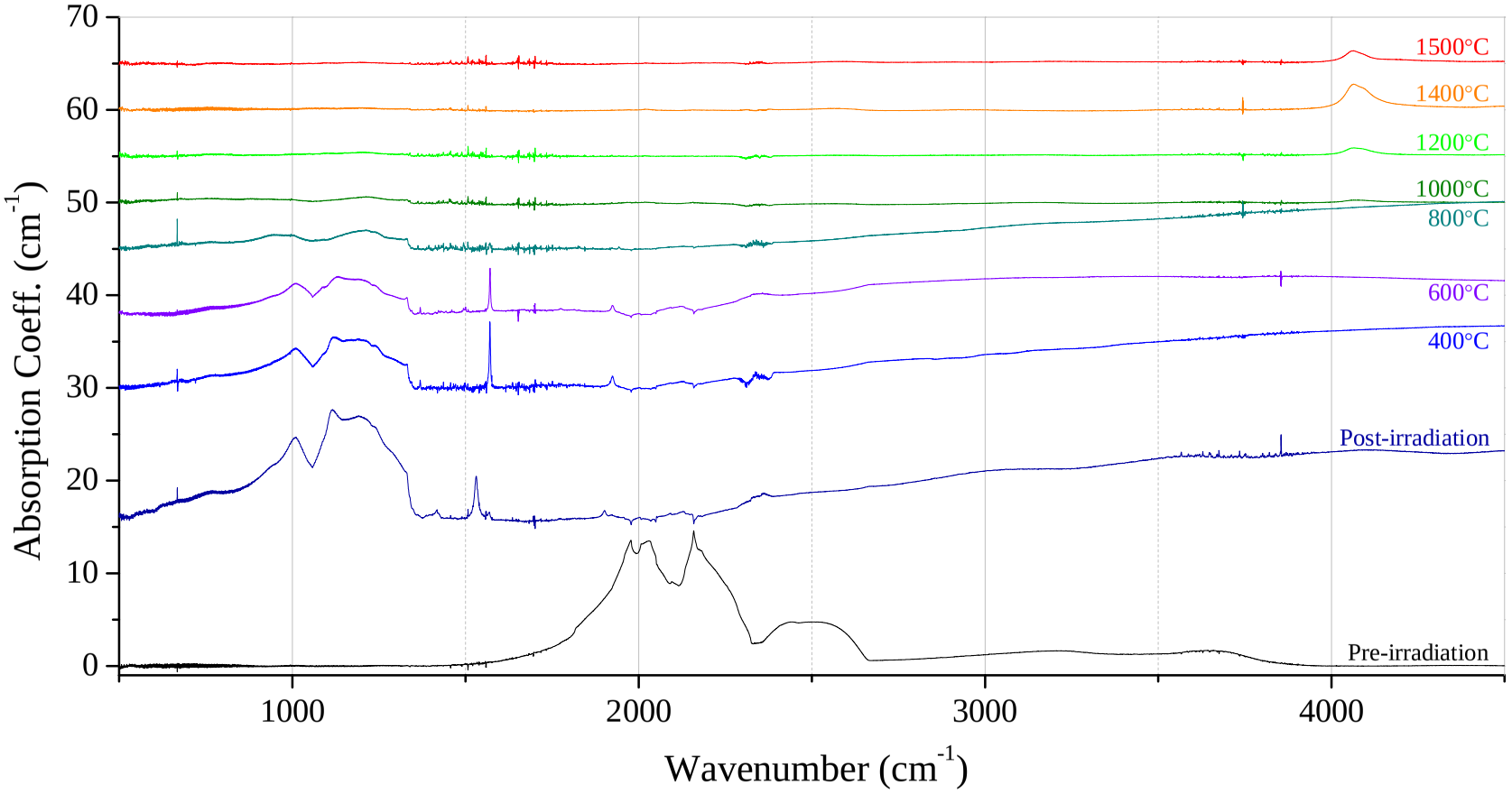

Figure 8-2: Annealing spectra (collected at room temperature) of type IIa neutron irradiated diamond. Spectra were taken using two different samples (Sample R: 400, 800, 1200, 1500℃ and Sample S: 600, 1000, 1400℃) and have been offset for clarity. In each spectrum, a type IIa spectrum has been subtracted to reveal absorption features purely resulting from irradiation and annealing.

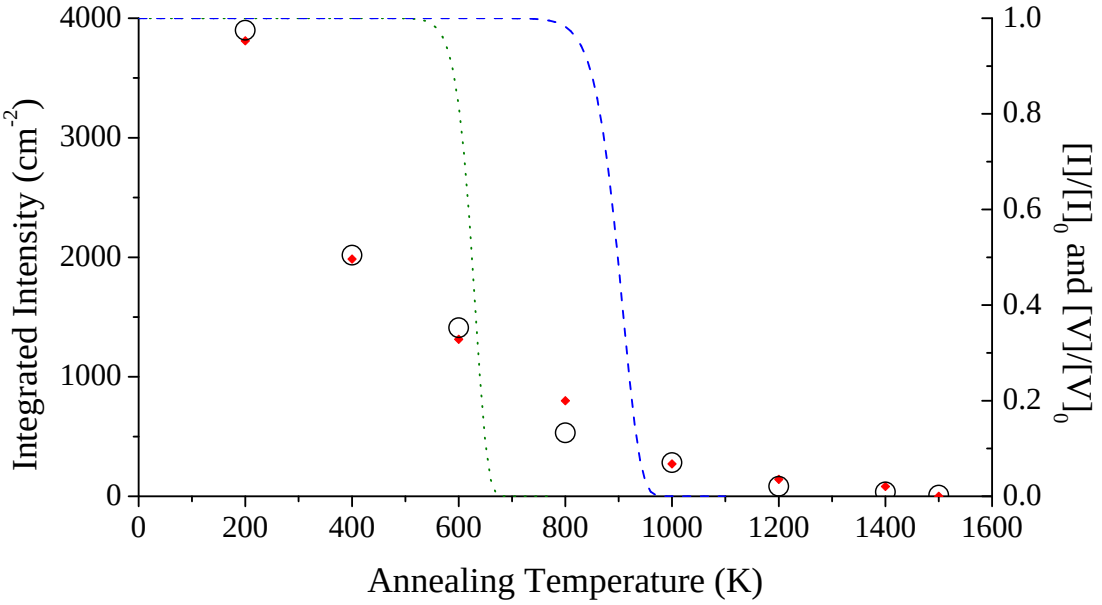

Figure 8-3: Isochronal (15 hours) annealing curve of irradiation damage in the one-phonon region. The red diamond symbols illustrate the integrated intensity of the structure between 500 and 1332 cm^{-1}. The large open circles illustrate the expected integrated intensity following first order kinetics. The blue dashed line is a plot of the $[V]/[V]_0$ with temperature (E_a = 2.3 eV and $\nu_0 = 1 \times 10^8$ s^{-1}) [24]. The green dotted line is a similar plot for the interstitial defect (E_a = 1.6 eV and $\nu_0 = 1 \times 10^8$ s^{-1}) [25].

but clearly regions of the diamond are so heavily damaged that recovery of long range order requires re-arrangement of many atoms.

After annealing at 1000℃, a feature at 4066 cm^{-1} became evident, which continued to increase in intensity with annealing to 1400℃, decreasing thereafter. For type IIa diamond, a series of lines in the range 4000–4200 cm^{-1} have been reported which do not appear in type Ib diamond [22]. The lack of observation of these features in type Ib diamond suggests that they are aggregates of intrinsic radiation damage defects. Presumably, the constituents are trapped by nitrogen impurities in type Ib diamond so that their production is not possible. Low temperature measurements sharpened the vibrational mode and helped to improve resolution of multiple, closely neighbouring absorption features (Figure 8-4).

Previous studies have reported lines at 4066, 4113, 4139 and 4168 cm^{-1} post annealing at 1700℃. This study reports observation of lines at 4064.5(1), 4095.8(1), 4113.2(1), 4137.7(2), 4150.0(3) cm^{-1} after annealing at 1400℃, suggesting that an intermediate result towards that reported by Mita has been achieved.

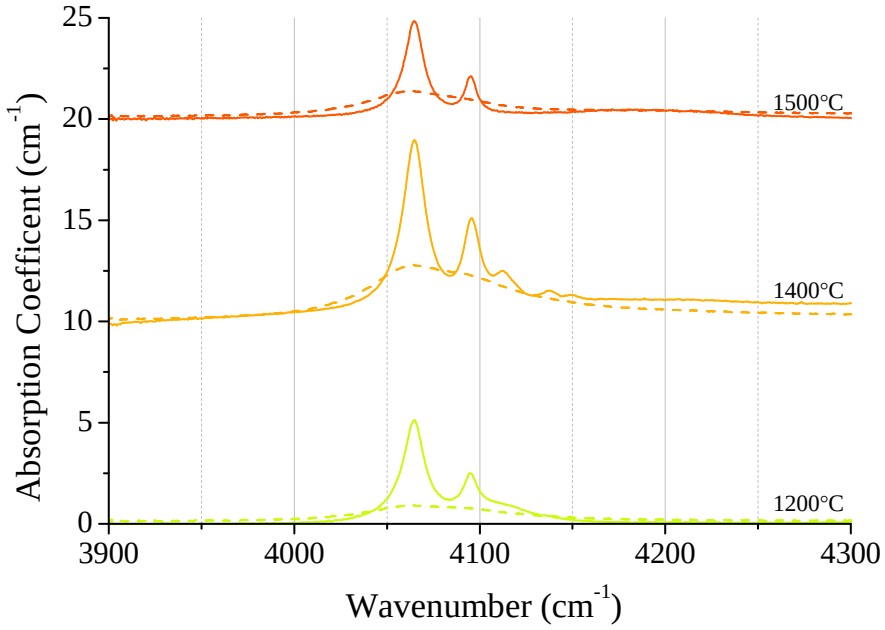

Figure 8-4: A comparison of room (dashed line) and low (77 K) temperature (solid line) spectra of the 4066 cm^{-1} line post annealing at 1200, 1400 and 1500℃. In the room temperature spectrum, a single but asymmetric broad feature is seen which resolves into 5 peaks when measured at liquid nitrogen temperatures. The intensity of these features maximises post annealing at 1400℃.

8.4.1.2 Isotopic sensitivity of the 1531 cm^{-1}absorption feature

The 1531 cm^{-1} feature is apparent post irradiation and was completely removed by annealing at 400℃ for 15 hours (Figure 8-2). Simultaneously, a sharp mode at 1570.8 cm^{-1} anneals in. These temperatures are in excellent agreement with those reported by Woods [16]. The 1531 cm^{-1} line was relatively broad, with a FWHM of 11.7(2) cm^{-1} and was absent in electron irradiated samples studied in this thesis. Upon isotopic investigation, the 1531 cm^{-1} line splits into 5 lines for a sample enriched with 50% ^{13}C (Figure 8-5).

The number of lines into which the local vibration mode splits upon ^{12}C:^{13}C substitution, gives an indication as to the number of equivalent atoms involved in the LVM. If we assume that a defect contains four equivalent carbon atoms, each of which vibrates independently, then for a ^{12}C:^{13}C enrichment of 50:50, it is expected that a 1:4:6:4:1 spectrum is observed. The ratio of the frequencies for the 100% enriched ^{13}C sample to the 100% ^{12}C doped sample would be $\sqrt{12/13}$ = 0.96. Indeed this is the case since 1472/1531 = 0.96. However, the intensities in Figure 8-5 do not match the expected 1:4:6:4:1 pattern, showing that this simple analysis

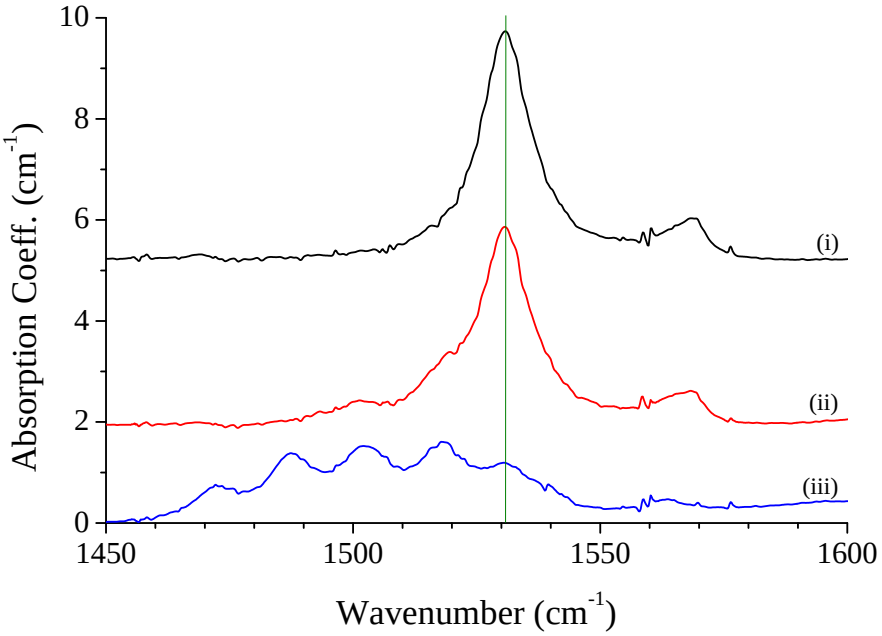

(a)

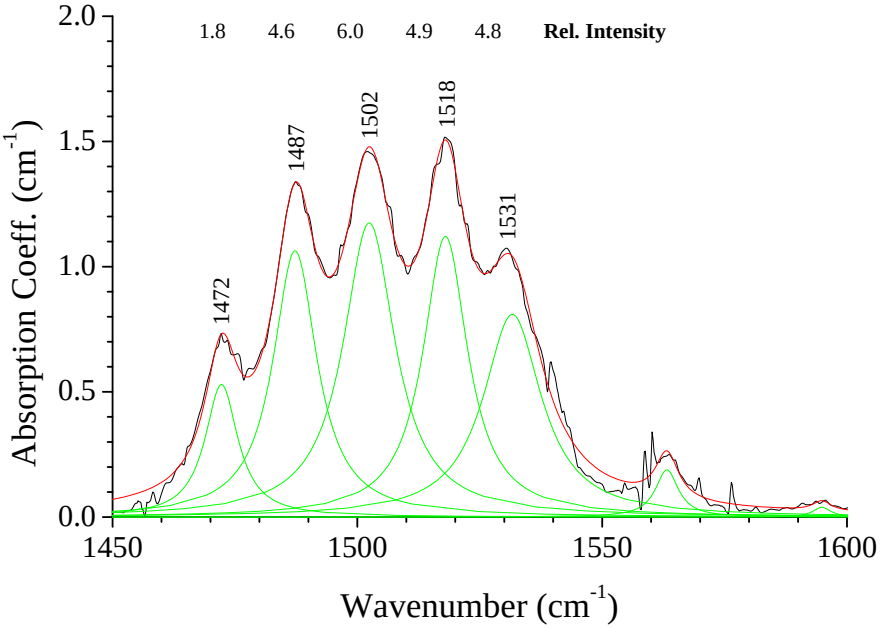

(b)

Figure 8-5: Isotopic shift of the 1531 cm^{-1} absorption feature with ^{13}C. In (a), spectra illustrate samples of (i) a natural abundance (1.1% ^{13}C) (ii) 10% ^{13}C enrichment and (iii) 50% ^{13}C enrichment. (b) highlights the deconvolved spectra resulting from a sample enriched with 50% ^{13}C. The relative intensities of the fitted lines are indicated. This highlights the deviation from the 1:4:6:4:1 intensity ratio that would be expected for four equivalent carbons in the defect. Spectra were taken at room temperature and spectra in (a) have been offset for clarity.

is not sufficient. Note also that the spacing between the lines varies between 13 and 15 cm^{-1}.

8.4.2 Neutron irradiation studies of type Ib diamond

8.4.2.1 Isotopic substitution studies of type Ib diamond

Two neutron irradiated HPHT type Ib samples, one with a natural abundance of ^{15}N (0.36%) and a second enriched with ~ 95% ^{15}N, were compared post annealing at 1500℃ for 15 hours (Figure 8-6). An absorption at 1858 cm^{-1} observed commonly in radiation damaged type Ia natural diamonds was apparent, arising from a defect containing two nitrogen atoms. The isotope shifts observed between these samples were in agreement with those previously reported.

A number of lines were also observed in the range of 2500–7000 cm^{-1} (Figure 8.6(b)). None of these lines showed any shift with ^{14}N to ^{15}N isotopic substitution. If these lines were resulting from electronic transitions of nitrogen related defects, only a very small shift would be expected, very much less than the linewidth of the feature.

A significant variation in the intensity of the features between the ^{14}N and ^{15}N enriched samples was apparent. The concentration of nitrogen in the ^{14}N sample was 4.0 times that of the ^{15}N doped sample. However, the ratios of the principal features at 2912, 4399, 4935 and 6459 cm^{-1} were found to be 5.6(3), 5.1(3), 0.6(1) and 1.9(2) between the ^{14}N and ^{15}N doped samples, respectively.

Absorption lines observed in the type IIa samples are present in samples with lower nitrogen doping but not in samples with higher nitrogen concentration. This result is perhaps not surprising. If the absorption features in the range 4000–4200 cm^{-1} in the IIa sample are vacancy aggregates, then assuming that the 5×10^{17} neutrons per cm^2 produces approximately 100–200 ppm of vacancies, in the heavily nitrogen doped samples where [N]>[V], nearly all vacancies will be trapped. However, in lightly doped samples, there [V]>[N], not all vacancies will be trapped and the production of the vacancy aggregates will be possible.

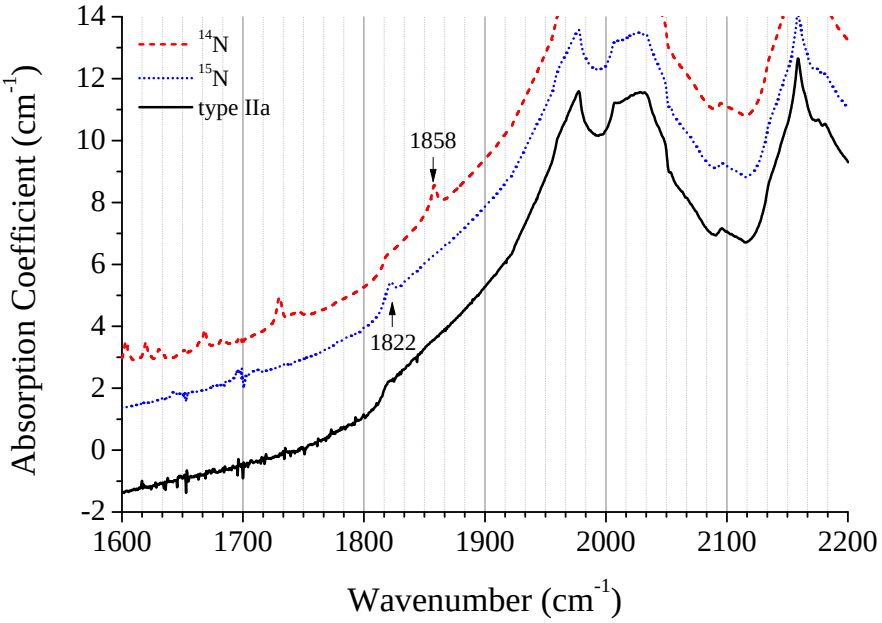

(a)

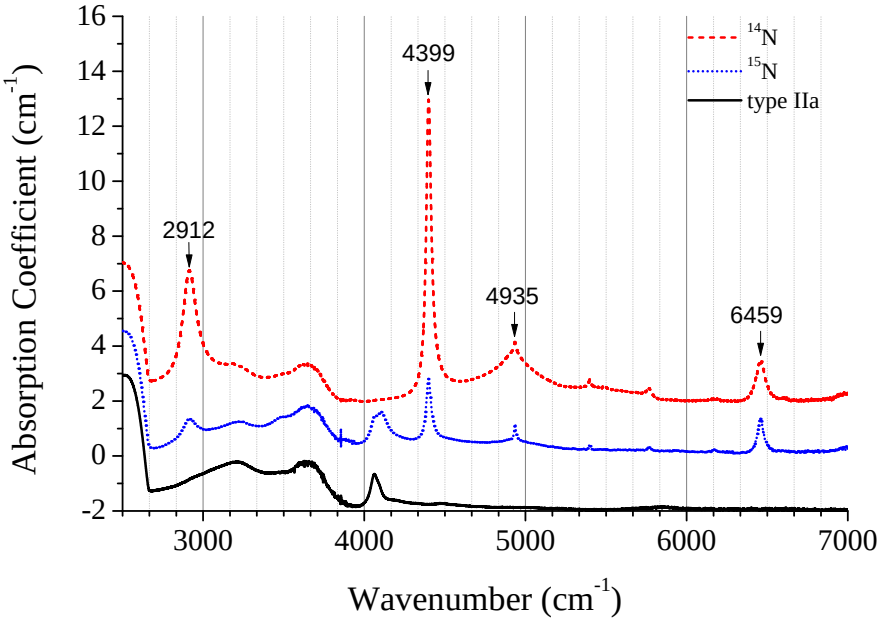

(b)

Figure 8-6: Spectra comparing type Ib neutron irradiated diamond of natural abundance ([N] = 240 ppm) and 95% enriched with ^{15}N ([N] = 60 ppm) after annealing at 1500℃ for 15 hours. (a) focusses on the absorption at 1858 cm^{-1} in ^{14}N doped samples, shifting to 1822 cm^{-1} in ^{15}N enriched diamond. (b) illustrates the 2500–7000 cm^{-1} region. Features in this region do not demonstrate a quantifiable shift with isotopic substitution. All spectra were taken at room temperature and have been offset for clarity.

8.4.2.2 Uniaxial stress studies of the 4399 cm^{-1} absorption feature

Uniaxial stress experiments were performed in conjunction with infrared spectroscopy to attempt to identify the symmetry and structure of the defect responsible for the 4399 cm^{-1} absorption feature. This was assumed to be the 4397 cm^{-1} absorption feature previously reported, which grew in under the same conditions.

Uniaxial stress experiments were performed at room temperature using the two nitrogen doped, irradiated (5×10^{15} neutrons per cm^2) and annealed (1500℃ for 15 hours) samples. For this study, the ^{14}N sample was cut such that the faces were (111), (11$\bar{2}$) and (1$\bar{1}$0) orientated and the ^{15}N enriched sample had faces parallel to the (001), (110) and (1$\bar{1}$0) planes. Together, these samples permitted a full investigation of defect symmetry.

Figure 8-7 shows the experimental stress spectra for the 4399 cm^{-1} absorption feature compared with that predicted theoretically for a monoclinic I defect with its dipole orientation along the $\langle 11\bar{3} \rangle$ direction. The number of splittings of the transitions under stress were characteristic of a monoclinic I defect and very similar in nature to that observed for the H1b defect. The rate of splitting was in excellent agreement with that of the monoclinic model outlined by Bech Nielsen *et al.* and Mohammed *et al.* (Figure 8-8) [26, 27]. For an $A \rightarrow A$ transition at a monoclinic I centre, the stress spectra are characterised by four parameters A_1, A_2, A_3 and A_4. The model lines in Figure 8-7 show the least squares fit to the proposed transition and symmetry, resulting in the parameters quoted in (8-2).

$$\begin{aligned} {}^{exp}A_1 &= +31.8(7)\ cm^{-1}GPa^{-1} \\ {}^{exp}A_2 &= -10.6(7)\ cm^{-1}GPa^{-1} \\ {}^{exp}A_3 &= +0.84(2)\ cm^{-1}GPa^{-1} \\ {}^{exp}A_4 &= +10.4(7)\ cm^{-1}GPa^{-1} \end{aligned} \tag{8-2}$$

A monoclinic centre has a twofold rotation axis (C_2). The symmetry is too low for degenerate states to exist and hence, the stress-induced splitting originates solely from the orientational degeneracy of the defect. For a monoclinic I centre, C_2 is parallel to the $\langle 110 \rangle$ direction, as opposed to the $\langle 001 \rangle$ axis for monoclinic II defects. The relative intensities of the stress-split components are therefore dependent upon the orientation of the optically active dipole. The relative intensities

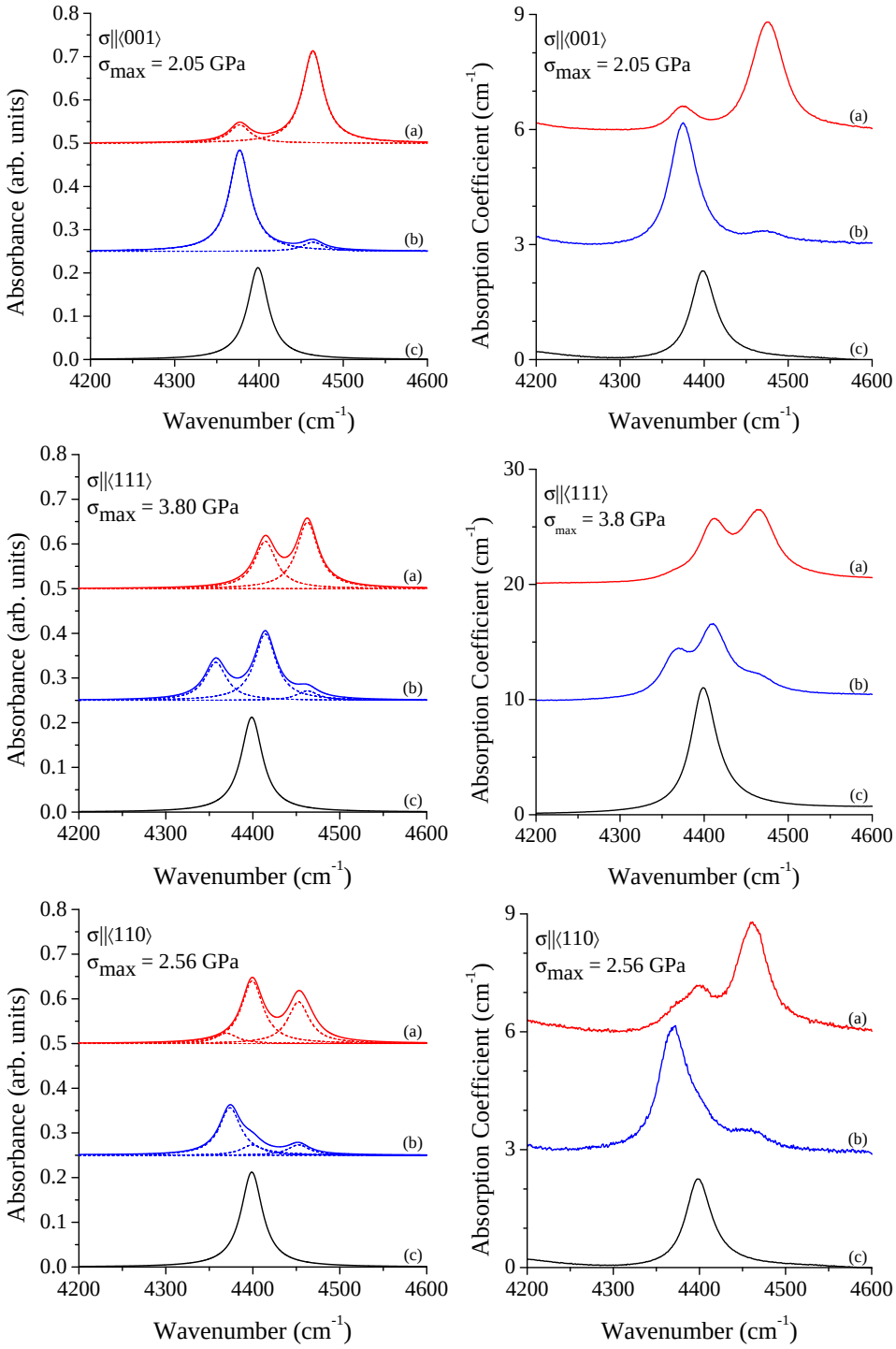

Figure 8-7: Uniaxial stress splitting data for the 4399 cm^{-1} absorption feature. The left hand column illustrates a simulated splitting of a monoclinic I defect (with θ = 25°), based on the experimentally determined piezospectroscopic parameters for the 4399 cm^{-1} mode. This is in comparison to the experimental spectra observed for the 4399 cm^{-1} defect in the right column. The simulated spectra shows the convolution of the contributions of each transition. In all spectra, the electric dipole vector is orientated (a) parallel and (b) perpendicular to the direction of stress. (c) represents the unstressed spectrum. Spectra were all collected at room temperature and have been offset for clarity.

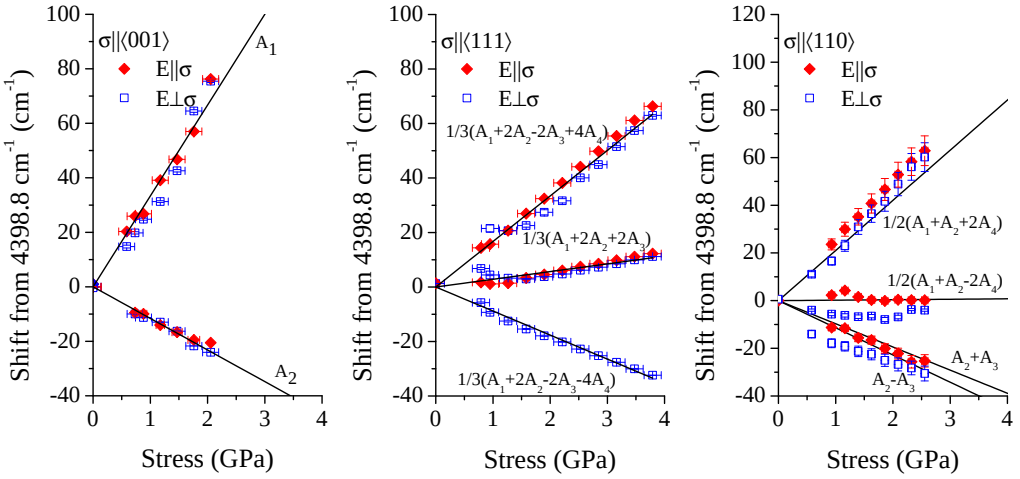

Figure 8-8: Transition frequency shifts for the 4399 cm^{-1} absorption feature for stress applied in the ⟨001⟩, ⟨111⟩ and ⟨110⟩ directions. Experimental data points are overlayed with the best fit model for a monoclinic I (C_{1h}) centre.

of the absorbance lines can be calculated based on tables published by Davies *et al.* and Bech Nielsen *et al.* and are summarised in Table 8-1 [27, 28].

A method of least squares fitting, comparing the theoretical intensities as predicted by Table 8-1 concluded a value for θ of 25°, i.e. approximately ⟨$\bar{1}$13⟩. Considering the modelling of a defect with this orientation, the experimental data and theoretical models are in good accord (Figure 8-7).

Figure 8-9 highlights the sensitivity the intensity of the transition has to the orientation of the dipole to the (001) plane. In the region around 25°, the rate of change in intensity with angle is at its greatest. The intensities found experimentally do not match perfectly with those modelled. Error in fitting of the lineshapes, especially for those for stress in the ⟨110⟩ direction, was significant due to the poor resolution between transitions. However, the rate of splitting of the defect and the number of active transitions under applied stress, match very well with the behaviour of a defect with monoclinic I symmetry.

8.4.2.3 Uniaxial stress studies of the other absorption features in the MIR region

For the 2912 cm^{-1} absorption feature, the lack of resolvable splitting and minimal shift at these pressures (Figure 8-10), would suggest the defect to be *hard* in nature. This would suggest the inclusion of vacancies in this defect to be unlikely and for

Table 8-1: Stress-induced shifting and splitting of transitions originating from a centre with monoclinic I symmetry [27]. ω_0 is the transition frequency at zero stress with the magnitude of the induced shift being governed by parameters A_1, A_2, A_3 and A_4. I denotes the relative intensities of these transitions considering the orientation of the electric field relative to the direction of applied stress. The optically active dipole is located in the {110} plane, orthogonal to the principal axis of the defect and at an angle θ to the ⟨100⟩ axis. See also Appendix B.

Direction		**Transition Energy**	$I_\parallel$		$I_\perp$
[001]	ω_a	$\hbar\omega + A_1\sigma$	$4\cos^2\theta$		$2\sin^2\theta$
	ω_b	$\hbar\omega + A_2\sigma$	$4\sin^2\theta$		$2(1+\cos^2\theta)$
[111]	ω_c	$\hbar\omega + \frac{1}{3}(A_1 + 2A_2 - 2A_3 + 4A_4)\sigma$	$1+\sin^2\theta+\sqrt{2}\sin 2\theta$		$\frac{1}{2}+\frac{1}{2}\cos^2\theta-\sqrt{2}\sin 2\theta/2$
	ω_d	$\hbar\omega + \frac{1}{3}(A_1 + 2A_2 - 2A_3 - 4A_4)\sigma$	$1+\sin^2\theta-\sqrt{2}\sin 2\theta$		$\frac{1}{2}+\frac{1}{2}\cos^2\theta-\sqrt{2}\sin 2\theta/2$
	ω_e	$\hbar\omega + \frac{1}{3}(A_1 + 2A_2 + 2A_3)\sigma$	$2\cos^2\theta$		$2+\sin^2\theta$
			$I_{[110]}$	$I_{[001]}$	$I_{[1\bar{1}0]}$
[110]	ω_f	$\hbar\omega + \frac{1}{2}(A_1 + A_2 + 2A_4)\sigma$	$1+\cos^2\theta+\sqrt{2}\sin 2\theta$	$2\sin^2\theta$	$1+\cos^2\theta-\sqrt{2}\sin 2\theta$
	ω_g	$\hbar\omega + \frac{1}{2}(A_2 - A_3)\sigma$	$2\sin^2\theta$	$2\cos^2\theta$	0
	ω_h	$\hbar\omega + \frac{1}{2}(A_1 + A_2 - 2A_4)\sigma$	$1+\cos^2\theta+\sqrt{2}\sin 2\theta$	$2\sin^2\theta$	$1+\cos^2\theta+\sqrt{2}\sin 2\theta$
	ω_i	$\hbar\omega + \frac{1}{2}(A_2 + A_3)\sigma$	0	$2\cos^2\theta$	$2\sin^2\theta$

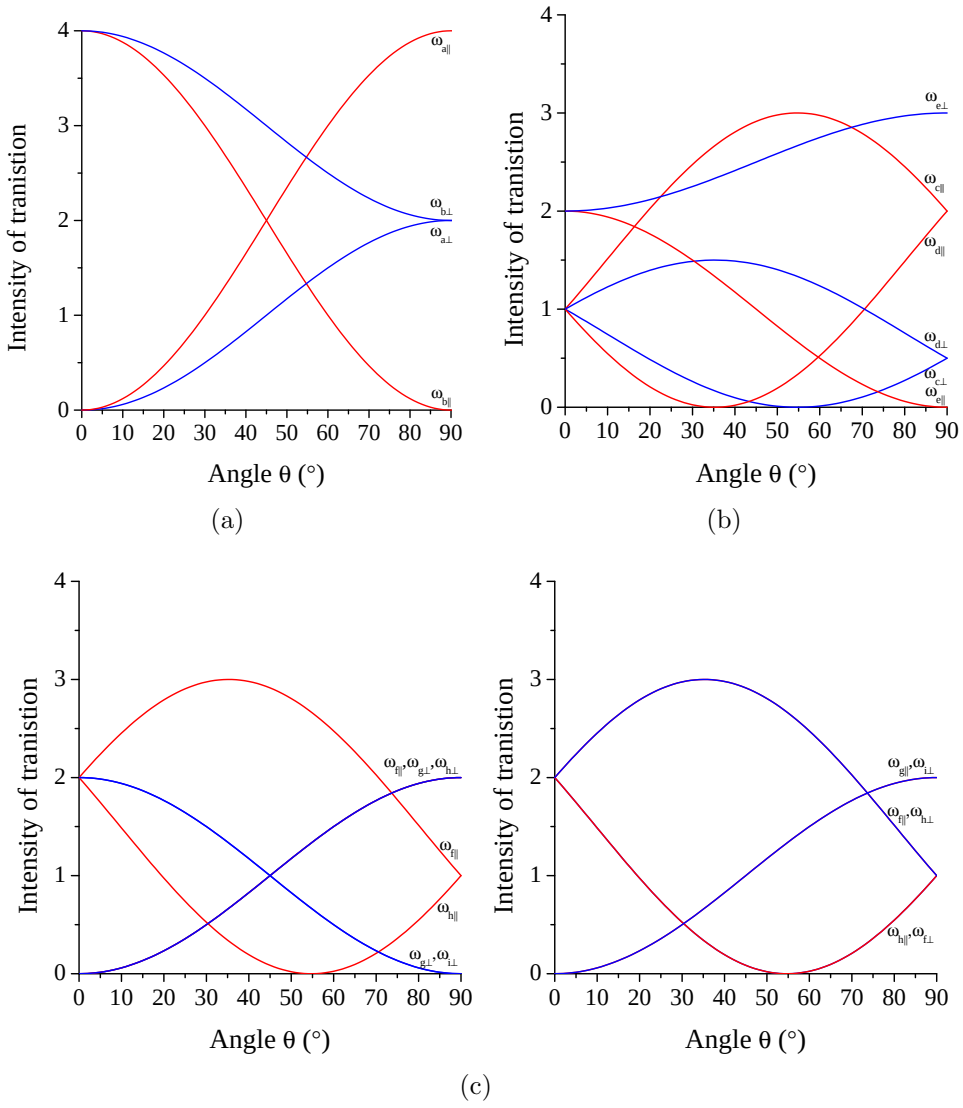

Figure 8-9: Plots show the changing intensity of a stress split transition with dipole orientation relative to the ⟨001⟩ axis arising from a monoclinic I defect. Transitions are shown which result from stress application in the (a) ⟨001⟩ direction, (b) ⟨111⟩ direction and (c) ⟨110⟩ direction (E∥⟨110⟩/⟨001⟩ and E∥⟨110⟩/⟨110⟩). These plots have been calculated using the formulae presented in Table 8-1.

it to more probably be associated with an interstitial type defect. An increase in the intensity of the unstressed transition would greatly aid in characterisation of this absorption feature as well as using higher pressures, increasing the relative splitting of the multiple transitions.

The H1b line at 4935 cm^{-1} behaved in a manor identical to that published by Collins *et al.* [20]. This provided confidence in the experimental procedure in producing accurate results that were reproducible and in agreement with those already published.

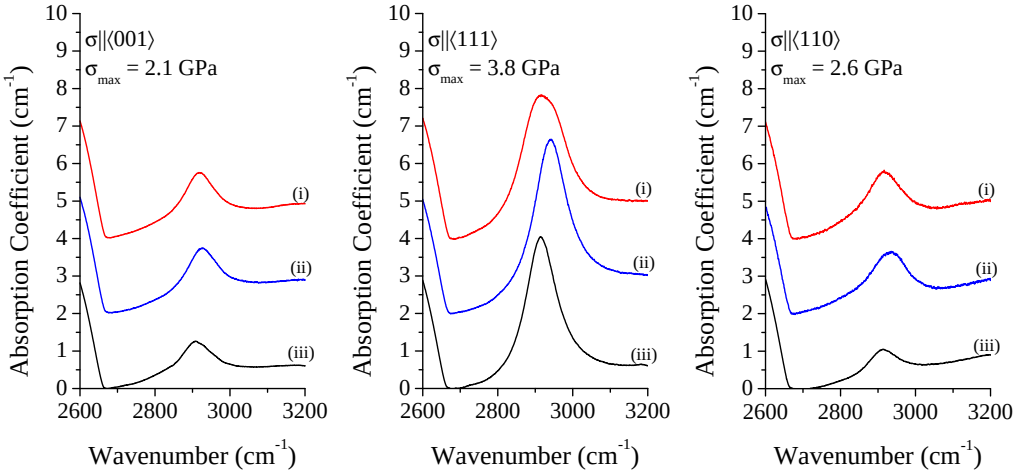

Figure 8-10: Stress induced splitting spectra of the 2912 cm^{-1} absorption feature arising post neutron irradiation and annealing at 1500℃ for 15 hours. Spectra shown are for stress applied along the ⟨001⟩, ⟨111⟩ and ⟨110⟩ directions at 2.1, 3.8 and 2.6 GPa. In each graph, spectra are shown for the electric dipole vector polarised (i) parallel and (ii) perpendicular to the direction of stress with (iii) illustrating the unstressed spectrum. With regards to the dramatic intensity difference for the absorption in the ⟨111⟩ direction, it should be noted that this is for the ^{14}N sample with a significantly greater concentration of nitrogen in the sample. Spectra were collected at room temperature and have been offset for clarity.

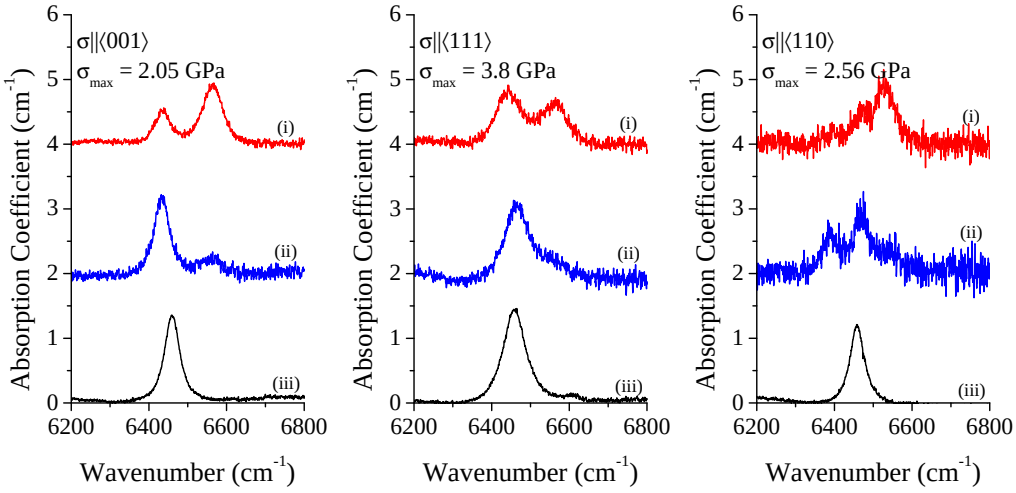

Figure 8-11: Stress induced splitting spectra of the 6459 cm^{-1} absorption feature arising post neutron irradiation and annealing at 1500℃ for 15 hours. Spectra shown are for stress applied along the ⟨001⟩, ⟨111⟩ and ⟨110⟩ directions at 2.1, 3.8 and 2.6 GPa. In each graph, spectra are shown for the applied stress polarised (i) parallel and (ii) perpendicular to the direction of stress with (iii) illustrating the unstressed spectrum. Spectra were collected at room temperature and have been offset for clarity.

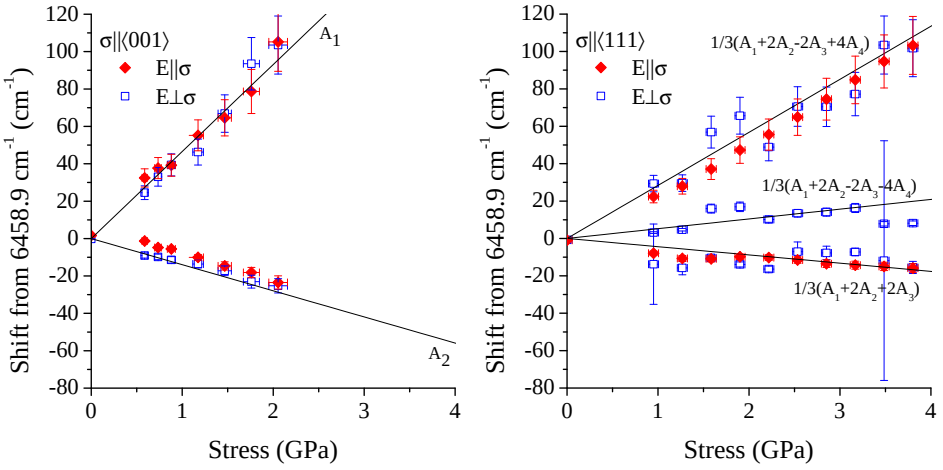

Figure 8-12: The graphs here indicate the stress induced shifting of the 6459 cm^{-1} absorption feature at room temperature. The solid lines indicate the predicted shift of the transitions of a defect with monoclinic I symmetry with the piezospectroscopic parameters as indicated in (8-3). Transitions were less well defined in the data from the ⟨111⟩ direction, which lead to larger errors in the identification of the peak positions.

The final absorption feature investigated was that at 6459 cm^{-1}. By eye, this displayed many similar splitting patterns to the 4399 cm^{-1} and 4935 cm^{-1} absorption features (Figure 8-11). The weakness of the signal made accurate determination of the split transitions intensities difficult. A monoclinic I splitting model could be theoretically fitted to the data (Figure 8-12), with the resulting parameters as quoted in (8-3).

$$\begin{aligned} {}^{\mathrm{exp}}\mathrm{A}_1 &= +47(2)\,\mathrm{cm}^{-1}\mathrm{GPa}^{-1} \\ {}^{\mathrm{exp}}\mathrm{A}_2 &= -14(1)\,\mathrm{cm}^{-1}\mathrm{GPa}^{-1} \\ {}^{\mathrm{exp}}\mathrm{A}_3 &= -16(1)\,\mathrm{cm}^{-1}\mathrm{GPa}^{-1} \\ {}^{\mathrm{exp}}\mathrm{A}_4 &= +8.7(8)\,\mathrm{cm}^{-1}\mathrm{GPa}^{-1} \end{aligned} \tag{8-3}$$

8.5 Conclusions

8.5.1 Type IIa neutron irradiated diamond

This chapter has aimed to further the fundamental research considering neutron irradiation damage and diamond. Neutron irradiation is highly damaging to the diamond lattice causing significant absorption in the one-phonon region. The

annealing behaviour can be fitted to first order kinetics but is neither consistent with the loss of absorption being attributed to vacancy nor interstitial defect migration. It would seem probable to attribute the irradiation damage induced absorption to the cascade damage; the recovery of this heavily damaged material deserves further study.

Neither the local vibrational modes at 1531 nor 1571 cm^{-1} follow the annealing behaviour expected for the isolated neutral $\langle 001 \rangle$-split self interstitial (I_{001}) defect. For the 1531 cm^{-1} local vibrational mode, the ^{12}C:^{13}C isotopic splitting suggests that the defect responsible may have four equivalent carbon atoms. Given the low thermal stability of this defect, it is tempting to speculate that this could be a T_d symmetry interstitial, although much more information such as from uniaxial stress studies is required to make this assignment with any certainty.

The 1571 cm^{-1} local vibrational mode survives to temperatures at which the vacancy would anneal out. Given that this mode is produced post irradiation by annealing, it would seem likely that it is an aggregate of primary irradiation damage defects but again, more research is required to determine the structure of this defect.

It would seem that a complex series of lines around 4100 cm^{-1} anneal in and out before the spectrum reported by Mita is observed. Given that the annealing temperature is above that where the di-vacancy anneals out, it is possible that the lines observed here and by Mita, relate to larger vacancy clusters. Given the recent interest in the properties of vacancy-clusters, for example with consideration to the brown colouration of diamond, further work is required on these defects.

8.5.2 Type Ib neutron irradiated diamond

The research reported here has determined the symmetry of the 4399 cm^{-1} (0.545 eV) centre to be monoclinic I, containing a $\{110\}$ mirror plane, with the dipole axis orientated along the $\langle \bar{1}13 \rangle$ direction. Given the larger piezospectroscopic parameters indicating the defect to be *soft*, it appears that the defect involves one or more vacancies. Its observation only in neutron irradiated samples would sway this argument towards the assignment of a multi-vacancy defect. The production of the defect only in nitrogen containing diamond, suggests the involvement of

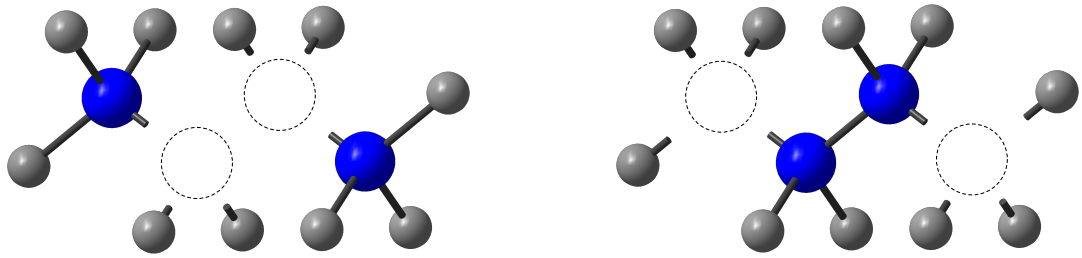

Figure 8-13: Potential models for the 4399 cm^{-1} defect. Both are appropriate for the identified symmetry of the 4399 cm^{-1} defect. Differentiation between these two structures would be difficult. In the figure, the larger blue atoms represent nitrogen and the dotted outlines, the position of the vacancy. The orientation of the dipole, found from uniaxial stress investigations, would suggest the defect with the two vacancies positioned between the two nitrogen atoms to be more probable.

nitrogen, although there is no direct evidence for its involvement in the defect structure. Nitrogen could be acting as a donor, putting the 4399 cm^{-1} defect into the appropriate charge state for detection.

Two possible structures for the 4399 cm^{-1} mode are shown in Figure 8-13. Both could be formed by the capture of a vacancy by the $NVN^{0/-}$ defect. Owing to the identification of the dipole axis orientation to be in the $\langle\bar{1}13\rangle$ direction, the NVVN structure seems more probable but deserves further study.

$$NVN + V \rightarrow NVVN \text{ or } VNNV \tag{8-4}$$

Since the 4399 cm^{-1} mode is photochromic, it is expected that at least one of the charge states be EPR active, encouraging further investigation. In addition, the transition identified at 6459 cm^{-1}, was shown to also fit to a monoclinic I symmetry, when considering the shifting and splitting response of the transition to stress. A fourth line at 2912 cm^{-1} did not split sufficiently for the transitions to be accurately resolved. The symmetry of the associated defect has therefore not been identified.

8.6 Further work

The results of this chapter have indicated that substantial further work is required regarding neutron irradiated diamond. Considering the one-phonon region, a more thorough annealing study with smaller temperature intervals and using a single

sample is required to better plot the annealing curve. This can then be compared across different sample types.

With regards to the 1531 and 1571 cm^{-1} defects, an investigation as to their presence in nitrogen doped diamond and isotopically enriched samples would be beneficial. Once produced in sufficient intensity, uniaxial stress experiments would help to identify the symmetry of the defect and its structure. Low temperature irradiation experiments would also be beneficial to understand the formation kinetics of these defects.

For the 4399 cm^{-1} defect, it is assumed that a charge state of this defect will be EPR active. Optical excitation experiments in conjunction with EPR could help to identify this alternate charge state and provide further structural information. In addition, an annealing study would aid the understanding of the annealing kinetics of the defect.

References

[1] C. Bauer, I. Baumann, C. Colledani, J. Conway, P. Delpierre, F. Djama, W. Dulinski, A. Fallou, K. K. Gan, R. S. Gilmore, et al., Nuclear Instruments and Methods in Physics Research Section A: Accelerators, Spectrometers, Detectors and Associated Equipment **367**, 207 (1995).

[2] C. Bauer, I. Baumann, C. Colledani, J. Conway, P. Delpierre, F. Djama, W. Dulinski, A. Fallou, K. K. Gan, R. S. Gilmore, et al., Nuclear Instruments and Methods in Physics Research Section A: Accelerators, Spectrometers, Detectors and Associated Equipment **380**, 183 (1996).

[3] M. Zoeller, W. Adam, C. Bauer, I. Baumann, C. Colledani, J. Conway, P. Delpierre, F. Djama, W. Dulinski, A. Fallou, et al., Nuclear Science, IEEE Transactions on DOI - 10.1109/23.603758 **44**, 815 (1997).

[4] D. Husson, C. Bauer, I. Baumann, C. Colledani, J. Conway, P. Delpierre, F. Djama, W. Dulinski, M. Edwards, A. Fallou, et al., Nuclear Instruments and Methods in Physics Research Section A: Accelerators, Spectrometers, Detectors and Associated Equipment **388**, 421 (1997).

[5] W. Trischuk, Nuclear Instruments and Methods in Physics Research Section A: Accelerators, Spectrometers, Detectors and Associated Equipment **419**, 251 (1998).

[6] P. Weilhammer, W. Adam, C. Bauer, E. Berdermann, F. Bogani, E. Borchi, M. Bruzzi, C. Colledani, J. Conway, W. Dabrowski, et al., Nuclear Instruments and Methods in Physics Research Section A: Accelerators, Spectrometers, Detectors and Associated Equipment **409**, 264 (1998).

[7] A. Mainwood, J. Cunningham, and D. Usher, Materials Science Forum **258-263**, 787 (1997).

[8] J. Koike, D. M. Parkin, and T. E. Mitchell, Applied Physics Letters **60**, 1450 (1992).

[9] M. W. Thompson, *Defects and radiation damage in metals* (Cambridge University Press, 1969).

[10] A. Mainwood, Diamond and Related Materials **7**, 504 (1998).

[11] J. B. Gibson, A. N. Goland, M. Milgram, and G. H. Vineyard, Physical Review **120**, 1229 (1960).

[12] C. Erginsoy, G. H. Vineyard, and A. Englert, Physical Review **133**, A595 (1964).

[13] G. Davies, Nature **269**, 498 (1977).

[14] J. E. Lowther and A. M. Stoneham, Journal of Physics C: Solid State Physics **11**, 2165 (1978).

[15] L. Allers, A. T. Collins, and J. Hiscock, Diamond and Related Materials **7**, 228 (1998).

[16] G. S. Woods, Philosophical Magazine B **50**, 673 (1984).

[17] A. T. Collins and G. S. Woods, Journal of Physics C: Solid State Physics **20**, L797 (1987).

[18] A. T. Collins, Journal of Physics C: Solid State Physics **13**, 2641 (1980).

[19] Y. Mita, Y. Yamada, Y. Nisida, M. Okada, and T. Nakashima, Physica B: Condensed Matter **376-377**, 288 (2006).

[20] A. T. Collins, G. Davies, and G. S. Woods, Journal of Physics C: Solid State Physics **19**, 3933 (1986).

[21] A. Kaplyanskii, Optics and Spectroscopy **16**, 329 (1964).

[22] Y. Mita, H. Kanehara, and Y. Nisida, Diamond and Related Materials **6**, 1722 (1997).

[23] Y. Mita, Y. Shiraki, and Y. Nisida, Solid State Communications **102**, 659 (1997).

[24] D. Hunt, PhD. thesis, St. Peter's College, University of Oxford (1999).

[25] G. Davies, S. C. Lawson, A. T. Collins, A. Mainwood, and S. J. Sharp, Physical Review B **46**, 13157 (1992).

[26] K. Mohammed, G. Davies, and A. T. Collins, Journal of Physics C: Solid State Physics **15**, 2779 (1982).

[27] B. Bech Nielsen and H. G. Grimmeiss, Physical Review B **40**, 12403 (1989).

[28] G. Davies, E. C. Lightowlers, M. Stavola, K. Bergman, and B. Svensson, Physical Review B **35**, 2755 (1987).

Chapter 9

Summary and further work

9.1 Introduction

Doping, annealing (HPHT and tube furnace methods) and irradiation damage (electron and neutron), have been used to produce point defects in diamond. These defects have been studied using optical spectroscopy, EPR and uniaxial stress with FTIR spectroscopy to further the understanding of their structure and properties. It has been shown that no one technique is sufficient for the complete assessment of a defect. However, the combination of uniaxial stress with FTIR spectroscopy, isotopic substitution and theoretical modelling has been demonstrated to be particularly effective in determining defect symmetries and structures. Furthermore, annealing experiments provide further information on the mechanisms involved in the formation and annihilation of defects so that a complete picture of the defect properties and interactions could be constructed.

9.2 Nitrogen related defects in diamond

Studies on HPHT diamond samples doped with ~95% ^{15}N in the as-grown state or following irradiation and annealing, have permitted the deconvolution of the complex one-phonon infrared spectrum into constituent spectra of $^{15}N_S^0$, $^{15}N_S^+$ and ^{15}A. Comparing the intensity of the component spectra for $^{15}N_S^0$ and the concentration of this centre as determined by EPR, the concentration conversion factor was calculated to be 27 ppm per 1 cm^{-1} absorption at 1121 cm^{-1}. This was calculated

to be, within error, equal to that reported for the $^{14}N_S^0$ variant. Using the newly deconvolved component spectra for the ^{15}N spectra, a revision of a *concentration calculator* for infrared spectra from ^{15}N doped samples was implemented.

The isotopic substitution investigation identified several features in the N_S^+ component spectra. These lines were weak in intensity compared to the 1332 cm^{-1} LVM but a shift in the absorption at 950 cm^{-1} to 940 cm^{-1} and 1046 cm^{-1} to 1040 cm^{-1} was observed for ^{15}N enriched diamond. For the A-centre component spectra, a shift resulting from the ^{15}N substitution was measured for the peak at 1282 cm^{-1}, shifting to 1267 cm^{-1} for the same enrichment.

Uniaxial stress FTIR measurements enabled the 1344 cm^{-1} LVM to be identified as a transition with $A \rightarrow E$ symmetry. The piezospectroscopic parameters for the 1344 cm^{-1} LVM from the stress induced splitting and shifting rates, were found to be in excellent agreement with those calculated by DFT modelling of the N_S^0 defect. Not only did this highlight the strength of computer simulation in predicting the stress induced behaviour of defects in the rigid diamond structure but also the accuracy that could be attained, even for LVMs only 12 cm^{-1} above the Raman cut-off frequency of diamond.

The theoretical intensities of the stress split components of the trigonal 1344 cm^{-1} LVM, assuming equal populations of the symmetry related sites, were not in agreement with those observed experimentally for stress applied in the $\langle 111 \rangle$ and $\langle 110 \rangle$ directions. The results indicated that the population for the different symmetry related sites was varying under the application of stress. In the $\langle 111 \rangle$ direction, stress application of 3.7 GPa induced a near complete depopulation of the unique extended N–C bond site (with the unpaired electron in this N–C anti-bonding orbital). It was shown that the reorientation of the N_S^0 defect was consistent with the thermally induced hopping and tunnelling observed by EPR for the N_S^0 centre [1, 2].

N_S^+ produced stress induced splittings and peak shifts that could not be successfully analysed by theory for a LVM of a defect with T_d symmetry. The stress induced splitting and shifting may result from a combination of a stress induced perturbation of: the diamond lattice, the N_S^+ defect and possibly some other centre contributing to the 1332 cm^{-1} LVM.

9.3 The H1a defect

In work presented in this thesis, it has been conclusively shown that the H1a LVM originates from the ⟨001⟩-split di-nitrogen interstitial defect, ending the years of debate. Confusion arising from the analysis of the isotopic substitution data with regard to the number of nitrogen atoms involved in the vibration, has been resolved by identifying the nature of the LVM in which the two nitrogen atoms are decoupled. Uniaxial stress studies identified the mode of the H1a LVM to arise from an $A \rightarrow E$ transition at a defect with D_{2d} symmetry, consistent with the ⟨001⟩-split di-nitrogen interstitial structure. The agreement between the experimentally determined piezospectroscopic parameters and those determined from DFT calculations is excellent. Furthermore, such calculations also make good predictions of the LVM energies and isotopic shifts. The bond centred proposal for the H1a defect was implausible after the recent identification of the ⟨001⟩-split nitrogen interstitial defect, WAR9.

9.4 Hydrogen related defects in diamond

Hydrogen is incorporated into CVD diamond during growth in a variety of different defect structures. Comparing the photo-/thermo- chromic behaviour of the 3123 cm^{-1} LVM and the NVH^- EPR defect, it has been possible to identify that the 3123 cm^{-1} LVM originates from the neutral charge state of the NVH defect. Correlations between the change in intensity of the 3123 cm^{-1} absorption feature and the change in concentration of the NVH^- defect as calculated from EPR, have permitted calculation of the absorption strength of the 3123 cm^{-1} LVM. 1 cm^{-1} absorption at 3123 cm^{-1} is equal to a defect concentration of 1400(150) ppb.

Data are presented highlighting LVMs potentially associated with the NVH^- defect. Predicted to occur at an energy less than that of the NVH^0 defect [3], absorption features at 2727 and 2807 cm^{-1} are possible candidates for the C–H stretch mode of the NVH^- defect. Both display appropriate photo-/thermochromic behaviour but neither could be sufficiently split by the application of stress to identify their symmetry (expected to be monoclinic I as identified for NVH^0).

Theoretical modelling of the stress induced behaviour of the N:H–C defect was in poor agreement with the experimentally observed behaviour of the 3107 cm^{-1} LVM to which is was assigned. A more complementary assignment is to the 3324 cm^{-1} mode. The 3324 cm^{-1} absorption feature is of the correct symmetry, does not display any photo-/thermo- chromic behaviour as expected for the N:H–C defect and has a suitable thermal stability compared to that predicted theoretically for the N:H–C structural model. However, this leaves the 3107 cm^{-1} absorption feature unidentified.

Results presented in this chapter have extended the knowledge of the production of the 3107 cm^{-1} LVM in CVD diamond. HPHT annealing at 2300℃ highlighted the extreme stability of this defect. It was found that the intensity of the 3107 cm^{-1} LVM produced upon annealing of CVD diamond at 2100(200)℃ for 60 minutes, correlated with the total substitutional nitrogen (N_S^0 + N_S^+) concentration squared in the as-grown material. Given the evidence from isotopic substitution experiments using ^{15}N enriched samples showing no observable shift of the 3107 cm^{-1} LVM and the identification by Kiflawi *et al.* of a linear dependence of mode intensity with nitrogen concentration in HPHT samples doped with a high concentration of nitrogen, careful thought needs to be given as to the role of nitrogen in the defect.

9.5 Neutron irradiation and diamond

Neutron irradiation is known to cause significantly more lattice damage compared to electron irradiation, as a result of a cascade effect of carbon atoms knocked from their lattice sites into interstitial positions. The high concentration of vacancies and interstitials available to migrate through the lattice and form complexes with other point defects results.

In type IIa diamond, the one-phonon defect related infrared absorption observed post neutron irradiation, anneals out in a manner which cannot be described by the migration of single vacancies or interstitials. A very small activation energy was observed with a rate constant that was almost independent of temperature. Further study of the recovery from such high damage is required.

Local vibrational modes at 1531 cm^{-1} post neutron irradiation and 1571 cm^{-1} post neutron irradiation and annealing, were identified and neither followed the annealing behaviour predicted for the ⟨001⟩-split self interstitial defect. In a sample enriched with 50% ^{13}C, the 1530 cm^{-1} absorption feature was observed to split in a manner similar to that expected for a vibration involving four equivalent carbon atoms. However, the intensities of the five components did not match the simple theoretical prediction. The 1571 cm^{-1} mode survives annealing at temperatures at which the vacancy is known to anneal out, suggesting it to arise from a more stable aggregate of primary irradiation damage defects.

In type Ib material, the 4399 cm^{-1} absorption feature formed post irradiation (at temperatures less than 200℃) and annealing at 1500℃, was identified by uniaxial stress to originate from a defect with monoclinic I symmetry. The large piezospectroscopic parameters suggests this defect to involve one or more vacancies and a multi-vacancy NVVN or VNNV type structure is tentatively proposed. The strong photochromic behaviour of this centre is an interesting topic for further research. In addition, the absorption feature at 6459 cm^{-1} was also identified as originating from a monoclinic I defect.

The common theme of this thesis and possibly the most important new aspect of this work, is the identification of the power of uniaxial stress as a tool for the determination of crystal symmetry from the characteristic stress induced shifting and splitting of transitions. Its accuracy in the assessment of transitions is clear when experimental results are compared to theoretical modelling of known defect structures. In addition to the characterisation of several new defects that arise from annealing and irradiation treatments of point defects in single crystal diamond, this work encourages the calculation of piezospectroscopic parameters for the vibrational modes of other defects, to aid in the assignment of the plethora of vibrational modes observed for defects in diamond. The combination of theory and experiment will help to assign transitions of the same symmetry, with substantially different parameters, to their correct atomistic models.

9.6 Further work

In this thesis it has been demonstrated that uniaxial stress FTIR spectroscopy can be used to investigate the nature of LVMs in diamond, for example the 1344 cm^{-1} LVM of N_S^0, 1450/1426 cm^{-1} for N_{2I} and 3324 cm^{-1} for the N:H–C defect, despite many of these modes being relatively "stiff". Furthermore, it is now apparent that DFT theories can predict the LVM for model defect structures with a high degree of accuracy and that robust predictions of piezospectroscopic parameters are possible. This invites the combined experimental and theoretical approach to be more widely exploited on unidentified LVMs in diamond. For example,

- 1858/1822 cm^{-1} ($^{14}N/^{15}N$) - high symmetry (at least C_{2v}) di-nitrogen defect (§8.2.1.1). Is this LVM related to the H2/H3 defect [4]?
- 3236 cm^{-1} - possible N–H complex [5]
- 1353 cm^{-1} (C_{2v}) and 1371 cm^{-1} (D_{2d}) - possible vacancy-hydrogen complexes [6]

Results of this thesis have provided evidence of the preferential orientation of defects under uniaxial stress, for example the 1344 cm^{-1} LVM of the N_S^0 defect (5.4.2.2). This effect now needs to be considered in conjunction with the assessment of the nature of defects from uniaxial stress experiments. For example, the 3123 cm^{-1} LVM assigned to the monoclinic I NVH^0 defect [6], displayed stress induced transitions with intensities not well modelled by theoretical predictions. Tunnelling of the hydrogen atom is known to occur in this defect. The application of stress may be forcing the tunnelling hydrogen atom into a specific orientation and hence the same analysis will be appropriate to simulate the preferential occupation of specific defect sites. Hydrogen tunnelling is expected to be common to all vacancy hydrogen defects in diamond [7] and therefore understanding of this effect is essential in understanding defect dynamics.

This thesis has identified the lack of understanding of the production of the defect responsible for the 3107 cm^{-1} LVM. Isothermal studies utilising HPHT annealing techniques are essential to gain an understanding of the defect's formation. The CVD synthesis of samples with a range of nitrogen abundances is required. The consequence of the span of nitrogen concentrations will be variation in the growth rates of the samples and therefore the probability of hydrogen abstraction

and the resultant concentration of hydrogen in the sample [8].

Investigations of neutron irradiation in diamond has proposed the repair of the lattice post heavy damage. This repairing mechanism needs to be understood. In addition, a range of defects have been identified in type IIa and Ib diamond that are only observed after neutron irradiation. An obvious progression of the investigation is the thorough cataloguing of their symmetry by uniaxial stress FTIR spectroscopy and assessment of their production kinetics by annealing experiments. EPR investigations may also be beneficial, motivated by the observed photochromic behaviour of the 4399 cm^{-1} defect. If these defects display a charge transfer effect, at least one of the states must be paramagnetic and therefore EPR active. Further understanding is also required of the production of vacancy clusters as a result of neutron irradiation, essential knowledge in the understanding of the brown colouration of diamond.

Our understanding of the properties and recovery of heavily damaged diamond on annealing is not very advanced. Given the development of diamond for radiation and particle detectors such as by project RD42 - "Development of diamond tracking detectors for high luminosity experiments at the LHC" at CERN and the possibility of using diamond as a plasma facing material in fusion reactors, this situation must be remedied.

References

[1] C. A. J. Ammerlaan and E. A. Burgemeister, Industrial Diamond Review **40**, 128 (1980).

[2] C. A. J. Ammerlaan and E. A. Burgemeister, Physical Review Letters **47**, 954 (1981).

[3] J. P. Goss, P. R. Briddon, R. Jones, and S. Sque, Journal of Physics: Condensed Matter **15**, S2903 (2003).

[4] A. T. Collins and G. S. Woods, Journal of Physics C: Solid State Physics **20**, L797 (1987).

[5] E. Fritsch, T. Hainschwang, L. Massi, and B. Rondeau, New Diamond and Frontier Carbon Technology **17**, 63 (2007).

[6] R. J. Cruddace, PhD. thesis, University of Warwick (2007).

[7] A. Kerridge, A. H. Harker, and A. M. Stoneham, Journal of Physics: Condensed Matter **16**, 8743 (2004).

[8] T. Van Regemorter and K. Larsson, Diamond and Related Materials **17**, 1076 (2008).

Appendices

Appendix A

Defect Symmetries

Following, is a list of common defect symmetries mentioned in this thesis. Included is an explanation of their symmetry operations and elements and representative stereographs and 3D objects.

A stereograph is to be interpreted as a schematic diagram of an object viewed down its principal axis. Equatorial rotation axes and mirror planes lie in the plan of the diagram. The ⬬, ▲, ■ etc. represent the axes of crystallographic symmetry (2-, 3-, 4–fold etc.) and the solid lines, the lines of reflection. The symbols + and ∘ represent positions in space that are related by the symmetry operation above and below the plane of the diagram respectively.

Table A-1: Possible symmetries for distorted tetrahedral point sites.

Symmetry	**Distortion**	**Stereograph**	**3D Object**
Tetragonal eg. D_{2d}	[001] axial distortion	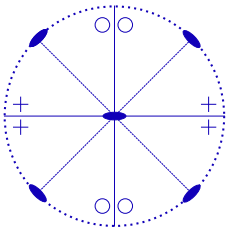	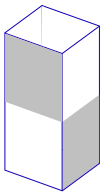
Rhombic I eg. C_{3v}	Rotation about [001] maintained with [110] distortion	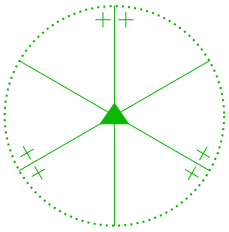	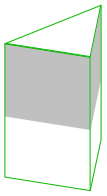
Rhombic II eg. D_2	[100] and [010] axial distortion	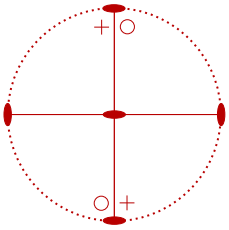	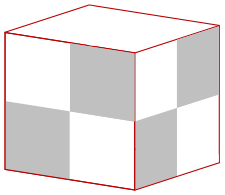
Monoclinic I eg. C_{1h}	[111] axial distortion without inversion symmetry	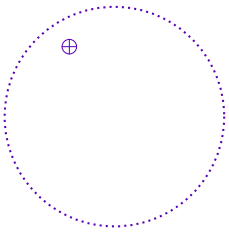	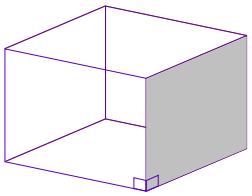
Monoclinic II eg. C_2	[100] and general non-axial distortion	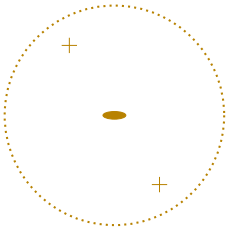	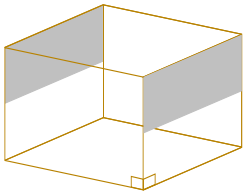

Appendix B

Effects of uniaxial stress on optical transitions

Table B-1 gives the theoretical effects of uniaxial stress on the vibrational transitions occurring for different symmetry class operations. The table outlines the effects of uniaxial stress when applied in the ⟨001⟩, ⟨111⟩ and ⟨110⟩ directions, resolving them both parallel and perpendicular to the direction of stress.

For each stress direction, the number of resulting transitions is given. Accordingly, the intensity of each transition is also stated. For example, for a tetragonal line stressed in the ⟨001⟩ direction, the line may be composed of 3 transitions. These appear in ratios of 0:1, 2:0 and 0:1, where 0:1 indicates the relative intensity of these transitions observed post parallel:perpendicular excitation with respect to the direction of stress. The situation is complicated slightly for stress in the ⟨110⟩ direction as a result of the crystal becoming biaxial under ⟨110⟩ stress.

Table B-1: Possible symmetries for distorted tetrahedral point sites, adapted from a paper by Kaplyanskii *et al.* [1].

		$\sigma \parallel \langle 001 \rangle$				$\sigma \parallel \langle 111 \rangle$				$\sigma \parallel \langle 110 \rangle$					
			Abs.	$E \parallel \sigma$	$E \perp \sigma$		Abs.	$E \parallel \sigma$	$E \perp \sigma$		Abs.	$E \parallel \sigma$		$E \perp \sigma$	
Type of centre	Transition	Energy	$E_\parallel$:$E_\perp$	$E_\parallel$:$E_\perp$	$E_\parallel$:$E_\perp$	Energy	$E_\parallel$:$E_\perp$	$E_\parallel$:$E_\perp$	$E_\parallel$:$E_\perp$	Energy	E_{110} : E_{001} : $E_{1\bar{1}0}$	E_{110} : E_{001}	E_{110} : $E_{1\bar{1}0}$	E_{110} : E_{001}	E_{110} : $E_{1\bar{1}0}$
Tetragonal	$A \leftrightarrow B$	A_1	1:0	2:0	0:0	$\frac{1}{3}(A_1+2A_2)$	1:1	2:2	2:1	$\frac{1}{2}(A_1+A_2)$	1:0:1	1:0	1:1	1:0	0:0
		A_2	0:1	0:0	0:1					(A_2)	0:1:0	0:0	0:0	0:0	0:0
	$A \leftrightarrow E$	A_1	0:1	0:0	0:2	$\frac{1}{3}(A_1+2A_2+C)$	4:1	16:4	16:5	$\frac{1}{2}(A_1+A_2+B)$	1:0:1	1:0	1:1	1:0	2:0
		A_2+B	2:0	4:0	2:0	$\frac{1}{3}(A_1+2A_2-C)$	0:3	0:12	0:9	$\frac{1}{2}(A_1+A_2-B)$	0:2:0	0:2	0:0	0:2	0:0
		A_2-B	0:1	0:2	0:1					$A_2+\frac{1}{2}C$	1:0:0	2:0	2:0	2:0	0:0
	$E \leftrightarrow E$	A_1	2:0	4:0	0:0	$\frac{1}{3}(A_1+2A_2+C)$	1:1	2:2	2:1	$\frac{1}{2}(A_1+A_2+B)$	1:0:1	1:0	1:1	1:0	1:1
		A_2+B	0:1	0:0	0:1	$\frac{1}{3}(A_1+2A_2-C)$	1:1	2:2	2:1	$\frac{1}{2}(A_1+A_2-B)$	1:0:1	1:0	1:1	1:0	1:1
		A_2-B	0:1	0:0	0:1					$A_2-\frac{1}{2}C$	0:1:0	0:0	0:0	0:0	0:0
										$A_2-\frac{1}{2}C$	0:1:0	0:0	0:0	0:0	0:0
Trigonal	$A \leftrightarrow A$	A_1	1:1	1:1	1:0	A_1+2A_2	3:0	27:0	2:0	A_1+A_2	2:1:0	2:1	2:0	0:0	1:0
						$\frac{1}{3}(3A_1-2A_2)$	1:4	1:4	4:8	A_2-A_2	0:1:2	0:0	0:0	0:1	0:1
	$A \leftrightarrow E$	A_1-2B	4:1	8:2	8:3	A_1+2A_2	0:6	0:0	0:54	A_1+A_2+C-B	0:0:3	0:0	0:3	0:0	0:6
		A_1+2B	0:3	0:6	0:3	$\frac{1}{3}(3A_1-2A_2-4C)$	16:1	128:8	80:7	A_1+A_2-C+B	1:2:0	1:2	1:0	3:6	2:0
						$\frac{1}{3}(3A_1-2A_2+4C)$	0:9	0:72	0:27	$A_1-A+2+C+B$	0:2:1	0:6	0:3	0:2	0:2
										A_1-A_2-C-B	3:0:0	9:0	9:0	3:0	6:0
Rhombic I	$A \leftrightarrow B$	A_1	0:1	0:0	0:0	$\frac{1}{3}(A_1+2A_2+2A_3)$	4:1	32:8	8:1	A_2+A_3	1:0:0	4:0	0:0	0:0	
		A_2	2:1	4:2	2:1	$\frac{1}{3}(A_1+2A_2-2A_3)$	0:3	0:0	0:9	$\frac{1}{2}(A_1+A_2)$	1:2:1	1:2	1:1	1:2	2:2
										A_2+A_3	0:0:1	0:0	0:0	0:0	0:0
	$A \leftrightarrow A$	A_1	1:0	2:0	0:0	$\frac{1}{3}(A_1+2A_2+2A_3)$	1:1	2:2	2:1	A_2+A_3	0:1:0	0:0	0:0	0:0	
		A_2	0:1	0:0	0:1	$\frac{1}{3}(A_1+2A_2-2A_3)$	1:1	2:2	2:1	$\frac{1}{2}(A_1+A_2)$	2:0:2	1:0	1:1	1:0	0:0
										A_2-A_3	0:1:0	0:0	0:0	0:0	0:0

Rhombic II	$A \leftrightarrow B$	A_1	0:1	0:0	0:1	$\frac{1}{3}(A_1+A_2+A_3)$	1:1	2:2	2:1	$\frac{1}{2}(A_1+A_2)$	1:0:1	1:0	1:1	1:0	0:0
		A_2	2:0	4:0	0:0					$\frac{1}{2}(A_1+A_3)$	0:2:0	0:0	0:0	0:0	0:0
		A_1	0:1	0:0	0:1					$\frac{1}{2}(A_2+A_3)$	1:0:1	1:0	1:1	1:0	0:0
Monoclinic I	$A'' \leftrightarrow A'$	A_1	0:1	0;0	0:0	$\frac{1}{3}(A_1+2A_2+2A_3)$	8:2	64:16	16:2	A_2+A_3	2:0:0	8:0	8:0	0:0	0:0
		A_2	2:1	2:1	2:1	$\frac{1}{3}(A_1+2A_2-2A_3-4A_4)$	0:3	0:0	0:9	$\frac{1}{2}(A_1+A_2-2A_4)$	0:2:1	1:2	1:1	1:2	2:2
						$\frac{1}{2}(A_1+2A_2-2A_3+4A_4)$	0:3	0:0	0:9	$\frac{1}{2}(A_1+A_2+2A_4)$	1:2:1	1:2	1:1	1:2	2:2
										A_2-A_3	0:0:2	0:0	0:0	0:0	0:0
	$A'' \leftrightarrow A''$	A_1	0:1	0:0	0:0	$\frac{1}{3}(A_1+2A_2+2A_3)$	0:6	0:0	0:18	A_2+A_3	0:0:2	0:0	0:0	0:0	0:0
		A_2	2:1	4:2	2:1	$\frac{1}{3}(A_1+2A_2-2A_3)$	4:1	32:8	8:1	$\frac{1}{2}(A_1+A_2-2A_4)$	1:2:1	1:2	1:1	1:2	2:2
						$\frac{1}{3}(A_1+2A_2-2A_3+4A_4)$	4:1	32:8	8:1	$\frac{1}{2}(A_1+A_2+2A_4)$	1:2:1	1:2	1:1	1:2	2:2
										A_2-A_3	2:0:0	8:0	8:0	0:0	0:0
Monoclinic II	$A \leftrightarrow A$	A_1	2:0	4:0	0:0	$\frac{1}{3}(A_1+A_2+A_3+2A_4)$	1:1	2:2	2:1	$\frac{1}{2}(A_2+A_3)$	1:0:1	1:0	1:0	0:0	
		A_2	0:1	0:0	0:1	$\frac{1}{3}(A_1+A_2+A_3-2A_4)$	1:1	2:2	2:1	$\frac{1}{2}(A_1+A_3)$	1:0:1	1:0	1:1	1:0	0:0
		A_3	0:1	0:0	0:1					$\frac{1}{2}(A_1+A_2+2A_4)$	0:1:0	0:0	0:0	0:0	0:0
										$\frac{1}{2}(A_1+A_2-2A_4)$	0:1:0	0:0	0:0	0:0	0:0
	$A \leftrightarrow B$	A_1	2:1	4:2	2:1	$\frac{1}{3}(A_1+A_2+A_3+2A_4)$	0:3	0:0	0:9	$\frac{1}{2}(A_2+A_3)$	1:2:1	1:2	1:1	1:2	2:2
		A_2	2:1	4:2	2:1	$\frac{1}{3}(A_1+A_2+A_3-2A_4$	4:1	32:8	8:1	$\frac{1}{2}(A_1+A_3)$	1:2:1	1:2	1:1	1:2	2:2
		A_3	0:2	0:0	0:0					$\frac{1}{2}(A_1+A_2+2A_4)$	0:0:2	0:0	0:0	0:0	
										$\frac{1}{2}(A_1+A_2-2A_4$	2:0:0	8:0	0:0	0:0	
Triclinic	$A \leftrightarrow$	A_1	8:2	64:16	16:0	$\frac{1}{3}(A_1+A_2+A_3+2A_4+2A_5+2A_6)$	4:7	32:56	56:49	$\frac{1}{2}(A_1+A_2-2A_4)$	16:32	16:0	0:0	32:0	
		A_2	2:5	4:10	10:9	$\frac{1}{3}(A_1+A_2+A_3+2A_4-2A_5-2A_6)$	4:7	32:56	56:49	$\frac{1}{2}(A_1+A_2+2A_4)$	0:8:4	0:0	0:0	0:32	0:32
		A_3	2:5	4:10	10:9	$\frac{1}{3}(A_1+A_2+A_3-2A_4+2A_5-2A_6)$	0:9	0:0	0:81	$\frac{1}{2}(A_1+A_3+2A_6)$	9:2:1	81:18	81:9	9:2	18:2
						$\frac{1}{3}(A_1+A_2+A_3-2A_4-2A_5+2A_6)$	16:1	512:32	32:1	$\frac{1}{2}(A_2+A_3+2A_5)$	1:2:9	1:2	1:9	9:18	2:18
										$\frac{1}{2}(A_1+A_3-2A_6)$	1:2:9	1:2	1:9	9:18	2:18
										$\frac{1}{2}(A_2+A_3-2A_5)$	9:2:1	81:18	81:9	9:2	18:2

References

[1] A. Kaplyanskii, Optics and Spectroscopy **16**, 557 (1964).